



Delft University of Technology

Towards a bottom-up reconstitution of the nuclear pore complex

Fragasso, A.

DOI

[10.4233/uuid:c717460d-eb79-495a-b239-4d030d0412c6](https://doi.org/10.4233/uuid:c717460d-eb79-495a-b239-4d030d0412c6)

Publication date

2021

Document Version

Final published version

Citation (APA)

Fragasso, A. (2021). *Towards a bottom-up reconstitution of the nuclear pore complex*. [Dissertation (TU Delft), Delft University of Technology]. <https://doi.org/10.4233/uuid:c717460d-eb79-495a-b239-4d030d0412c6>

Important note

To cite this publication, please use the final published version (if applicable).
Please check the document version above.

Copyright

Other than for strictly personal use, it is not permitted to download, forward or distribute the text or part of it, without the consent of the author(s) and/or copyright holder(s), unless the work is under an open content license such as Creative Commons.

Takedown policy

Please contact us and provide details if you believe this document breaches copyrights.
We will remove access to the work immediately and investigate your claim.

**TOWARDS A BOTTOM-UP RECONSTITUTION
OF THE NUCLEAR PORE COMPLEX**

TOWARDS A BOTTOM-UP RECONSTITUTION OF THE NUCLEAR PORE COMPLEX

Dissertation

for the purpose of obtaining the degree of doctor
at Delft University of Technology,
by the authority of the Rector Magnificus, Prof.dr.ir. T.H.J.J. van der Hagen,
chair of the Board for Doctorates to be defended publicly on
Friday 12th November 2021 at 15:00 o' clock

by

Alessio FRAGASSO

Master of Science in Nanotechnologies for ICTs,
Politecnico di Torino, Grenoble INP Phelma, and École
Polytechnique Fédérale de Lausanne,
born in Camposampiero, Italy.

This dissertation has been approved by the
promotor: Prof. dr. C. Dekker

Composition of the doctoral committee:

Rector Magnificus	chairperson
Prof. dr. C. Dekker	Delft University of Technology

Independent members:

Prof. dr. M. Dogterom	Delft University of Technology
Prof. dr. R. Lim	University of Basel
Prof. dr. A. Zilman	University of Toronto
Prof. dr. L. M. Veenhoff	University of Groningen
Dr. S. Caneva	Delft University of Technology
Prof. dr. B. Rieger	Delft University of Technology, reserve member

Other members:

Prof. dr. P. R. Onck	University of Groningen
----------------------	-------------------------



Keywords: nuclear pore complex; nanopores; FG nups; intrinsically disordered proteins; biomimetics; DNA origami; 1/f noise

Printed by: Gildeprint

Front & Back: Erik Major

Copyright © 2021 by A. Fragasso

Casimir PhD Series, Delft-Leiden 2021-28

ISBN 978.90.8593.494.3

An electronic version of this dissertation is available at
<http://repository.tudelft.nl/>.

CONTENTS

1	General Introduction	1
1.1	Introduction	2
1.2	The nuclear pore complex	3
1.3	Bottom-up approaches to unravel the NPC	7
1.4	Single-molecule sensing with nanopores	7
1.5	DNA origami nanotechnology	10
1.6	In this thesis	12
	References	14
2	Comparing current noise in biological and solid-state nanopores	21
2.1	Introduction	22
2.2	Noise sources in nanopores	23
2.3	Noise in biological nanopores	26
2.4	Noise in solid-state nanopores	28
2.5	Comparing the performance of biological and solid-state nanopores	29
2.6	Approaches to overcome noise limitations	32
2.7	Conclusion	34
	References	35
3	1/f noise in solid-state nanopores is governed by access and surface regions	45
3.1	Introduction	46
3.2	Results	47
3.3	Conclusion	53
3.4	Supporting Information.	55
	References	62
4	Nanopores: beyond DNA sequencing	69
4.1	Introduction	70
4.2	Characterization of single proteins with nanopores	72
4.3	Single-Molecule Chemistry	75
4.4	Synthetic nanopores as a tool to study biological questions	78
4.5	Nanopore sensors for biomarker identification and quantification in clinical samples	80
4.6	Conclusion and perspectives	83
	References	84
5	A designer FG-Nup that reconstitutes the selective transport barrier of the nuclear pore complex	93
5.1	Introduction	94
5.2	Results	95

5.3 Conclusion	109
5.4 Methods	111
5.5 Supporting information.	119
References	138
6 Studying karyopherins occupancy in the nuclear pore complex using biomimetic nanopores	145
6.1 Introduction	146
6.2 Results	147
6.3 Conclusion	153
6.4 Methods	155
6.5 Supporting information.	157
References	159
7 Reconstitution of ultrawide DNA origami pores in liposomes for transmembrane transport of macromolecules	163
7.1 Introduction	164
7.2 Results	164
7.3 Conclusion	173
7.4 Methods	176
7.5 Supporting information.	181
References	215
8 Future directions	219
8.1 Designer FG-Nups – a playground for studying NPC selectivity	220
8.2 Study how the Kaps regulate the FG-Nup barrier	222
8.3 Towards building an artificial nucleus.	224
8.4 Final outlook	226
References	227
Summary	231
Samenvatting	235
Acknowledgements	239
Curriculum Vitæ	243
List of Publications	245

1

GENERAL INTRODUCTION

In this chapter I present a general introduction to the thesis. While the main interest is to understand the mechanism by which the nuclear pores in our cells operate, various topics and techniques are touched upon. Starting from a brief overview of the cellular organization, I narrow down into the nuclear pore complex, from the first discoveries of its architecture and composition to recent theories describing how nuclear transport is regulated. Furthermore, I discuss the importance of biomimetic approaches to study nuclear transport, with a particular emphasis on solid-state-nanopore and DNA-origami technologies.

1.1. INTRODUCTION

Life on earth is extremely diverse and variegated, from single-cell entities like bacteria or yeast, to complex multi-tissue organisms such as humans. To achieve the sophistication found in more complex systems like eukaryotes, molecules are organized into organelles which, just like the organs in our body, carry out different specialized tasks (Figure 1.1a) [1]. For example, mitochondria produce the chemical energy needed to perform biochemical reactions in the cell, ribosomes read strings of mRNA to synthesize new proteins, while the nucleus stores the hereditary information in the form of DNA [2]. To safely protect the genetic material, eukaryotic cells feature a double membrane nuclear envelope (NE) that encloses and physically isolates the nucleus from the rest of the cell [3].

Nuclear Pore Complexes (NPCs) are large protein assemblies that form $\sim 40\text{nm}$ -wide channels across the NE and behave as gatekeepers by controlling the trafficking of RNAs, proteins, and metabolites between the nucleus and the cytoplasm (Fig. 1.1b) [4]. In a single cell, the number of nuclear pores can vary from 75–150 in a yeast cell [5] to ~ 3000 –5000 pores in a human cell [6], to $\sim 5 \times 10^7$ in a mature *Xenopus* oocyte [7]. A fascinating aspect of the NPC is its unique combination of high versatility while retaining specificity. In fact, up to 30 different types of transporter proteins are recognized and allowed to efficiently translocate through the NPC, while precluding the transport to all other large molecules [8]. The secret for such highly selective transport relies in a group of key proteins, called FG-Nups, which form a tangled spaghetti-like mesh within the central channel of the NPC [9].

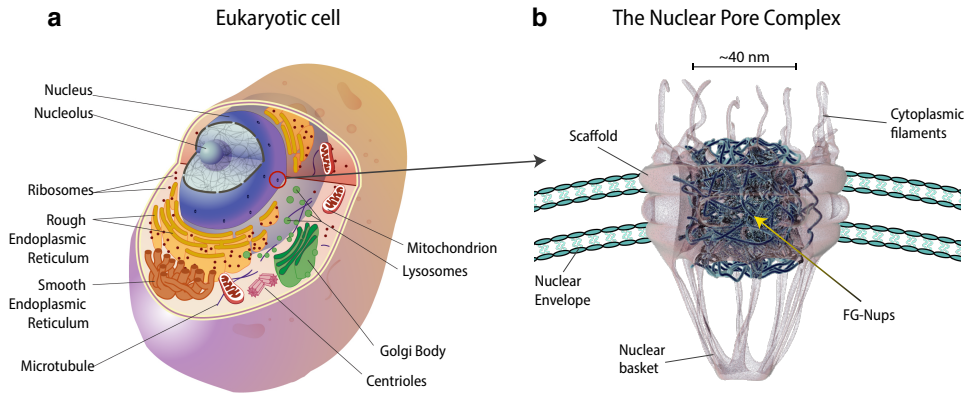


Figure 1.1: a, Schematic of an eukaryotic cell, adapted from [10]. b, Illustration of the nuclear pore complex embedded in the nuclear envelope. FG-Nups (blue) line the central channel forming a spaghetti-like mesh. Adapted from a design of Samir Patel.

In this thesis, we work towards understanding the physical principles underlying this remarkable NPC selectivity, leveraging on techniques from molecular biology to nanotechnology. To understand and properly interpret the signal coming from our nanodevices, we first delve into a physical characterization of the noise sources that affect ion current measurements in solid-state nanopores. We then move on to engineer a fully

synthetic FG-Nup from scratch and study its selective properties by reconstituting an artificial mimic of the NPC transport barrier using such a designer protein. Additionally, we provide supporting evidence that point to a mechanistic description of nuclear transport by studying the behavior of a purified native FG-Nup. Finally, we take a major step towards the reconstitution of an artificial nucleus by embedding 30nm-wide DNA-origami pores into the membrane of a lipid vesicle. The present work opens the way to multiple exciting applications and follow-up projects towards the recapitulation and physical understanding of nuclear transport, as well as creating artificial models of the nucleus that can be employed in synthetic cells.

1.2. THE NUCLEAR PORE COMPLEX

1.2.1. ARCHITECTURE AND COMPOSITION

First evidence of the existence of the NE and nuclear pores was provided in 1950 by Callan and Tomlin [11], who performed imaging of the nuclear membrane of oocytes from amphibia using electron microscopy (EM). Further investigation by Gall in 1967 [12] revealed the octagonal symmetry of nuclear pores (Figure 1.2a,b), which was confirmed by other follow-up studies [13, 14]. Further refinements of the NPC structure using EM allowed to resolve other peripheral parts of the NPC, which include the cytoplasmic filaments and nuclear basket (Fig.1.2c–e, [refs]) [15, 16]. The biochemical composition of the NPC consists of ~30 different types of nucleoporins (Nups) repeated in multiple copies following the octagonal symmetry of the pore. The distribution of Nups is modular and they can be distinguished in three categories [17, 18]: (1) transmembrane Nups that anchor the NPC to the NE; (2) scaffold Nups that form a rigid ring-like

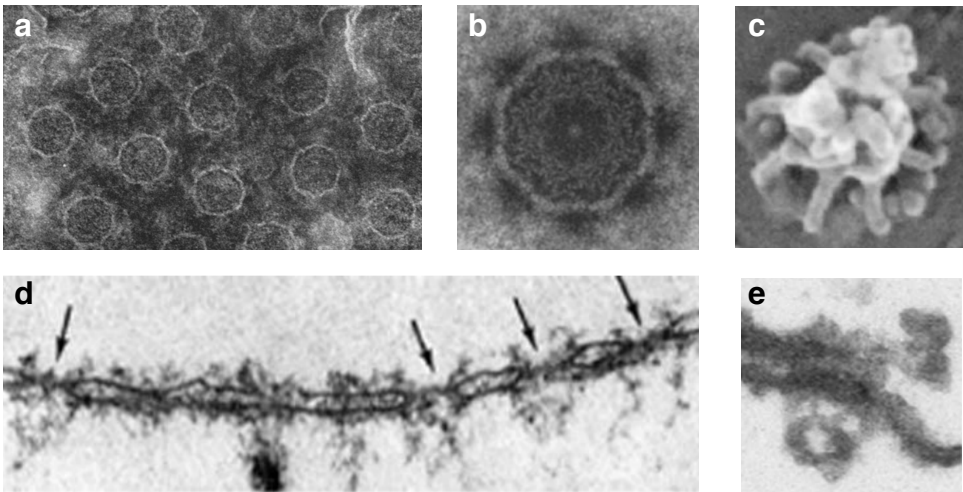


Figure 1.2: a,b, Negative staining EM showing octagonal cross-sections of nuclear pore complexes extracted from *Triturus alpestrus* nuclei (adapted from [12]). c, Electron microscopy structure of the nuclear pore complex from the nucleoplasmic side. Adapted from [15]. d, Negative staining EM of the nuclear envelope featuring embedded NPCs (pointed by arrows). Adapted from [16]). e, Transmission electron microscopy image of a nuclear pore complex. Adapted from [19].

structure to which intrinsically disordered (3) FG-Nups, rich in tandem ‘Phenylalanine-Glycine’ (FG) repeats, are anchored by their C-terminal domain and fill up the NPC central channel forming a gel-like mesh.

1.2.2. FG-NUPS – TYPES AND MOTIFS

The central channel of the NPC is lined with intrinsically disordered FG-Nups (11 different types in yeast [20]). Based on their amino-acid sequence, FG-Nups appear quite redundant, with all of them featuring tandem Phe-Gly (FG) repeats separated by spacer sequences of ~5-20 amino-acids (Fig.1.3a) [21]. Moreover, they are evolutionary conserved in their overall composition and structure [22]. FG-Nups can be broadly divided into two main categories [20, 21]: (1) FXFG-Nups which are abundant in Phe-Any-Phe-Gly (FXFG) repeats, where ‘X’ can be any amino-acid, featuring spacers relatively high in charge (~26-36% of amino-acids has a charge), which confer FXFG-Nups with an overall extended and dynamic conformation; (2) GLFG-Nups that instead are rich in Gly-Leu-Phe-Gly (GLFG) repeats with spacer sequences enriched in ‘Q’ and ‘N’ amino-acids. Unlike FXFG-Nups, these possess a low amount of charged amino-acids (2-3%) resulting in a more collapsed coil configuration. Strikingly, deletion of all FG-Nups other than the GLFG-Nups Nup100, Nup116, and Nup145, was shown to still support efficient nuclear transport *in vivo* without impairing the viability of the cell, which showcases the outstanding robustness and redundancy of the FG-Nup barrier [24].

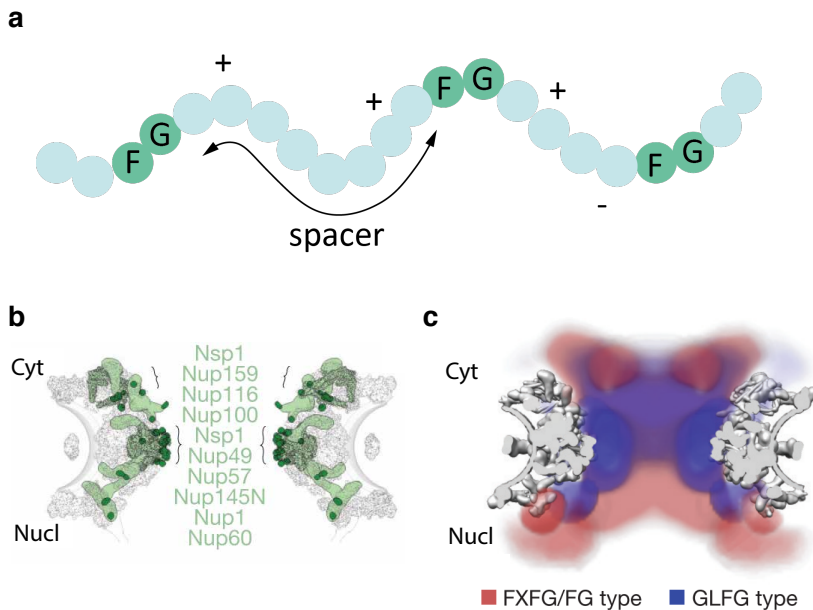


Figure 1.3: a, Representation of a characteristic FG-Nup protein sequence. b, Structure of the NPC scaffold (grey) with highlighted FG-Nups anchor domains (light green) and FG-repeat emanating points (dark green). c, Heat map of the GLFG (purple) and FXFG (red) domains from Brownian dynamics simulations. b and c were adapted from [23].

1.2.3. NUCLEOCYTOPLASMIC TRANSPORT

FG-Nups are key players in regulating molecular transport across the NE [9]. While allowing the passive diffusion of small molecules, *e.g.* water, ions, and proteins up to a size cut-off of ~40 kDa, transport of large molecules (>40 kDa) occurs selectively [25]: inert macromolecules are hindered by the FG-mesh unless they are bound to a nuclear transport receptor (NTR). Karyopherins (or Kaps) constitute the largest family of NTRs [26], with importin- β (Imp β , Kap95 in yeast) being the most characterized as it plays a central role in nuclear import [27]. It features ~9-10 hydrophobic pockets on its convex surface that can specifically bind FG-motifs [28], which in turn facilitates its partitioning into the NPC channel. In this way, cargoes that feature a nuclear localization signal (NLS) sequence can form a complex with a NTR and be ferried across the NPC within a few milliseconds (~5 ms [29]).

While maintenance of an efficient and selective transport by the FG-mesh comes at no energy cost, energy is spent in form of GTP hydrolysis to enforce transport directionality of cargoes [30, 31]. For nuclear import (Fig.1.4) of cargo from the cytoplasm into the nucleus, cargo-bound NTRs bind to the nuclear factor RanGTP which induces a NTR conformational change that causes the release of the cargo into the nucleus. The NTR-RanGTP complex is subsequently recycled back into the cytoplasm, where RanGTP is hydrolyzed into RanGDP by the cytoplasmic factor RanGAP1. Such release of energy induces a conformational change that causes the dissociation of the RanGDP-NTR complex, making the NTR available for a new import cycle. RanGDP is then transported back into the nucleus by the transport factor NTF2, where it finally gets converted back into RanGTP by RanGEF. Nuclear export occurs in an analogous way to the import [33].

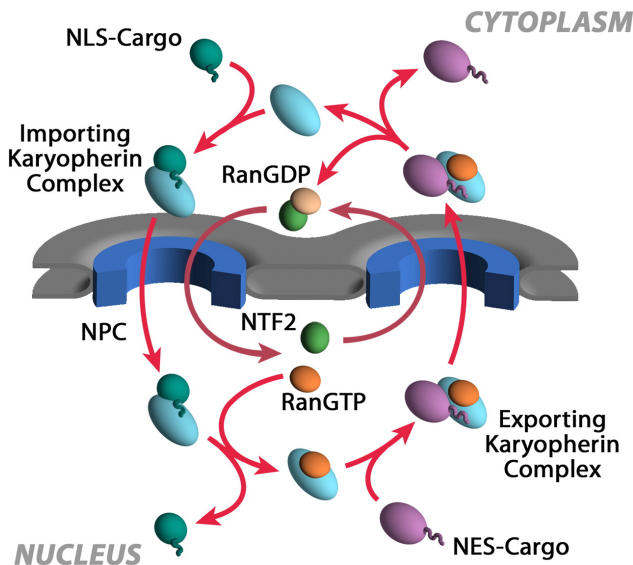


Figure 1.4: Schematic of the RanGTP-regulated nuclear transport and their cargoes. Adapted from [32].

1.2.4. MODELS OF SELECTIVE TRANSPORT

While nucleocytoplasmic transport is well characterized in terms of key players and regulation processes, the exact mechanism governing the selective transportation of cargo-bound NTRs through the NPC channel is still disputed. In fact, a number of models have been proposed which can be broadly classified into two opposing theories, termed ‘FG-centric’ and ‘Kap-centric’ models:

FG-centric models: The first class of models includes the ‘virtual gate model’ [36], ‘selective-phase’ or ‘hydrogel model’ [37, 38], and ‘forest model’ [20], which predict that FG-Nups are the sole necessary ingredient in establishing the selective barrier. As a corollary, this implies that Kaps act as mere transporters of cargo molecules, without in any way altering the structure of the FG-mesh or taking part into forming the selective barrier (Fig.1.5, left).

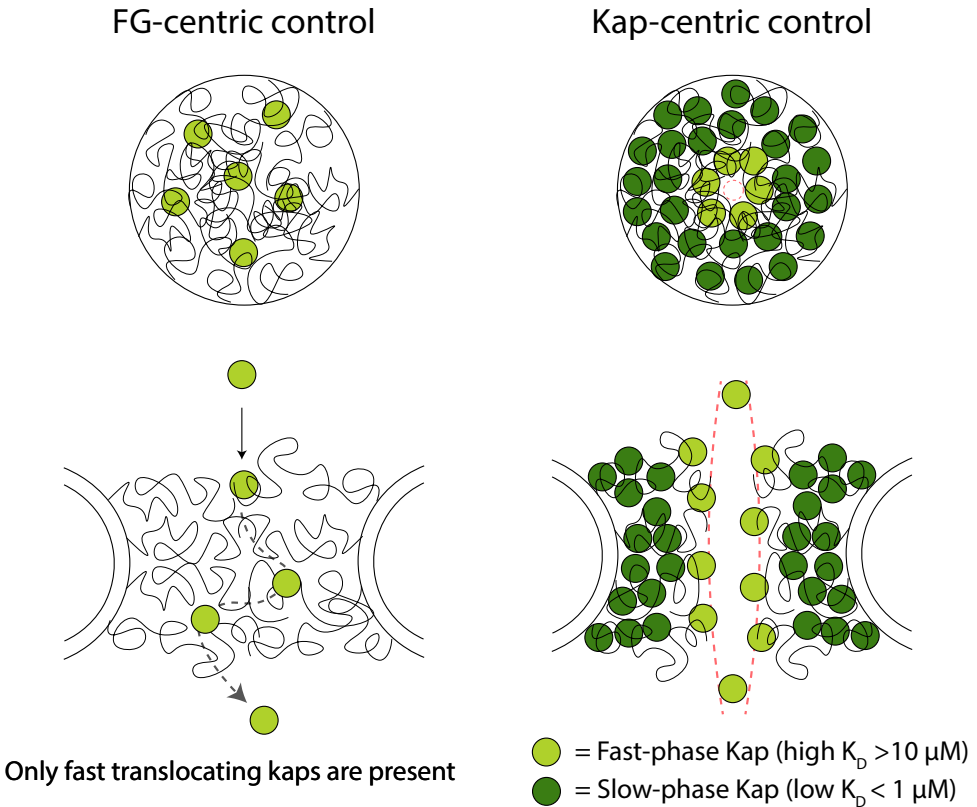


Figure 1.5: Simplified schematic of ‘FG-centric’ (left) and ‘Kap-centric’ (right) transport. Black curved lines represent FG-Nups, light and dark green circles correspond to the fast-phase and slow-phase Kap population, respectively, dashed black arrow (left) represent a Kap trajectory, dashed red lines (right) indicate the central channel opening. Inspired by [34] and [35].

Kap-centric models: The second class of models, such as the ‘reduction of dimensionality model’ [39], ‘molecular velcro model’ [40], and further refinements [34, 35, 41–43], supports the existence of two distinct populations of Kaps – a ‘slow-phase’ and a ‘fast-phase’, where the slow-phase Kaps are involved in reshaping the FG-mesh while opening a central channel by means of avid multivalent binding to FG-repeats, whereas fast-phase Kaps are the actual transporters that shuttle the cargo across the NPC (Fig.1.5, right). Importantly, occupation of the FG-mesh by the slow-phase Kaps would result in a partial depletion of the available FG-repeats hence lowering the affinity between the Kap-laden FG-mesh and the fast-phase Kaps.

1.3. BOTTOM-UP APPROACHES TO UNRAVEL THE NPC

Studying transport through the nuclear pore complex *in vivo* still faces significant challenges and limitations due to a lack of spatiotemporal resolution. The NPC is a complex machine, comprising ~200 intrinsically disordered FG-Nups confined into a ~40nm-wide central lumen, with ~1000 molecules per second being transported across in both directions [44]. Gaining mechanistic information on the translocation process of Kap-cargo complexes through the FG-mesh has thus far remained prohibitively difficult.

To overcome such challenges, biomimetic techniques have emerged as an alternative approach to study nuclear transport, where the FG-mesh that is found in the central channel of the NPC is reconstituted *in vitro* and characterized using a variety of tools. Notable examples include surface techniques, such as ellipsometry and QCM-D [45, 46], SPR [34, 47], and AFM force spectroscopy [40, 48], which contributed greatly to the characterization of the binding affinity between Kaps and FG-Nup brushes, where such brushes were formed by anchoring FG-Nups to a planar surface with a grafting density comparable to the one found in the real NPC. Importantly, such techniques revealed the presence of distinct binding modes between Kaps and FG-Nup brushes that vary as a function of Kap concentration and that stem from the multivalent nature of the interaction.

While studying the affinity between transporters and FG-Nups is beneficial and insightful, selective transmembrane transport is arguably the most crucial, yet puzzling, feature of the NPC. To study such important aspect, in the last decade NPC mimics based on artificial nanopores have been built by tethering purified FG-Nups to the inner walls of a nanopore [49, 50]. The appeal of this approach resides in the possibility to reconstitute the selective FG-Nup barrier into a confined nanopore system with virtually the same geometry and FG-Nup density as the NPC central channel. We will now introduce two major realizations of biomimetic nanopores that take advantage of state-of-the-art solid-state and DNA-origami nanotechnology.

1.4. SINGLE-MOLECULE SENSING WITH NANOPORES

Advancements in nanotechnology have enabled the fabrication and development of solid-state nanopores [51, 52]. In simple terms, a solid-state nanopore can be described as a nanometer-sized hole formed across a thin (typically ~20 nm) freestanding membrane built from a solid-state material. Over the years, a variety of membranes have been employed as substrates for nanopore fabrication, from the more common low stress sili-

con nitride [53, 54] (SiN) to silicon dioxide (SiO_2), as well as ultrathin 2D-materials such as graphene [55, 56], hexagonal boron nitride (hBN) [57, 58], or molybdenum disulfide (MoS_2) [59]. To create such nanoholes various techniques have been developed that respond to different needs in terms of precision, cost, and throughput. To create pores with nanometer-precision a transmission electron microscope (TEM) is usually the preferred choice (Fig. 1.6a,b), where a beam of electrons is focused onto a freestanding membrane which results in removal of atoms from the material and the formation of a hole [60]. A more high-throughput, though less precise, method to fabricate pores is milling using a focused ion beam (FIB) [61, 62], which works analogously to the TEM but with ions (typically Ga^+ or He^+) instead of electrons. Other techniques are dielectric breakdown [63, 64], laser etching [65], reactive ion etching (RIE) [66], and mechanical pulling of glass capillaries [67].

The most common application of nanopore technology consists in single-molecule sensing, which is achieved by encasing the nanopore chip in a flow cell where the nanopore constitutes the sole connection between two otherwise insulated compartments [68]. Such compartments are filled with a saline aqueous solution, *e.g.* potassium chloride (KCl), which results in free K^+ and Cl^- ions. Application of a voltage difference across the freestanding membrane results in an electric field across the pore that drives positive ions K^+ to the side with negative potential and Cl^- to the positive one. Such flow of ions across the pore results in an ionic current which can be sensed by the electronics and that serves as the signal to perform sensing [69].

The basic principle of nanopore sensing is illustrated in Figure 1.6c,d, where the analyte of interest, such as a protein or a DNA molecule, is electrophoretically driven across the pore by the applied voltage difference which causes the flow of ions to be temporarily interrupted due to the presence of the molecule. This effectively results in a transient, detectable decrease of the ionic current (Fig. 1.6d). Single-molecule translocation events are associated with such current ‘spikes’ and are typically characterized in terms of amplitude (or blockade), namely the depth of the current decrease which is roughly propor-

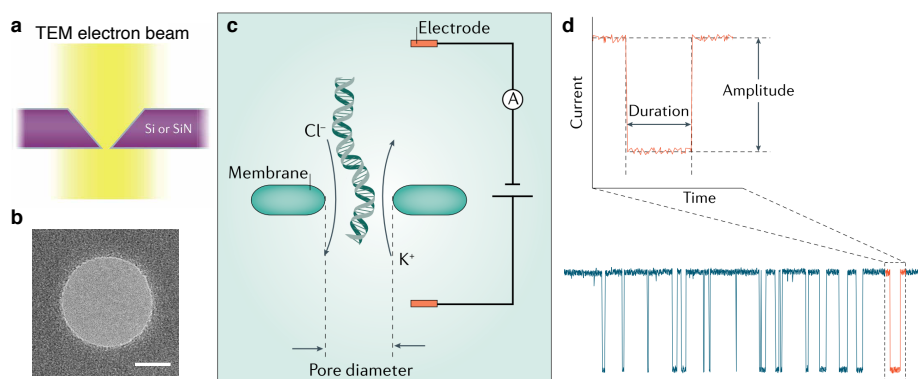


Figure 1.6: a, Illustration of nanopore fabrication by TEM drilling. b, TEM micrograph of a nanopore. Scale bar, 30nm. c-d Principle of nanopore sensing: molecules are electrically driven through the pore by an applied potential difference causing transient dips (d) in the ionic current. a, c, d, were adapted from [52].

tional to the size of the analyte, and dwell time which corresponds to the duration of the event and, to a first approximation, reflects how much time the molecule spends in the pore.

1.4.1. BIOMIMETIC SOLID-STATE NANOPORES

While nanopores are usually thought of as next-generation sequencers of DNA [70] and proteins [71], an exciting application consists in mimicking biological processes by recapitulating the behavior of naturally occurring pores such as the NPC. In the context of this thesis, a biomimetic solid-state nanopore consists of a solid-state nanopore that is functionalized with FG-nucleoporins from the nuclear pore complex with the aim to mimic as closely as possible the native FG-mesh in terms of spatial confinement, geometry, and protein density, while being able to probe the transport across the pore with single-molecule resolution by measuring the ionic current (Fig.1.7a). Functionalization of the nanopore surface is generally carried out by a chemical conjugation protocol [50, 72], which ensures proper covalent attachment of the proteins to the solid-state material. To test the selective properties of the reconstituted FG-mesh, transporter proteins, such as Imp β , are used as positive control since they are naturally capable of interacting with and overcoming the FG-Nup barrier. On the contrary, inert proteins like BSA that lack binding sites for FG-repeats are repelled by the FG-mesh and thereby fail to traverse the pore.

Current measurements are carried out similarly as in a standard nanopore experiment, where the current flowing across the FG-Nup-coated pore reports in real-time on the passage of proteins (Fig.1.7b), and thus allows to assess the selective transport properties in terms of event rate, *i.e.* number of translocations per second, which is a measure of the transport efficiency of the analyte across the pore. Notably, such current measurements revealed that biomimetic pores built using a single type of FG-Nup (*e.g.*, Nup98 or Nup153) were enough to impart a selective barrier, where Imp β can efficiently translocate while BSA is blocked (Fig.1.7c) [49, 50, 72].

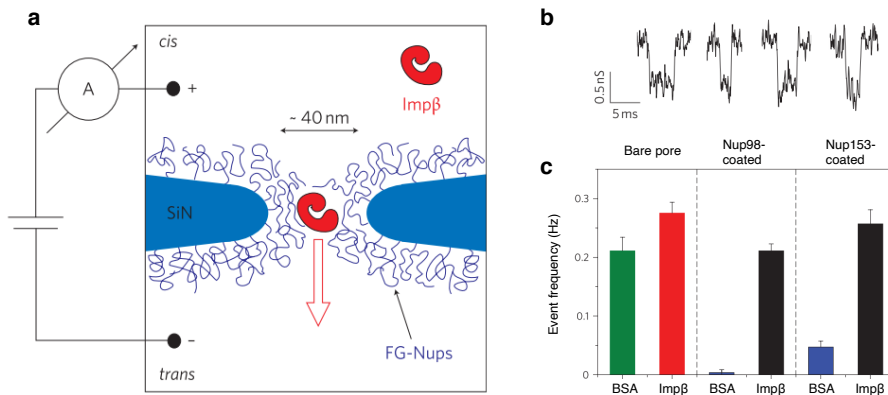


Figure 1.7: a, Schematic of a biomimetic solid-state nanopore system. b, Examples of translocation events of Imp β through a FG-Nup coated pore. c, Event rate of translocations of BSA and Imp β through a bare (left), Nup98-coated (center), and Nup153-coated (right) pores. Adapted from [50].

1.5. DNA ORIGAMI NANOTECHNOLOGY

While DNA (deoxyribonucleic acid) in biology assumes the passive role of mere information carrier, as unlike proteins it does not perform any sensory or actuator function in the cell, in the last three decades scientists have been able to use DNA molecules to build 3D nanostructures from scratch in a fully programmable way [73, 74]. Such promising technology, known as ‘DNA origami’, exploits the structure of the DNA molecule that consists of two strands of nitrogenous bases (adenine (A), guanine (G), thymine (T), and cytosine (C)) that are mutually held together by hydrogen bonds resulting in a double helix, where such bonds can occur only between complementary bases A-T and G-C.

Creation of DNA nanostructures relies on using a long single strand of DNA as a scaffold which, upon adding many short DNA strands that staple different parts of the scaffold, is folded into a 3D shape (Fig 1.8a) [75]. Using this relatively simple concept it has been possible to build a multitude of nanostructure for various purposes, from regular shapes such as 2D-sheets and cubes (Fig.1.8b) [73], to more complex structures such as spirals and rings (Fig.1.8c) [76].

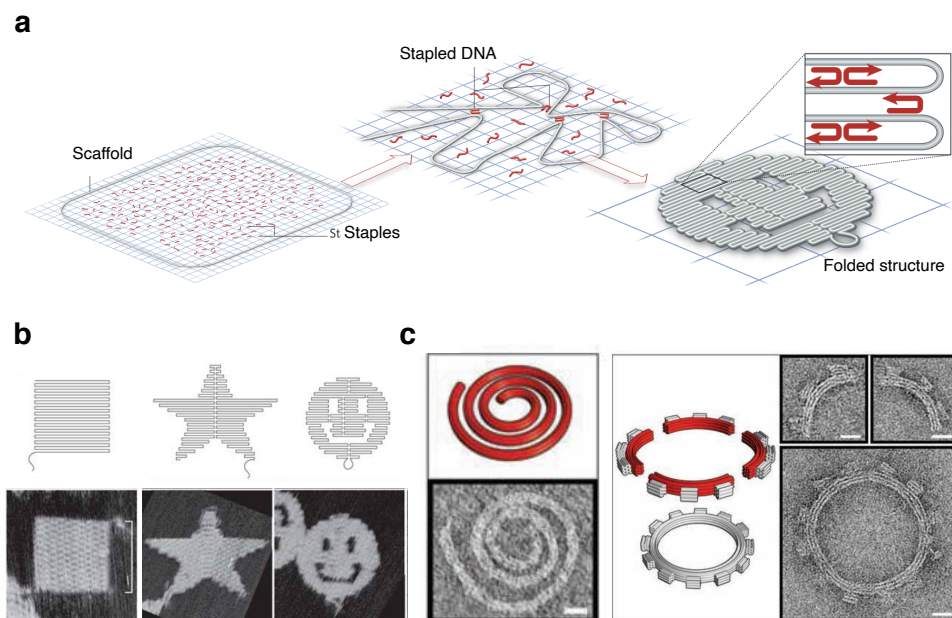


Figure 1.8: a, Illustration of the typical DNA origami workflow. A long scaffold of DNA is stapled together by short pieces of DNA to form a stably folded structure. Adapted from [75]. b, Examples of design (top) and AFM images (bottom) of simple DNA-origami structures. Adapted from [73]. c, Examples of complex twisted DNA-origami structures. Scale bars, 20nm. Adapted from [76].

1.5.1. DNA ORIGAMI NANOPORES AND NPC MIMICS

A relevant application in the context of this thesis is the construction of DNA-origami pores that mimic the pore-forming properties of naturally occurring protein pores such as α -hemolysin [77]. Similarly to a biological pore, DNA-origami pores from the literature have been engineered with hydrophobic moieties, such as cholesterol or porphyrins, that aid in the insertion of the highly hydrophilic DNA-object into a lipid bilayer membrane (Fig.1.9) [78]. Using this approach, pores with inner diameters from a few nanometers [79, 80] up to 10 nm [81, 82] have been constructed and shown to spontaneously insert into a lipid membrane by allowing the transmembrane transport of ions [79, 83], fluorophores [81, 84], and short artificial polymers such as PEG [80] and dextran [81, 82].

An exciting feature of DNA-origami pores is the possibility to functionalize the inner walls of the pore to build a mimic of the NPC where FG-Nups distribution and density of the anchor points can be programmed by design. Using this approach, it has been possible to reconstitute NPC mimics by folding DNA-origami rings of ~ 35 – 40 nm in inner diameter (similar to the native NPC) and by attaching FG-Nups to their inner surface [85, 86]. However, one major limitation of this approach is the impossibility to measure transport across the reconstituted FG-mesh, since it is extremely challenging to insert such large DNA-objects into a lipid bilayer.

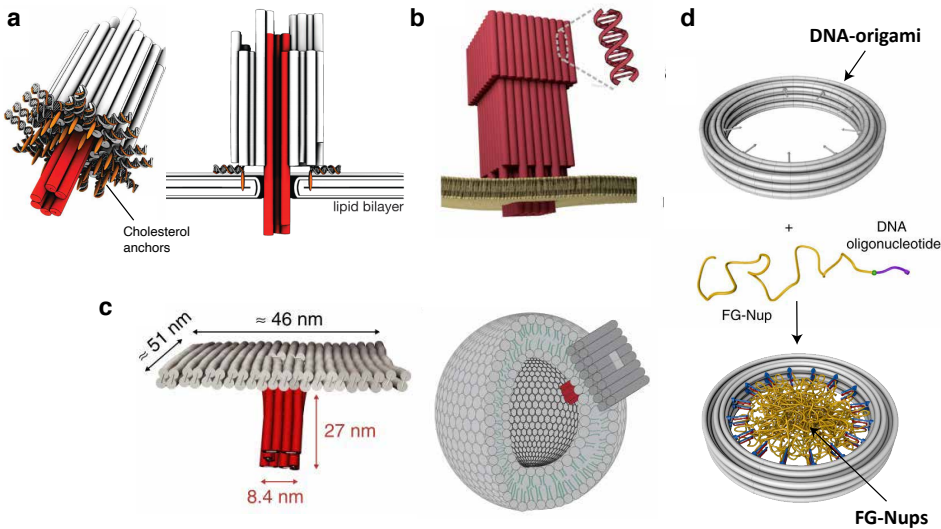


Figure 1.9: a, First reported DNA-origami pore with a inner diameter of 2 nm, functionalized with 26 cholesterol anchors (orange). Adapted from [79]. b, Funnel-shaped transmembrane DNA-pore with 6 nm inner diameter. Adapted from [83]. c, T-shaped DNA-origami pore with ~ 4 nm inner diameter. Adapted from [84]. d, DNA-origami ring scaffold (grey) for FG-Nup (yellow) attachment. Adapted from [85].

1.6. IN THIS THESIS

This thesis aims to contribute with novel bottom-up approaches to the field of nuclear transport using biomimetic nanopores. We propose a new model system to understand and capture the essence of FG-Nups, as well as alternative strategies to circumvent the current technical difficulties in current biomimetic DNA-origami nanopore systems. The next two chapters following the introduction are focused on characterization of the noise sources in solid-state nanopores. **Chapter 2**, provides a side-by-side comparison of the noise and performance of biological and solid-state pores. First, the physical origin of the noise at different frequencies is provided together with literature studies and measurements on a few exemplary nanopore systems. Second, the performance of the most relevant biological and solid-state nanopores is compared in terms of signal-to-noise ratio (SNR). We find that SiN_x pores offer the highest SNR of ~ 37 when measuring free translocations of short DNA homopolymers through the pores. Introducing a slowdown mechanism using a DNA-translocating motor protein on top of a MspA pore was shown to boost the SNR by >160 -fold. Finally, we review reported methods from the literature that were shown to lower the noise for various nanopore systems and frequency ranges. In **Chapter 3**, we explore the low-frequency $1/f$ noise in solid-state nanopores for varying pore diameters and find that the $1/f$ noise magnitude decreases for increasing diameter of the pore. To capture this behavior, we build a generalized version of the previously proposed Hooge's model for nanopores that includes explicit contributions from access region and pore surface. Additionally, we define different Hooge parameters for bulk and surface $1/f$ noise, which represent different mechanisms of fluctuations affecting the ionic current. Such model refinement allows for a more accurate characterization of the $1/f$ noise in solid-state nanopore systems. **Chapter 4** reviews the state-of-the-art in the field of nanopores, with particular emphasis on applications beyond sequencing. These include single-molecule proteomics, biomarker detection by single-molecule liquid biopsy, pore nanoreactors to confine and study the chemistry of single polymers, and biomimetic nanopore-based approaches to study biological questions.

In **Chapter 5** we introduce a novel, fully bottom-up approach to study nuclear transport by designing an artificial protein, termed 'NupX', that mimics and models native FG-Nups. To design such sequence, we proceed by first analyzing the properties of the naturally occurring GLFG-Nups from yeast. We hypothesize that a finite set of properties characteristic of GLFG-Nups is sufficient for recapitulating their selective behavior, namely: (i) regularly spaced FG and GLFG repeats, (ii) a bimodal distribution of amino acids forming a repulsive and a cohesive domain, and (iii) intrinsic disorder of the amino acid sequence. We first assess the affinity between brushes of our designer NupX and transporter Kap95 using QCM-D, finding that Kap95 binds the protein brush in a concentration-dependent manner. On the contrary, flushing the inert protein BSA does not result in any detectable interaction, thereby proving the binding specificity between Kap95 and NupX. Next, we reconstitute NupX in biomimetic nanopores and test its selective properties, finding that while Kap95 can efficiently translocate through the pore resulting in frequent current spikes, BSA is blocked. Our experiments are complemented by molecular dynamics simulations which provide insights into microscopic features of NupX brushes and coated pores. In summary, this work validates our initial

hypothesis that a rationally designed FG-Nup can reconstitute the archetypal selectivity of the nuclear pore complex.

In **Chapter 6** we reconstitute biomimetic solid-state nanopores using a native FG-Nup, Nsp1, and test its transport properties as a function of Kap95 concentration with the aim to provide new evidence that can aid to discriminate between the different models of transport, specifically between 'FG-centric' and 'Kap-centric' models. Upon titrating Kap95 onto a Nsp1-coated pore we observe a Kap95 concentration-dependent step-wise decrease of the pore conductance, which indicates Kap95 incorporation into the Nsp1-mesh. Additionally, fast Kap translocations are also observed on top of the current decrease at low (~ 100 nM) Kap concentrations, similarly to previous reports. On the contrary, flushing inert BSA on a Nsp1-coated pore at increasing concentrations did not result in any detectable current decrease, nor fast translocations, confirming that the observed incorporation of Kap95 into the Nsp1-mesh originates from specific protein-protein interactions and not merely as an effect of the applied bias. Next to a decrease in the pore conductance, we also report a decrease of the low-frequency $1/f$ noise which is consistent with a stiffening of the Nsp1-mesh upon binding of Kap95. Ion current measurements are corroborated with QCM-D data that, similarly, show a concentration-dependent binding and incorporation of Kap95 into the Nsp1 brush. Altogether, our data are consistent with the 'slow-phase' and 'fast-phase' Kaps notions introduced by the Kap-centric models.

Chapter 7 provides an alternative approach to solve the current challenges faced by DNA-origami nanopore systems, namely the difficulty of inserting large DNA-origami objects into lipid membranes. To mimic the eight-fold symmetry and geometry of the NPC, we first design an octagonal DNA-origami scaffold with a nominal inner diameter of 35 nm. Next, we chemically decorate its external surface with hydrophobic moieties which are meant to facilitate the partitioning of the DNA-origami structure into the hydrophobic lipid bilayer. We show that, while DNA-pores do not spontaneously insert into pre-formed lipid bilayers, as expected given the large size, it is possible to circumvent this problem by administering the pores during the vesicle formation by employing an inverted-emulsion cDICE technique to produce the vesicles. To assess the correct insertion of the pores, we carry out influx experiments with the fluorescent protein GFP and find that $\sim 50\%$ of the vesicle population features open pores. We quantify the influx rate by using a FRAP assay and, using a diffusion model to fit the FRAP data, find that up to hundreds of pores can be properly reconstituted into the membrane of a single vesicle. Furthermore, we show that our pores are size-selective, since dextran molecules with sizes up to 28 nm can translocate the pores, whereas larger molecules are excluded. In **Chapter 8**, finally, I provide my perspective on future possible directions and key experiments aimed to address some major open questions in the field of nuclear transport.

REFERENCES

- [1] L. H. B. A. Z. SL, and E. Al., *Molecular Cell Biology*, 4th ed. (W. H. Freeman, New York, 2000).
- [2] D. L. Nelson and M. Cox, *Principles of biochemistry* (W.H. Freeman and Company, New York, 2008).
- [3] M. W. Hetzer, *The Nuclear Envelope*, Cold Spring Harbor perspectives in biology **2**, 1 (2010).
- [4] S. R. Wentz and M. P. Rout, *The nuclear pore complex and nuclear transport*. Cold Spring Harbor perspectives in biology **2**, 1 (2010).
- [5] M. Winey, D. Yarar, T. H. Giddings, and D. N. Mastrorade, *Nuclear pore complex number and distribution throughout the Saccharomyces cerevisiae cell cycle by three-dimensional reconstruction from electron micrographs of nuclear envelopes*, Molecular Biology of the Cell **8**, 2119 (1997).
- [6] D. Görlich and U. Kutay, *Transport between the cell nucleus and the cytoplasm*, **15**, 607 (1999).
- [7] V. C. Cordes, S. Reidenbach, and W. W. Franke, *High content of a nuclear pore complex protein in cytoplasmic annulate lamellae of Xenopus oocytes*, European Journal of Cell Biology **68**, 240 (1995).
- [8] M. Mackmull, B. Klaus, I. Heinze, M. Chokkalingam, A. Beyer, R. B. Russell, A. Ori, and M. Beck, *Landscape of nuclear transport receptor cargo specificity*, Molecular Systems Biology **13**, 962 (2017).
- [9] S. R. Wentz, *Gatekeepers of the Nucleus*, Science **288**, 1374 (2000).
- [10] <https://www.genome.gov/genetics-glossary/Organelle>, .
- [11] H. G. Callan and S. G. Tomlin, *Experimental studies on amphibian oocyte nuclei. I. Investigation of the structure of the nuclear membrane by means of the electron microscope*. Proceedings of the Royal Society of London. Series B, Containing papers of a Biological character. Royal Society (Great Britain) **137**, 367 (1950).
- [12] J. G. Gall, *Octagonal nuclear pores*. The Journal of cell biology **32**, 391 (1967).
- [13] R. P. Aaronson and G. Blobel, *On the attachment of the nuclear pore complex*, The Journal of Cell Biology **62**, 746 (1974).
- [14] W. W. Franke and U. Scheer, *The ultrastructure of the nuclear envelope of amphibian oocytes: a reinvestigation. II. The immature oocyte and dynamic aspects*, Journal of Ultrastructure Research **30**, 317 (1970).
- [15] M. W. Goldberg, J. M. Cronshaw, E. Kiseleva, and T. D. Allen, *Nuclear-pore-complex dynamics and transport in higher eukaryotes*, Protoplasma **209**, 144 (1999).

- [16] N. Pante and U. Aebi, *Molecular dissection of the nuclear pore complex*, Critical Reviews in Biochemistry and Molecular Biology **31**, 153 (1996).
- [17] D. Devos, S. Dokudovskaya, R. Williams, F. Alber, N. Eswar, B. T. Chait, M. P. Rout, and A. Sali, *Simple fold composition and modular architecture of the nuclear pore complex*, Proceedings of the National Academy of Sciences of the United States of America **103**, 2172 (2006).
- [18] E. Onischenko, J. H. Tang, K. R. Andersen, K. E. Knockenhauer, P. Vallotton, C. P. Derrer, A. Kralt, C. F. Mugler, L. Y. Chan, T. U. Schwartz, and K. Weis, *Natively Unfolded FG Repeats Stabilize the Structure of the Nuclear Pore Complex*, Cell **171**, 904 (2017).
- [19] R. Y. Lim, U. Aebi, and B. Fahrenkrog, *Towards reconciling structure and function in the nuclear pore complex*, Histochemistry and Cell Biology **129**, 105 (2008).
- [20] J. Yamada, J. L. Phillips, S. Patel, G. Goldfien, A. Calestagne-Morelli, H. Huang, R. Reza, J. Acheson, V. V. Krishnan, S. Newsam, A. Gopinathan, E. Y. Lau, M. E. Colvin, V. N. Uversky, and M. F. Rexach, *A Bimodal Distribution of Two Distinct Categories of Intrinsically Disordered Structures with Separate Functions in FG Nucleoporins*, Molecular and Cellular Proteomics **9**, 2205 (2010).
- [21] L. J. Terry and S. R. Wentz, *Flexible Gates: Dynamic Topologies and Functions for FG Nucleoporins in Nucleocytoplasmic Transport*, Eukaryotic Cell **8**, 1814 (2009).
- [22] M. Peyro, M. Soheilypour, B. L. Lee, and M. R. Mofrad, *Evolutionarily Conserved Sequence Features Regulate the Formation of the FG Network at the Center of the Nuclear Pore Complex*, Scientific Reports **5**, 1 (2015).
- [23] S. J. Kim, J. Fernandez-Martinez, I. Nudelman, Y. Shi, W. Zhang, B. Raveh, T. Hericks, B. D. Slaughter, J. A. Hogan, P. Upla, I. E. Chemmama, R. Pellarin, I. Echeverria, M. Shivaraju, A. S. Chaudhury, J. Wang, R. Williams, J. R. Unruh, C. H. Greenberg, E. Y. Jacobs, Z. Yu, M. J. de la Cruz, R. Mironska, D. L. Stokes, J. D. Aitchison, M. F. Jarrold, J. L. Gerton, S. J. Ludtke, C. W. Akey, B. T. Chait, A. Sali, and M. P. Rout, *Integrative structure and functional anatomy of a nuclear pore complex*, Nature **555**, 475 (2018).
- [24] R. L. Adams, L. J. Terry, and S. R. Wentz, *A Novel Saccharomyces cerevisiae FG Nucleoporin Mutant Collection for Use in Nuclear Pore Complex Functional Experiments*, G3: Genes|Genomes|Genetics **6**, 51 (2016).
- [25] A. Zilman, S. Di Talia, B. T. Chait, M. P. Rout, and M. O. Magnasco, *Efficiency, selectivity, and robustness of nucleocytoplasmic transport*, PLoS Computational Biology **3**, 1281 (2007).
- [26] L. C. Tu and S. M. Musser, *Single molecule studies of nucleocytoplasmic transport*, Biochimica et Biophysica Acta - Molecular Cell Research **1813**, 1607 (2011).
- [27] A. Harel and D. J. Forbes, *Importin beta: Conducting a much larger cellular symphony*, Molecular Cell **16**, 319 (2004).

- [28] R. Bayliss, T. Littlewood, and M. Stewart, *Structural basis for the interaction between FxFG nucleoporin repeats and importin- β in nuclear trafficking*, *Cell* **102**, 99 (2000).
- [29] T. Dange, D. Grünwald, A. Grünwald, R. Peters, and U. Kubitscheck, *Autonomy and robustness of translocation through the nuclear pore complex: A single-molecule study*, *Journal of Cell Biology* **183**, 77 (2008).
- [30] D. Görlich, N. Panté, U. Kutay, U. Aebi, and F. R. Bischoff, *Identification of different roles for RanGDP and RanGTP in nuclear protein import*, *EMBO Journal* **15**, 5584 (1996).
- [31] T. Jovanovic-Talisman and A. Zilman, *Protein Transport by the Nuclear Pore Complex: Simple Biophysics of a Complex Biomachine*, *Biophysical Journal* **113**, 6 (2017).
- [32] J. D. Aitchison and M. P. Rout, *The yeast nuclear pore complex and transport through it*, *Genetics* **190**, 855 (2012).
- [33] B. Cautain, R. Hill, N. De Pedro, and W. Link, *Components and regulation of nuclear transport processes*, *FEBS Journal* **282**, 445 (2015).
- [34] L. E. Kapinos, R. L. Schoch, R. S. Wagner, K. D. Schleicher, and R. Y. Lim, *Karyopherin-centric control of nuclear pores based on molecular occupancy and kinetic analysis of multivalent binding with FG nucleoporins*, *Biophysical Journal* **106**, 1751 (2014).
- [35] L. E. Kapinos, B. Huang, C. Rencurel, and R. Y. Lim, *Karyopherins regulate nuclear pore complex barrier and transport function*, *Journal of Cell Biology* **216**, 3609 (2017).
- [36] M. P. Rout, J. D. Aitchison, M. O. Magnasco, and B. T. Chait, *Virtual gating and nuclear transport: The hole picture*, *Trends in Cell Biology* **13**, 622 (2003).
- [37] S. Frey, *FG-Rich Repeats of Nuclear Pore Proteins with Hydrogel-Like Properties*, *Science (New York, N.Y.)* **314**, 815 (2006).
- [38] S. Frey and D. Görlich, *A Saturated FG-Repeat Hydrogel Can Reproduce the Permeability Properties of Nuclear Pore Complexes*, *Cell* **130**, 512 (2007).
- [39] R. Peters, *Translocation through the nuclear pore complex: Selectivity and speed by reduction-of-dimensionality*, *Traffic* **6**, 421 (2005).
- [40] K. D. Schleicher, S. L. Dettmer, L. E. Kapinos, S. Pagliara, U. F. Keyser, S. Jeney, and R. Y. Lim, *Selective transport control on molecular velcro made from intrinsically disordered proteins*, *Nature Nanotechnology* **9**, 525 (2014).
- [41] R. Y. Lim and L. E. Kapinos, *How to operate a nuclear pore complex by kap-centric control*, *Nucleus* **6**, 366 (2015).
- [42] R. S. Wagner, L. E. Kapinos, N. J. Marshall, M. Stewart, and R. Y. Lim, *Promiscuous binding of karyopherin β 1 modulates FG nucleoporin barrier function and expedites NTF2 transport kinetics*, *Biophysical Journal* **108**, 918 (2015).

- [43] S. Barbato*, L. E. Kapinos*, C. Rencurel, and R. Y. Lim, *Karyopherin enrichment at the nuclear pore complex attenuates Ran permeability*, Journal of Cell Science (2020).
- [44] T. Jamali, Y. Jamali, M. Mehrbod, and M. R. Mofrad, *International Review of Cell and Molecular Biology*, 1st ed., Vol. 287 (Elsevier Inc., 2011) pp. 233–286.
- [45] N. B. Eisele, S. Frey, J. Piehler, D. Görlich, and R. P. Richter, *Ultrathin nucleoporin phenylalanine-glycine repeat films and their interaction with nuclear transport receptors*, EMBO Reports **11**, 366 (2010).
- [46] N. B. Eisele, A. A. Labokha, S. Frey, D. Görlich, and R. P. Richter, *Cohesiveness tunes assembly and morphology of FG nucleoporin domain meshworks - Implications for nuclear pore permeability*, Biophysical Journal **105**, 1860 (2013).
- [47] R. L. Schoch, L. E. Kapinos, and R. Y. Lim, *Nuclear transport receptor binding avidity triggers a self-healing collapse transition in FG-nucleoporin molecular brushes*, Proceedings of the National Academy of Sciences of the United States of America **109**, 16911 (2012).
- [48] R. Y. H. Lim, B. Fahrenkrog, J. Köser, K. Schwarz-Herion, J. Deng, and U. Aebi, *Nanomechanical basis of selective gating by the nuclear pore complex*, Science **318**, 640 (2007).
- [49] T. Jovanovic-Talisman, J. Tetenbaum-Novatt, A. S. McKenney, A. Zilman, R. Peters, M. P. Rout, and B. T. Chait, *Artificial nanopores that mimic the transport selectivity of the nuclear pore complex*, Nature **457**, 1023 (2009).
- [50] S. W. Kowalczyk, L. Kapinos, T. R. Blosser, T. Magalhães, P. van Nies, R. Y. H. Lim, and C. Dekker, *Single-molecule transport across an individual biomimetic nuclear pore complex*, Nature Nanotechnology **6**, 433 (2011).
- [51] C. Dekker, *Solid-state nanopores (Review Article)*, Nature Nanotechnology, 1 (2007).
- [52] L. Xue, H. Yamazaki, R. Ren, M. Wanunu, A. P. Ivanov, and J. B. Edel, *Solid-state nanopore sensors*, Nature Reviews Materials (2020), 10.1038/s41578-020-0229-6.
- [53] A. Balan, B. Machielse, D. Niedzwiecki, J. Lin, P. Ong, R. Engelke, K. L. Shepard, and M. Drndić, *Improving signal-to-noise performance for DNA translocation in solid-state nanopores at MHz bandwidths*, Nano Letters **14**, 7215 (2014).
- [54] K. Venta, G. Shemer, M. Puster, J. A. Rodríguez-Manzo, A. Balan, J. K. Rosenstein, K. Shepard, and M. Drndić, *Differentiation of short, single-stranded DNA homopolymers in solid-state nanopores*, ACS Nano **7**, 4629 (2013).
- [55] C. a. Merchant, K. Healy, M. Wanunu, V. Ray, N. Peterman, J. Bartel, M. D. Fischbein, K. Venta, Z. Luo, a. T. C. Johnson, and M. Drndić, *DNA translocation through graphene nanopores*, Nano Letters **10**, 2915 (2010).

- [56] G. F. Schneider, S. W. Kowalczyk, V. E. Calado, G. Pandraud, H. W. Zandbergen, L. M. Vandersypen, and C. Dekker, *DNA translocation through graphene nanopores*, Nano Letters **10**, 3163 (2010).
- [57] Z. Zhou, Y. Hu, H. Wang, Z. Xu, W. Wang, X. Bai, X. Shan, and X. Lu, *DNA Translocation through hydrophilic nanopore in hexagonal boron nitride*, Scientific Reports **3**, 1 (2013).
- [58] K. B. Park, H. J. Kim, H. M. Kim, S. A. Han, K. H. Lee, S. W. Kim, and K. B. Kim, *Noise and sensitivity characteristics of solid-state nanopores with a boron nitride 2-D membrane on a pyrex substrate*, Nanoscale **8**, 5755 (2016).
- [59] M. Graf, M. Lihter, M. Thakur, V. Georgiou, J. Topolancik, B. R. Ilic, K. Liu, J. Feng, Y. Astier, and A. Radenovic, *Fabrication and practical applications of molybdenum disulfide nanopores*, Nature Protocols **14**, 1130 (2019).
- [60] A. J. Storm, J. H. Chen, X. S. Ling, H. W. Zandbergen, and C. Dekker, *Fabrication of solid-state nanopores with single-nanometre precision*, Nature Materials **2**, 537 (2003).
- [61] Y. H. Lanyon, G. De Marzi, Y. E. Watson, A. J. Quinn, J. P. Gleeson, G. Redmond, and D. W. Arrigan, *Fabrication of nanopore array electrodes by focused ion beam milling*, Analytical Chemistry **79**, 3048 (2007).
- [62] B. Schiedt, L. Auvray, L. Bacri, G. Oukhaled, A. Madouri, E. Bourhis, G. Patriarche, J. Pelta, R. Jede, and J. Gierak, *Direct FIB fabrication and integration of "single nanopore devices" for the manipulation of macromolecules*, Microelectronic Engineering **87**, 1300 (2010).
- [63] H. Kwok, K. Briggs, and V. Tabard-Cossa, *Nanopore fabrication by controlled dielectric breakdown*, PLoS ONE **9** (2014), 10.1371/journal.pone.0092880.
- [64] S. Pud, D. Verschueren, N. Vukovic, C. Plesa, M. P. Jonsson, and C. Dekker, *Self-Aligned Plasmonic Nanopores by Optically Controlled Dielectric Breakdown*, Nano Letters **15**, 7112 (2015).
- [65] T. Gilboa, E. Zvuloni, A. Zrehen, A. H. Squires, and A. Meller, *Automated, Ultra-Fast Laser-Drilling of Nanometer Scale Pores and Nanopore Arrays in Aqueous Solutions*, Advanced Functional Materials **1900642**, 1 (2019).
- [66] D. V. Verschueren, W. Yang, and C. Dekker, *Lithography-based fabrication of nanopore arrays in freestanding SiN and graphene membranes*, **29**, 145302 (2018), arXiv:15334406.
- [67] J. D. Piper, R. W. Clarke, Y. E. Korchev, L. Ying, and D. Klenerman, *A renewable nanosensor based on a glass nanopipette*, Journal of the American Chemical Society **128**, 16462 (2006).
- [68] G. Maglia, A. J. Heron, D. Stoddart, D. Japrun, and H. Bayley, *Methods in Enzymology*, 1st ed., Vol. 475 (Elsevier Inc., 2010) pp. 591–623, arXiv:NIHMS150003.

- [69] S. Howorka and Z. Siwy, *Nanopore analytics: Sensing of single molecules*, Chemical Society Reviews **38**, 2360 (2009).
- [70] E. Manrao, T. Z. Butler, M. Pavlenok, M. D. Collins, M. Niederweis, J. H. Gundlach, and I. M. Derrington, *Nanopore DNA sequencing with MspA*, Proceedings of the National Academy of Sciences **107**, 16060 (2010).
- [71] H. Brinkerhoff, A. S. W. Kang, J. Liu, A. Aksimentiev, and C. Dekker, *Infinite re-reading of single proteins at single-amino-acid resolution using nanopore sequencing*, bioRxiv, 2021.07.13.452225 (2021).
- [72] A. N. Ananth, A. Mishra, S. Frey, A. Dwarkasing, R. Versloot, E. van der Giessen, D. Görlich, P. Onck, and C. Dekker, *Spatial structure of disordered proteins dictates conductance and selectivity in nuclear pore complex mimics*, eLife **7**, 1 (2018).
- [73] P. W. Rothemund, *Folding DNA to create nanoscale shapes and patterns*, Nature **440**, 297 (2006), arXiv:0202466 [cond-mat] .
- [74] K. F. Wagenbauer, F. A. Engelhardt, E. Stahl, V. K. Hecht, P. Stömm, F. Seebacher, L. Meregalli, P. Ketterer, T. Gerling, and H. Dietz, *How We Make DNA Origami*, ChemBioChem **18**, 1873 (2017).
- [75] K. Sanderson, *What to make with DNA origami*, Nature **464**, 158 (2010).
- [76] H. Dietz, S. M. Douglas, and W. M. Shih, *Folding DNA into twisted and curved nanoscale shapes*, Science **325**, 725 (2009), arXiv:9910002 [quant-ph] .
- [77] T. Sugawara, D. Yamashita, K. Kato, Z. Peng, J. Ueda, J. Kaneko, Y. Kamio, Y. Tanaka, and M. Yao, *Structural basis for pore-forming mechanism of staphylococcal α -hemolysin*, Toxicon **108**, 226 (2015).
- [78] S. Hernández-Ainsa and U. F. Keyser, *DNA origami nanopores: Developments, challenges and perspectives*, Nanoscale **6**, 14121 (2014).
- [79] T. G. Martin, F. C. Simmel, V. Arnaut, M. Mayer, H. Dietz, M. Langecker, S. Renner, and J. List, *Synthetic Lipid Membrane Channels Formed by Designed DNA Nanostructures*, Science **338**, 932 (2012).
- [80] J. R. Burns, A. Seifert, N. Fertig, and S. Howorka, *A biomimetic DNA-based channel for the ligand-controlled transport of charged molecular cargo across a biological membrane*, Nature Nanotechnology **11**, 152 (2016).
- [81] R. P. Thomsen, M. G. Malle, A. H. Okholm, S. Krishnan, S. S. Bohr, R. S. Sørensen, O. Ries, S. Vogel, F. C. Simmel, N. S. Hatzakis, and J. Kjems, *A large size-selective DNA nanopore with sensing applications*, Nature Communications **10** (2019), 10.1038/s41467-019-13284-1.
- [82] S. Iwabuchi, I. Kawamata, S. Murata, and S.-i. M. Nomura, *Large, square-shaped, DNA origami nanopore with sealing function on giant vesicle membrane*, Chemical Communications (2021), 10.1039/d0cc07412h.

- [83] K. Göpfrich, C.-Y. Li, M. Ricci, S. P. Bhamidimarri, J. Yoo, B. Gyenes, A. Ohmann, M. Winterhalter, A. Aksimentiev, and U. F. Keyser, *Large-Conductance Transmembrane Porin Made from DNA Origami*, *ACS Nano* **10**, 8207 (2016).
- [84] S. Krishnan, D. Ziegler, V. Arnaut, T. G. Martin, K. Kapsner, K. Henneberg, A. R. Bausch, H. Dietz, and F. C. Simmel, *Molecular transport through large-diameter DNA nanopores*, *Nature Communications* **7**, 1 (2016).
- [85] P. Ketterer, A. N. Ananth, D. S. Laman Trip, A. Mishra, E. Bertosin, M. Ganji, J. Van Der Torre, P. Onck, H. Dietz, and C. Dekker, *DNA origami scaffold for studying intrinsically disordered proteins of the nuclear pore complex*, *Nature Communications* **9**, 1 (2018).
- [86] P. D. E. Fisher, Q. Shen, B. Akpinar, L. K. Davis, K. K. H. Chung, D. Baddeley, A. Šarić, T. J. Melia, B. W. Hoogenboom, C. Lin, and C. P. Lusk, *A Programmable DNA Origami Platform for Organizing Intrinsically Disordered Nucleoporins within Nanopore Confinement*, *ACS Nano* **12**, 1508 (2018).

2

COMPARING CURRENT NOISE IN BIOLOGICAL AND SOLID-STATE NANOPORES

Nanopores bear great potential as single-molecule tools for bioanalytical sensing and sequencing, due to their exceptional sensing capabilities, high-throughput, and low cost. The detection principle relies on detecting small differences in the ionic current as biomolecules traverse the nanopore. A major bottleneck for the further progress of this technology is the noise that is present in the ionic current recordings, because it limits the signal-to-noise ratio and thereby the effective time resolution of the experiment. Here, we review the main types of noise at low and high frequencies and discuss the underlying physics. Moreover, we compare biological and solid-state nanopores in terms of the signal-to-noise ratio (SNR), the important figure of merit, by measuring translocations of a short ssDNA through a selected set of nanopores under typical experimental conditions. We find that SiN_x solid-state nanopores provide the highest SNR, due to the large currents at which they can be operated and the relatively low noise at high frequencies. However, the real game-changer for many applications is a controlled slowdown of the translocation speed, which for MspA was shown to increase the SNR >160-fold. Finally, we discuss practical approaches for lowering the noise for optimal experimental performance and further development of the nanopore technology.

This chapter has been published as: Alessio Fragasso, Sonja Schmid, Cees Dekker. "Comparing Current Noise in Biological and Solid-State Nanopores". ACS Nano 14(2), 1338–1349, (2020) [1].

2.1. INTRODUCTION

Nanopores are promising tools for biosensing applications and sequencing of DNA and proteins, as they can resolve single analyte molecules, resolve structural modifications of molecules, and even discriminate between nucleotide sequences [2–11]. The detection mechanism is simple: while passing through the pore, a (part of a) molecule transiently blocks the ionic current, thereby inducing a small dip in the current signal, which is detectable by the electronics (Fig.2.1). The electrical read-out is carried out by an amplifier, which senses and amplifies the current signal, followed by a digitizer that performs the analog-to-digital conversion (ADC) of the data. Digital low-pass (LP) filtering is typically used to reduce the high-frequency noise, and thus improve the signal-to-noise ratio (SNR). Such a gain in SNR comes, however, at the expense of a lower time resolution, thereby imposing an inherent trade-off.

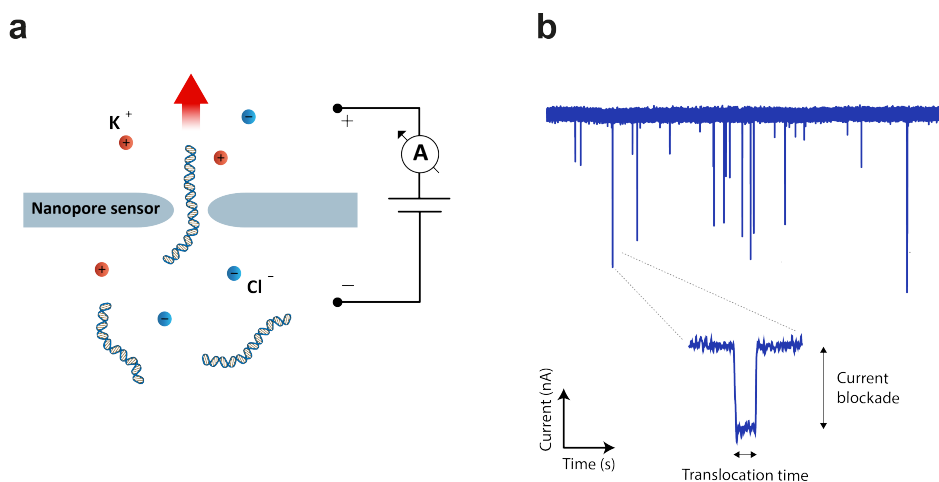


Figure 2.1: Fundamental principle of nanopore sensing. (a) A nanopore separates two aqueous compartments filled with electrolyte solution (e.g. potassium chloride) and small molecules (e.g. DNA) are electrokinetically pulled through the pore by an applied potential. (b) While passing through the nanopore, the molecule temporarily induces a partial current blockade which is detected by an amplifier. The signature of a single-molecule translocation event is generally characterized by the amplitude of the current blockade, which is proportional to the volume of the molecule in the nanopore, and by the dwell time, which depends on the electrophoretic driving force and transient interactions between the passing molecule and the pore surface.

The detection of analytes with nanopores thus is, on the one hand, limited by the ionic current noise which requires LP filtering that sets a finite operating bandwidth [12, 13], but on the other hand, by the fast speed (typically sub-milliseconds) at which molecules translocate through the pore, which conversely requires a high time resolution for accurate sampling. Various approaches have been investigated in order to slow down the molecular translocation. For biological nanopores, a DNA-translocating motor protein (such as a helicase or polymerase) has been used to slowly feed a ssDNA strand into a protein pore for DNA sequencing [14–16]. For solid-state nanopores fabricated in thin SiN_x membranes [17–19] or 2D materials (graphene [20–22], boron nitride [23–25], molybdenum disulfide [26–28]), various efforts have been made to either increase time

resolution [17–19, 29–31], or slow down the translocation process [32] by the use of ionic liquids [28], pore surface engineering [33] mechanical manipulation with a double pore system [34], optical trapping [35], and sequential DNA unzipping [36]. Nevertheless, while fingerprinting approaches have been developed to detect individual portions of a DNA sequence using dCas9 [8, 37], streptavidin [38], DNA hairpins [39], or DNA-origami as probes [40], the SNR has not yet allowed *de novo* DNA sequencing with solid-state pores. An understanding of the noise sources that affect nanopore systems and how these govern the SNR is key for achieving signals wherein molecular structures can be resolved fast and reliably. Noise characteristics of nanopores have been reported in various isolated reports, but a systematic overview and comparison between biological and solid-state nanopores is lacking.

In this review, we first describe the typical noise sources that affect the ionic current recordings of biological and solid-state nanopores, both at low and high frequencies. Next, we compare their respective performances of various nanopores using ssDNA poly(dT) translocations as a test system. We assess the SNR under typical experimental conditions for different protein pores *Mycobacterium smegmatis* porin A (the M2 mutant with a neutral constriction and positively charged vestibule, subsequently referred to as MspA) [41], *Staphylococcus aureus* alpha-hemolysin (α -HL) [42, 43], *Fragaceatoxin C* (the mutant of FraC with a positively charged constriction, referred to as ReFraC) [44, 45], and SiN_x [19] and MoS₂ [26] solid state nanopores. We find that biological pores generally exhibit lower noise (Fig.2.2a). Nevertheless, solid-state nanopores achieve the best SNR, largely because of the higher voltages and bandwidths that such devices can operate at, as compared to biological nanopores. Finally, we discuss approaches for lowering the ionic current noise and improving the SNR in biological and solid-state nanopores.

2.2. NOISE SOURCES IN NANOPORES

Noise refers to any statistical fluctuation of a signal. It can be characterized by the standard deviation σ or root-mean-square (rms) variation around the average value as measured over the full bandwidth B of the signal, and by its power spectral density (PSD). Generally, noise is undesirable, as it can distort or even completely mask the actual signal. Nanopores typically operate by measuring a through-pore ionic current that is driven by a constant applied bias voltage. For the open-pore current measurement, where no analyte molecules are present, any deviation from the baseline current can be regarded as noise (Fig.2.2a).

Understanding the origins of noise is fundamental for optimizing signal detection. Nanopore systems exhibit a range of different noise sources [47, 48]. In Fig.2.2b, we illustrate the major current noise sources that affect nanopore systems at different frequencies. Generally, these can be divided in: (i) low-frequency ($\lesssim 100$ Hz) $1/f$ noise and protonation noise; (ii) shot noise and thermal current noise (~ 0.1 -2 kHz), which are both white noise sources (i.e., frequency-independent); (iii) high-frequency dielectric (~ 1 -10 kHz) and (iv) capacitive (> 10 kHz) noise.

In the low-frequency range, $1/f$ noise (also referred to as ‘flicker’ or ‘pink’ noise) typically is the dominant source of noise. Its power decreases with frequency f following a $1/f^\beta$ scaling, with $\beta \approx 1$. While this type of noise is found in many biological and physical systems, a fundamental understanding of it is still missing [49]. Based on

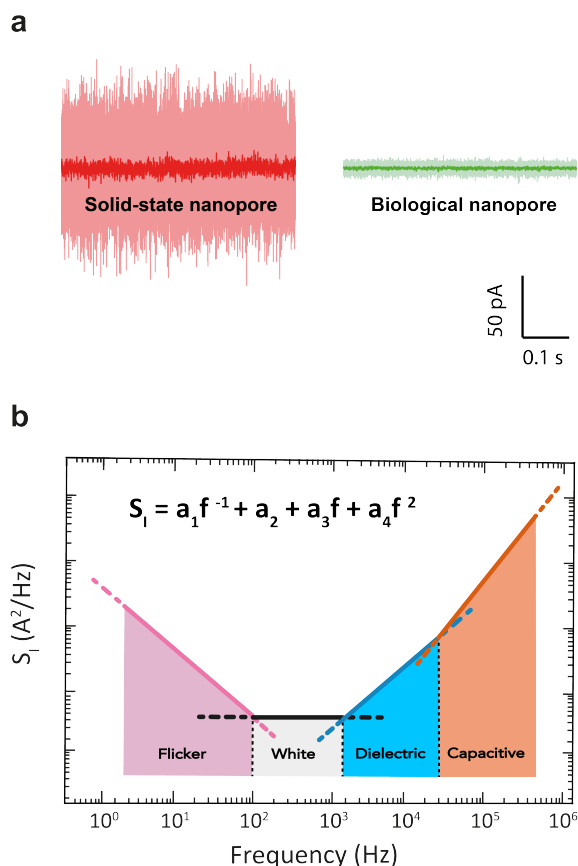


Figure 2.2: Ionic current noise in nanopores. (a) Example current traces for a 1.3 nm diameter solid-state SiN_x nanopore (red) and a 1.4 nm diameter biological α -HL pore (green), performed at a constant applied bias of 100 mV in 1 M KCl buffer at pH 7 at a bandwidth of 10 kHz (light) and 1 kHz (dark). α -HL pore was measured using the typical Montal-Muller approach [46], with a bilayer diameter of $100 \mu\text{m}$, as described by Maglia *et al.* (2010)[4]. The solid-state pore was fabricated on a Si-supported 20 nm-thick SiN_x freestanding membrane using transmission electron microscopy. Currents through both pores were amplified with Axopatch 200B. (b) Schematic of the current Power Spectral Density (PSD) for a typical nanopore. Common types of noise are highlighted in the various frequency ranges.

phenomenological evidence, $1/f$ noise in nanopores has been associated with physical processes such as slow fluctuations in the number and mobility of the charge carriers [50–53], nanometer-sized bubbles in the pore channel [54], noise arising from the electrodes [55], mechanical fluctuations of the freestanding membrane (e.g. for 2D materials) [24, 56, 57], and conformational changes in the case of biological nanopores [58, 59]. Smeets *et al.* (2008) [60] found that Hooge's phenomenological formula [53] could effectively describe the $1/f$ noise in solid-state [55, 60–63] nanopores,

$$S_{I,1/f} = \frac{\alpha_H I^2}{N_c f \beta}, \quad (2.1)$$

where Hooge's constant α_H is an empirical parameter that quantifies the magnitude of $1/f$ noise fluctuations, I the ionic current, and N_c the number of charge carriers in the pore volume, which was further validated by follow-up studies [55, 61–63]. As discussed below, solid-state nanopores typically feature a relatively pronounced $1/f$ noise, whose microscopic origin often remains unresolved. For biological pores, the low-frequency noise is typically dominated by protonation noise, which is generated by protonation/deprotonation of ionizable sites within the protein channel [64–66]. It can be described by fluctuations between two different current levels with mean lifetimes τ_1 and τ_2 for the protonated and deprotonated states, respectively, yielding a Lorentzian-shaped component in the frequency spectrum (for a complete derivation see Machlup et al., 1954 [67]),

$$S_{I,protonation} = \frac{4(\Delta i)^2 \tau^2}{\tau_1 + \tau_2} \frac{1}{1 + (2\pi f \tau)^2}, \quad (2.2)$$

where Δi is the difference in current between the two levels, and τ is the characteristic relaxation time, that can be expressed as $\tau = (\tau_1 \tau_2) / (\tau_1 + \tau_2)$. For alpha-hemolysin, for example, τ was found to be 3.1×10^{-5} s [66]. A distribution of multiple Lorentzian processes such as in Eq.2.2 can lead to $1/f$ noise [50]. Temporal conformational changes of the pore channel can also generate conductance fluctuations resulting in $1/f$ noise. Such a phenomenon, also known as 'channel breathing', was reported to affect protein pores such as bacterial porin channels [58, 59].

In the mid-frequency range (typically ~ 0.1 -2 kHz), a frequency-independent white noise is observed that derives from thermal noise (also known as Johnson-Nyquist noise) and shot noise. Thermal current noise is fundamental to any dissipative element [68, 69] and adds to the current noise as

$$S_{I,thermal} = \frac{4k_B T}{R}, \quad (2.3)$$

where k_B is the Boltzmann constant, T is temperature, and R the equivalent resistance of the nanopore. Shot noise, on the other hand, is due to the quantization of charge and is generated when charge carriers flow across a potential barrier [70, 71]. Its current-dependent contribution to the noise can be expressed as

$$S_{I,shot} = 2Iq, \quad (2.4)$$

where q is the charge of a single carrier. In practice, shot noise and thermal noise are comparable in magnitude for the conditions that are typically used in nanopore experiments.

Another contribution to the nanopore noise originates from the loss conductance of the membrane and chip support [47, 48]. Such dissipation, resulting from dipolar relaxation and charge carrier migration (details can be found in Chen *et al.*, 2014 [72]), generates thermal energy causing thermal noise, also known as dielectric noise [73, 74]. As this loss conductance scales linearly with frequency, this noise can be described by

$$S_{I,dielectric} = 8kT\pi C_{chip}Df, \quad (2.5)$$

where C_{chip} is the parasitic capacitance and D a dissipation factor of the dielectric materials constituting the membrane and support chip. This source of noise typically dominates in the 2-10 kHz frequency range. To estimate C_{chip} , one can simply use the expression for a parallel plate capacitor $C = \epsilon A/d$, where ϵ is the dielectric constant of the membrane material and A and d are the area and the thickness of the membrane, respectively. For $f > 10$ kHz, the current noise is determined by the input-referred thermal voltage noise v_n across the total capacitance C_{tot} at the amplifier input [47, 48],

$$S_{I,capacitance} = 4\pi^2 C_{tot}^2 v_n^2 f^2, \quad (2.6)$$

where v_n is the input voltage noise (3 nV/Hz^{1/2} for the commonly used amplifier Axopatch 200B [74], Molecular Devices, San Jose, USA). C_{tot} is the total capacitance including the membrane and support chip capacitance C_{chip} , the capacitance C_{amp} at the input of the amplifier, and the capacitance C_w of the wiring between the electronics and the pore. Notably, $S_{I,capacitance}$ has an even stronger, f^2 , frequency dependence than $S_{I,dielectric}$. The total current noise of a nanopore system over its full bandwidth is the sum of all contributions (Fig.2.2b), i.e., the sum of Eqs.2.1–2.6.

2.3. NOISE IN BIOLOGICAL NANOPORES

Biological nanopores are formed by the spontaneous insertion of membrane proteins into a lipid bilayer, which creates nanopores with typical diameters ranging from ~1-4 nm [75], although larger pores with diameters up to ~40 nm, e.g. the nuclear pore complex [76], are also found in nature. Figure 2.3a shows a schematic of a standard setup for measuring the ionic current through such a protein pore. Briefly, a thick (tens of micrometers) insulating film of amorphous polytetrafluoro-ethylene (PTFE, or Teflon) separates two liquid compartments and contains a ~50-100 μ m sized hole where the lipid bilayer is assembled [4, 77]. Teflon is the preferred support material due to the relatively low high-frequency noise, and ease of fabrication [78]. Insertion of a protein pore (Fig.2.3b) short-circuits the insulating bilayer membrane and an ionic current between the two reservoirs can be measured by a pair of Ag/AgCl electrodes. The current signal is amplified by a transimpedance amplifier (e.g. Axopatch 200B) and digitized by an analog-to-digital converter (ADC, e.g. Axon Digidata, same supplier). To shield from external radiative electric noise, the flow-cell and the amplifier headstage are enclosed in a metallic Faraday cage [4]. For biological nanopores, ionic conductances are typically on the order of 0.1-2 nS.

Characteristic examples of the current PSD for 3 biological nanopores (α -HL [42], MspA, and ReFraC [44]) are shown in Figure 2.3c, as measured at 1 M KCl, pH 7.5, under 50 mV applied bias. Noticeably, both α -HL and MspA exhibit a noise plateau at low frequencies (< 1 kHz) which is due to protonation noise, cf. Eq.2.2 for $f \ll 1/\tau$. The associated PSD is ~10–4 to 10–3 pA²/Hz, which is higher than the corresponding white noise of ~10–5 pA²/Hz, set by the sum of thermal and shot noise, Eq.2.3 and 2.4. In the context of single-molecule sensing, protonation noise in biological nanopores was first investigated by Bezrukov and Kasianowicz in the mid 1990s [65, 66].

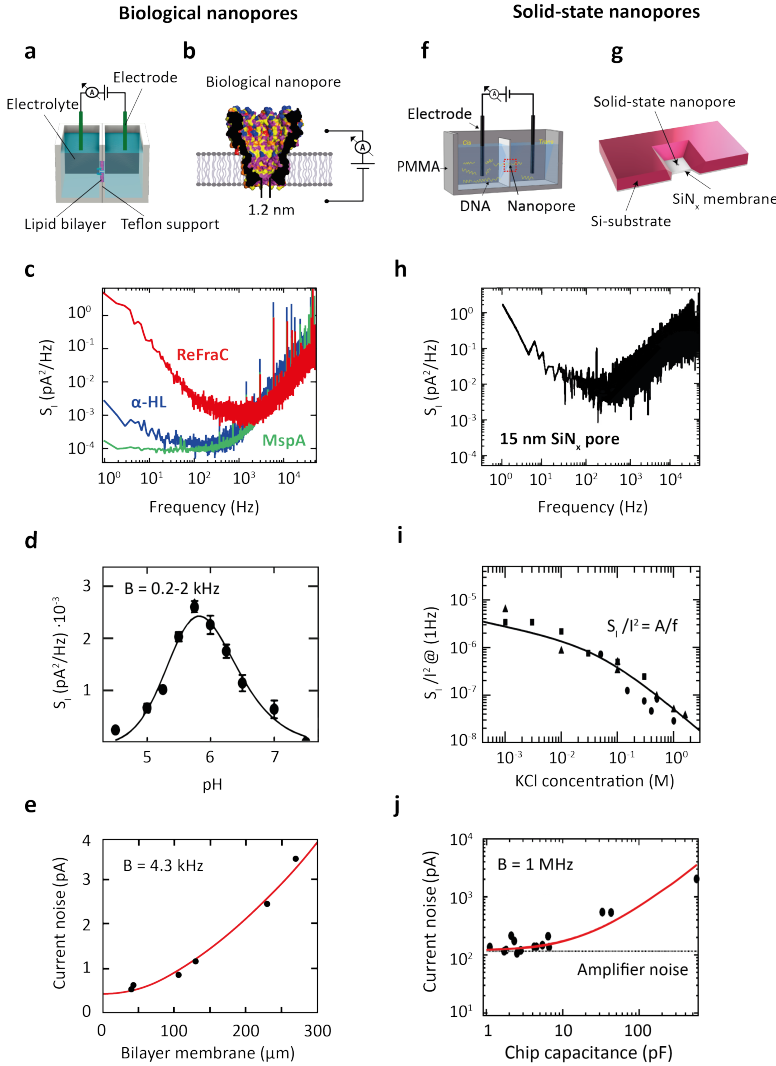


Figure 2.3: Noise in biological and solid-state nanopores. (a) Standard setup used for measuring the ionic current through a biological nanopore embedded within a lipid membrane. (b) Sketch of a biological MspA nanopore [15]. Adapted with permission from Derrington, I. M. *et al.*, 2010; (c) Typical current PSD for three biological nanopores, ReFraC (D10R/K159E mutant of FraC)[44] (red), α -HL (blue), and the D90N/D91N/D93N/D118R/E139K/D134R mutant of MspA (green), measured in the same setup at 50 mV applied voltage, 1 M KCl salt, pH 7. (d) Low-frequency protonation noise of α -HL as a function of pH.67 Adapted with permission from Kasianowicz, J. J. *et al.* 1995. (e) Current noise I_{rms} measured at a 4.3 kHz bandwidth of a lipid bilayer setup (where no pore was inserted) vs the size of the bilayer membrane [78]. Adapted with permission from Mayer, M. *et al.*, 2003 (f) Schematic of a typical flow cell for measuring the ionic current through a solid-state nanopore [5]. Adapted with permission from Feng, Y. *et al.*, 2015. (g) Sketch of a solid-state nanopore fabricated onto a Si-supported SiN_x membrane. (h) Current PSD for a 15.6 nm SiN_x solid-state nanopore. Data were measured at 100 mV applied voltage for 1 M KCl salt [60]. (i) Relative low-frequency noise S_I/I^2 at 1 Hz versus salt concentration [60]. Solid line shows a fit to the data using Hooge's relation, cf. Eq.2.1. (h) and (i) were adapted with permission from Smeets, R. M. M. *et al.*, 2008. (j) Current noise I_{rms} measured at a 1 MHz bandwidth vs capacitance of the nanopore chip[17]. Adapted with permission from Balan, A. *et al.*, 2014.

Spectral analysis of the current noise of alpha-hemolysin pores revealed the presence of a Lorentzian-shaped component at low-frequencies (0.2–2 kHz). Given the strong dependence on pH (Fig.2.3d), this noise source was associated to the reversible protonation of ionizable residues occurring in the alpha-hemolysin constriction. This notion was further established in a later work by Nestorovich *et al.* [64], where the bacterial porin, OmpF, was shown to produce a similar pH-dependence of the protonation noise. ReFraC instead shows a pronounced 1/f noise with a PSD of $\sim 10^{-1} \text{ pA}^2/\text{Hz}$ at 1 Hz, which is almost three times more than for α -HL and MspA. 1/f noise in biological nanopores was first studied by Benz and coworkers [58, 79], and described using Hooge's model, Eq.2.1. The low-frequency fluctuations observed in a family of bacterial porins were associated with a number of possible phenomena, *e.g.* gating of the pore channel [58]. In later work by Bezrukov and Winterhalter [59], conformational changes of the protein pore channel, termed 'channel breathing' [80], were discussed as the main cause for the observed 1/f noise.

At higher frequencies ($> 1 \text{ kHz}$), the noise in biological nanopores is dominated by dielectric noise arising from the loss conductance of the lipid membrane. In fact, since the dielectric loss and dielectric constant of the teflon are relatively low ($D = (0.8 - 2) \times 10^{-4}$ and $\epsilon_r = 1.89 - 1.93$, respectively), the major contribution to the dielectric noise is set by the capacitance of the thin lipid bilayer membrane. This can be attenuated by reducing the area of the teflon hole (Fig.2.3e) [78, 81]. A noise characterization at even higher frequencies (MHz-GHz; above the experimentally accessible frequency range) was performed using molecular dynamics simulations based on a comprehensive model of MspA [82].

2.4. NOISE IN SOLID-STATE NANOPORES

Solid-state nanopores are generally fabricated in a freestanding membrane of a solid-state material such as silicon nitride (SiN_x) [83], graphene [20], hexagonal boron nitride (h-BN) [84], or molybdenum disulfide (MoS_2) [26], with thicknesses ranging from ~ 0.3 -30 nm. In common nanopore chips (Fig.2.3g), such a membrane is structurally supported by a ~ 200 -500 μm thick substrate material, typically silicon (Si) [83], glass (SiO_2) [17], or Pyrex [85, 86]. Nanopores can be drilled into the membrane in a variety of ways, *e.g.* by using a transmission electron microscope (TEM) [87, 88], focused ion beam milling (FIB) [89, 90], reactive ion etching (RIE) [[91]], laser-etching [92, 93], or by dielectric breakdown [94, 95], resulting in pore diameters from sub-1 nm to tens of nanometers. In a standard solid-state-nanopore experiment, the chip is sandwiched between two rubber O-rings that seal two compartments containing the electrolyte solution (Fig.2.3f). Alternatively, solid-state pores of ~ 5 -50 nm size can be made by mechanical pulling of hollow glass (SiO_2) pipettes [96–98], which are immersed in electrolyte during the measurement. Current sensing, amplification, and recording is the same as for biological nanopores.

Figure 2.3h displays a typical current PSD measured for a 15 nm diameter SiN_x solid-state nanopore [60] in a 20 nm thick membrane. Characteristic of solid-state nanopores is the pronounced 1/f noise that dominates the low-frequency part of the spectrum ($< 100 \text{ Hz}$). It can originate from a range of physical processes, see Eq.2.1 and associated discussion. Smeets *et al.* 2006 [54] showed that poor wettability of the pore surface,

associated with the formation of nanobubbles, resulted in high $1/f$ noise in SiN_x . Tabard-Cossa *et al.* [99] discussed that high $1/f$ noise in SiN_x pores correlates with surface contamination: inhomogeneities of the pore surface resulted in fluctuations of the number and mobility of charge carriers due to trapping at the pore surface [62, 99], analogous to $1/f$ noise found in semiconductors [100]. As shown by Smeets *et al.* [60, 61], such low-frequency noise in SiN_x pores obeys Hooge's relation, Eq.2.1, which describes an inverse proportionality between the $1/f$ current noise power and the number of charge carriers present within the nanopore volume (Fig.2.3i) [53]. For nanopores made in 2D materials, the $1/f$ noise depends strongly on the size of the freestanding area [23, 56, 57, 101], indicating that mechanical fluctuations of the ultrathin 2D membrane (thickness < 1 nm) are the main source. The high-frequency noise in solid-state nanopores is dominated by dielectric (~ 2 -10 kHz) and capacitive noise (> 10 kHz) [17, 102], see Fig.2.3j. The PSD of these noise sources depends mostly on the capacitance of the chip, cf. Eq.2.5 and 2.6, which in turn is set by the membrane and substrate size, thickness, and dielectric constant. Additionally, parasitic capacitances from the amplifier and the interconnects between nanopore and amplifier contribute to the total capacitance at the amplifier input.

2.5. COMPARING THE PERFORMANCE OF BIOLOGICAL AND SOLID-STATE NANOPORES

So far, we provided a general overview of the typical noise sources in biological and solid-state nanopores. We now turn to a mutual comparison between these two classes of nanopores. We compare their performances in terms of the SNR – a more relevant figure of merit than the mere magnitude of the current noise. We define the SNR as the ratio between the signal modulation ΔI produced by the translocation of a ssDNA molecule, and the baseline current rms (I_{rms}) measured at the operating bandwidth (Fig.2.4a). Although other definitions of SNR are found in the literature, *e.g.* as the ratio between open pore current and baseline current noise I_o/I_{rms} [103] or the capability to discern current levels when sequencing DNA [14, 41], we find this definition the most appropriate for the diverse nanopore systems compared in our study.

Given that the experimental conditions reported in the literature differ considerably, we carried out a dedicated comparative study by complementing reported data with new data that were, to the extent possible, obtained in our lab under the same experimental conditions. The bandwidth was chosen such as to fully resolve the current blockade ΔI generated by the poly(dT) substrate (avoiding a reduced ΔI due to a too narrow bandwidth). The translocation time in turn, is determined by a combination of electrophoresis, electro-osmosis, and interactions between the passing molecule and the pore surface, which will depend on each individual nanopore system. The applied bias was chosen as to maximize the current signal and is limited by experimental conditions, as will be discussed below. We selected 5 popular nanopore systems, MspA, α -HL, ReFraC, MoS_2 , and SiN_x , that are commonly used and that were shown to possess good spatiotemporal resolution, allowing for accurate discrimination of short homopolymers [14, 19, 28, 44, 105]. All pores considered had a similar diameter of ~ 1.3 nm. Figure 2.4b illustrates the relative sizes of the different pores.

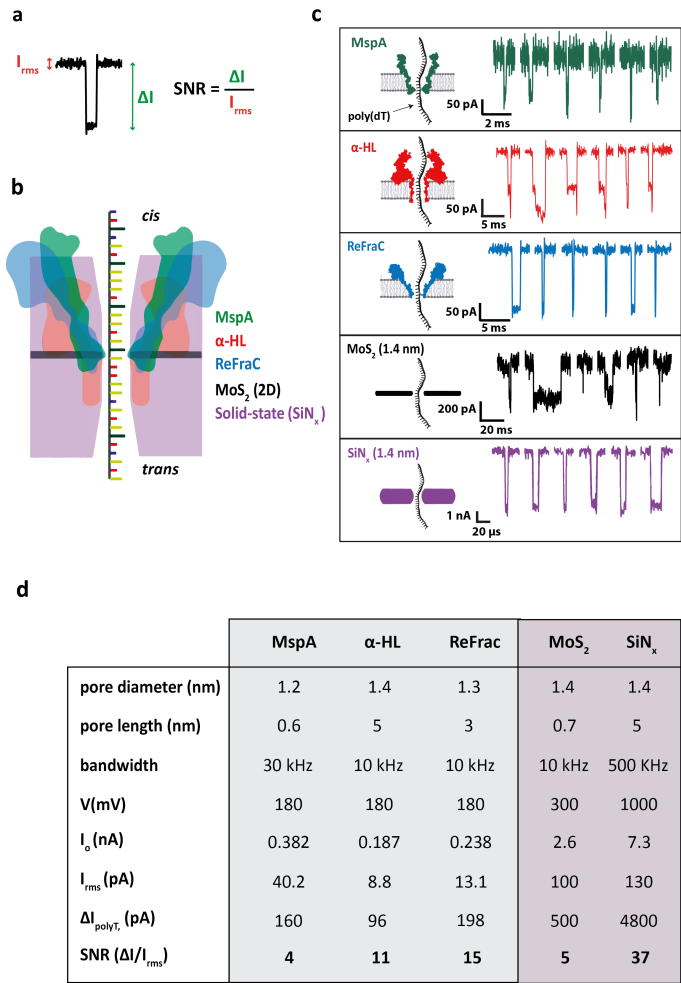


Figure 2.4: Detection of DNA homopolymer poly(dT) with protein and solid-state nanopores. (a) Example of a translocation event, illustrating the signal-to-noise ratio. (b) Schematic comparing the relative sizes of MspA (green), α -HL (red), ReFraC (blue), MoS₂ (black), and solid-state SiN_x (purple). Adapted with permission from Carson, S. *et al.*, 2015. (c) Example of translocation events of poly(dT) molecules through MspA [15] channel (green), α -HL pore (red), ReFraC pore (blue), 1.4 nm MoS₂ pore (black), and 1.4 nm SiN_x pore (purple, Adapted with permission from Venta, K. *et al.*, 2013) all in 1 M KCl solution at a transmembrane voltage of 180 mV, 180 mV, 180 mV, 300mV, and 1V, and at a bandwidth of 30 kHz, 10 kHz, 10 kHz, 10 kHz, and 500 kHz, respectively. Experiments for biological pores were done using an Axopatch 200B amplifier, a teflon-supported lipid membrane (~50-100 μ m wide; DPhPC lipids), 10-30 kHz bandwidth, 1 M KCl, pH 7.5, and a forward bias voltage of 180 mV, as in Ref.[104]. The solid-state SiN_x pore was built on a glass chip and measured with the VC100 high-bandwidth, low-noise voltage-clamp amplifier (Chimera Instruments, New York, NY, USA) which allowed for low-noise measurements at high bandwidth. A broad bandwidth of 500 kHz was required in order to fully resolve the fast translocations (~22 μ s) [19] of poly(dT)₃₀ through the solid-state SiN_x pore. Notably, the positively charged constriction of ReFraC causes the negatively charged poly(dT)₅₀ to translocate with much slower (491 \pm 114 μ s) translocation times compared to MspA (17.7 \pm 1.1 μ s), which permitted to filter out more high-frequency noise. (d) Comparison of various figures of merit for different nanopore systems under typical experimental conditions. I₀ indicates the open pore ionic current at the applied bias V.

Nanopore experiments probing the translocation of poly(dT)₅₀ were carried out in-house using three biological pores, MspA, α -HL, and ReFraC. We compared these data to experimental results on two types of solid-state nanopores, SiN_x [19] and MoS₂ [28] that were measured at the same electrolyte conditions. Translocation data of poly(dT)₈₀ through a 1.4 nm MoS₂ pore were kindly shared by the Radenovic lab [26], whereas poly(dT)₃₀ data for a 1.4 nm SiN_x pore with ~ 5 nm length were taken from the literature [19]. Figure 2.4c shows examples of single-molecule poly(dT) translocations for the 5 pores. A range of SNR values are observed, with, at face value, a better performance for SiN_x and ReFraC than for MoS₂, α -HL, and MspA.

Figure 2.4d quantitatively compares the data for the different nanopore systems. For the biological nanopores, ReFraC gives the best SNR = 15, while MspA resulted in a much lower SNR of 4. This is mainly due to the faster translocations of poly(dT) through MspA, which required a higher bandwidth (30 kHz), and hence larger noise, in order to resolve the translocation events. Conversely, translocations through the positively charged constriction of ReFraC were significantly slower, thus permitting to employ a lower bandwidth (10 kHz).

Amongst the solid-state nanopores, SiN_x showed the best SNR: an impressive value of 37, which was higher than the SNR = 5 obtained for MoS₂, as well as higher than the values for all biological nanopores. The greater SNR for SiN_x results from the very high voltage applied (1000 mV vs 300 mV for MoS₂), producing a particularly large current signal ΔI . The applied voltage for MoS₂ pores was limited by the degradation of the 2D membrane and pore growth under high bias voltages, which typically limited the applied bias to < 400 mV.

In biological nanopores the range of bias voltages is limited by the membrane stability, affected by electroporation and rupture around 200-300 mV [106, 107]. Note furthermore that the SiN_x nanopore system was operated at a much higher bandwidth (500 kHz vs 10 kHz for MoS₂), the regime where dielectric and capacitive noise dominate.

This is advantageous for high-voltage sensing, since these noise sources do not scale with voltage, cf. Eq.2.5 and Eq.2.6. As a result, the high bias voltage improves the signal (ΔI) while it does not affect the noise. Lastly, we note that, while MoS₂ has a lower SNR than SiN_x, it features a better spatial resolution along the molecule, given its 0.7 nm pore length, as compared to the ~ 5 nm of SiN_x.

Finally, it is important to point out that the above comparison was carried out for voltage-driven translocation of DNA through nanopores. A controlled slowdown of the translocation speed can change these numbers dramatically. Indeed, despite the fact that Figure 2.4d shows that the best SNR was obtained for the solid-state SiN_x nanopores, with values exceeding those of biological nanopores, today's commercialized nanopore-based DNA sequencers employ protein pores to read off DNA bases with (sub)-nucleotide resolution over very long reads [16, 108]. Using a helicase to slow down ssDNA molecules through MspA, allowed Laszlo *et al.* [41] to use a very low LP filter frequency of ~ 200 Hz, and fully resolve the step-wise DNA translocation at half-base resolution. By comparing the noise at a 200 Hz bandwidth with the signal obtained for voltage-driven poly(dT) translocations in our experiments, we find an exquisite SNR of ~ 650 for MspA – two orders of magnitude higher than the SNR = 4 noted above. Applying the same reasoning to α -HL and ReFraC increases their SNR to ~ 270 and ~ 220 , respectively, *i.e.*, some-

what lower values, consistent with their higher low-frequency noise compared to MspA (Fig.2.3c). Thus, in the context of DNA sequencing, the real game-changer lies in the enzymatic control over the translocation speed by use of an additional motor protein [14, 16, 41, 105, 109]. For solid-state nanopores, despite the progresses in slowing down the DNA translocation [28, 32–36], time control has so far remained a challenge, and accordingly, DNA sequencing has not yet been realized with such nanopores. Furthermore, mechanical instability of solid-state nanopores over time, which particularly affects smaller pores, should be minimized in order to achieve sufficiently long observation times.

2.6. APPROACHES TO OVERCOME NOISE LIMITATIONS

Figure 2.5 shows important approaches to lower the ionic current noise in nanopores. We first describe efforts to reduce the low-frequency noise. As protonation noise is the main source of low-frequency noise in biological nanopores, it is advantageous to choose a pH value that is far away from the pK_a of the ionizable amino acids to attenuate the noise. Another way to reduce it, is to remove charged amino acids near the constriction site, which is expected to yield lower noise levels. Furthermore, increasing the conformational stiffness of biological pores can help to reduce conductance fluctuations associated with channel breathing.

For solid-state nanopores, the low-frequency $1/f$ noise can be efficiently suppressed by surface functionalization of the SiN_x nanopore with a hydrophilic surface layer, such as Al_2O_3 or SiO_2 [110–113]. In principle, any surface treatment that reduces the amount of contaminants and improves hydrophilicity of the pore surface will lower the $1/f$ noise. Indeed, Tabard-Cossa *et al.* [99] showed that piranha treatment (30% H_2O_2/H_2SO_4 , 1:3) substantially reduced the $1/f$ noise by up to three orders of magnitude. Beamish *et al.* [114] demonstrated that cyclic application of high electric fields to the nanopore also suppressed this noise source. Similar to protein pores, work from Wen *et al.* [55] showed that the $1/f$ noise could be minimized by choosing a pH that is far from the isoelectric point of the nanopore material (~ 5 for Si_3N_4) [115, 116]. Nanopores built with 2D materials suffer from pronounced $1/f$ noise that was found to correlate with the area and thickness of the freestanding 2D-membrane [46, 47]. A decrease of the freestanding area was shown to reduce the $1/f$ noise, while employing multi-layer membranes was also helpful for obtaining less noise, though that approach is less desirable due to a loss of spatial resolution [24, 56, 57]. Use of freestanding 2D-membranes that are directly grown on a SiN_x -supporting membrane was also shown to lower the $1/f$ noise for both graphene [117] and MoS_2 [118] pores, as compared to transferred 2D-membranes [20, 56].

The noise at higher frequencies, constituted by dielectric and capacitive noise, has a well-characterized physical origin, namely the thermal voltage noise in conjunction with the loss conductance of the membrane and substrate materials as well as the amplifier input capacitance. Suppression of dielectric noise is generally achieved by minimizing the capacitance C_{chip} and dielectric loss D of the chip, cf. Eq.2.5. To effectively decrease capacitive noise, the total input capacitance C_{tot} needs to be reduced, see Eq.2.6 and related discussion. In biological nanopores, the high-frequency noise can be reduced by decreasing the area of the lipid bilayer. Mayer *et al.* [78] fabricated teflon holes of only $\sim 25 \mu m$ in diameter with soft lithography using SU-8 resist as master mold, providing

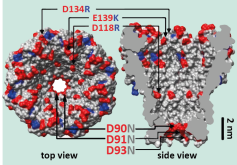
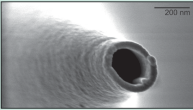
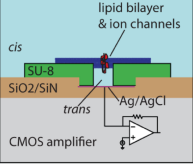
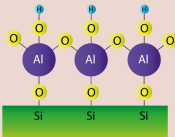
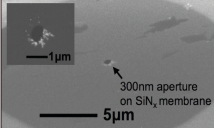
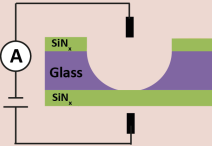
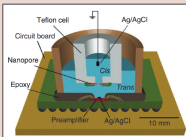
Nanopore system	Low-frequency noise	High-frequency noise
Biological nanopores	<p>Adjust pH far from pK_a of the pore</p> <p>Mutagenesis of ionizable amino-acids</p>  <p>Select pore with low conformational changes</p>	<p>Reduce bilayer area</p>  <p>CMOS integration</p> 
Solid-state nanopores	<p>Surface engineering</p>  <p>Reduce freestanding 2D-area</p> 	<p>Dielectric substrate materials</p>  <p>CMOS integration</p> 

Figure 2.5: Approaches to reduce the noise in nanopore systems. For biological nanopores, low-frequency protonation noise can be minimized by adjusting the pH far from pK_a of the amino acids in the pore constriction, as reported in Ref.[65], or by mutating the ionizable amino acids (Arg, Lys, Asp, Glu) to neutral ones (e.g., Asn), as was done for MspA . Reprinted with permission from Butler, T. Z. *et al.*, 2008 [104]. Low-frequency $1/f$ noise instead can only be avoided by selecting a pore that is mechanically stable under an applied bias, e.g. MspA or α -HL. High-frequency noise can be minimized by reducing the size of the freestanding lipid membrane by, e.g., employing a nanocapillary as a support (Reprinted with permission from Gornall, J. L. *et al.*, 2011 [121]) and by reducing the capacitance of the interconnects by smart CMOS integration (Reprinted with permission from Rosenstein, J. K. *et al.*). For solid-state nanopores, low-frequency $1/f$ noise can be reduced by coating the surface with a hydrophilic, homogeneous material, e.g. Al_2O_3 , as reported in Ref.[113]. For 2D-materials, $1/f$ noise can be suppressed by lowering the area of the freestanding 2D membrane . Adapted with permission from Balan, A. *et al.*, 2015 [18]. High-frequency noise can be minimized by employing dielectric chip substrate materials, e.g. glass (adapted with permission from Balan, A. *et al.*, 2015 [18], or by tight integration of the amplifier and nanopore chip (adapted with permission from Rosenstein, J. K. *et al.*, 2012 [29]).

a C_{chip} of 10-28 pF. By using a U-shaped teflon patch tube as the support, Akeson and coworkers [81, 104] built horizontal bilayers $< 20 \mu\text{m}$ in diameter. Lipid bilayers with a comparable size were also created with the droplet-interface-bilayer (DIB) technique [119]. Kitta *et al.* [120] reported on the fabrication of yet smaller bilayers, with sizes down to $2\text{-}3 \mu\text{m}$ in diameter, by using a heated tungsten tip to create a microhole across the teflon film. Similarly sized $1\text{-}3 \mu\text{m}$ bilayers can be obtained by inserting protein pores into GUVs (Giant Unilamellar Vesicles) and using patch-clamp pipets to measure the conductance of the pores [122, 123]. More recently, Gornall *et al.* [121] showed that borosilicate glass nanopipets with diameters as low as 230 nm could be fabricated and used for current recordings on an OmpF protein channel. Hartel *et al.* [124] achieved high-bandwidth ($> 500 \text{ kHz}$) recordings with biological pores with CMOS-suspended (Complementary Metal-Oxide-Semiconductor) membranes that were built directly over a $\sim 30 \mu\text{m}$ well on top of a CMOS-amplifier chip. This offered a reduction of the total input capacitance C_{tot} to $< 4 \text{ pF}$ and provided a bandwidth as high as 1 MHz and a SNR > 8 at 500 kHz, for detecting the gating of a RyR1 pore (type 1 ryanodine receptor) [124]. Combined with extended β distribution data analysis [125] (which exploits the characteristics of the excess current noise to reconstruct the true current signal), it was possible to achieve a time resolution of 35 ns [124].

For reducing the high-frequency noise in SiN_x solid-state nanopores, an established method, first reported by Tabard-Cossa *et al.* [99], is to lower C_{chip} by coating the area of the chip around the pore with a dielectric, e.g. PDMS, thereby providing additional thickness to the chip membrane surrounding the pore and thus a low series capacitance. Similarly, a substantial reduction of C_{chip} was achieved by employing a dielectric, e.g. amorphous glass [17, 18] or Pyrex [24, 86] as substrate material instead of the commonly used crystalline silicon which is intrinsically conductive. In work by Balan *et al.*, [18] glass chips were shown to reduce C_{chip} to $< 1 \text{ pF}$, compared to $> 300 \text{ pF}$ for standard silicon chips [60]. Similarly to biological nanopores, the highest working bandwidths were so far achieved by integrating a low C_{chip} nanopore device with an on-chip CMOS-amplifier [29, 30], which lowered the total input capacitance to $C_{tot} \approx 4 \text{ pF}$. In this way, ssDNA molecules were recorded using ultrathin ($< 4 \text{ nm}$) sub-2 nm pores yielding a $\text{SNR} > 10$ at 5 MHz [30]. In 2D nanopores, the high-frequency noise can be addressed in similar ways to SiN_x pores. The use of glass as substrate material, combined with a small $\sim 300 \text{ nm}$ freestanding 2D-membrane of graphene or MoS_2 , resulted in a $C_{chip} < 2 \text{ pF}$ [18].

2.7. CONCLUSION

In this paper, we illustrated the main sources of noise affecting various nanopore systems, with a particular emphasis on comparing biological and solid-state nanopores, and we discussed practical approaches to lower the noise. We compared the SNR of poly(dT) translocations through a representative set of biological and solid-state pores, and found that silicon nitride nanopores gave the highest SNR. This can be attributed to the higher currents (*i.e.* larger signals) that solid-state systems offer, and to the relatively low high-frequency noise. Despite these good noise characteristics, prominent applications such as DNA or protein sequencing have so far remained out of reach for solid-state nanopores, because the fast translocation speed provides only a short observation time

per single molecule. There are two ways to improve this: one can either shift the sampling rate into even higher frequencies (\gg MHz), or alternatively slow down the translocation of the molecule. The latter strategy has led to the successful commercialization of DNA sequencers based on protein nanopores that are coupled with an enzymatic stepping motor. In our comparison, we found that the SNR of MspA increased > 160 -fold by such speed control, mainly due to the decoupling of the signal from the high-frequency noise. Additionally, the motor protein provides a ratcheting mechanism that translocates the substrate with a constant discrete step size. Since the sensing region of the pore is typically larger than the individual monomer size (nucleotide or amino-acid), such a mechanism is indispensable to reproducibly resolve and identify the sequence. Future improvements of the solid-state nanopore system could thus be directed towards either a further increase of the temporal resolution, e.g. by reducing even more the overall parasitic capacitances, or by creating an efficient slowdown mechanism, similar to biological nanopores. In general, the understanding of noise sources, associated timescales, and techniques to lower the noise at both low and high frequencies are greatly beneficial to maximize the sensitivity of nanopore detection and thereby extend the range of its applications.

REFERENCES

- [1] A. Fragasso, S. Schmid, and C. Dekker, *Comparing Current Noise in Biological and Solid-State Nanopores*, ACS Nano , acsnano.9b09353 (2020).
- [2] C. Dekker, *Solid-state nanopores (Review Article)*, Nature Nanotechnology , 1 (2007).
- [3] S. Carson and M. Wanunu, *Challenges in DNA motion control and sequence read-out using nanopore devices*, Nanotechnology **26**, 74004 (2015).
- [4] G. Maglia, A. J. Heron, D. Stoddart, D. Japrun, and H. Bayley, *Methods in Enzymology*, 1st ed., Vol. 475 (Elsevier Inc., 2010) pp. 591–623, arXiv:NIHMS150003 .
- [5] Y. Feng, Y. Zhang, C. Ying, D. Wang, and C. Du, *Nanopore-based fourth-generation DNA sequencing technology*, Genomics, Proteomics and Bioinformatics **13**, 4 (2015), arXiv:NIHMS150003 .
- [6] Y. Lin, Y. L. Ying, and Y. T. Long, *Nanopore confinement for electrochemical sensing at the single-molecule level*, Current Opinion in Electrochemistry **7**, 172 (2018).
- [7] E. Atas, A. Singer, and A. Meller, *DNA sequencing and bar-coding using solid-state nanopores*, (2012).
- [8] W. Yang, A. Birnie, L. Restrepo-Pérez, J. van der Torre, M. Bengtson, S. J. Heerema, and C. Dekker, *Detection of CRISPR-dCas9 on DNA with Solid-State Nanopores*, Nano Letters **18**, 6469 (2018).
- [9] A. H. Squires, J. S. Hersey, M. W. Grinstaff, and A. Meller, *A nanopore-nanofiber mesh biosensor to control DNA translocation*, Journal of the American Chemical Society **135**, 16304 (2013).

- [10] B. N. Miles, A. P. Ivanov, K. a. Wilson, F. Doğan, D. Japrun, and J. B. Edel, *Single molecule sensing with solid-state nanopores: novel materials, methods, and applications*, Chemical Society Reviews **42** (2012), 10.1039/c2cs35286a.
- [11] D. Wu, S. Bi, L. Zhang, and J. Yang, *Single-molecule study of proteins by biological nanopore sensors*, Sensors (Switzerland) **14**, 18211 (2014).
- [12] A. J. Storm, C. Storm, J. Chen, H. Zandbergen, J. F. Joanny, and C. Dekker, *Fast DNA translocation through a solid-state nanopore*, Nano Letters **5**, 1193 (2005).
- [13] C. Plesa, S. W. Kowalczyk, R. Zinsmeister, A. Y. Grosberg, Y. Rabin, and C. Dekker, *Fast translocation of proteins through solid state nanopores*, Nano Letters **13**, 658 (2013).
- [14] E. a. Manrao, I. M. Derrington, A. H. Laszlo, K. W. Langford, M. K. Hopper, N. Gillgren, M. Pavlenok, M. Niederweis, and J. H. Gundlach, *Reading DNA at single-nucleotide resolution with a mutant MspA nanopore and phi29 DNA polymerase*, Nature Biotechnology **30**, 349 (2012).
- [15] I. M. Derrington, T. Z. Butler, M. D. Collins, E. Manrao, M. Pavlenok, M. Niederweis, and J. H. Gundlach, *Nanopore DNA sequencing with MspA*, Proceedings of the National Academy of Sciences **107**, 16060 (2010).
- [16] J.-M. Carter and S. Hussain, *Robust long-read native DNA sequencing using the ONT CsgG Nanopore system*, Wellcome Open Research **2**, 1 (2018).
- [17] A. Balan, B. Machielse, D. Niedzwiecki, J. Lin, P. Ong, R. Engelke, K. L. Shepard, and M. Drndić, *Improving signal-to-noise performance for DNA translocation in solid-state nanopores at MHz bandwidths*, Nano Letters **14**, 7215 (2014).
- [18] A. Balan, C. C. Chien, R. Engelke, and M. Drndic, *Suspended Solid-state Membranes on Glass Chips with Sub 1-pF Capacitance for Biomolecule Sensing Applications*, Scientific Reports **5**, 1 (2015).
- [19] K. Venta, G. Shemer, M. Puster, J. A. Rodríguez-Manzo, A. Balan, J. K. Rosenstein, K. Shepard, and M. Drndić, *Differentiation of short, single-stranded DNA homopolymers in solid-state nanopores*, ACS Nano **7**, 4629 (2013).
- [20] C. a. Merchant, K. Healy, M. Wanunu, V. Ray, N. Peterman, J. Bartel, M. D. Fischbein, K. Venta, Z. Luo, a. T. C. Johnson, and M. Drndić, *DNA translocation through graphene nanopores*, Nano Letters **10**, 2915 (2010).
- [21] G. F. Schneider, S. W. Kowalczyk, V. E. Calado, G. Pandraud, H. W. Zandbergen, L. M. Vandersypen, and C. Dekker, *DNA translocation through graphene nanopores*, Nano Letters **10**, 3163 (2010).
- [22] G. F. Schneider, Q. Xu, S. Hage, S. Luik, J. N. Spoor, S. Malladi, H. Zandbergen, and C. Dekker, *Tailoring the hydrophobicity of graphene for its use as nanopores for DNA translocation*, Nature Communications **4**, 1 (2013).

- [23] Z. Zhou, Y. Hu, H. Wang, Z. Xu, W. Wang, X. Bai, X. Shan, and X. Lu, *DNA Translocation through hydrophilic nanopore in hexagonal boron nitride*, Scientific Reports **3**, 1 (2013).
- [24] K. B. Park, H. J. Kim, H. M. Kim, S. A. Han, K. H. Lee, S. W. Kim, and K. B. Kim, *Noise and sensitivity characteristics of solid-state nanopores with a boron nitride 2-D membrane on a pyrex substrate*, Nanoscale **8**, 5755 (2016).
- [25] K. Liu, M. Lihter, A. Sarathy, S. Caneva, H. Qiu, D. Deiana, V. Tileli, D. T. Alexander, S. Hofmann, D. Dumcenco, A. Kis, J. P. Leburton, and A. Radenovic, *Geometrical Effect in 2D Nanopores*, Nano Letters **17**, 4223 (2017).
- [26] M. Graf, M. Lihter, M. Thakur, V. Georgiou, J. Topolancik, B. R. Ilic, K. Liu, J. Feng, Y. Astier, and A. Radenovic, *Fabrication and practical applications of molybdenum disulfide nanopores*, Nature Protocols **14**, 1130 (2019).
- [27] K. Liu, J. Feng, A. Kis, and A. Radenovic, *Atomically thin molybdenum disulfide nanopores with high sensitivity for dna translocation*, ACS Nano **8**, 2504 (2014).
- [28] J. Feng, K. Liu, R. D. Bulushev, S. Khlybov, D. Dumcenco, A. Kis, and A. Radenovic, *Identification of single nucleotides in MoS₂ nanopores*, Nature Nanotechnology **10**, 1070 (2015).
- [29] J. K. Rosenstein, M. Wanunu, C. A. Merchant, M. Drndic, and K. L. Shepard, *Integrated nanopore sensing platform with sub-microsecond temporal resolution*, Nature Methods **9**, 487 (2012).
- [30] S. Shekar, D. J. Niedzwiecki, C. C. Chien, P. Ong, D. A. Fleischer, J. Lin, J. K. Rosenstein, M. Drndić, and K. L. Shepard, *Measurement of DNA translocation dynamics in a solid-state nanopore at 100 ns temporal resolution*, Nano Letters **16**, 4483 (2016).
- [31] G. Thiel, K. L. Shepard, A. J. Hartel, S. Shekar, I. Schroeder, and P. Ong, *High bandwidth approaches in nanopore and ion channel recordings – A tutorial review*, Analytica Chimica Acta **1061** (2019), 10.1016/j.aca.2019.01.034.
- [32] U. F. Keyser, *Controlling molecular transport through nanopores*, Journal of the Royal Society Interface **8**, 1369 (2011).
- [33] M. Wanunu and A. Meller, *Chemically modified solid-state nanopores*, Nano Letters **7**, 1580 (2007).
- [34] S. Pud, S. H. Chao, M. Belkin, D. Verschueren, T. Huijben, C. Van Engelenburg, C. Dekker, and A. Aksimentiev, *Mechanical Trapping of DNA in a Double-Nanopore System*, Nano Letters **16**, 8021 (2016).
- [35] T. Gilboa and A. Meller, *Optical sensing and analyte manipulation in solid-state nanopores*, Analyst **140**, 4733 (2015).

- [36] H. Yamazaki, R. Hu, Q. Zhao, and M. Wanunu, *Photothermally Assisted Thinning of Silicon Nitride Membranes for Ultrathin Asymmetric Nanopores*, ACS Nano **12**, 12472 (2018).
- [37] N. E. Weckman, N. Ermann, R. Gutierrez, K. Chen, J. Graham, R. Tivony, A. Heron, and U. F. Keyser, *Multiplexed DNA Identification Using Site Specific dCas9 Barcodes and Nanopore Sensing*, ACS Sensors **4**, 2065 (2019).
- [38] K. Chen, M. Juhasz, F. Gularek, E. Weinhold, Y. Tian, U. F. Keyser, and N. A. Bell, *Ionic Current-Based Mapping of Short Sequence Motifs in Single DNA Molecules Using Solid-State Nanopores*, Nano Letters **17**, 5199 (2017).
- [39] K. Chen, J. Kong, J. Zhu, N. Ermann, P. Predki, and U. F. Keyser, *Digital Data Storage Using DNA Nanostructures and Solid-State Nanopores*, Nano Letters **19**, 8 (2019).
- [40] N. A. Bell and U. F. Keyser, *Digitally encoded DNA nanostructures for multiplexed, single-molecule protein sensing with nanopores*, Nature Nanotechnology **11**, 645 (2016).
- [41] A. H. Laszlo, I. M. Derrington, and J. H. Gundlach, *MspA nanopore as a single-molecule tool: From sequencing to SPRNT*, Methods **105**, 75 (2016).
- [42] L. Song, M. R. Hobaugh, C. Shustak, S. Cheley, H. Bayley, and J. E. Gouaux, *Structure of staphylococcal α -hemolysin, a heptameric transmembrane pore*, Science **274**, 1859 (1996).
- [43] G. Menestrina, *Ionic Channels Formed by Staphylococcus aureus Alpha-Toxin: Voltage-Dependent Inhibition by Divalent and Trivalent Cations*, The Journal of Membrane Biology **90**, 177 (1986).
- [44] C. Wloka, N. L. Mutter, M. Soskine, and G. Maglia, *Alpha-Helical Fragaceatoxin C Nanopore Engineered for Double-Stranded and Single-Stranded Nucleic Acid Analysis*, Angewandte Chemie - International Edition **55**, 12494 (2016).
- [45] G. Huang, K. Willems, M. Soskine, C. Wloka, and G. Maglia, *Electro-osmotic capture and ionic discrimination of peptide and protein biomarkers with FraC nanopores*, Nature Communications **8**, 1 (2017).
- [46] M. Montal and P. Mueller, *Formation of bimolecular membranes from lipid monolayers and a study of their electrical properties*. Proceedings of the National Academy of Sciences of the United States of America **69**, 3561 (1972).
- [47] B. Sakmann and E. Neher, *Single-channel recording* (2009).
- [48] V. Tabard-Cossa, *Instrumentation for Low-Noise High-Bandwidth Nanopore Recording*, in *Engineered Nanopores for Bioanalytical Applications: A Volume in Micro and Nano Technologies* (2013) pp. 59–93.
- [49] E. Milotti, *1/F Noise: a Pedagogical Review*, arXiv (2002), arXiv:0204033 [physics] .

- [50] P. Dutta and P. M. Horn, *Low-frequency fluctuations in solids: 1/f noise*, Reviews of Modern Physics **53** (1981).
- [51] D. Zhang, P. Solomon, S. L. Zhang, and Z. Zhang, *An impedance model for the low-frequency noise originating from the dynamic hydrogen ion reactivity at the solid/liquid interface*, Sensors and Actuators, B: Chemical **254**, 363 (2018).
- [52] R. P. Jindal and A. Van Der Ziel, *Model for mobility fluctuation 1/f noise*, Applied Physics Letters **38**, 290 (1981).
- [53] F. Hooge, *1/F Noise*, Physica B+C **83**, 14 (1976).
- [54] R. M. M. Smeets, U. F. Keyser, M. Y. Wu, N. H. Dekker, and C. Dekker, *Nanobubbles in solid-state nanopores*, Physical Review Letters **97**, 1 (2006).
- [55] C. Wen, S. Zeng, K. Arstila, T. Sajavaara, Y. Zhu, Z. Zhang, and S. L. Zhang, *Generalized Noise Study of Solid-State Nanopores at Low Frequencies*, ACS Sensors **2**, 300 (2017).
- [56] S. J. Heerema, G. F. Schneider, M. Rozemuller, L. Vicarelli, H. W. Zandbergen, and C. Dekker, *1/F Noise in Graphene Nanopores*, Nanotechnology **26** (2015), 10.1088/0957-4484/26/7/074001.
- [57] Z.-Y. Zhang, Y.-S. Deng, H.-B. Tian, H. Yan, H.-L. Cui, and D.-Q. Wang, *Noise Analysis of Monolayer Graphene Nanopores*, International Journal of Molecular Sciences **19**, 2639 (2018).
- [58] F. Wohnsland and R. Benz, *1/f-Noise of open bacterial porin channels*, Journal of Membrane Biology **158**, 77 (1997).
- [59] S. M. Bezrukov and M. Winterhalter, *Examining noise sources at the single-molecule level: 1/f noise of an open maltoporin channel*, Physical Review Letters **85**, 202 (2000).
- [60] R. M. M. Smeets, U. F. Keyser, N. H. Dekker, and C. Dekker, *Noise in solid-state nanopores*, Proceedings of the National Academy of Sciences of the United States of America **105**, 417 (2008).
- [61] R. M. M. Smeets, N. H. Dekker, and C. Dekker, *Low-frequency noise in solid-state nanopores*, Nanotechnology **20** (2009), 10.1088/0957-4484/20/9/095501.
- [62] A. Fragasso, S. Pud, and C. Dekker, *1/F Noise in Solid-State Nanopores Is Governed By Access and Surface Regions*, Nanotechnology **30**, 395202 (2019).
- [63] C. Tasserit, A. Koutsioubas, D. Lairez, G. Zalczer, and M. C. Clochard, *Pink noise of ionic conductance through single artificial nanopores revisited*, Physical Review Letters **105**, 1 (2010).
- [64] E. M. Nestorovich, T. K. Rostovtseva, and S. M. Bezrukov, *Residue Ionization and Ion Transport through OmpF Channels*, Biophysical Journal **85**, 3718 (2003).

- [65] J. J. Kasianowicz and S. M. Bezrukov, *Current Noise Reveals Protonation Kinetics and Number of Ionizable Sites in an Open Protein Ion Channel*, Physical Review Letters **70**, 2352 (1993).
- [66] J. J. Kasianowicz and S. M. Bezrukov, *Protonation dynamics of the alpha-toxin ion channel from spectral analysis of pH-dependent current fluctuations*, Biophysical Journal **69**, 94 (1995).
- [67] S. Machlup, *Noise in semiconductors: Spectrum of a two-parameter random signal*, Journal of Applied Physics **25**, 341 (1954).
- [68] J. Johnson, *Thermal agitation of electricity in conductors*, Physical Review **32** (1928).
- [69] H. Nyquist, *Thermal agitation of electric charge in conductors*, Physical Review **32** (1928).
- [70] Y. M. Blanter and M. Büttiker, *Shot noise in mesoscopic conductors*, Physics Report **336**, 1 (2000).
- [71] W. Schottky, *Über spontane Stromschwankungen in verschiedenen Elektrizitätsleitern*, Annalen der Physik **362**, 541 (1918).
- [72] L. F. Chen, C. K. Ong, C. P. Neo, V. V. Varadan, and V. K. Varadan, *Microwave Electronics: Measurement and Materials Characterization*, edited by John Wiley & Sons (Wiley, 2004) pp. 7–15.
- [73] J. D. Uram, K. Ke, and M. L. Mayer, *Noise and bandwidth of current recordings from submicrometer pores and nanopores*, ACS Nano **2**, 857 (2008).
- [74] R. Sherman-Gold, *The Axon CNS Guide to Electrophysiology and Biophysics Laboratory Techniques* (2012).
- [75] M. Ayub and H. Bayley, *Engineered transmembrane pores*, Current Opinion in Chemical Biology **34**, 117 (2016).
- [76] Z. Yu, M. F. Jarrold, R. Williams, S. J. Ludtke, I. Echeverria, B. D. Slaughter, I. E. Chemmama, J. R. Unruh, R. Mironska, M. J. de la Cruz, J. A. Hogan, M. Shivaraju, A. S. Chaudhury, B. Raveh, J. Wang, R. Pellarin, P. Upla, S. J. Kim, T. Herricks, I. Nudelman, A. Sali, W. Zhang, D. L. Stokes, J. D. Aitchison, M. P. Rout, Y. Shi, C. W. Akey, C. H. Greenberg, J. Fernandez-Martinez, B. T. Chait, J. L. Gerton, and E. Y. Jacobs, *Integrative structure and functional anatomy of a nuclear pore complex*, Nature **555**, 475 (2018).
- [77] J. W. Robertson, *Engineered Nanopores for Bioanalytical Applications: A Volume in Micro and Nano Technologies*, first edit ed. (Elsevier Inc., 2013) pp. 95–119.
- [78] M. Mayer, J. K. Kriebel, M. T. Tosteson, and G. M. Whitesides, *Microfabricated Teflon membranes for low-noise recordings of ion channels in planar lipid bilayers*, Biophysical Journal **85**, 2684 (2003).

- [79] S. Nekolla, C. Andersen, and R. Benz, *Noise analysis of ion current through the open and the sugar-induced closed state of the LamB channel of Escherichia coli outer membrane: evaluation of the sugar binding kinetics to the channel interior*, Biophysical Journal **66**, 1388 (1994).
- [80] P. Lauger, *Structural fluctuations and current noise of ionic channels*, Biophysical Journal **48**, 369 (1985).
- [81] M. Akeson, E. Brandin, D. Branton, D. W. Deamer, and J. J. Kasianowicz, *Microsecond Time-Scale Discrimination Among Polycytidylic Acid, Polyadenylic Acid, and Polyuridylic Acid as Homopolymers or as Segments Within Single RNA Molecules*, Biophysical Journal **77**, 3227 (2009).
- [82] S. Bhattacharya, J. Yoo, and A. Aksimentiev, *Water Mediates Recognition of DNA Sequence via Ionic Current Blockade in a Biological Nanopore*, ACS Nano **10**, 4644 (2016).
- [83] T. Gibb and M. Ayub, *Solid-State Nanopore Fabrication*, Engineered Nanopores for Bioanalytical Applications: A Volume in Micro and Nano Technologies, 121 (2013).
- [84] S. M. Gilbert, G. Dunn, A. Azizi, T. Pham, B. Shevitski, E. Dimitrov, S. Liu, S. Aloni, and A. Zettl, *Fabrication of Subnanometer-Precision Nanopores in Hexagonal Boron Nitride*, Scientific Reports **7**, 1 (2017).
- [85] M. H. Lee, A. Kumar, K. B. Park, S. Y. Cho, H. M. Kim, M. C. Lim, Y. R. Kim, and K. B. Kim, *A low-noise solid-state nanopore platform based on a highly insulating substrate*, Scientific Reports **4**, 1 (2014).
- [86] W. H. Pitchford, H. J. Kim, A. P. Ivanov, H. M. Kim, J. S. Yu, R. J. Leatherbarrow, T. Albrecht, K. B. Kim, and J. B. Edel, *Synchronized optical and electronic detection of biomolecules using a low noise nanopore platform*, ACS Nano **9**, 1740 (2015).
- [87] A. J. Storm, J. H. Chen, X. S. Ling, H. W. Zandbergen, and C. Dekker, *Fabrication of solid-state nanopores with single-nanometre precision*, Nature Materials **2**, 537 (2003).
- [88] M. Van Den Hout, A. R. Hall, M. Y. Wu, H. W. Zandbergen, C. Dekker, and N. H. Dekker, *Controlling nanopore size, shape and stability*, Nanotechnology **21** (2010), 10.1088/0957-4484/21/11/115304.
- [89] Y. H. Lanyon, G. De Marzi, Y. E. Watson, A. J. Quinn, J. P. Gleeson, G. Redmond, and D. W. Arrigan, *Fabrication of nanopore array electrodes by focused ion beam milling*, Analytical Chemistry **79**, 3048 (2007).
- [90] B. Schiedt, L. Auvray, L. Bacri, G. Oukhaled, A. Madouri, E. Bourhis, G. Patriarche, J. Pelta, R. Jede, and J. Gierak, *Direct FIB fabrication and integration of "single nanopore devices" for the manipulation of macromolecules*, Microelectronic Engineering **87**, 1300 (2010).

- [91] D. V. Verschuieren, W. Yang, and C. Dekker, *Lithography-based fabrication of nanopore arrays in freestanding SiN and graphene membranes*, **29**, 145302 (2018), arXiv:15334406.
- [92] T. Gilboa, E. Zvuloni, A. Zreben, A. H. Squires, and A. Meller, *Automated, Ultra-Fast Laser-Drilling of Nanometer Scale Pores and Nanopore Arrays in Aqueous Solutions*, *Advanced Functional Materials* **1900642**, 1 (2019).
- [93] T. Gilboa, A. Zreben, A. Girsault, and A. Meller, *Optically-Monitored Nanopore Fabrication Using a Focused Laser Beam*, *Scientific Reports* **8**, 1 (2018).
- [94] S. Pud, D. Verschuieren, N. Vukovic, C. Plesa, M. P. Jonsson, and C. Dekker, *Self-Aligned Plasmonic Nanopores by Optically Controlled Dielectric Breakdown*, *Nano Letters* **15**, 7112 (2015).
- [95] H. Kwok, K. Briggs, and V. Tabard-Cossa, *Nanopore fabrication by controlled dielectric breakdown*, *PLoS ONE* **9** (2014), 10.1371/journal.pone.0092880.
- [96] J. D. Piper, R. W. Clarke, Y. E. Korchev, L. Ying, and D. Klennerman, *A renewable nanosensor based on a glass nanopipette*, *Journal of the American Chemical Society* **128**, 16462 (2006).
- [97] X. Xu, C. Li, Y. Zhou, and Y. Jin, *Controllable Shrinking of Glass Capillary Nanopores Down to sub-10 nm by Wet-Chemical Silanization for Signal-Enhanced DNA Translocation*, *ACS Sensors* **2**, 1452 (2017).
- [98] J. A. Bafna and G. V. Soni, *Fabrication of Low Noise Borosilicate Glass Nanopores for Single Molecule Sensing*, *PloS one* **11**, e0157399 (2016).
- [99] V. Tabard-Cossa, D. Trivedi, M. Wiggin, N. N. Jetha, and A. Marziali, *Noise analysis and reduction in solid-state nanopores*, *Nanotechnology* **18** (2007), 10.1088/0957-4484/18/30/305505.
- [100] L. K. J. Vandamme and D. Rigaud, *1/f noise in MOS devices, mobility or number fluctuations?* *IEEE Trans. Electron Devices* **41**, 1936 (1994).
- [101] S. Garaj, S. Liu, J. A. Golovchenko, and D. Branton, *Molecule-hugging graphene nanopores*, *Proceedings of the National Academy of Sciences of the United States of America* **110**, 12192 (2013).
- [102] Z. Roelen, J. A. Bustamante, A. Carlsen, A. Baker-Murray, and V. Tabard-Cossa, *Instrumentation for low noise nanopore-based ionic current recording under laser illumination*, *Review of Scientific Instruments* **89** (2018), 10.1063/1.5006262.
- [103] J. K. Rosenstein, S. Ramakrishnan, J. Roseman, and K. L. Shepard, *Single ion channel recordings with CMOS-anchored lipid membranes*, *Nano Letters* **13**, 2682 (2013).
- [104] T. Z. Butler, M. Pavlenok, I. M. Derrington, M. Niederweis, and J. H. Gundlach, *Single-molecule DNA detection with an engineered MspA protein nanopore*, *Proceedings of the National Academy of Sciences* **105**, 20647 (2008).

- [105] E. Manrao, T. Z. Butler, M. Pavlenok, M. D. Collins, M. Niederweis, J. H. Gundlach, and I. M. Derrington, *Nanopore DNA sequencing with MspA*, Proceedings of the National Academy of Sciences **107**, 16060 (2010).
- [106] M. Pavlin, T. Kotnik, D. Miklavčič, P. Kramar, and A. Maček Lebar, *Electroporation of Planar Lipid Bilayers and Membranes*, in *Advances in Planar Lipid Bilayers and Liposomes*, Vol. 6 (2008) pp. 165–226.
- [107] M. Tarek, *Membrane electroporation: A molecular dynamics simulation*, Biophysical Journal **88**, 4045 (2005).
- [108] M. Jain, S. Koren, K. H. Miga, J. Quick, A. C. Rand, T. A. Sasani, J. R. Tyson, A. D. Beggs, A. T. Dilthey, I. T. Fiddes, S. Malla, H. Marriott, T. Nieto, J. O’Grady, H. E. Olsen, B. S. Pedersen, A. Rhie, H. Richardson, A. R. Quinlan, T. P. Snutch, L. Tee, B. Paten, A. M. Phillippy, J. T. Simpson, N. J. Loman, and M. Loose, *Nanopore sequencing and assembly of a human genome with ultra-long reads*, Nature Biotechnology **36**, 338 (2018).
- [109] M. Jain, H. E. Olsen, B. Paten, and M. Akeson, *The Oxford Nanopore MinION: delivery of nanopore sequencing to the genomics community*, Genome Biology **17**, 1 (2016).
- [110] C. M. Wang, D. L. Kong, Q. Chen, and J. M. Xue, *Surface engineering of synthetic nanopores by atomic layer deposition and their applications*, Frontiers of Materials Science **7**, 335 (2013).
- [111] J. Nilsson, J. R. Lee, T. V. Ratto, and S. E. Létant, *Localized functionalization of single nanopores*, Advanced Materials **18**, 427 (2006).
- [112] C. Danelon, C. Santschi, J. Brugger, and H. Vogel, *Fabrication and functionalization of nanochannels by electron-beam-induced silicon oxide deposition*, Langmuir **22**, 10711 (2006).
- [113] P. Chen, T. Mitsui, D. B. Farmer, J. Golovchenko, R. G. Gordon, and D. Branton, *Atomic layer deposition to fine-tune the surface properties and diameters of fabricated nanopores*, Nano Letters **4**, 1333 (2004).
- [114] E. Beamish, H. Kwok, V. Tabard-Cossa, and M. Godin, *Precise control of the size and noise of solid-state nanopores using high electric fields*, Nanotechnology **23** (2012), 10.1088/0957-4484/23/40/405301.
- [115] M. Kosmulski, *The pH-dependent surface charging and the points of zero charge*, Journal of Colloid and Interface Science **253**, 77 (2002).
- [116] M. Firnkes, D. Pedone, J. Knezevic, M. Döblinger, and U. Rant, *Electrically facilitated translocations of proteins through silicon nitride nanopores: Conjoint and competitive action of diffusion, electrophoresis, and electroosmosis*, Nano Letters **10**, 2162 (2010).

- [117] P. Waduge, J. Larkin, M. Upmanyu, S. Kar, and M. Wanunu, *Programmed synthesis of freestanding graphene nanomembrane arrays*, *Small* **11**, 597 (2015).
- [118] P. Waduge, I. Bilgin, J. Larkin, R. Y. Henley, K. Goodfellow, A. C. Graham, D. C. Bell, N. Vamivakas, S. Kar, and M. Wanunu, *Direct and Scalable Deposition of Atomically Thin Low-Noise MoS₂ Membranes on Apertures*, *ACS Nano* **9**, 7352 (2015).
- [119] H. Bayley, B. Cronin, A. Heron, M. a. Holden, W. L. Hwang, R. Syeda, J. Thompson, and M. Wallace, *Droplet interface bilayers RID B-8725-2008*, *Molecular Biosystems* **4**, 1191 (2008).
- [120] M. Kitta, H. Tanaka, and T. Kawai, *Rapid fabrication of Teflon micropores for artificial lipid bilayer formation*, *Biosensors and Bioelectronics* **25**, 931 (2009).
- [121] J. L. Gornall, K. R. Mahendran, O. J. Pambos, L. J. Steinbock, O. Otto, C. Chimere, M. Winterhalter, and U. F. Keyser, *Simple reconstitution of protein pores in nano lipid bilayers*, *Nano Letters* **11**, 3334 (2011).
- [122] M. Criado and B. U. Keller, *A membrane fusion strategy for single-channel recordings of membranes usually non-accessible to patch-clamp pipette electrodes*, *FEBS Letters* **224**, 172 (1987).
- [123] G. Riquelme, E. Lopez, L. M. Garcia-segura, J. A. Ferragut, and J. M. Gonzalez-ros, *Giant Liposomes : A Model System in Which To Obtain Patch-Clamp Recordings*, *Society* , 11215 (1990).
- [124] A. J. W. Hartel, P. Ong, I. Schroeder, M. H. Giese, S. Shekar, O. B. Clarke, R. Zalk, A. R. Marks, W. A. Hendrickson, and K. L. Shepard, *Single-channel recordings of RyR1 at microsecond resolution in CMOS-suspended membranes*, *Proceedings of the National Academy of Sciences* **115**, E1789 (2018).
- [125] I. Schroeder, *How to resolve microsecond current fluctuations in single ion channels: The power of beta distributions*, *Channels* **9**, 262 (2015).

3

1/F NOISE IN SOLID-STATE NANOPORES IS GOVERNED BY ACCESS AND SURFACE REGIONS

The performance of solid-state nanopores as promising biosensors is severely hampered by low-frequency 1/f noise in the through-pore ionic current recordings. Here, we develop a model for the 1/f noise in such nanopores, that, unlike previous reports, accounts for contributions from both the pore-cylinder, pore-surface, and access regions. To test our model, we present measurements of the open-pore current through solid-state nanopores of different diameters (1-50 nm). To describe the observed trends, it appears essential to include the access resistance in the modelling of the 1/f noise. We attribute a different Hooge constant for the charge carrier fluctuations occurring in the bulk electrolyte and at the pore surface. The model reported here can be used to accurately analyze different contributions to the nanopore low-frequency noise, rendering it a powerful tool for characterizing and comparing different membrane materials in terms of their 1/f-noise properties.

3.1. INTRODUCTION

Solid-state nanopores are versatile single-molecule biosensors [2], [3], [4], [5] which hold great promise for bio-medical sensing [6–10] and sequencing [11]. The success of nanopores [12–15] is due to their simplicity and elegant working principle, where upon passing the nanopore, single molecules induce the modulation of the through-pore ionic current, which can be detected by the electronics. Solid-state nanopores, i.e., small pores within a SiN membrane, can efficiently detect the analyte molecules [16, 17], read-out certain structural features of the detected molecules [9, 18, 19], and even discriminate short nucleotide sequences [20]. However, they still lack the precision of their biological counterparts, with which DNA sequencing has been achieved, either by direct reading of DNA bases [21, 22], or by sequencing-by-synthesis techniques [23–25]. This is due to the large translocation speeds [26, 27] and the sizeable ionic current noise [28]. Indeed, for many applications [26, 29, 30] the ionic current noise is a limiting factor.

The ionic current noise in solid-state nanopores originates from multiple sources, *viz.*, the nanopore chip substrate, the membrane dielectric properties, the interface between the nanopore surface and the electrolyte solution, and the bulk of the electrolyte [31, 32]. An in-depth overview of noise spectroscopy and its application for nanopore sensors can be found in [33, 34]. Briefly, the high-frequency part of the ionic current noise arises from capacitance and dielectric loss of the chip [35] and thus can be engineered to lower values by chip design [35–37]. On the contrary, there is no established solution to dampen the low-frequency noise, which is mainly characterized by $1/f$ noise [32], the nature of which is poorly understood. Chen *et al.* [38] demonstrated that atomically thin films of aluminum oxide deposited onto the nanopore surface can suppress low-frequency noise in solid-state nanopores, but notably the initial noise that they had as a starting point in their experiments was extremely high as compared to the values commonly measured for bare silicon nitride [32, 36]. Smeets *et al.* [32] established that $1/f$ noise in nanopores obeys Hooge's empirical equation which relates the noise to the number of charge carriers in the pore volume. Wen *et al.* [39] further investigated the $1/f$ noise in solid-state nanopores, by analyzing pore-surface and pore-cylinder $1/f$ noise contributions as a function of pH and salt concentration. However, despite some success in describing the $1/f$ noise behaviour at different electrolyte conditions, none of these models so far has been able to quantitatively account for the $1/f$ noise for different nanopore geometries and membrane materials. This lack of a general theory to describe the noise hinders the analysis and search for low-noise nanopore materials and the development of methods for $1/f$ noise suppression. Indeed, a comprehensive model capable of predicting $1/f$ noise behavior of solid-state nanopore sensors is very much welcome for further improvement of the sensor ionic-current measurement resolution.

Here, we present a general theoretical noise model for nanopores that, unlike previous reports, accounts for contributions from both the pore-cylinder, pore-surface, and access regions, as indicated in Fig.3.1A. Furthermore, we present experimentally measured values of the $1/f$ noise in SiN solid-state nanopores of different diameters (1–50 nm), and we find an excellent agreement between the model and the data. We show that the dependence of $1/f$ noise on geometrical parameters of the pores is governed by the distribution of the electric potential between the nanopore and the access region, which has been previously defined [40] and measured for different nanopore systems [41, 42].

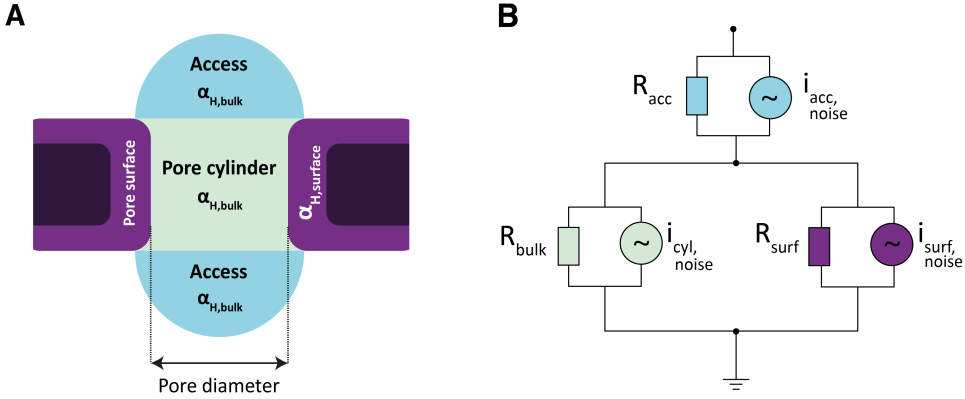


Figure 3.1: (A) Schematic representation of the relevant nanopore regions: access region (blue), pore-cylinder region (green), pore-surface (purple). (B) Equivalent circuit of the nanopore sensor. Nanopore regions are modelled as resistive elements connected in parallel to noise current generators.

Fitting the model to our experimental data, we deduce that the $1/f$ noise generated by the bulk (access and pore-cylinder) and surface regions stem from different noise mechanisms and should be described by distinct Hooke constants that differ by more than 3 orders of magnitude. We find that the surface noise dominates the nanopore noise for small pores up to 20 nm in diameter, which emphasizes the importance of surface properties for the nanopore performance. For larger pores, the access resistance dominates the noise properties. Our findings provide a framework for a fair comparison of the low-frequency properties of different membrane materials for nanopore experiments and thus may be of use in the search for new approaches to minimize $1/f$ noise in solid-state nanopores.

3.2. RESULTS

We develop our model for the low-frequency ionic current noise of the nanopore system based on the equivalent electric circuit of the nanopore, see Fig.3.1B. The access region is modelled as a resistor (R_{acc}) that is connected in series to the resistances of the pore-cylinder (R_{cyl}) and pore surface (R_{surf}) that are connected in parallel. R_{cyl} accounts for the dissipative transport of ions in the cylindrical volume of the nanopore, whereas R_{surf} accounts for the contribution of the counterions that are shielding the nanopore surface charge [43].

We thus define

$$R_{pore} = R_{surf} || R_{cyl}, \quad (3.1)$$

$$R_{tot} = R_{pore} + R_{acc}. \quad (3.2)$$

From basic considerations of ion mobilities and geometry [42], [43], these resistances can be expressed as

$$R_{acc} = \frac{1}{ecN_A(\mu_{Cl^-} + \mu_{K^+})d}, \quad (3.3)$$

$$R_{cyl} = \frac{4L}{\pi ecN_A(\mu_{Cl^-} + \mu_{K^+})d^2}, \quad (3.4)$$

$$R_{surf} = \frac{L}{\pi\sigma_{surf}\mu_{K^+}d}, \quad (3.5)$$

where L is the membrane thickness (approximated as $L = 8.6\text{nm}$ due to the hourglass shape of the nanopore [44]), d is the diameter, e is the electron charge, c is the molar concentration of the electrolyte, N_A is the Avogadro's number, μ_{Cl^-} and μ_{K^+} are the carrier mobilities, and σ_{surf} is the surface charge density. Noise sources are modelled as noise-current generators that are connected in parallel to the noiseless resistors. The total current noise power spectral density $S_{I,tot}$ can now be expressed as

$$S_{I,tot} = S_{I,acc} \left(\frac{R_{acc}}{R_{tot}} \right)^2 + (S_{I,cyl} + S_{I,surf}) \left(\frac{R_{pore}}{R_{tot}} \right)^2. \quad (3.6)$$

Derivation of Eq.3.6 is a result of application of Kirchoff's law for the circuit in Fig.3.1. In our model for the low-frequency noise, we consider only the $1/f$ noise for each of the nanopore regions (nanopore cylinder, nanopore surface, access region), which in each case is given by Hooge's model [45],

$$S_I = \frac{\alpha_H I^2}{N_c f} \quad (3.7)$$

where α_H is the Hooge parameter which is an empirical constant that indicates the strength of the $1/f$ noise, I is the dc current, N_c is the number of charge carriers participating in generating the ionic current, and f is the frequency. By measuring current fluctuations in bulk samples of different metals and semiconductors [45], Hooge found that low-frequency noise stems from fluctuations of sample conductance, which is inversely proportional to the amount of charge carriers. Importantly, this relation was found to suitably describe $1/f$ noise of the ionic current in solid-state nanopores [32], [39]. To account for the different contributions to the $1/f$ noise, the ionic currents and number of charge carriers need to be expressed separately for the three regions. We define the number of charge carriers present in the access region, $N_{c,acc}$, pore-cylinder region, $N_{c,cyl}$, and pore-surface region, $N_{c,surf}$, as

$$N_{c,acc} = \pi c N_A \frac{d^3}{6}, \quad (3.8)$$

$$N_{c,cyl} = \pi c N_A L \frac{d^2}{4}, \quad (3.9)$$

$$N_{c,surf} = \pi \sigma_{surf} L \frac{d}{e}, \quad (3.10)$$

where $N_{c,acc}$ is defined as the number of carriers in both hemispherical access regions (as shown in Fig.3.1A), which account for most of ($\sim 95\%$) the total $1/f$ noise occurring

in the access regions (details in section 3.4.6). Referring to the equivalent circuit model of Figure 3.1B, we can express the currents for the access I_{acc} , pore-cylinder I_{cyl} , and pore-surface I_{surf} , simply using Ohm's law and the voltage divider rule,

$$I_{acc} = \frac{V}{R_{tot}}, \quad (3.11)$$

$$I_{cyl} = \frac{V_{cyl}}{R_{cyl}} = \frac{V}{R_{bulk}} \frac{R_{pore}}{R_{tot}}, \quad (3.12)$$

$$I_{surf} = \frac{V_{surf}}{R_{surf}} = \frac{V}{R_{surf}} \frac{R_{pore}}{R_{tot}}, \quad (3.13)$$

where V is the applied bias across the entire circuit. I_{surf} represents the current generated by the counterions adjacent to the pore walls. Since the conductance through such layer is different from the pore-cylinder it needs to be accounted as a separate term. To express the total 1/f current noise of the nanopore system, we substitute Equations 3.11–3.13 into Equation 3.7 to obtain

$$S_{I,acc} = \frac{\alpha_H I_{acc}^2}{N_{c,acc} f} = \frac{\alpha_{H,b}}{N_{c,acc} f} \frac{V^2}{R_{tot}^2}, \quad (3.14)$$

$$S_{I,cyl} = \frac{\alpha_H I_{cyl}^2}{N_{c,cyl} f} = \frac{\alpha_{H,b}}{N_{c,cyl} f} \frac{V^2}{R_{cyl}^2} \frac{R_{pore}^2}{R_{tot}^2}, \quad (3.15)$$

$$S_{I,surf} = \frac{\alpha_H I_{surf}^2}{N_{c,surf} f} = \frac{\alpha_{H,s}}{N_{c,surf} f} \frac{V^2}{R_{surf}^2} \frac{R_{pore}^2}{R_{tot}^2}. \quad (3.16)$$

Finally, combining Equations 3.14–3.16 into 3.6, we can express the total 1/f noise $S_{I,tot}$ as

$$S_{I,tot} = \frac{V^2}{f R_{tot}^4} \frac{\alpha_{H,b} R_{acc}^2}{N_{c,acc}} + \frac{V^2}{f R_{tot}^4} \frac{\alpha_{H,b} R_{pore}^4}{R_{cyl}^2 N_{c,cyl}} + \frac{V^2}{f R_{tot}^4} \frac{\alpha_{H,s} R_{pore}^4}{R_{surf}^2 N_{c,surf}} \quad (3.17)$$

where $\alpha_{H,b}$ and $\alpha_{H,s}$ are the Hooge parameters for the bulk and surface 1/f noise. Note that this model has only two fit parameters $\alpha_{H,b}$ and $\alpha_{H,s}$ whereas all other quantities are given or can be calculated explicitly.

We experimentally tested this model by carefully examining the dependence of the 1/f noise on nanopore diameter, since the voltage drop over access and inner nanopore regions varies strongly with nanopore diameter Eq.3.3–3.5. We thus prepared and studied a range of solid-state nanopores with sizes from 1.3 nm to 46 nm that were drilled within 20 nm-thick free-standing Si-supported membranes of silicon nitride using a transmission electron microscope (TEM). The details of the fabrication process and experimental setup are described elsewhere [46],[47]. Briefly, the membrane with a drilled nanopore was mounted into a microfluidic flow-cell, such that the nanopore was surrounded by two compartments filled with electrolyte solution. A buffer with 1 M KCl, 10 mM Tris-HCl, 1 mM EDTA, at pH 7 was used for measuring the ionic current through

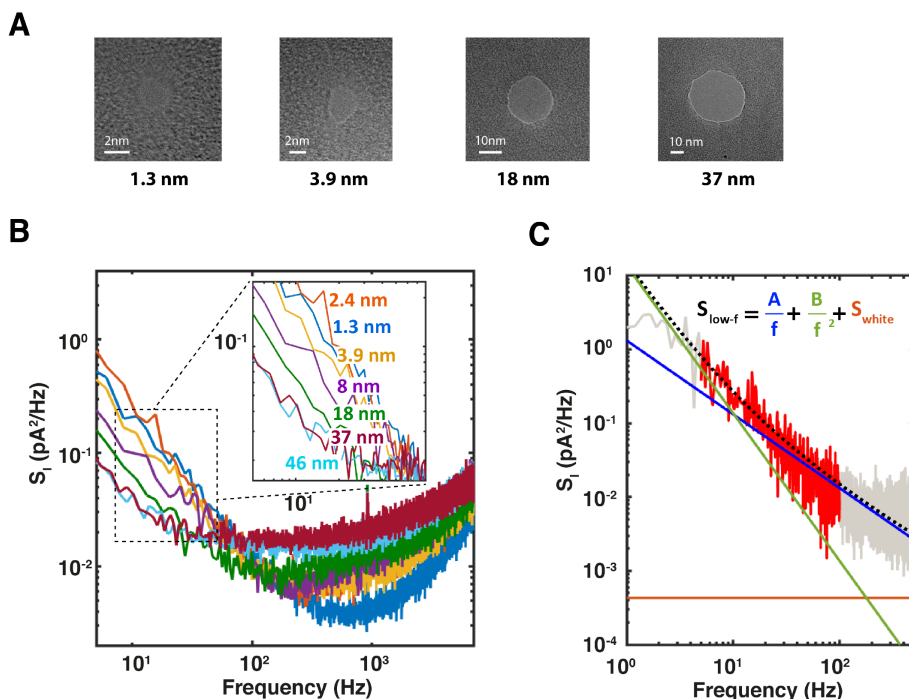


Figure 3.2: (A) TEM micrographs of the measured pores. Diameters were calculated from conductance measurements using Eq.S3.23. (B) Current power spectral density of nanopores with different diameters between 1.3 and 46 nm. The inset shows a zoom-in of the low frequency regions. (C) Example fit of the low-frequency ionic current power spectral density for a 2.4 nm pore. Dotted black line is the fit to the data (red) as reported by Equation 3.19, which comprises $1/f$ (blue), Lorentzian (green) and white noise (orange) contributions. The rest of the spectrum, out of the fitted region, is shown in light grey. Extracted values of A , B , and the calculated S_{white} are reported in Table S3.1.

the nanopores. The ionic current through the nanopore was run using Ag/AgCl electrodes connected to an amplifier (Axopatch 200B, Axon Instruments) operating in resistive feedback mode. Current signals were acquired at a bandwidth of 100 kHz and digitized at 250 kHz. All experiments were performed at the room temperature. To ensure consistency, all chips were fabricated from the same wafer and handled equally. Nanopore diameters were calculated from the measured resistance (using Eq.S3.23), and generally found to be close (within 5-10%) to the values measured by TEM imaging (Fig. 3.2A). Nanopores, which were hard to wet or that demonstrated an excessively noisy ionic current baseline (several orders of magnitude larger than across the whole set of nanopores) were excluded from the study. Ionic currents were recorded under a constant 100 mV applied bias. The power spectral density (PSD) of the ionic currents was computed over a time span of up to 60 seconds using a custom-written Matlab script. We fitted the spectra in the low-frequency range (<100 Hz) to extract the $1/f$ component. All fits were computed using the Matlab Curve Fitting Toolbox.

The acquired current power spectral density spectra are shown in Fig.3.2B. These are

characteristic for nanopore noise behavior: at the low-frequency range, the 1/f noise dominates the PSD, then it transitions into a white noise region represented by shot and thermal noise, and subsequently into dielectric and capacitive noise for high-frequencies [48]. Notably, for pores larger than ~ 3 nm, the low-frequency noise decreases with increasing nanopore size. On the contrary, the white noise contribution, which we observe in the frequency range from 0.1-1 kHz, increases for larger pores. This is expected as the white noise, constituted by thermal and shot current noise scales linearly with the conductance G as

$$S_{I,white} = S_{I,thermal} + S_{I,shot} = G(4kT + 2Vq), \quad (3.18)$$

where G is the total conductance, k is the Boltzmann constant, T is the absolute temperature in Kelvin (here 290 K), and q is the effective charge of the current carrying species. To extract the magnitude of 1/f noise from the PSD, we used a fitting function constituted by the sum of different low-frequency noise contributions, (Fig.3.2C), namely

$$S_{I,tot}|_{f=1\text{Hz}} = S_{I,white} + \frac{A}{f} + \frac{B}{f^2}. \quad (3.19)$$

Here, the first term comprises the white noise contributions (*i.e.*, both the thermal and shot noise), the second term represents the 1/f noise, and the third term accounts for a Lorentzian-shaped noise component, which is particularly pronounced in the smaller size nanopores. It can be attributed to fluctuations of the surface charge due to capture/release of ions from the electrolyte onto the nanopore surface [49–51]. This Lorentzian-shaped component is very slow (the characteristic crossover frequency is sub-1Hz) and unlike 1/f noise, is not inherent in all our nanopore data. It is not of major importance but is included in the fits to enable the most accurate determination of the 1/f noise level. Note that the higher-frequency dielectric or capacitive noise contributions are not included into Equation 3.19 as their magnitude is negligible in the low-frequency range considered. By contrast, the white noise needs to be taken into account, as it is not negligible for the large pores (> 20 nm) in the 1-100 Hz range (Figure S3.5).

A major result of the current paper is presented in Fig.3.3A which plots the extracted 1/f noise magnitudes versus nanopore size. We observe a decrease of 1/f noise of almost two orders of magnitude upon going from sub-5 nm pores to > 40 nm diameter pores. Notably the variation in the 1/f noise is much weaker below a pore size of ~ 10 nm. To describe this behavior, we first consider previously developed models [28], [32], [39] that model the 1/f noise as coming only from the cylindrical nanopore, neglecting an access resistance contribution. Following this assumption, the total 1/f noise can be expressed [39] as

$$S_{I,pore} = \frac{\alpha_H I_{surf}^2}{N_{c,surf} f} + \frac{\alpha_H I_{cyl}^2}{N_{c,cyl} f} \quad (3.20)$$

where the first term describes the pore-surface 1/f noise, the second term describes the pore-cylinder 1/f noise, α_H is the (single) Hooge parameter, and I_{cyl} , I_{surf} , $N_{c,cyl}$, and $N_{c,surf}$ are calculated explicitly using Equations 3.9–3.10 and 3.12–3.13. Equation 3.20 describes a monotonic increase of the magnitude of 1/f noise with pore size (for details, see Supporting Information), as illustrated by the green dashed line (Fig.3.3A). Even

qualitatively, this clearly contradicts our experimental observations and shows that it is crucial to take the access region into account to describe the size dependence of the $1/f$ noise. The pink line denotes such a model that accounts for the access resistance, where we have considered the simplest case of an equal Hooge parameter for the $1/f$ noise from the nanopore bulk and surface, i.e., we fitted Equation 3.17 to the data with $\alpha_{H,s} = \alpha_{H,b} = \alpha_H$ as the only fit parameter. This model qualitatively describes the trend of the data, but quantitatively clearly fails to fit well. However, by using two different Hooge constants for the $1/f$ noise at the surface of the nanopore and in the bulk of the electrolyte as fit parameters, an excellent fit to the experimental data can be obtained, as depicted by the purple line. This indicates that $1/f$ noise arising from the bulk and surface of the nanopore do differ substantially.

The decrease of the total $1/f$ noise for increasing pore diameter can be attributed to two underlying causes: (i) a voltage drop redistribution across access and pore region as determined by their resistances (Fig.3.1B), which strongly depend on the pore diameter (Eq.3.3–3.5): whereas the pore resistance dominates for smaller pore diameters, the access resistance dominates for larger pores (Fig.S3.4); and (ii), the magnitude of $1/f$ fluctuations is much larger for the surface contribution than for the bulk noise. As a result of these two points, the surface $1/f$ noise dominates for small pores while the total $1/f$ noise decreases for larger pores where the weaker access noise dominates. From the fit, we find the surface and bulk Hooge parameters to be $\alpha_{H,s} = (2.1 \pm 0.2) \cdot 10^{-3}$ and $\alpha_{H,b} = (1.4 \pm 1.5) \cdot 10^{-6}$, respectively. Notably, the value we found for the surface noise coefficient is more than three orders of magnitude higher than the bulk value, showing that surface noise dominates. In passing we find it interesting to note that low-frequency noise studies in solid-state semiconductor devices also feature surface currents with a much higher Hooge parameter compared to the bulk ones [52] that arise from fluctuations of electrophoretic mobility of ions in the electrolyte [53]. Our value for $\alpha_{H,s}$ is also higher than the value of $\sim 1.1 \cdot 10^{-4}$ published previously for solid-state nanopores [32]. However, this value has been extracted using the ‘pore-only’ model and represents a convolution between $\alpha_{H,s}$ and $\alpha_{H,b}$. If we calculate the α_H using a model as in [32] for a ~ 10 nm nanopore from our data set (similar size to the one used in [32]), then we find values that agree well with this reference.

A mechanism responsible for the high surface $1/f$ noise can possibly be charge carrier number fluctuations occurring at the pore-electrolyte interface due trapping at the surface. Whereas a single adsorption/dissociation process would lead to a Lorentzian noise spectrum, inhomogeneities at the pore surface will lead to a variety of trapping strengths which yields a $1/f$ spectrum [54], [49]. Such mechanism will strongly depend on the surface properties of the material (in this case SiN_x). $1/f$ noise measurements on solid-state nanopores fabricated from two different wafers (Fig.S3.6) yielded a factor 3 difference in $\alpha_{H,s}$, consistent with this notion. Obviously, our finding of the dominance of surface noise suggests strategies to lower the noise of nanopores, e.g. by surface engineering and choice of surface materials.

Fig.3.3B sketches the relative contributions of access, pore-cylinder, and pore-surface regions to the total $1/f$ noise $S_{I,tot}$. Using Eq.3.6 and 3.14–3.17, the various colored lines plot the access $S_{I,acc} \left(\frac{R_{acc}}{R_{tot}} \right)^2 / S_{I,tot}$ (blue), pore-cylinder $S_{I,cyl} \left(\frac{R_{pore}}{R_{tot}} \right)^2 / S_{I,tot}$ (green), and

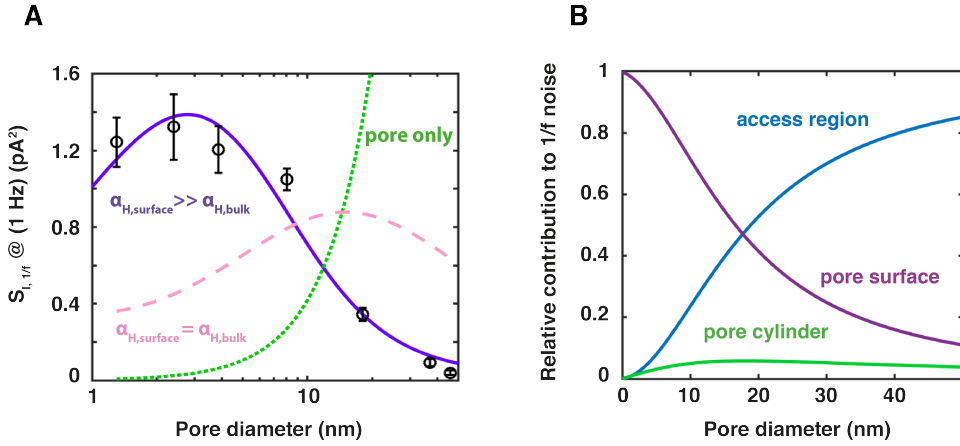


Figure 3.3: (A) Low-frequency 1/f noise plotted as a function of the pore diameter (black circles). We observe a decreasing trend of 1/f noise with increasing nanopore size, which spans more than one order of magnitude over the analyzed pore diameter range. Error bars represent standard deviations. The three lines represent model fits to the nanopore data: The green dotted line accounts for the model with no access resistance contribution; pink dashed line includes the access resistance, but treats 1/f noise as coming from one mechanism with a single Hooke parameter; and the purple curve shows the model comprising the access resistance and two independent Hooke parameters associated with bulk and surface noise. (B) Relative contribution to the total 1/f noise originating from the three different nanopore regions: pore-surface (purple), pore-cylinder (green), and access region (blue), as a function of the nanopore diameter.

pore-surface $S_{I,surf} \left(\frac{R_{pore}}{R_{tot}} \right)^2 / S_{I,tot}$ (purple) contributions as a function of pore diameter. Clearly, the 1/f noise for small pores is dominated by surface noise, while for larger pores (> 20 nm) the noise mainly comes from the bulk noise associated with the nanopore access region. The latter may appear remarkable given that its $\alpha_{H,b}$ is three orders of magnitude lower than $\alpha_{H,s}$, but is explained by the fact that the access resistance strongly dominates the pore resistance for pore diameters larger than 20 nm. More generally, our model allows to quantify and predict 1/f noise behavior for nanopores of different geometries. It is clear that ultra-small pores (< 5 nm) are mainly showing surface 1/f noise and the large ones (> 40 nm) mainly demonstrate the bulk noise of the access region. However, our model allows to quantify that the mid-range pores, which are most often used for biosensing applications, still have a surprisingly strong contribution from the surface 1/f noise (Fig.3.3B). Therefore, the noise of these pores can be significantly improved by selection of the nanopore material or coating. Moreover, our model is also suitable for nanopores made in ultrathin membranes (e.g. 2D materials) and it predicts a lower 1/f current noise coming from the nanopore itself because of the major role of the access region even for the smaller nanopore diameters.

3.3. CONCLUSION

Summing up, we have developed a generalized predictive model for the 1/f noise in solid-state nanopores, which accounts for the dominant role of the access region of the nanopore sensor and for the different origins of 1/f noise in the solid-state nanopore. We

find that $1/f$ noise of a solid-state nanopore derives from two sources, the nanopore surface and the bulk electrolyte, with Hooge parameters that differ by three orders of magnitude. Although the surface noise is more pronounced, the noise coming from the bulk electrolyte in the access region is the predominant source of noise for nanopore diameters larger than 20 nm. The developed model fits the experimental data remarkably well and can thus be used to compare $1/f$ noise performance of different nanopore materials. Importantly, it may be used to describe the $1/f$ noise for nanopores in very thin membranes, such as 2D-materials (graphene, boron nitride, molybdenum disulfide), where the access region is reported to dominate also for the smaller pore diameters.

3.4. SUPPORTING INFORMATION

3.4.1. MODEL

From Reference [42, 43] the R_{pore} , R_{acc} , and R_{tot} can be expressed as

$$R_{pore} = R_{cyl} || R_{surf} = \frac{L}{\pi d} \left[ecN_A(\mu_{Cl^-} + \mu_{K^+}) \frac{d}{4} + \sigma_{surf} \mu_{K^+} \right]^{-1}, \quad (S3.21)$$

$$R_{acc} = [ecN_A(\mu_{Cl^-} + \mu_{K^+})d]^{-1} \quad (S3.22)$$

$$R_{tot} = R_{pore} + R_{acc}, \quad (S3.23)$$

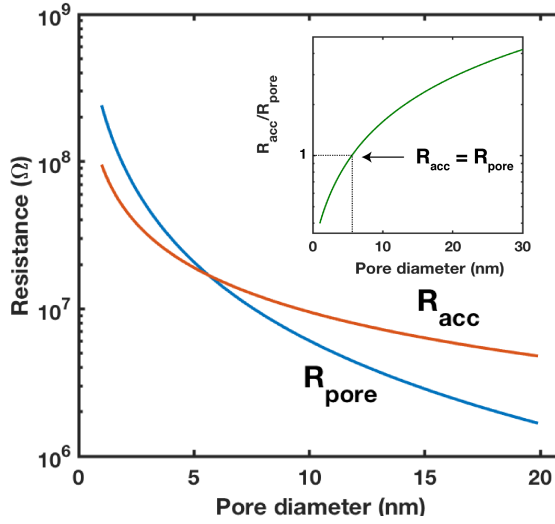


Figure S3.4: Access and nanopore resistances vs pore diameter. Inset: Ratio of access resistance over nanopore resistance vs pore diameter.

where L is the membrane thickness (assumed to be 8.6 nm, due to the hourglass shape of the nanopore [42]), d is the diameter, e is the charge of the electron, c is the molar concentration, N_A is the Avogadro's number, μ_{Cl^-} and μ_{K^+} the carrier mobilities, and σ_{surf} the surface charge density.

3.4.2. FITTING THE CURRENT NOISE SPECTRAL DENSITY VERSUS PORE DIAMETER

To remove one free parameter and improve the goodness of the fit, the analysis was restricted to the frequency region of the spectra where $f \gg f_c$, such that the fit function could be well approximated to

$$S_{I,tot}|_{f=1\text{Hz}} = \frac{A}{f} + \frac{B'}{1 + \left(\frac{f}{f_c}\right)^2} + S_{I,white} \approx \frac{A}{f} + \frac{B}{f^2} + S_{I,white}. \quad (S3.24)$$

where B' and f_c are factors defining the Lorentzian function, S_{white} was calculated from the pore conductance, and A and B were fit parameters. The results of the fitting of Eq.S3.24 are illustrated in Figure S3.5, and the extracted parameters are reported in Table S3.1.

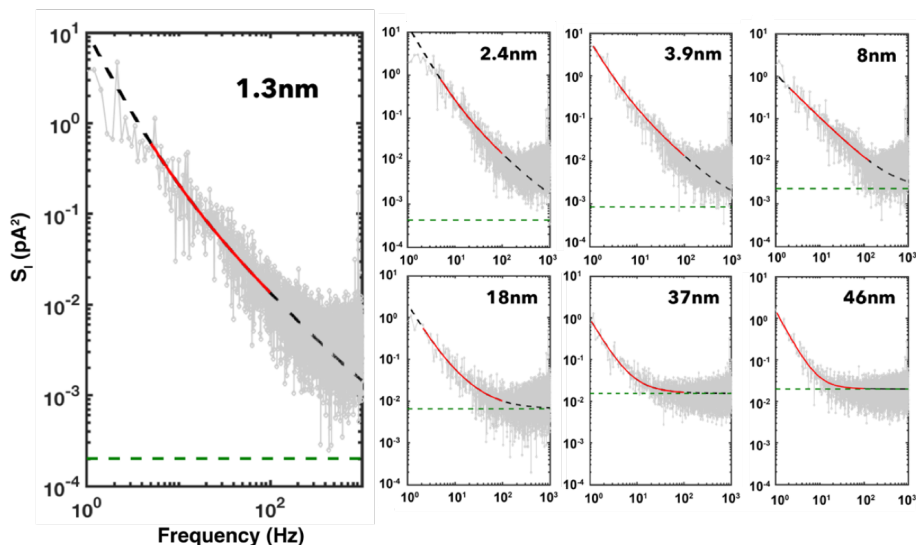


Figure S3.5: Current power spectral density for different pore diameters. Black dashed line shows the fit to the data, using Equation 3.19. Red line shows the region of the spectrum where the fit was computed. Green dashed line represents the white noise, calculated using Equation 3.18.

Pore diameter (nm)	A (pA^2)	B ($\text{pA}^2 \cdot \text{Hz}$)	S_{white} (pA^2/Hz)
1.3	1.24 ± 0.13	8.8 ± 1.1	$2.9 \cdot 10^{-4}$
2.4	1.32 ± 0.17	13.7 ± 1.4	$4.3 \cdot 10^{-4}$
3.9	1.21 ± 0.12	5.62 ± 0.23	$8.5 \cdot 10^{-4}$
8	1.05 ± 0.06	0.11 ± 0.19	$2.3 \cdot 10^{-3}$
18	0.34 ± 0.03	1.82 ± 0.10	$6.5 \cdot 10^{-3}$
37	0.09 ± 0.02	0.84 ± 0.03	$15.4 \cdot 10^{-3}$
46	0.04 ± 0.01	1.50 ± 0.02	$19.7 \cdot 10^{-3}$

Table S3.1: Fit parameters for different pore diameters. A and B were free parameters. $S_{I,white}$ was calculated from the measured conductance and the voltage applied according to Equation 3.18.

3.4.3. FITTING 1/F NOISE VERSUS DIAMETER WITH THE ALTERNATIVE MODELS

FITTING THE 'PORE ONLY' MODEL

The green dashed line in Figure 3.3A represents a 1/f noise model where the access resistance is omitted. In such a scenario, Equations 3.9–3.10 and 3.12–3.13 are still used

to express the number of charge carriers and currents for the surface and bulk regions. However, the total 1/f noise $S_{I,pore}$ expression would differ from Equation 3.17, as in this case

$$S_{I,pore} = S_{I,cyl} + S_{I,surf}. \quad (S3.25)$$

Substituting Eq.3.12–3.13 into Eq.3.7 and into S3.25, and noting that $R_{tot} = R_{pore}$, one gets

$$S_{I,pore} = \frac{\alpha_H I_{cyl}^2}{N_{c,cyl} f} + \frac{\alpha_H I_{surf}^2}{N_{c,surf} f} = \frac{\alpha_H V^2}{f} \left[\frac{1}{N_{c,cyl} R_{cyl}^2} + \frac{1}{N_{c,surf} R_{surf}^2} \right]. \quad (S3.26)$$

Note that here only one Hooge constant α_H is taken to describe both the bulk and surface contributions. From Eq. 3.4–3.5 and 3.9–3.10 we can extract the scaling for R_{cyl} , R_{surf} , $N_{c,cyl}$, and $N_{c,surf}$ as a function of the pore diameter D .

$$R_{cyl} = \frac{4L}{\pi e c N_A (\mu_{Cl^-} + \mu_{K^+}) D^2} \propto d^{-2}, \quad (S3.27)$$

$$R_{surf} = \frac{L}{\pi \sigma_{surf} \mu_{K^+} D} \propto d^{-1}, \quad (S3.28)$$

$$N_{c,cyl} = \pi c N_A L \frac{d^2}{4} \propto d^2, \quad (S3.29)$$

$$N_{c,surf} = \pi \sigma_{surf} L \frac{d}{e} \propto d. \quad (S3.30)$$

We can thus rewrite Eq.S3.26 as

$$S_{I,pore} = p \cdot d^2 + \cdot d, \quad (S3.31)$$

where p and q are constants. This explains the monotonic increasing behavior observed in Figure 3.3A for the green dotted line.

FITTING THE ' $\alpha_{H,s} = \alpha_{H,b}$ ' MODEL

The pink dashed curve in Figure 3.3A is obtained by fitting the model described by Equation 3.17 with only one fit Hooge parameter $\alpha = \alpha_{H,s} = \alpha_{H,b}$, which was found to be $\alpha = (1.2 \pm 1.0) \cdot 10^{-5}$.

Parameter	Value	Ref.
Effective membrane thickness L	8.6 nm	[42]
Potassium ion mobility μ_{K^+}	$7.616 \cdot 10^{-8} \left[\frac{m^2}{V \cdot s} \right]$	[55]
Chloride ion mobility μ_{Cl^-}	$7.909 \cdot 10^{-8} \left[\frac{m^2}{V \cdot s} \right]$	[55]
Surface charge density for Si_3N_4 at pH 7-8, σ_{surf}	$0.02 \left[\frac{C}{m^2} \right]$	[56]
Bulk conductivity at 1 M KCl σ_{bulk}	$10.5 \left[\frac{S}{m} \right]$	[57]

Table S3.2: Parameters used.

3

3.4.4. WAFER-TO-WAFER VARIABILITY OF $\alpha_{H,s}$

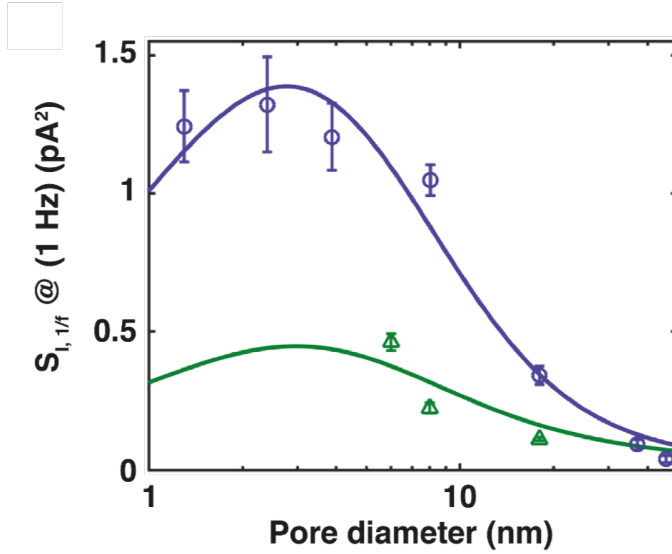


Figure S3.6: Low-frequency $1/f$ noise plotted as a function of the pore size. Nanopores fabricated from different wafers display different surface Hooke constant. We find $\alpha_{H,s} = (2.1 \pm 0.2) \cdot 10^{-3}$ for the first batch of pores (purple circles), whereas $\alpha_{H,s} = (6.6 \pm 3.4) \cdot 10^{-4}$ for the second one (green triangles). Purple and green curves represent the model fitting the $1/f$ noise data. Error bars represent standard deviations due to the fitting.

3.4.5. OTHER NOISE SOURCES

BACKGROUND NOISE

DIELECTRIC NOISE

In the frequency range 3-10 kHz, dielectric noise can be fitted using the linear function

$$S_{dielectric} = 8\pi kTDC_{chip}f = a \cdot f \quad (S3.32)$$

where $kT = 4.11 \cdot 10^{-21} J$ at room temperature, D is the dielectric loss, C_{chip} is the chip capacitance, f is the frequency, and a is the fit parameter, found to be $a = (5.03 \pm 0.01) \cdot 10^{-6} (pA/Hz)^2$. We find the dielectric noise contribution to be negligible, being more than one order of magnitude lower in the frequency range of interest (1-100 Hz).

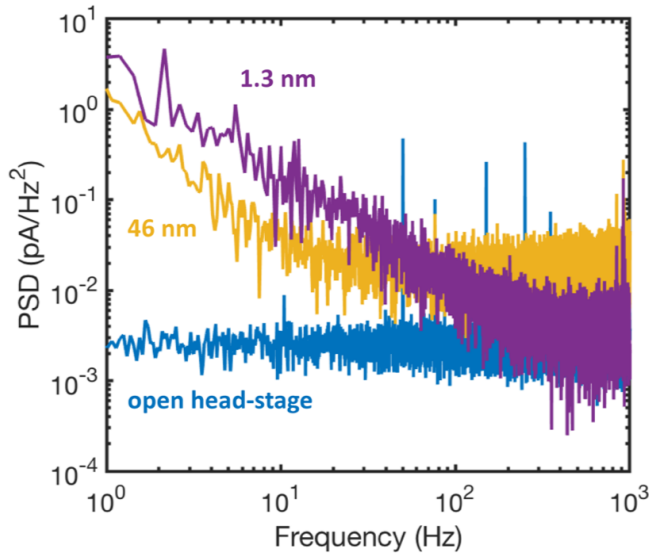


Figure S3.7: Comparison of PSD spectra for 1.3 nm (purple) and 46 nm (yellow) vs background noise (blue) coming from the open head-stage of the amplifier. We find the background noise to be at least an order of magnitude lower than the 1/f noise coming from the nanopores in the frequency range of interest (1-100 Hz).

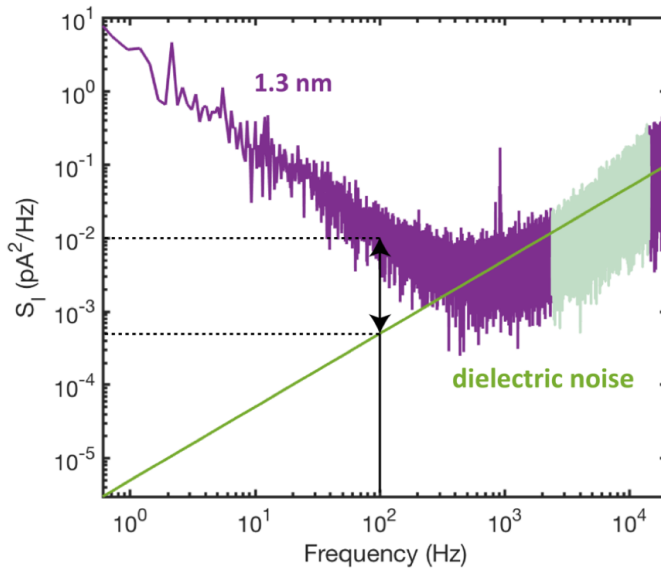


Figure S3.8: PSD spectrum of the ionic current for a 1.3 nm pore (purple) with a fit to the dielectric noise (light green, 3-10 kHz). Green straight line represents the fit. Dielectric noise was fitted using Equation S3.32. Arrows and dashed lines highlight that dielectric noise is negligible in the frequency range of interest (1-100 Hz).

3.4.6. 1/f NOISE IN THE ACCESS REGION

In this section, we estimate what volume of the access region contributes most to the 1/f noise. Using the formalism developed by Hille [58], we derive the amount of 1/f noise coming from the infinite region outside the hemisphere of nanopore radius (Figure S3.9A). We define the total S_V coming from this region as $S_{V_{inf}}$. To quantify this value, one can imagine the space as a series connection of hollow hemispheres of electrolyte solution, each with the thickness of dr (Figure S3.9B). Since all the hollow hemispheres are connected in series, the total voltage PSD is a sum of voltage PSD's of all hollow hemispheres $dS_{V_{inf}}$. The voltage PSD of hollow hemisphere can be defined as follows:

$$dS_{V_{inf}} = dS_{I_{inf}} R_{hh}^2 = \frac{\alpha_H I^2}{f N_{hh}} R_{hh}^2, \quad (S3.33)$$

where R_{hh} is the resistance of the hollow hemisphere:

$$R_{hh} = \frac{1}{\sigma} \frac{dr}{2\pi r^2}, \quad (S3.34)$$

and N_{hh} is the amount of charge carriers in the hollow hemisphere:

$$N_{hh} = c N_A 2\pi r^2 dr. \quad (S3.35)$$

Substituting these values yields the final differential form of $dS_{V_{inf}}$:

$$dS_{V_{inf}} = \frac{\alpha_H I^2}{8 f c N_A \pi^3 \sigma^2} \frac{dr}{r^6}. \quad (S3.36)$$

Finally, the total $S_{V_{inf}}$ is derived by integration of $dS_{V_{inf}}$ from the pore radius to infinity

$$dS_{V_{inf}} = \frac{\alpha_H I^2}{8 f c N_A \pi^3 \sigma^2} \int_{r_{pore}}^{\infty} \frac{dr}{r^6} = \frac{\alpha_H I^2}{40 f c N_A \pi^3 \sigma^2 r_{pore}^5}. \quad (S3.37)$$

These calculations do not take into account the region within the hemisphere of the pore radius (the volume of electrolyte closest to the pore). To quantify this, we need to derive the resistance and amount of carriers within this hemisphere:

$$S_{V_{hemisphere}} = \frac{\alpha_H I^2}{f N_{hemisphere}} R_{hemisphere}^2. \quad (S3.38)$$

The resistance of the hemisphere of the nanopore radius can be calculated as a difference between resistances of the access region derived using Hall [40] and Hille [58] models (Figure S3.9)

$$R_{hemisphere} = R_{Hall} - R_{Hille} = \frac{1}{4\sigma r_{pore}} - \frac{1}{4\pi\sigma r_{pore}} = \frac{\pi - 1}{4\pi\sigma r_{pore}}. \quad (S3.39)$$

The amount of carriers within the hemisphere is given by:

$$N_{hemisphere} = c N_A \frac{2}{3} \pi r_{pore}^3. \quad (S3.40)$$

Therefore the 1/f noise within the hemisphere is:

$$S_{V_{hemisphere}} = \frac{3\alpha_H I^2 (\pi - 1)^2}{32 f c N_A \pi^3 \sigma^2 r_{pore}^5}. \quad (S3.41)$$

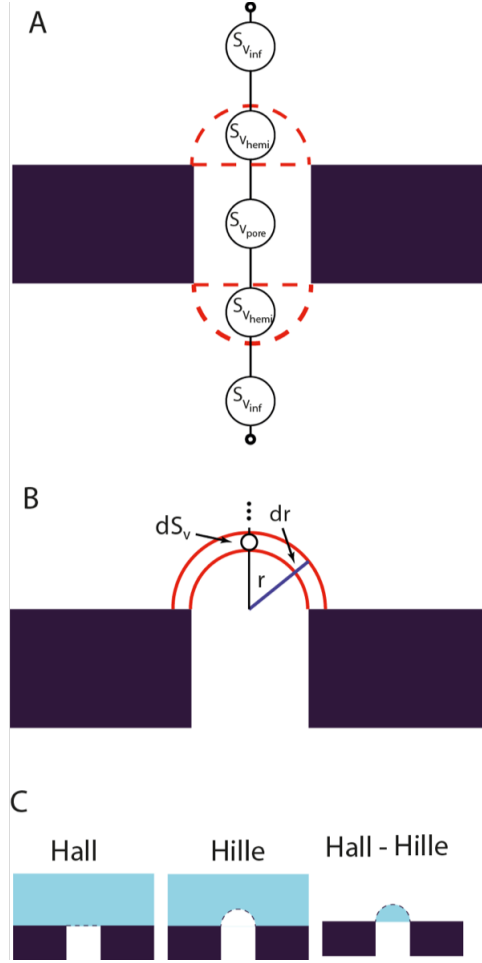


Figure S3.9: A. Representation of total voltage PSD of a nanopore sensor as an equivalent circuit with voltage generators defined by nanopore region, hemisphere around the nanopore, infinite space of the electrolyte. B. Schematic to illustrate the representation of voltage PSD of 1/f noise in the infinite bulk solution as a sum of voltage PSD's of hollow hemispheres. C. Illustration of the volumes considered by Hall and Hille models of the access regions. Blue color indicates the volume taken into account for estimation of the access resistance.

Now we can analytically derive which part of the access region contributes most to 1/f noise:

$$\frac{S_{V_{hemisphere}}}{S_{V_{hemisphere}} + S_{V_{inf}}} = \frac{\frac{3(\pi-1)^2}{32}}{\frac{3(\pi-1)^2}{32} + \frac{1}{40}} \approx 0.95. \quad (S3.42)$$

We conclude that 95% of the $1/f$ noise of the access region derives from the hemisphere directly adjacent to the pore.

3.4.7. $1/f$ NOISE VS VOLTAGE APPLIED ON A 45 NM PORE

PSD spectra of the ionic current were acquired at different excitation voltages (20-100 mV) for a 45 nm pore. We find that, as expected, the $1/f$ noise increases with the square of the current.

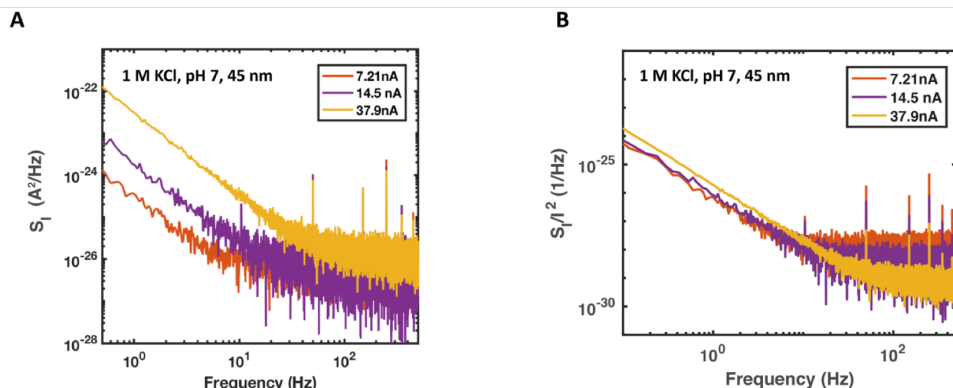


Figure S3.10: A. PSD spectra of the ionic current for a 45 nm pore at different bias voltages. B. PSD spectra of the same pore normalized by square of the bias current.

3.4.8. EXAMPLE OF CURRENT TRACE FOR A 1.3 NM PORE

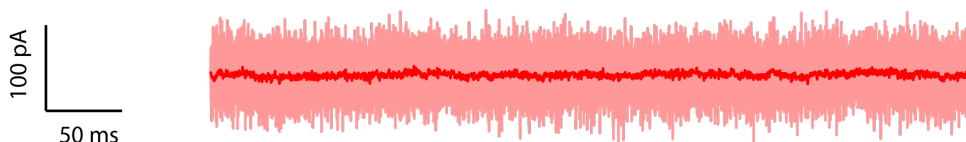


Figure S3.11: Example of ionic current trace measured across a small 1.3 nm pore filtered at 10 kHz (light red) and 1 kHz (dark red).

REFERENCES

- [1] A. Fragasso, S. Pud, and C. Dekker, *1/f Noise in Solid-State Nanopores Is Governed By Access and Surface Regions*, *Nanotechnology* **30**, 395202 (2019).
- [2] C. Dekker, *Solid-state nanopores (Review Article)*, *Nature Nanotechnology*, 1 (2007).
- [3] Y. L. Ying, J. Zhang, R. Gao, and Y. T. Long, *Nanopore-based sequencing and detection of nucleic acids*, *Angewandte Chemie - International Edition* **52**, 13154 (2013).

- [4] X. Shi, Q. Li, R. Gao, W. Si, S. C. Liu, A. Aksimentiev, and Y. T. Long, *Dynamics of a Molecular Plug Docked onto a Solid-State Nanopore*, Journal of Physical Chemistry Letters **9**, 4686 (2018).
- [5] Y. Lin, Y. L. Ying, and Y. T. Long, *Nanopore confinement for electrochemical sensing at the single-molecule level*, Current Opinion in Electrochemistry **7**, 172 (2018).
- [6] E. Atas, A. Singer, and A. Meller, *DNA sequencing and bar-coding using solid-state nanopores*, (2012).
- [7] A. H. Squires, J. S. Hersey, M. W. Grinstaff, and A. Meller, *A nanopore-nanofiber mesh biosensor to control DNA translocation*, Journal of the American Chemical Society **135**, 16304 (2013).
- [8] B. N. Miles, A. P. Ivanov, K. a. Wilson, F. Doğan, D. Japrun, and J. B. Edel, *Single molecule sensing with solid-state nanopores: novel materials, methods, and applications*, Chemical Society Reviews **42** (2012), 10.1039/c2cs35286a.
- [9] J. Y. Sze, A. P. Ivanov, A. E. Cass, and J. B. Edel, *Single molecule multiplexed nanopore protein screening in human serum using aptamer modified DNA carriers*, Nature Communications **8**, 1 (2017).
- [10] W. Yang, A. Birnie, L. Restrepo-Pérez, J. van der Torre, M. Bengtson, S. J. Heerema, and C. Dekker, *Detection of CRISPR-dCas9 on DNA with Solid-State Nanopores*, Nano Letters **18**, 6469 (2018).
- [11] C. a. Merchant, K. Healy, M. Wanunu, V. Ray, N. Peterman, J. Bartel, M. D. Fischbein, K. Venta, Z. Luo, a. T. C. Johnson, and M. Drndić, *DNA translocation through graphene nanopores*, Nano Letters **10**, 2915 (2010).
- [12] S. Howorka and Z. Siwy, *Nanopore analytics: Sensing of single molecules*, Chemical Society Reviews **38**, 2360 (2009).
- [13] J. J. Kasianowicz, J. W. Robertson, E. R. Chan, J. E. Reiner, and V. M. Stanford, *Nanoscopic Porous Sensors*, Annual Review of Analytical Chemistry **1**, 737 (2008).
- [14] D. Deamer, M. Akeson, D. Branton, J. J. Kasianowicz, and S. M. Bezrukov, *Three decades of nanopore sequencing*, Nature Biotechnology **34**, 481 (2016).
- [15] J. J. Kasianowicz and S. M. Bezrukov, *On 'three decades of nanopore sequencing'*, Nature Biotechnology **34**, 481 (2016).
- [16] R. Wei, V. Gatterdam, R. Wieneke, R. Tampé, and U. Rant, *Stochastic sensing of proteins with receptor-modified solid-state nanopores*, Nature Nanotechnology **7**, 257 (2012).
- [17] S. W. Kowalczyk, L. Kapinos, T. R. Blosser, T. Magalhães, P. van Nies, R. Y. H. Lim, and C. Dekker, *Single-molecule transport across an individual biomimetic nuclear pore complex*, Nature Nanotechnology **6**, 433 (2011).

- [18] N. A. Bell and U. F. Keyser, *Digitally encoded DNA nanostructures for multiplexed, single-molecule protein sensing with nanopores*, *Nature Nanotechnology* **11**, 645 (2016).
- [19] C. Plesa, D. Verschueren, S. Pud, J. van der Torre, J. W. Ruitenberg, M. J. Witteveen, M. P. Jonsson, A. Y. Grosberg, Y. Rabin, and C. Dekker, *Direct observation of DNA knots using a solid-state nanopore*, *Nature Nanotechnology*, 1 (2016).
- [20] K. Venta, G. Shemer, M. Puster, J. A. Rodríguez-Manzo, A. Balan, J. K. Rosenstein, K. Shepard, and M. Drndić, *Differentiation of short, single-stranded DNA homopolymers in solid-state nanopores*, *ACS Nano* **7**, 4629 (2013).
- [21] J. J. Kasianowicz, E. Brandin, D. Branton, and D. W. Deamer, *Characterization of individual polynucleotide molecules using a membrane channel*, *Proceedings of the National Academy of Sciences* **93**, 13770 (2002).
- [22] E. a. Manrao, I. M. Derrington, A. H. Laszlo, K. W. Langford, M. K. Hopper, N. Gillgren, M. Pavlenok, M. Niederweis, and J. H. Gundlach, *Reading DNA at single-nucleotide resolution with a mutant MspA nanopore and phi29 DNA polymerase*, *Nature Biotechnology* **30**, 349 (2012).
- [23] S. Kumar, C. Tao, M. Chien, B. Hellner, A. Balijepalli, J. W. F. Robertson, Z. Li, J. J. Russo, J. E. Reiner, J. J. Kasianowicz, and J. Ju, *PEG-labeled nucleotides and nanopore detection for single molecule DNA sequencing by synthesis*, *Scientific Reports* **2**, 1 (2012).
- [24] J. W. F. Robertson, C. G. Rodrigues, V. M. Stanford, K. A. Robinson, O. V. Krasilnikov, and J. J. Kasianowicz, *Single-molecule mass spectrometry in solution using a solitary nanopore*, *Proceedings of the National Academy of Sciences* **104**, 8207 (2007).
- [25] C. W. Fuller, S. Kumar, M. Porel, M. Chien, A. Bibillo, P. B. Stranges, M. Dorwart, C. Tao, Z. Li, W. Guo, S. Shi, D. Korenblum, A. Trans, A. Aguirre, E. Liu, E. T. Harada, J. Pollard, A. Bhat, C. Cech, A. Yang, C. Arnold, M. Palla, J. Hovis, R. Chen, I. Morozova, S. Kalachikov, J. J. Russo, J. J. Kasianowicz, R. Davis, S. Roevers, G. M. Church, and J. Ju, *Real-time single-molecule electronic DNA sequencing by synthesis using polymer-tagged nucleotides on a nanopore array*, *Proceedings of the National Academy of Sciences* **113**, 5233 (2016).
- [26] C. Plesa, S. W. Kowalczyk, R. Zinsmeister, A. Y. Grosberg, Y. Rabin, and C. Dekker, *Fast translocation of proteins through solid state nanopores*, *Nano Letters* **13**, 658 (2013).
- [27] A. J. Storm, C. Storm, J. Chen, H. Zandbergen, J. F. Joanny, and C. Dekker, *Fast DNA translocation through a solid-state nanopore*, *Nano Letters* **5**, 1193 (2005).
- [28] R. M. M. Smeets, N. H. Dekker, and C. Dekker, *Low-frequency noise in solid-state nanopores*, *Nanotechnology* **20** (2009), 10.1088/0957-4484/20/9/095501.

- [29] P. Ketterer, A. N. Ananth, D. S. Laman Trip, A. Mishra, E. Bertosin, M. Ganji, J. Van Der Torre, P. Onck, H. Dietz, and C. Dekker, *DNA origami scaffold for studying intrinsically disordered proteins of the nuclear pore complex*, Nature Communications **9**, 1 (2018).
- [30] S. J. Heerema, G. F. Schneider, M. Rozemuller, L. Vicarelli, H. W. Zandbergen, and C. Dekker, *1/F Noise in Graphene Nanopores*, Nanotechnology **26** (2015), 10.1088/0957-4484/26/7/074001.
- [31] J. D. Uram, K. Ke, and M. L. Mayer, *Noise and bandwidth of current recordings from submicrometer pores and nanopores*, ACS Nano **2**, 857 (2008).
- [32] R. M. M. Smeets, U. F. Keyser, N. H. Dekker, and C. Dekker, *Noise in solid-state nanopores*, Proceedings of the National Academy of Sciences of the United States of America **105**, 417 (2008).
- [33] Z. Roelen, J. A. Bustamante, A. Carlsen, A. Baker-Murray, and V. Tabard-Cossa, *Instrumentation for low noise nanopore-based ionic current recording under laser illumination*, Review of Scientific Instruments **89** (2018), 10.1063/1.5006262.
- [34] L. J. DeFelice, *Introduction to Membrane Noise*, 1st ed. (Springer US, 1981) pp. 1–516.
- [35] V. Tabard-Cossa, D. Trivedi, M. Wiggin, N. N. Jetha, and A. Marziali, *Noise analysis and reduction in solid-state nanopores*, Nanotechnology **18** (2007), 10.1088/0957-4484/18/30/305505.
- [36] A. Balan, C. C. Chien, R. Engelke, and M. Drndic, *Suspended Solid-state Membranes on Glass Chips with Sub 1-pF Capacitance for Biomolecule Sensing Applications*, Scientific Reports **5**, 1 (2015).
- [37] K. B. Park, H. J. Kim, H. M. Kim, S. A. Han, K. H. Lee, S. W. Kim, and K. B. Kim, *Noise and sensitivity characteristics of solid-state nanopores with a boron nitride 2-D membrane on a pyrex substrate*, Nanoscale **8**, 5755 (2016).
- [38] P. Chen, T. Mitsui, D. B. Farmer, J. Golovchenko, R. G. Gordon, and D. Branton, *Atomic layer deposition to fine-tune the surface properties and diameters of fabricated nanopores*, Nano Letters **4**, 1333 (2004).
- [39] C. Wen, S. Zeng, K. Arstila, T. Sajavaara, Y. Zhu, Z. Zhang, and S. L. Zhang, *Generalized Noise Study of Solid-State Nanopores at Low Frequencies*, ACS Sensors **2**, 300 (2017).
- [40] J. E. Hall, *Access resistance of a small circular pore*, The Journal of General Physiology **66**, 531 (1975).
- [41] S. M. Bezrukov, I. Vodyanoy, R. A. Brutyan, and J. J. Kasianowicz, *Dynamics and Free Energy of Polymers Partitioning into a Nanoscale Pore*, Macromolecules **29**, 8517 (1996).

- [42] S. W. Kowalczyk, A. Y. Grosberg, and Y. Rabin, *Modeling the conductance and DNA blockade of solid-state nanopores*, **22** (2011), 10.1088/0957-4484/22/31/315101.
- [43] R. M. M. Smeets, U. F. Keyser, M. Y. Wu, N. H. Dekker, and C. Dekker, *Nanobubbles in solid-state nanopores*, *Physical Review Letters* **97**, 1 (2006).
- [44] M. J. Kim, M. Wanunu, D. C. Bell, and A. Meller, *Rapid fabrication of uniformly sized nanopores and nanopore arrays for parallel DNA analysis*, *Advanced Materials* **18**, 3149 (2006).
- [45] F. Hooge, *1/F Noise*, *Physica B+C* **83**, 14 (1976).
- [46] X. J. a. Janssen, M. P. Jonsson, C. Plesa, G. V. Soni, C. Dekker, and N. H. Dekker, *Rapid manufacturing of low-noise membranes for nanopore sensors by trans-chip illumination lithography*, *Nanotechnology* **23**, 475302 (2012).
- [47] M. Van Den Hout, A. R. Hall, M. Y. Wu, H. W. Zandbergen, C. Dekker, and N. H. Dekker, *Controlling nanopore size, shape and stability*, *Nanotechnology* **21** (2010), 10.1088/0957-4484/21/11/115304.
- [48] A. Balan, B. Machielse, D. Niedzwiecki, J. Lin, P. Ong, R. Engelke, K. L. Shepard, and M. Drndić, *Improving signal-to-noise performance for DNA translocation in solid-state nanopores at MHz bandwidths*, *Nano Letters* **14**, 7215 (2014).
- [49] Z.-Y. Zhang, Y.-S. Deng, H.-B. Tian, H. Yan, H.-L. Cui, and D.-Q. Wang, *Noise Analysis of Monolayer Graphene Nanopores*, *International Journal of Molecular Sciences* **19**, 2639 (2018).
- [50] S. Bezrukov and J. J. Kasianowicz, *Current Noise Reveals Protonation Kinetics and Number of Ionizable Sites in an Open Protein Ion Channel*, *Physical Review Letters* **70**, 2352 (1993).
- [51] D. P. Hoogerheide, S. Garaj, and J. A. Golovchenko, *Probing surface charge fluctuations with solid-state nanopores*, *Physical Review Letters* **102** (2009), 10.1103/PhysRevLett.102.256804.
- [52] L. K. J. Vandamme and D. Rigaud, *1/f noise in MOS devices, mobility or number fluctuations?* *IEEE Trans. Electron Devices* **41**, 1936 (1994).
- [53] R. P. Jindal and A. Van Der Ziel, *Model for mobility fluctuation 1/f noise*, *Applied Physics Letters* **38**, 290 (1981).
- [54] P. Dutta and P. M. Horn, *Low-frequency fluctuations in solids: 1/f noise*, *Reviews of Modern Physics* **53** (1981).
- [55] D. R. Lide, *CRC Handbook of Chemistry and Physics*, 85th ed. (2005).
- [56] J. Sonnefeld, *Determination of surface charge density parameters of silicon nitride*, *Colloids and Surfaces A: Physicochemical and Engineering Aspects* **108**, 27 (1996).
- [57] W. M. Haynes, *CRC Handbook of Chemistry and Physics*, 91st ed. (2010).

- [58] B. Hille, *Pharmacological Modifications of the Sodium Channels of Frog Nerve*, The Journal of General Physiology **51**, 199 (1968).

4

NANOPORES: BEYOND DNA SEQUENCING

The biological cell is full of many types of nanopores that govern the passage of individual molecules. Leaning from nature, nanopore techniques have developed into the ultimate analytical tool for sensing single molecules. Nanopore-based single-molecule DNA sequencing has propelled genomic science with improved sensitivity, lower costs, and long reads. Notably however, the sensing capabilities of the unique nanopore technique extend well beyond DNA sequencing. Here, we offer a comprehensive review that illuminates nanopore applications beyond DNA sequencing, with clear prospects for protein analysis and sequencing, single-molecule covalent chemistry, single-molecule liquid biopsy, and biomimetic pore engineering for understanding natural systems. These developments showcase nanopores as a general tool for biophysics, bioinformatics, and cheminformatics.

This chapter is based on a manuscript in preparation as: Y. Ying, Z. Hu, S. Zhang, Y. Qing, A. Fragasso, X. Zhang, G. Maglia, A. Meller, H. Bayley, C. Dekker, L. Jiang, Y. Long. Nanopores: Beyond DNA Sequencing.

4.1. INTRODUCTION

Nanopores are an emerging class of single-molecule biosensors which have been developed primarily for ultra-sensitive DNA sequencing, as well as for other label-free biomolecular sensing. Nanopores can be formed by several ways: biological nanopores are formed by self-assembly of either protein sub-units, peptides or even DNAs scaffold in lipid bilayers or in block copolymer membranes. Solid-state nanopores are crafted in freely suspended thin membrane by a variety of nanoscale milling tools including electron/ion/laser beam drilling, by laser-based optical-etching method, or using dielectric breakdown of ultrathin solid membranes [1–4]. Alternatively, nanopores can be formed by controlled pulling of glass capillaries in designated instruments [5].

Nanopores provides a geometric confinement to molecules that are temporarily lodged in its interior volume, to allow label free sensing. Additionally, nanopores may offer a controllable chemical environment for single molecules and ions used to facilitate chemical reactions in this nanoscale volume. Both features may be utilized for single-molecule manipulation and sensing. In the most common nanopore measurement, the individual analyte is inserted inside the nanopore under applied potentials, hence altering the physical free flow of ions through the nanopore and permitting a straightforward temporal Ohmic measurement. Ideally, the geometry of the nanopore should be comparable to that of the analyte, to produce a significant change in the ion current amplitude from the presence of the analyte above the noise level. Additionally, a tight fit between the nanopore and analyte enhances the interactions between them, which accounts for the overall sensitivity and selectivity of the device [6]. The size, shape and chemical properties of the nanopore could be tuned and manipulated at nanometer to subnanometer scale to further enhance its properties. For example, site-direct mutagenesis of protein nanopores may contribute to optimal interactions in nanopore confinement for specific analyte recognitions. This feature allows nanopore to controllably capture, identify, and transport any molecules and ions from the bulk solution.

Nanopore sensors were initially used to stochastically characterize single molecules in a relatively simple, high-throughput, label-free format. By analyzing modulations of the ionic current in blockade amplitude, duration and frequency, nanopores have applied to sense and characterize a vast range of molecules, including DNAs, messenger and transfer RNAs, peptides, proteins, protein-DNA complexes and even metabolites [7–14]. Today, the success of nanopore-based DNA sequencing has stimulated potential applications in many fields.

Although DNA sequencing has been the main focus for the nanopore method in the past two decades, the technique currently extends well beyond sequencing, as it has been adapted to analyze molecular heterogeneities and stochastic processes in many different biochemical systems with single-molecule precision. This is due to a number of factors. First, a key advantage of nanopores lies in its ability to successively capture many single molecules one after the other at relatively high rate. This feature permits nanopores to explore large populations of molecules at single-molecule level in reasonable timeframes to understand their properties and dynamic behavior. Consequently, nanopores can be used to gain new molecular and mechanistic insights in a broad spectrum of molecular biosystems. Second, as nanopores essentially convert structural and chemical properties of the analytes into a measurable ion current signal, the nanopore

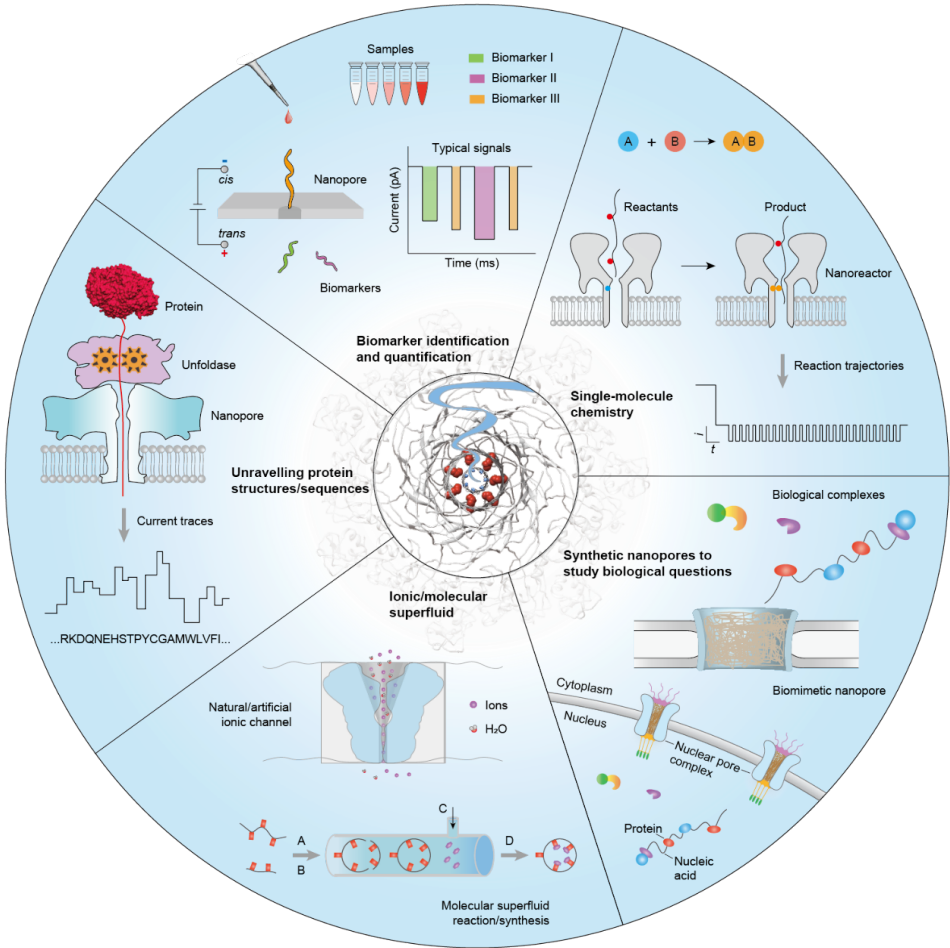


Figure 4.1: Nanopore techniques beyond DNA sequencing. The figure illustrates five areas of research where nanopores have great potential to contribute to new knowledge and new technologies.

can be used to report on multiple molecular features while circumventing the use of labelling chemistries, which complicate the analysis process and may affect the molecular structures. For example, recent studies showed that nanopore could discriminate 13 amino acids in a label-free manner, including some minute structural differences [15]. An important aspect is the ability of nanopores to identify rare or aberrant species, which lack suitable labels for the signal amplification or whose information are hidden in the noise of analytical devices. Consequently, the nanopore may serve well in molecular diagnostic applications required for precision medicine, which make use of protein analyses, as well as other biomarker identification. Third, nanopores provide a well-defined scaffold to controllably design and construct biomimetic systems, which involve complex network of biomolecular interactions. These nanopore systems may be used to study the binding dynamics of transport biomolecules as they interact with the nanopore surfaces, hence serving as a sophisticated platform for unraveling complex biological processes [16, 17]. Forth, chemical groups can be spatially aligned along the sensing interface of the protein nanopore, providing a sterically confined chemical environment for site-selective or regioselective covalent chemistry. This strategy has been used to engineer biological nanopores to serve as nanoreactors for the analysis of single-molecule reactions, such as the making and breaking of disulfide bonds [18, 19].

In this review paper, we discuss the state of the art in current nanopore research, as well as opportunities and the main challenges for the next decade, as the field shifts beyond DNA sequencing applications. We specifically address emerging nanopore methods for protein analysis and protein sequencing, single-molecule liquid biopsy, single-molecule covalent chemistry, and insights of biomimetic pores in analyzing complex biological processes.

4.2. CHARACTERIZATION OF SINGLE PROTEINS WITH NANOPORES

After the spectacular success following the sequencing of nucleic acids by nanopores, academic efforts are now shifting towards studying proteins. As an organism such as ourselves exhibits millions of different proteins, the challenge in proteomics involve identifying proteins, quantifying their abundance, and characterizing the choreography of post translational modifications that underlie their function. Several approaches to protein identifications are being explored.

Folded proteins have been sensed using solid-state [20] and biological [21] nanopores. Properties such as protein volume, dipole and shape can be inferred by analyzing the translocation dynamics of proteins through nanopores [22], indicating that nanopores are useful for extracting generic properties of proteins. Alternatively, ligands such as biotin [23], aptamers [24], protein domains [25], or antibodies [26] directly attached to nanopores or ligands attached to DNA carriers have been used to identify specific proteins (Fig. 4.2a), even in the presence of complex media such as serum [27]. Beyond characterizing single proteins, nanopore arrays or specific fractionation protocols will be required to address the complexity of a proteome.

Work is underway to use nanopores to detect single peptides as an alternative to mass spectrometry, the workhorse of proteomic analysis. Following initial work with

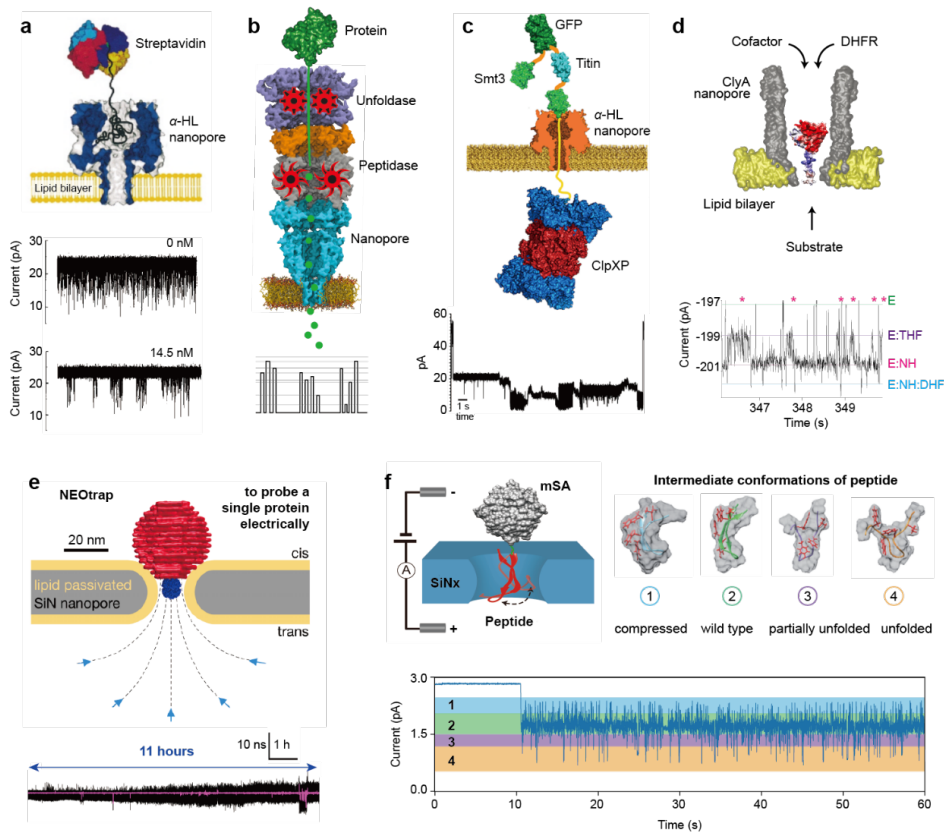


Figure 4.2: Unravelling proteins with nanopores. **a**, Identification of streptavidin with α -hemolysin (α -HL) nanopore covalently modified with a PEG-biotin (top) as observed by a reduction of current noise (bottom) [23]. **b**, Schematic of a single-molecule identifier in which a protein (e.g. GFP, dark green) is fed to an unfoldase (purple) into peptidase (e.g. proteasome, green and orange) attached to a nanopore (cyan) [28]. An idealized peptide fragmentation pattern is depicted (bottom). **c**, Unfolded transport of a construct including Smt3 (light green), GFP (dark green), and titin (cyan) – previously electrophoretic captured using a peptide thread (yellow) – through a nanopore operated by ClpXP (blue and red)(top). The unfolded translocation is shown in the electrical signal (bottom) [29]. **d**, Catalytic activity of DHFR (colored according to the vacuum electrostatics) inside ClyA nanopores (grey) (top), as shown by a representative traces (bottom). The formation of the product is shown by a pink asterisk [30]. **e**, Immobilization of a protein (blue) inside a nanopore (grey) using a DNA-origami sphere (red) in the NEOTrap [31]. The current trace indicates a trapping time of several hours. **f**, Dynamic conformation of a single peptide confined in a SiNx solid-state nanopore. The β -hairpin peptide was bound to a monovalent streptavidin (mSA). The ionic current (bottom) reflects different conformations of the target peptide (top right) [7]. Figures are adapted from the indicated references.

model peptides [32] and their post-translational modifications [33], it has been reported that, as observed earlier for PEG molecules [34], peptide signals relate to their volume [35] (hence to a first approximation to the peptide mass). Another important step was the realization that by lowering the pH to <4 , all peptides can be captured despite their chemical composition [36]. Based on peptide-volume recognition, a single-molecule protein identifier has been proposed, in which a protease is placed directly above a nanopore, and the fragmented peptides are sequentially read by a nanopore sensor (Fig. 4.2b) [37]. Initial steps to integrate a peptidase with a nanopore have been made [28].

The ideal approach to nanopore proteomics, however, would be *de novo* protein sequencing, where proteins are unfolded, linearly translocated across a nanopore amino acid by amino acid, and individual amino acids recognized by specific current signatures. Among the many challenges in such a *de novo* sequencing, amino acid recognition appears tractable. Several laboratories could observe differences in single amino acids, on either peptides [15] or stretched polypeptides [38], and even differences between isomeric molecules have been reported [39]. Therefore, at least a subset of amino acids or post translational modifications should be addressable by nanopore currents. Attempts have also been made to control of the translocation of linearized proteins using unfoldases - enzymes that unfold protein using ATP as fuel. In a first example, transport was obtained using ClpXP which was used to pull on proteins pre-threaded through an α -HL nanopore. The narrow entry of the nanopore was then used as a sieve to forcefully unfold the proteins (Fig. 4.2c) [40]. Differences between proteins or modifications that affected the folded state of the protein have been reported [29]. Another approach used a proteolytically inactivated proteasome – a cylindrical multicomplex system that degrades proteins – genetically fused atop of a β -barrel nanopore [28]. The proteasome acted as a docking station for an unfoldase, which would then feed unfolded protein to the proteasome chamber and eventually through the nanopore. Both approaches require further developments, either to reduce the electrical signal generated by the unfolding process at the mouth of the nanopore [29], or to control the stretching of the proteins as they translocate across the nanopore [28]. Recent work appears to provide a breakthrough towards protein sequencing, where a helicase was used to pull a DNA-peptide hybrid molecule through a nanopore in single amino acids steps, and single amino-acid substitutions were reliably detected within individual peptides [41].

Beside identifying proteins, nanopores can be used as single-molecule sensors to characterize protein activity, dynamics, and conformational changes. Among the unique advantages of nanopores is the ability to sample native proteins at the single-molecule level with microsecond resolution with no intrinsic limitation on the observation period. In first implementations of nanopore enzymology, nanopores were used to monitor the formation of the product of bulk enzymatic reactions [42], which might be useful when a straightforward spectroscopic assay is not available. However, this approach does not allow sampling the activities of individual enzymes. The latter has been first achieved by following the enzymatic ratcheting of a DNA strand across a nanopore [43], a method developed for DNA sequencing applications. For example, these studies revealed that Hel308 helicase moves a distance corresponding to half a DNA base during nucleotide binding and half a base during nucleotide hydrolysis, and that Phi29 DNA polymerase occasionally backsteps during amino acid incorporations [44]. Another approach has

been to monitor the enzymes binding to the nanopore itself. Conformational changes of GroEL binding to a GroES-nanopore [35], or kinases binding or phosphorylating a peptide introduced within the transmembrane region of a nanopore [45] have been observed. However, the relatively complex engineering of nanopores is likely to limit this approach to bespoke examples.

A more generic approach is to temporarily trap a protein inside a nanopore. Conformational changes or dynamics can then be monitored through changes in the nanopore signal (Fig. 4.2d-e). Proteins of 20-65 kDa can be captured by the electroosmotic flow within asymmetric biological nanopores, such as ClyA21 or PlyAB [46], for variable periods. Importantly, at moderate voltages (<150 mV) no evidence of protein unfolding was observed [47]. Ligand-induced conformational changes for a range of proteins [48, 49] have been reported. This included the tiny conformational changes of dihydrofolate reductase during ligand-binding [48] and catalysis [30], which previously could not be attained by single-molecule FRET studies [50]. These studies revealed that DHFR exists in multiple fixed conformation – conformers –, which exchange during catalysis is most likely used to tune the enzyme's efficiency [30, 48]. Solid-state nanopores have also been used to sample proteins conformations [51]. However, the fast transport across the nanopores often prevents addressing multiple exchanges within single enzymes. This limitation has been addressed recently. In one example, a protein stopper was introduced to immobilize a biotinylated peptide inside a nanopore [7], allowing the measurement of multiple conformational exchanges. In another recent report a DNA lid was added to one side of a lipid-coated nanopore and proteins were added to the opposite side (Fig. 4.2e-f) [31]. The electrophoretic force allowed the DNA sphere to cover the nanopore, and the induced electroosmotic flow was used to trap a range of different proteins on the opposite side [31]. Multiple conformational transitions of individual chaperone Hsp90 protein could be observed with this so-called NEOTrap.

4.3. SINGLE-MOLECULE CHEMISTRY

Single-molecule sensing generally involves non-covalent interactions [52]. Advances in this area suggested that covalent chemistry may be examined in a similar manner, and indeed bond making and bond breaking events of individual molecules attached to the interior wall of a nanopore can be analysed based on their modulation of the ionic current [53]. Nanopores engineered to contain reactive sites are referred to as protein nanoreactors.

Examples include many aspects of the chemistry of thiols, introduced as cysteine side chains [54]. Groups other than thiols can be examined after they have been introduced by site-directed chemical modification [55] or as non-canonical amino acids incorporated by native chemical ligation [56]. The nanoreactor approach has been used to examine various aspects of photochemistry [57], to unravel the stereochemical course of transformations [54], to observe polymerization step-by-step [58], and to monitor a primary isotope effect [59]. Catalytic cycles have been reconstituted by sampling partial reaction sequences in a nanopore after extricating intermediates from solution [60] and reaction networks of considerable complexity that would be hard to deconvolute by say NMR have been disentangled [54].

The strengths and weaknesses of the nanoreactor approach to single-molecule covalent

lent chemistry must be considered. On the plus side, no tagging of reactants is required. Because the pores formed by bacterial proteins are generally tough, a wide range of pH values, salt concentrations, and temperatures [61] can be used. However, at this point, only aqueous chemistry has been examined. Both irreversible and reversible chemistry has been explored, and, because there are two compartments in a bilayer set up, incompatible spatially-separated reactants can be employed [62]. While attachment to the wall of the lumen is required to beat diffusion, it also prevents kinetic complications, such as the dimerisation of intermediates [56]. If repeated turnover at a defined site is considered to be catalysis, examples have been observed [62], but further progress on the use of nanopores to alter the course and rate of reactions is expected. Computer analysis of the frequency and lifetime of current states produces reaction schemes and kinetic constants for covalent chemistry with time resolution that can reach the 100- μ s range [63]. In general, standard deviations in rate constants are more than $\pm 5\%$, which can be limiting, *e.g.* only large isotope effects can be detected [59]. While the nanoreactor approach provides a single-molecule reaction trajectory in which all steps are visible whether or not they are rate limiting [59], the molecular identification of intermediates can be problematic, as in any single-molecule approach.

In early work, the kinetics of covalent chemistry within a nanoreactor were assumed to approximate the kinetics of ensemble reactions in bulk solution, and this is roughly correct for small molecules [53]. More recently, interest has turned to considerations of how the environment within a nanopore, notably confinement, neighbouring groups, and chirality can affect chemistry, especially that of polymers, and how electrophoresis and electroosmosis [64] can drive reactants into and out of pores. To enable chemistry on a polymer, its translocation through a nanoreactor can be arrested by either a terminal stopper protein or covalent linkage to the internal wall (Fig. 4.3a). In the presence of a pulling force, imposed by either electrophoresis or electroosmosis [64], the polymer will extend and elongate within the tubular structure (Fig. 4.3a). Additional force is exerted as the polymer emerges from confinement and regains conformational entropy (Fig. 4.3a). Two features of nanopore confinement are advantageous for chemical manipulation. First, reactive groups spatially separated along the polymer chain can be aligned with inward-facing reactive side-chains. Second, the direction of the pulling force on a covalently-attached polymer, and thereby the polymer's orientation, can be switched by reversing the applied potential (Fig. 4.3a), resetting the chemical landscape.

Alignment within a nanoreactor has been exploited to effect selective chemistry under confinement [19]. As proof-of-concept, the interchange between disulfides within polymer backbones and cysteine thiols at different positions within a nanopore was examined (Fig. 4.3b). The turnover of polymer substrates was enabled by using a competing small-molecule reductant (1,4-dithiothreitol, DTT, Fig. 4.3b). Site selectivity was assessed as the fraction of a particular polymer that reacted at a particular location within a nanoreactor. The regioselectivity between two chemically equivalent sulfur atoms within a disulfide was determined by observing the characteristic currents associated with each reaction product (Fig. 4.3b). Both site selectivity and regioselectivity showed strong dependences on the locations of cysteines in the nanopore and the disulfide in the polymer. This strategy might be adapted to other synthetic tubular nano-systems, such as metal-organic frameworks, to deliver site-selective or regioselective chemistry.

The selective chemistry promoted by confinement has been further elaborated into a processive molecular machine [65], a ‘hopper’ which moves along a cysteine track within a nanopore while carrying a DNA cargo (Fig. 4.3c) [18]. The hopper takes sub-nm steps through consecutive thiol-disulfide interchange reactions (Fig. 4.3c). Reactions producing backward motion are strongly disfavoured when there is a pulling force on the DNA, endowing the hopper with remarkable directionality (Fig. 4.3c). External control of the applied potential reorients the DNA within the nanopore and thereby resets the direction of hopping and the endpoint of the process (Fig. 4.3c). Hopping is highly processive [18] and may provide a chemical alternative to the enzymatic ratchets used in sequencing technologies, which could be applied to polypeptides and polysaccharides as well as nucleic acids if longer tracks can be provided, for example on a patterned surface.

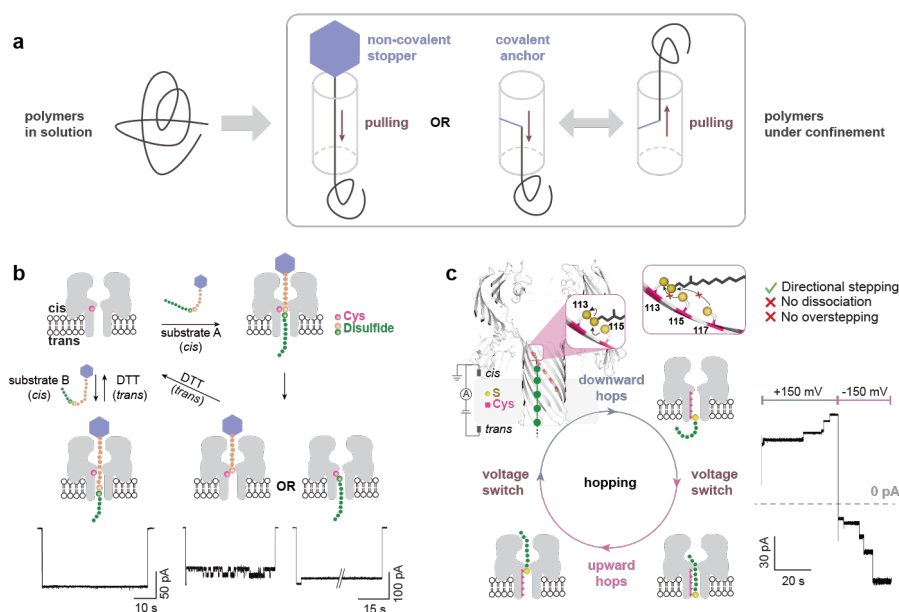


Figure 4.3: Chemistry of polymers under confinement. a, Polymers, which coil in solution, are extended when confined within a tubular protein nanoreactor. This is achieved by non-covalently or covalently anchoring one end of the polymer and applying a pulling force, *e.g.* an applied electric potential. In the case of covalent linkage, the polymer can be extended in either direction. b, Extending a polymer within a tubular nanoreactor exposes its reactive site (*e.g.* a disulfide) to a reactive group positioned on the nanoreactor interior (*e.g.* a cysteine thiol). In this way, spatial alignment differentiates between chemically equivalent reactive sites. Site selectivity and regioselectivity are determined at the single-molecule level by ionic current recording. The turnover of polymer substrates is enabled by 1,4-dithiothreitol (DTT). c, A molecular hopper moves along a multi-cysteine track under an applied potential while carrying a DNA cargo (green circles). Ratcheted by selective thiol-disulfide interchange reactions, the hopper makes steps in the direction of the pulling force. Real-time tracking of the hopper on track is achieved by monitoring the ionic current. Reversal of the applied potential flips the hopper, which then moves in the opposite direction.

4.4. SYNTHETIC NANOPORES AS A TOOL TO STUDY BIOLOGICAL QUESTIONS

While nanopores understandably attract most attention for their use in sequencing and bioanalytical applications, they also offer exciting opportunities to study questions that arise in cell biology. Cells feature a wide variety of nanometer-sized pores within their membranes (Fig. 4.4a), that act as gateways for molecular transport between compartments. For example, the flow of ions and small molecules (*e.g.* ATP) is regulated by ion channels and transporters, with crucial roles in homeostasis, energy production, cellular communication, and sensory transduction [66]. Larger pores, such as the mitochondrial translocase [67] and the nuclear pore complex (NPC) [68] are responsible for regulating the transport of proteins and RNAs between cellular compartments. Yet other examples are the SecYEG protein-secretion pore [69], the ClpXP protease [70] used for protein degradation, ceramide pores involved in cellular apoptosis [71], pore-forming toxins like α -HL [72], and the viral motor protein for packaging of DNA [73]. Biomolecular transport across all these pores poses many mechanistic questions, which often can be studied by extracting pores from the cell and docking them within a planar lipid membrane for *in vitro* characterization of their transport properties. Yet, more complex pores such as NPCs defy such a reconstitution approach.

With advances in solid-state nanopores [74], protein nanopore engineering [75], and DNA nanotechnology [76], it is now possible to build artificial systems that recapitulate the functionality of biological pores *in vitro*. Examples include the realization of ion pumps using asymmetrical solid-state nanopores [77], or the mimicking of a ligand-gated ion channel using a synthetic DNA pore [78]. Beyond reproducing the behavior of biological channels, such biomimetic pores bear great potential for understanding complex biological processes that cannot be probed directly *in vivo*.

A notable example is the nuclear pore complex, a huge (~ 52 MDa in yeast [68]) multi-protein complex that forms large pores (~ 40 nm) within the nuclear envelope to regulate all molecular trafficking in and out of the nucleus (Fig. 4.4b). Although much is known about its biological function [79], a solid understanding of the transport properties is lacking. In fact, the astounding complexity of the *in vivo* environment, combined with the fact that the NPC central channel is composed of intrinsically disordered proteins (IDPs), prevents to draw a full mechanistic picture of nuclear transport. The NPC conduit is filled with a 'spaghetti-like' mesh of IDPs, called FG-Nups (rich in 'F' and 'G' amino-acid repeats) that are the key element of the gatekeeper function. While small molecules can freely pass, larger cargo (>40 kDa proteins or mRNA) is blocked, unless it is bound to nuclear transport receptors (NTRs), which can actively partition into the FG-mesh. The basis for such selectivity is still debated, and many open questions remain, *e.g.* on the spatial arrangement of FG-Nups and whether NTRs are an integral part of the selective barrier beyond being mere transporters. The NPC is a prime example where biomimetic nanopores can help to disentangle such major mechanistic questions.

Biomimetic NPCs were developed in the past decade. Jovanovic-Talisman *et al.* [80] showed that 30 nm pore arrays functionalized with purified FG-Nups could behave selectively, *i.e.*, allowing NTRs to efficiently pass but blocking other proteins. This proved for the first time that the FG-Nup mesh alone is sufficient to impart a selective transport

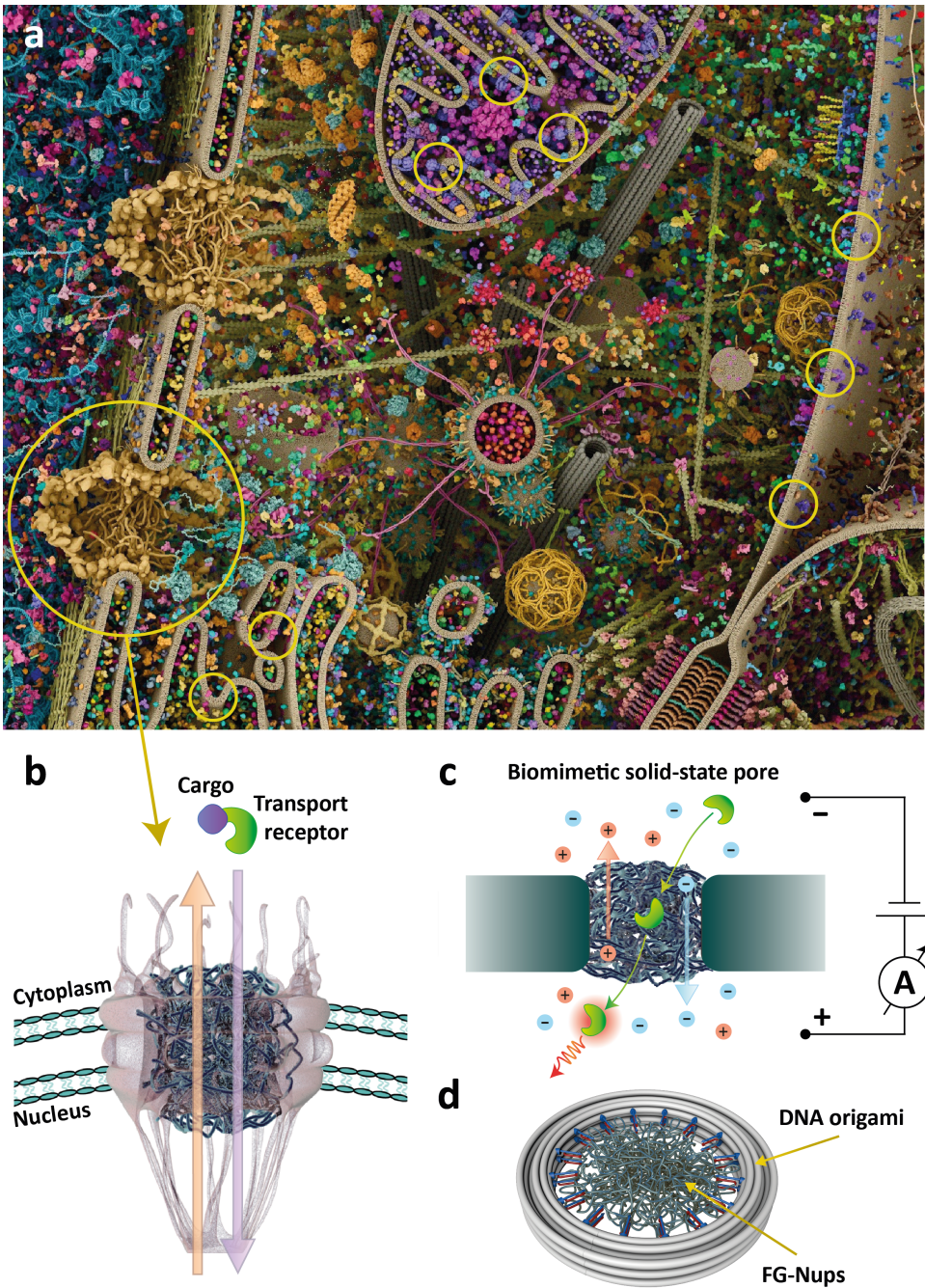


Figure 4.4: a, Sketch of the interior of a eukaryotic cell (adapted from <https://gaelmcgill.artstation.com/projects/Pm0JL1>). Yellow circles indicate a nuclear pore complex (left) and three mitochondrial pores (right). b, Schematic of the NPC (adapted from <https://sites.google.com/site/sspatel/nuclearporecomplex2>). The blue filaments represent the FG-Nup mesh. Import (purple) and export (orange) transport pathways are indicated. c, Schematic of a biomimetic solid-state nanopore, where FG-Nups are grafted onto a solid-state nanopore, whereupon transport of biomolecules can be measured electrically or optically. d, Sketch of a biomimetic NPC, built by attaching FG-Nups (blue) to a DNA-origami scaffold (grey).

barrier – a striking finding considering that the biomimetic NPCs consisted of only 1 type of FG-Nups while native NPCs feature more than 10 different FG-Nups types. Kowalczyk *et al.* [81] measured selective transport across individual biomimetic nanopores, formed by grafting FG-Nups to the inner walls of a solid-state nanopore (Fig. 4.4c), where ion current measurements provided single-molecule resolution. These biomimetic NPCs provided first insights into the FG-Nups conformation within the pore by examining the behavior of the conductance as a function of pore diameter. Follow-up work by Ananth *et al.* [82] emphasized the key role of the hydrophobic residues of the FG-Nups, as a mutant where hydrophobic amino acids were replaced by hydrophilic ones lost the selectivity altogether. These experiments, coupled with molecular dynamics simulations, revealed the important role of cohesiveness of the FG-mesh for achieving proper selective behavior. More recently, nanopores functionalized with user-defined protein sequences that mimic native FG-Nups were also shown to be selective, demonstrating the outstanding robustness of FG-Nups to drastic changes in their amino acid sequence [16]. A creative alternative approach to mimic NPCs is the use of a DNA-origami ring as a scaffold with programmable sites for anchoring FG-Nups (Fig. 4.4d) [83, 84]. This platform was employed for imaging the spatial arrangements of confined FG-Nups using cryo-electron microscopy and atomic force microscopy, and allows the exploration more complex FG-meshes that combine different types of FG-Nups.

4.5. NANOPORE SENSORS FOR BIOMARKER IDENTIFICATION AND QUANTIFICATION IN CLINICAL SAMPLES

The adaptation of nanopore sensing technologies for clinical samples presents new challenges associated with the greater complexity and heterogenous nature of medical specimens, as compared to lab-made samples (Fig. 4.5). Additionally, clinical sensing often requires extremely high precision, specificity, and sensitivity which further complicate its implementation. Nevertheless, the potential ability of nanopores to offer a generic and highly flexible sensing platform for liquid biopsy stands out as a high-impact opportunity that has begun to be addressed only in recent years.

Two primary factors can be identified as the main roadblocks in realizing this vision: First, unlike lab-made ‘analytical samples’, the target biomolecules in clinical samples (often nucleic acids or protein biomarkers) span large range of concentrations from as low as tens of aM (10^{-18} M) for some blood pathogenic infections and circulating tumor DNAs to sub-nM (10^{-9} M) concentrations for SARS, influenza as well as other biomarkers [85]. In many cases the super low biomarkers concentration severely limit the use of standard purification/concentration techniques [9]. Second, most clinical samples contain an abundance of constituents that may interfere with the nanopore sensor itself (*i.e.* blocking the nanopore or causing false translocation events). In particular, bodily fluids such as plasma, urine, and nasal secretions can clog the nanopore prematurely. At the same time bulk purification assays, including liquid chromatography and ‘clean-up’ columns, that are broadly used in life sciences research, are not optimal for nanopore based single-molecule sensing as they are lossy, time-consuming, and may not transfer well to point-of-care applications.

In recent years researchers have begun to tackle these challenges by developing smart

assays and devices for treatment of clinical samples, which take advantage of some of the unique capabilities of nanopore sensors. Particularly, owing to their extremely small and compact form factor, nanopore sensors can be integrated in microfluidic devices serving either sample preparation or analyte concentration, further increasing its yield of detection [9]. Moreover, biophysical concentration strategies involving for example dielectrophoretic trapping or isotacophoresis focusing can in principle concentrate the target species by several orders of magnitude, and therefore bear potential towards the future development of liquid biopsy applications involving biomolecule-based disease prognostics and diagnostics [86, 87].

To enhance molecular specificity and circumvent the negative effects of background molecules on nanopore functionality, a number of biochemical assays have already been developed. These assays involve minimal losses of target molecules during the sample preparation while at the same time they protect the nanopore by selective degradation of background molecules. For example, nanopore-based direct, digital counting of single nucleotide polymorphic sites marked with Locked Nucleic Acids synthetic molecules was used for detection of Shiga toxin producing *Escherichia coli* serotype and cancer-derived driver mutations [88, 89]. Another approach utilized the extremely high specificity of DNA ligase to pull-down selected circulating tumor DNA mutations associated with breast cancer genes (*i.e.* ERBB2 and PIK3Ca) in blood samples [90]. These mutations were sensed optically by tagging the probe oligonucleotides with fluorescent dyes and supplementing the electrical sensing of the nanopore with a single-molecule optical detection approach. In another recent studies the high selectivity of DNA aptamers was used to fabricate specific DNA ‘carriers’ with high affinity for specific protein biomarkers in plasma sample, producing characteristic electrical current traces when translocated through a nanopore formed at the end of glass-pulled pipettes [91]. Taking advantage of

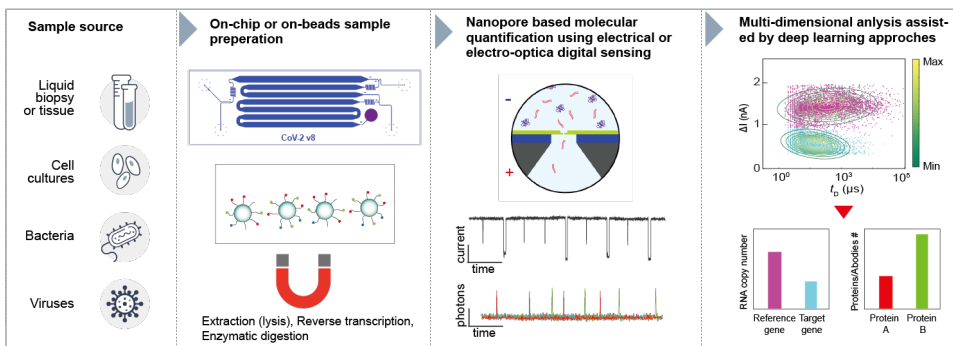


Figure 4.5: Adapting nanopore sensing to biological samples and clinical diagnostics. A variety of biomedical samples sources including bodily fluids or tissue biopsies or biological specimen including cell cultures, bacteria and viruses can be harvested in a minimal and non-lossy biochemical treatment for single-molecule sensing with protein or solid-state nanopores. The ultra-small sample volume (*e.g.* μL or less) required for the analysis lends itself for hands-free assay development utilizing on-chip microfluids and/or magnetic beads. Nanopore sensing may involve either pure electrical digital counting of biomolecules or a combined electro-optical sensing to enhance the system multiplexing ability. Data analysis is supported by advanced machine learning approaches to classify and count the target biomolecules.

electro-optical sensing, short hairpin structure oligonucleotide containing fluorophore and quencher moieties ('molecular beacons') were used to mark and identify specific cDNA molecules from human serum and urine, as they were forced through the tip of a nanopipette [92].

An alternative strategy for sensing of protein biomarkers in bio-fluids involved the creation of a protein bait antibody connected to a biological nanopore hence serving as a local 'trap' for the target protein [26, 93, 94]. Specifically, Fahie and coworkers modified the outer membrane protein G (OmpG) with a short, biotinylated polymer chain that was used as a sensing probe. The binding/unbinding kinetics of several anti-biotin antibodies (including mAb, pAb.1 and pAb.2) were studied in buffered solution of diluted serum. Interestingly the different anti-biotin antibodies showed remarkably different binding/unbinding kinetic rates presumably due to different antibodies size, shape or charge. A similar approach demonstrated by Thakur and Movileanu involved the truncated t-FhuA protein pore, equipped with a short hexapeptide tether, a barnase (Bn) protein receptor and a dodecapeptide adapter. The capture and release events of a protein analyte by the tethered protein bait occur outside the nanopore and are accompanied by uniform current openings, whereas nonspecific pore penetrations by nontarget components of serum, involve irregular current blockades. As a result of this unique peculiarity of the readout between specific protein captures and nonspecific pore penetration events which result in a highly dynamic ion-current signature, this selective sensor could quantitatively sample proteins and potentially provides richer information on the detected analytes than classical immunosorbent assays.

The α -hemolysin protein pore was used to selectively detect microRNAs (miR) molecules hybridized in solution to oligonucleotides probes, allowing the quantification of the miR-155 biomarker from purified plasma samples of lung cancer patients [95]. Specific binding of the miR to the probe molecules generated long voltage driven unzipping events, that were readily sensed by analyzing the ion current traces [96]. More recently, a purification-free method for nanopore based digital counting of mRNA expression was demonstrated [97]. The method involves Reverse Transcription (RT) of the target genes, directly followed by enzymatic degradation of the background molecules with no intermediate purification stages [97]. The accuracy of the assay relies on designing highly specific RT primers and avoiding PCR amplification, which could lead to erroneous amplification in cases where the clinical sample contains small amounts of the target mRNA biomarker. The method was used to quantify mRNA cancer biomarkers, such as MACC1, as well as for PCR-free sensing of SARS-Cov-2 clinical samples, potentially showing greater accuracy than the gold standard RT-qPCR method [9, 95].

Nanopore sensing of clinical samples is not limited only to nucleic acids and proteins. Recently, Galenkamp and co-workers demonstrated that the cytolysin A (ClyA) nanopore can be used to sense the concentration of metabolites such as glucose and asparagine, directly from bodily fluids (blood, sweat, urine, saliva) [9]. Glucose-binding protein (GBP) or substrate-binding domain analogous to GBP were used to sense glucose and asparagine molecules, respectively, by inducing shifts in the dwell-time of the open and closed conformations of the probing proteins, as they were lodged in the nanopore. In all the examples provided for nanopore based sensing of clinical biomarkers, the ability to sense multiple species (DNAs, RNAs, metabolites, *etc.*) using the same nanopore is

a direct consequence of the single-molecule nature of the technique in which only one molecule is sensed at the time and a dynamical ion current trajectory over time is used as the basis for target multiplexing. This illustrates the great potential nanopore sensing holds for future complex bio-fluids characterization often involving a multitude of biomarkers.

4.6. CONCLUSION AND PERSPECTIVES

This review outlined diverse nanopore research directions and applications beyond DNA sequencing. Tremendous progress has been made. Specifically, over the past two decades, nanopores have become an essential single-molecule tool in multiple disciplines including chemistry, biophysics, nanoscience, and others. The ongoing refinement of nanopores structures and shapes provide a well-defined confinement for single-molecule reaction catalysis. By taking advantage of designable nanopores at the molecular scale, the protein nanopore reactor is expected to provide a bottom-up approach for in situ production of customized chemicals. The nanopore has also found growing use as a force transducer allowing controlled localization and trapping of a diverse range of biomolecules for single-molecule biophysics studies. Finally, nanopore-based biomedical applications have grown beyond single DNA sequencing and epigenetic modification analyses, and is currently used in diverse fields from sensing molecular biomarkers (proteins, metabolites and nucleic acids) in biofluids, and other biological specimen. Based on the fast growth rate of nanopore applications, it is likely that it may become the prominent future technique in single-molecule *in vitro* diagnostics.

However, challenges remain for nanopores to meet its full potential. For example, in order to uncover the exact chemical compositions of single molecules (e.g., protein, polysaccharides and glycoprotein), improvements in sensing accuracy and temporal resolution will be necessary. Unlike the relatively simple primary structure of the four canonical DNAs nucleobases, many biopolymers are composed of larger number of chemically diverse building blocks. Specifically, proteins consist of 20 different amino-acids, and polysaccharides of 8-10 monosaccharides units. Therefore, nanopores must be rationally tailored to meet the resolution requirement for each application: their sensing volume should be as small to match the size of a single unit of the sensed monomer, but not too small to allow it to smoothly slide through the nanopore under the applied electric field. More important, the nanopore should be optimally sensitive to the chemical or physical properties of the building blocks, producing distinguishable ionic current signatures for each unit. This could be achieved by carefully functionalizing of the pore inner surfaces to manipulate the interactions between the biopolymer moiety and the nanopore, hence providing the required sensitivity and selectivity.

To achieve this long-term vision joint efforts of multi-disciplinary fields will be required, including engineering of motor proteins to finely control the biopolymers' translocation rate through the nanopore, as well as molecular dynamic simulations and advanced analysis methods involving machine learning. In parallel with advances in future nanopore designs, the ability to produce large-scale nanopore devices consisting of millions of individual pores on an small footprint, may greatly impact bioinformatics, producing enormous volumes of sensing data at high speeds. The ongoing developments in nanopore-based sensing strategies will also be beneficial for future venturing in the

promising field of molecular-based data storage and retrieval, offering new solutions for some of the most pressing challenges in this area.

REFERENCES

- [1] N. Varongchayakul, J. Song, A. Meller, and M. W. Grinstaff, *Single-molecule protein sensing in a nanopore: a tutorial*. Chemical Society reviews **47**, 8512 (2018).
- [2] Y.-L. Ying, C. Cao, Y.-X. Hu, and Y.-T. Long, *A single biomolecule interface for advancing the sensitivity, selectivity and accuracy of sensors*, National Science Review **5**, 450 (2018).
- [3] L. Restrepo-Pérez, C. Joo, and C. Dekker, *Paving the way to single-molecule protein sequencing*, Nature Nanotechnology **13**, 786 (2018).
- [4] S. McGinn, D. Bauer, T. Brefort, L. Dong, A. El-Sagheer, A. Elsharawy, G. Evans, E. Falk-Sörqvist, M. Forster, S. Fredriksson, P. Freeman, C. Freitag, J. Fritzsche, S. Gibson, M. Gullberg, M. Gut, S. Heath, I. Heath-Brun, A. J. Heron, J. Hohlbein, R. Ke, O. Lancaster, L. Le Reste, G. Maglia, R. Marie, F. Mauger, F. Mertes, M. Mignardi, L. Moens, J. Oostmeijer, R. Out, J. N. Pedersen, F. Persson, V. Picaud, D. Rotem, N. Schracke, J. Sengenès, P. F. Stähler, B. Stade, D. Stoddart, X. Teng, C. D. Veal, N. Zahra, H. Bayley, M. Beier, T. Brown, C. Dekker, B. Ekström, H. Flyvbjerg, A. Franke, S. Guenther, A. N. Kapanidis, J. Kaye, A. Kristensen, H. Lehrach, J. Mangion, S. Sauer, E. Schyns, J. Tost, J. M. L. M. van Helvoort, P. J. van der Zaag, J. O. Tegenfeldt, A. J. Brookes, K. Mir, M. Nilsson, J. P. Willcocks, and I. G. Gut, *New technologies for DNA analysis – a review of the READNA Project*, New Biotechnology **33**, 311 (2016).
- [5] R.-J. Yu, Y.-L. Ying, R. Gao, and Y.-T. Long, *Confined Nanopipette Sensing: From Single Molecules, Single Nanoparticles, to Single Cells*, Angewandte Chemie International Edition **58**, 3706 (2019).
- [6] A. Meller, *Dynamics of polynucleotide transport through nanometre-scale pores*, Journal of Physics Condensed Matter **15**, 581 (2003).
- [7] S.-C. Liu, Y.-L. Ying, W.-H. Li, Y.-J. Wan, and Y.-T. Long, *Snapshooting the transient conformations and tracing the multiple pathways of single peptide folding using a solid-state nanopore*, Chemical Science **12**, 3282 (2021).
- [8] C. Cao, Y.-L. Ying, Z.-L. Hu, D.-F. Liao, H. Tian, and Y.-T. Long, *Discrimination of oligonucleotides of different lengths with a wild-type aerolysin nanopore*, Nature Nanotechnology **11**, 713 (2016).
- [9] N. S. Galenkamp, M. Soskine, J. Hermans, C. Wloka, and G. Maglia, *Direct electrical quantification of glucose and asparagine from bodily fluids using nanopores*, Nature Communications **9**, 4085 (2018).
- [10] D. Zhang, P. Solomon, S. L. Zhang, and Z. Zhang, *Correlation of Low-Frequency Noise to the Dynamic Properties of the Sensing Surface in Electrolytes*, ACS Sensors **2**, 1160 (2017).

- [11] M. Wanunu, W. Morrison, Y. Rabin, A. Y. Grosberg, and A. Meller, *Electrostatic focusing of unlabelled DNA into nanoscale pores using a salt gradient*, *Nature Nanotechnology* **5**, 160 (2010).
- [12] I. Nir, D. Huttner, and A. Meller, *Direct Sensing and Discrimination among Ubiquitin and Ubiquitin Chains Using Solid-State Nanopores*, *Biophysical Journal* **108**, 2340 (2015).
- [13] A. Squires, E. Atas, and A. Meller, *Nanopore sensing of individual transcription factors bound to DNA*, *Scientific Reports* **5**, 11643 (2015).
- [14] D. P. Depledge, K. P. Srinivas, T. Sadaoka, D. Bready, Y. Mori, D. G. Placantonakis, I. Mohr, and A. C. Wilson, *Direct RNA sequencing on nanopore arrays redefines the transcriptional complexity of a viral pathogen*, *Nature Communications* **10**, 754 (2019).
- [15] H. Ouldali, K. Sarthak, T. Ensslen, F. Piguet, P. Manivet, J. Pelta, J. C. Behrends, A. Aksimentiev, and A. Oukhaled, *Electrical recognition of the twenty proteinogenic amino acids using an aerolysin nanopore*, *Nature Biotechnology* **38**, 176 (2020).
- [16] A. Fragasso, H. W. de Vries, J. Andersson, E. O. van der Sluis, E. van der Giessen, A. Dahlin, P. R. Onck, and C. Dekker, *A designer FG-Nup that reconstitutes the selective transport barrier of the nuclear pore complex*, *Nature communications* **12**, 2010 (2021).
- [17] M.-Y. Li, Y.-L. Ying, J. Yu, S.-C. Liu, Y.-Q. Wang, S. Li, and Y.-T. Long, *Revisiting the Origin of Nanopore Current Blockage for Volume Difference Sensing at the Atomic Level*, *JACS Au* **1**, 967 (2021).
- [18] Y. Qing, S. A. Ionescu, G. S. Pulcu, and H. Bayley, *Directional control of a processive molecular hopper*, *Science* **361**, 908 LP (2018).
- [19] Y. Qing, H. Tamagaki-Asahina, S. A. Ionescu, M. D. Liu, and H. Bayley, *Catalytic site-selective substrate processing within a tubular nanoreactor*, *Nature Nanotechnology* (2019), 10.1038/s41565-019-0579-7.
- [20] M. Firnkes, D. Pedone, J. Knezevic, M. Döblinger, and U. Rant, *Electrically facilitated translocations of proteins through silicon nitride nanopores: Conjoint and competitive action of diffusion, electrophoresis, and electroosmosis*, *Nano Letters* **10**, 2162 (2010).
- [21] M. Soskine, A. Biesemans, B. Moeyaert, S. Cheley, H. Bayley, and G. Maglia, *An Engineered ClyA Nanopore Detects Folded Target Proteins by Selective External Association and Pore Entry*, *Nano Letters* **12**, 4895 (2012).
- [22] J. Houghtaling, C. Ying, O. M. Eggenberger, A. Fennouri, S. Nandivada, M. Acharjee, J. Li, A. R. Hall, and M. Mayer, *Estimation of Shape, Volume, and Dipole Moment of Individual Proteins Freely Transiting a Synthetic Nanopore*, *ACS Nano* **13**, 5231 (2019).

- [23] L. Movileanu, S. Howorka, O. Braha, and H. Bayley, *Detecting protein analytes that modulate transmembrane movement of a polymer chain within a single protein pore*, Nature Biotechnology **18**, 1091 (2000).
- [24] D. Rotem, L. Jayasinghe, M. Salichou, and H. Bayley, *Protein Detection by Nanopores Equipped with Aptamers*, Journal of the American Chemical Society **134**, 2781 (2012).
- [25] A. K. Thakur and L. Movileanu, *Real-time measurement of protein–protein interactions at single-molecule resolution using a biological nanopore*, Nature Biotechnology **37**, 96 (2019).
- [26] M. Fahie, C. Chisholm, and M. Chen, *Resolved Single-Molecule Detection of Individual Species within a Mixture of anti-Biotin Antibodies Using an Engineered Monomeric Nanopore*, ACS Nano **9**, 1089 (2015).
- [27] K. Chuah, Y. Wu, S. R. C. Vivekchand, K. Gaus, P. J. Reece, A. P. Micolich, and J. J. Gooding, *Nanopore blockade sensors for ultrasensitive detection of proteins in complex biological samples*, Nature Communications **10**, 2109 (2019).
- [28] S. Zhang, G. Huang, R. Versloot, B. M. Herwig, P. C. T. de Souza, S.-J. Marrink, and G. Maglia, *Bottom-up fabrication of a multi-component nanopore sensor that unfolds, processes and recognizes single proteins*, bioRxiv, 2020.12.04.411884 (2020).
- [29] J. Nivala, L. Mulroney, G. Li, J. Schreiber, and M. Akeson, *Discrimination among Protein Variants Using an Unfoldase-Coupled Nanopore*, ACS Nano **8**, 12365 (2014).
- [30] N. S. Galenkamp and G. Maglia, *Substrate binding and turnover modulate the affinity landscape of dihydrofolate reductase to increase its catalytic efficiency*, bioRxiv, 2020.04.14.040733 (2020).
- [31] S. Schmid, P. Stömmmer, H. Dietz, and C. Dekker, *Nanopore electro-osmotic trap for the label-free study of single proteins and their conformations*, Nature Nanotechnology **18**, 2 (2021).
- [32] T. C. Sutherland, Y.-T. Long, R.-I. Stefureac, I. Bediako-Amoa, H.-B. Kraatz, and J. S. Lee, *Structure of Peptides Investigated by Nanopore Analysis*, Nano Letters **4**, 1273 (2004).
- [33] L. Restrepo-Pérez, C. H. Wong, G. Maglia, C. Dekker, and C. Joo, *Label-Free Detection of Post-translational Modifications with a Nanopore*, Nano Letters **19**, 7957 (2019).
- [34] J. W. F. Robertson, C. G. Rodrigues, V. M. Stanford, K. A. Robinson, O. V. Krasilnikov, and J. J. Kasianowicz, *Single-molecule mass spectrometry in solution using a solitary nanopore*, Proceedings of the National Academy of Sciences **104**, 8207 (2007).
- [35] A. E. Chavis, K. T. Brady, G. A. Hatmaker, C. E. Angevine, N. Kothalawala, A. Dass, J. W. F. Robertson, and J. E. Reiner, *Single Molecule Nanopore Spectrometry for Peptide Detection*, ACS Sensors **2**, 1319 (2017).

- [36] G. Huang, K. Willems, M. Soskine, C. Wloka, and G. Maglia, *Electro-osmotic capture and ionic discrimination of peptide and protein biomarkers with FraC nanopores*, Nature Communications **8**, 1 (2017).
- [37] G. Huang, A. Voet, and G. Maglia, *FraC nanopores with adjustable diameter identify the mass of opposite-charge peptides with 44 dalton resolution*, Nature Communications **10**, 835 (2019).
- [38] L. Restrepo-Pérez, G. Huang, P. R. Bohländer, N. Worp, R. Eelkema, G. Maglia, C. Joo, and C. Dekker, *Resolving Chemical Modifications to a Single Amino Acid within a Peptide Using a Biological Nanopore*, ACS Nano **13**, 13668 (2019).
- [39] A. J. Boersma and H. Bayley, *Continuous Stochastic Detection of Amino Acid Enantiomers with a Protein Nanopore*, Angewandte Chemie International Edition **51**, 9606 (2012).
- [40] J. Nivala, D. B. Marks, and M. Akeson, *Unfoldase-mediated protein translocation through an α -hemolysin nanopore*, Nature Biotechnology **31**, 247 (2013).
- [41] H. Brinkerhoff, A. S. W. Kang, J. Liu, A. Aksimentiev, and C. Dekker, *Infinite re-reading of single proteins at single-amino-acid resolution using nanopore sequencing*, bioRxiv, 2021.07.13.452225 (2021).
- [42] M. Kukwikila and S. Howorka, *Nanopore-Based Electrical and Label-Free Sensing of Enzyme Activity in Blood Serum*, Analytical Chemistry **87**, 9149 (2015).
- [43] J. Chu, M. González-López, S. L. Cockroft, M. Amorin, and M. R. Ghadiri, *Real-Time Monitoring of DNA Polymerase Function and Stepwise Single-Nucleotide DNA Strand Translocation through a Protein Nanopore*, Angewandte Chemie International Edition **49**, 10106 (2010).
- [44] E. a. Manrao, I. M. Derrington, A. H. Laszlo, K. W. Langford, M. K. Hopper, N. Gillgren, M. Pavlenok, M. Niederweis, and J. H. Gundlach, *Reading DNA at single-nucleotide resolution with a mutant MspA nanopore and phi29 DNA polymerase*, Nature Biotechnology **30**, 349 (2012).
- [45] S. Cheley, H. Xie, and H. Bayley, *A Genetically Encoded Pore for the Stochastic Detection of a Protein Kinase*, ChemBioChem **7**, 1923 (2006).
- [46] G. Huang, K. Willems, M. Bartelds, P. van Dorpe, M. Soskine, and G. Maglia, *Electro-Osmotic Vortices Promote the Capture of Folded Proteins by PlyAB Nanopores*, Nano Letters **20**, 3819 (2020).
- [47] S. Zernia, N. J. van der Heide, N. S. Galenkamp, G. Gouridis, and G. Maglia, *Current Blockades of Proteins inside Nanopores for Real-Time Metabolome Analysis*, ACS Nano **14**, 2296 (2020).
- [48] N. S. Galenkamp, A. Biesemans, and G. Maglia, *Directional conformer exchange in dihydrofolate reductase revealed by single-molecule nanopore recordings*, Nature Chemistry **12**, 481 (2020).

- [49] V. Van Meervelt, M. Soskine, S. Singh, G. K. Schuurman-Wolters, H. J. Wijma, B. Poolman, and G. Maglia, *Real-Time Conformational Changes and Controlled Orientation of Native Proteins Inside a Protein Nanoreactor*, *Journal of the American Chemical Society* **139**, 18640 (2017).
- [50] P. T. R. Rajagopalan, Z. Zhang, L. McCourt, M. Dwyer, S. J. Benkovic, and G. G. Hammes, *Interaction of dihydrofolate reductase with methotrexate: Ensemble and single-molecule kinetics*, *Proceedings of the National Academy of Sciences* **99**, 13481 LP (2002).
- [51] P. Waduge, R. Hu, P. Bandarkar, H. Yamazaki, B. Cressiot, Q. Zhao, P. C. Whitford, and M. Wanunu, *Nanopore-Based Measurements of Protein Size, Fluctuations, and Conformational Changes*, *ACS Nano* **11**, 5706 (2017).
- [52] H. Bayley and P. S. Cremer, *Stochastic sensors inspired by biology*, *Nature* **413**, 226 (2001).
- [53] H. Bayley, T. Luchian, S.-H. Shin, and M. Steffensen, *Single Molecule Covalent Chemistry in a Protein Nanoreactor* (2008) pp. 251–277.
- [54] M. B. Steffensen, D. Rotem, and H. Bayley, *Single-molecule analysis of chirality in a multicomponent reaction network*, *Nature Chemistry* **6**, 603 (2014).
- [55] W. J. Ramsay and H. Bayley, *Single-Molecule Determination of the Isomers of d-Glucose and d-Fructose that Bind to Boronic Acids*, *Angewandte Chemie International Edition* **57**, 2841 (2018).
- [56] J. Lee and H. Bayley, *Semisynthetic protein nanoreactor for single-molecule chemistry*, *Proceedings of the National Academy of Sciences* **112**, 13768 LP (2015).
- [57] T. Luchian, S.-H. Shin, and H. Bayley, *Kinetics of a Three-Step Reaction Observed at the Single-Molecule Level*, *Angewandte Chemie International Edition* **42**, 1926 (2003).
- [58] G. S. Pulcu, N. S. Galenkamp, Y. Qing, G. Gasparini, E. Mikhailova, S. Matile, and H. Bayley, *Single-Molecule Kinetics of Growth and Degradation of Cell-Penetrating Poly(disulfide)s*, *Journal of the American Chemical Society* **141**, 12444 (2019).
- [59] S. Lu, W.-W. Li, D. Rotem, E. Mikhailova, and H. Bayley, *A primary hydrogen–deuterium isotope effect observed at the single-molecule level*, *Nature Chemistry* **2**, 921 (2010).
- [60] W. J. Ramsay, N. A. W. Bell, Y. Qing, and H. Bayley, *Single-Molecule Observation of the Intermediates in a Catalytic Cycle*, *Journal of the American Chemical Society* **140**, 17538 (2018).
- [61] X.-f. Kang, L.-Q. Gu, S. Cheley, and H. Bayley, *Single Protein Pores Containing Molecular Adapters at High Temperatures*, *Angewandte Chemie International Edition* **44**, 1495 (2005).

- [62] T. Luchian, S.-H. Shin, and H. Bayley, *Single-Molecule Covalent Chemistry with Spatially Separated Reactants*, *Angewandte Chemie International Edition* **42**, 3766 (2003).
- [63] Y. Qing, G. S. Pulcu, N. A. W. Bell, and H. Bayley, *Bioorthogonal Cycloadditions with Sub-Millisecond Intermediates*, *Angewandte Chemie International Edition* **57**, 1218 (2018).
- [64] L.-Q. Gu, S. Cheley, and H. Bayley, *Electroosmotic enhancement of the binding of a neutral molecule to a transmembrane pore*, *Proceedings of the National Academy of Sciences* **100**, 15498 LP (2003).
- [65] R. D. Astumian, *Microscopic reversibility as the organizing principle of molecular machines*, *Nature Nanotechnology* **7**, 684 (2012).
- [66] S. M. W. Dale Purves, George J. Augustine, David Fitzpatrick, Lawrence C. Katz, Anthony-Samuel LaMantia, James O. McNamara, *Channels and Transporters*, 2nd ed., edited by Neuroscience (Sinauer Associates, Sunderland (MA), 2001) p. Chapter 4.
- [67] P. J. T. Dekker, M. T. Ryan, J. Brix, H. Müller, A. Hönlinger, and N. Pfanner, *Preprotein Translocase of the Outer Mitochondrial Membrane: Molecular Dissection and Assembly of the General Import Pore Complex*, *Molecular and Cellular Biology* **18**, 6515 (1998).
- [68] S. J. Kim, J. Fernandez-Martinez, I. Nudelman, Y. Shi, W. Zhang, B. Raveh, T. Hericks, B. D. Slaughter, J. A. Hogan, P. Upla, I. E. Chemmama, R. Pellarin, I. Echeverria, M. Shivaraju, A. S. Chaudhury, J. Wang, R. Williams, J. R. Unruh, C. H. Greenberg, E. Y. Jacobs, Z. Yu, M. J. de la Cruz, R. Mironska, D. L. Stokes, J. D. Aitchison, M. F. Jarrold, J. L. Gerton, S. J. Ludtke, C. W. Akey, B. T. Chait, A. Sali, and M. P. Rout, *Integrative structure and functional anatomy of a nuclear pore complex*, *Nature* **555**, 475 (2018).
- [69] N. Driessen, Arnold J. M. and Nouwen, *Protein Translocation Across the Bacterial Cytoplasmic Membrane*, *Annu. Rev. Biochem.* **77**, 643 (2008).
- [70] T. A. Baker and R. T. Sauer, *ClpXP, an ATP-powered unfolding and protein-degradation machine*, *Biochimica et Biophysica Acta - Molecular Cell Research* **1823**, 15 (2012).
- [71] A. H. Delcour, *Electrophysiology of Unconventional Channels and Pores*, Vol. 18 (Springer, 2015) pp. 75–100.
- [72] T. Sugawara, D. Yamashita, K. Kato, Z. Peng, J. Ueda, J. Kaneko, Y. Kamio, Y. Tanaka, and M. Yao, *Structural basis for pore-forming mechanism of staphylococcal α -hemolysin*, *Toxicon* **108**, 226 (2015).
- [73] S. Wang, Z. Ji, E. Yan, F. Haque, and P. Guo, *Three-step channel conformational changes common to DNA packaging motors of bacterial viruses T3, T4, SPPI, and Phi29*, *Virology* **500**, 285 (2017).

- [74] L. Xue, H. Yamazaki, R. Ren, M. Wanunu, A. P. Ivanov, and J. B. Edel, *Solid-state nanopore sensors*, *Nature Reviews Materials* (2020), 10.1038/s41578-020-0229-6.
- [75] S. Wang, Z. Zhao, F. Haque, and P. Guo, *Engineering of protein nanopores for sequencing, chemical or protein sensing and disease diagnosis*, *Current Opinion in Biotechnology* **51**, 80 (2018).
- [76] H. Ramezani and H. Dietz, *Building machines with DNA molecules*, *Nature Reviews Genetics* **21**, 5 (2020).
- [77] Z. Siwy and A. Fuliński, *Fabrication of a Synthetic Nanopore Ion Pump*, *Physical Review Letters* **89**, 4 (2002).
- [78] J. R. Burns, A. Seifert, N. Fertig, and S. Howorka, *A biomimetic DNA-based channel for the ligand-controlled transport of charged molecular cargo across a biological membrane*, *Nature Nanotechnology* **11**, 152 (2016).
- [79] T. Jovanovic-Talisman and A. Zilman, *Protein Transport by the Nuclear Pore Complex: Simple Biophysics of a Complex Biomachine*, *Biophysical Journal* **113**, 6 (2017).
- [80] T. Jovanovic-Talisman, J. Tetenbaum-Novatt, A. S. McKenney, A. Zilman, R. Peters, M. P. Rout, and B. T. Chait, *Artificial nanopores that mimic the transport selectivity of the nuclear pore complex*, *Nature* **457**, 1023 (2009).
- [81] S. W. Kowalczyk, L. Kapinos, T. R. Blosser, T. Magalhães, P. van Nies, R. Y. H. Lim, and C. Dekker, *Single-molecule transport across an individual biomimetic nuclear pore complex*, *Nature Nanotechnology* **6**, 433 (2011).
- [82] A. N. Ananth, A. Mishra, S. Frey, A. Dwarkasing, R. Versloot, E. van der Giessen, D. Görlich, P. Onck, and C. Dekker, *Spatial structure of disordered proteins dictates conductance and selectivity in nuclear pore complex mimics*, *eLife* **7**, 1 (2018).
- [83] P. Ketterer, A. N. Ananth, D. S. Laman Trip, A. Mishra, E. Bertosin, M. Ganji, J. Van Der Torre, P. Onck, H. Dietz, and C. Dekker, *DNA origami scaffold for studying intrinsically disordered proteins of the nuclear pore complex*, *Nature Communications* **9**, 1 (2018).
- [84] P. D. E. Fisher, Q. Shen, B. Akpınar, L. K. Davis, K. K. H. Chung, D. Baddeley, A. Šarić, T. J. Melia, B. W. Hoogenboom, C. Lin, and C. P. Lusk, *A Programmable DNA Origami Platform for Organizing Intrinsically Disordered Nucleoporins within Nanopore Confinement*, *ACS Nano* **12**, 1508 (2018).
- [85] S. O. Kelley, *What Are Clinically Relevant Levels of Cellular and Biomolecular Analytes?* *ACS Sensors* **2**, 193 (2017).
- [86] K. J. Freedman, L. M. Otto, A. P. Ivanov, A. Barik, S.-H. Oh, and J. B. Edel, *Nanopore sensing at ultra-low concentrations using single-molecule dielectrophoretic trapping*, *Nature Communications* **7**, 10217 (2016).

- [87] J. D. Spitzberg, X. F. van Kooten, M. Bercovici, and A. Meller, *Microfluidic device for coupling isotachophoretic sample focusing with nanopore single-molecule sensing*, *Nanoscale* **12**, 17805 (2020).
- [88] K. Tian, X. Chen, B. Luan, P. Singh, Z. Yang, K. S. Gates, M. Lin, A. Mustapha, and L.-Q. Gu, *Single Locked Nucleic Acid-Enhanced Nanopore Genetic Discrimination of Pathogenic Serotypes and Cancer Driver Mutations*, *ACS Nano* **12**, 4194 (2018).
- [89] Y. Wang, K. Tian, R. Shi, A. Gu, M. Pennella, L. Alberts, K. S. Gates, G. Li, H. Fan, M. X. Wang, and L.-Q. Gu, *Nanolock–Nanopore Facilitated Digital Diagnostics of Cancer Driver Mutation in Tumor Tissue*, *ACS Sensors* **2**, 975 (2017).
- [90] N. Burck, T. Gilboa, A. Gadi, M. Patkin Nehrer, R. J. Schneider, and A. Meller, *Nanopore Identification of Single Nucleotide Mutations in Circulating Tumor DNA by Multiplexed Ligation*, *Clinical Chemistry* (2021), 10.1093/clinchem/hvaa328.
- [91] J. Y. Sze, A. P. Ivanov, A. E. Cass, and J. B. Edel, *Single molecule multiplexed nanopore protein screening in human serum using aptamer modified DNA carriers*, *Nature Communications* **8**, 1 (2017).
- [92] S. Cai, J. Y. Y. Sze, A. P. Ivanov, and J. B. Edel, *Small molecule electro-optical binding assay using nanopores*, *Nature Communications* **10**, 1797 (2019).
- [93] M. A. Fahie, B. Yang, M. Mullis, M. A. Holden, and M. Chen, *Selective Detection of Protein Homologues in Serum Using an OmpG Nanopore*, *Analytical Chemistry* **87**, 11143 (2015).
- [94] A. K. Thakur and L. Movileanu, *Single-Molecule Protein Detection in a Biofluid Using a Quantitative Nanopore Sensor*, *ACS Sensors* **4**, 2320 (2019).
- [95] Y. Wang, D. Zheng, Q. Tan, M. X. Wang, and L.-Q. Gu, *Nanopore-based detection of circulating microRNAs in lung cancer patients*, *Nature Nanotechnology* **6**, 668 (2011).
- [96] J. Mathé, H. Visram, V. Viasnoff, Y. Rabin, and A. Meller, *Nanopore Unzipping of Individual DNA Hairpin Molecules*, *Biophysical Journal* **87**, 3205 (2004).
- [97] Y. Rozevsky, T. Gilboa, X. F. van Kooten, D. Kobelt, D. Huttner, U. Stein, and A. Meller, *Quantification of mRNA Expression Using Single-Molecule Nanopore Sensing*, *ACS Nano* **14**, 13964 (2020).

5

A DESIGNER FG-NUP THAT RECONSTITUTES THE SELECTIVE TRANSPORT BARRIER OF THE NUCLEAR PORE COMPLEX

Nuclear Pore Complexes (NPCs) regulate bidirectional transport between the nucleus and the cytoplasm. Intrinsically disordered FG-Nups line the NPC lumen and form a selective barrier, where transport of most proteins is inhibited whereas specific transporter proteins freely pass. The mechanism underlying selective transport through the NPC is still debated. Here, we reconstitute the selective behaviour of the NPC bottom-up by introducing a rationally designed artificial FG-Nup that mimics natural Nups. Using QCM-D, we measure selective binding of the artificial FG-Nup brushes to the transport receptor Kap95 over cytosolic proteins such as BSA. Solid-state nanopores with the artificial FG-Nups lining their inner walls support fast translocation of Kap95 while blocking BSA, thus demonstrating selectivity. Coarse-grained molecular dynamics simulations highlight the formation of a selective meshwork with densities comparable to native NPCs. Our findings show that simple design rules can recapitulate the selective behaviour of native FG-Nups and demonstrate that no specific spacer sequence nor a spatial segregation of different FG-motif types are needed to create selective NPCs.

This chapter has been published as: Alessio Fragasso, Hendrik W. de Vries, John Andersson, Eli O. van der Sluis, Erik van der Giessen, Andreas Dahlin, Patrick R. Onck, Cees Dekker. *A designer FG-Nup that reconstitutes the selective transport barrier of the Nuclear Pore Complex*. Nature Communications 12, 2010 (2021) [1].

5.1. INTRODUCTION

Nucleocytoplasmic transport is orchestrated by the Nuclear Pore Complex (NPC), which imparts a selective barrier to biomolecules [2, 3]. The NPC is a large eightfold-symmetric protein complex (with a size of ~52 MDa in yeast and ~112 MDa in vertebrates) that is embedded within the nuclear envelope and comprises ~30 different types of Nucleoporins (Nups) [4, 5]. Intrinsically disordered proteins, termed FG-Nups, line the central channel of the NPC. FG-Nups are characterized by the presence of phenylalanine-glycine (FG) repeats separated by spacer sequences [6] and they are highly conserved throughout species [7]. FG-Nups carry out a dual function: By forming a dense barrier (100-200 mg/mL) within the NPC lumen, they allow passage of molecules in a selective manner [8–11]. Small molecules can freely diffuse through, whereas larger particles are generally excluded [12]. At the same time, FG-Nups mediate the transport of large NTR-bound (Nuclear Transport Receptor) cargoes across the NPC through transient hydrophobic interactions between FG repeats and hydrophobic pockets on the convex side of NTRs [13]. Various models have been developed in order to connect the physical properties of FG-Nups to the selective properties of the NPC central channel, e.g. the ‘virtual-gate’ [14], ‘selective phase’ [15, 16], ‘reduction of dimensionality’ [17], ‘kappacentric’ [18–20], ‘polymer brush’ [21], and ‘forest’ [6] models. No consensus on the NPC transport mechanisms has yet been reached.

The NPC is highly complex in its architecture and dynamics, being constituted by many different Nups that simultaneously interact with multiple transiting cargoes and NTRs. In fact, the NTRs with their cargoes may amount to almost half of the mass of the central channel, so they may be considered an intrinsic part of the NPC3. These NPC properties complicate in-vivo studies [4, 22–24], for which it is very challenging to identify contributions coming from individual FG-Nups [25, 26]. On the other hand, in-vitro approaches to study nucleocytoplasmic transport using biomimetic NPC systems [18, 27–33] have thus far been limited to single native FG-Nups and mutations thereof, attempting to understand the physical behaviour of FG-Nups and their interactions with NTRs. The reliance on a few selected Nups from yeast or humans in these studies with sequences that evolved over time in different ways for each of these specific organisms makes it difficult to pinpoint the essential and minimal properties that provide FG-Nups with their specific selective functionality.

Here, we describe a bottom-up approach to studying nuclear transport selectivity, where we rationally design, synthesize, and assess artificial FG-Nups with user-defined properties that are set by an amino acid sequence that is chosen by the user. With this approach we address the question: can we build a synthetic protein that mimics the selective behaviour of native FG-Nups? By combining experiments and coarse-grained molecular dynamics simulations, we illustrate the design and synthesis of an artificial 311-residue long FG-Nup, which we coin NupX, and characterize its selective behaviour with respect to Kap95 (a well-characterized NTR from yeast, 95 kDa) versus Bovine Serum Albumin (BSA, 66 kDa). Firstly, we explore the interactions between Kap95 and NupX brushes with varying grafting densities using quartz crystal microbalance with dissipation monitoring (QCM-D), finding that NupX brushes bind Kap95 while showing no binding to BSA. We confirm this finding by calculating the potential of mean force (PMF) associated with the entry of Kap95 or an inert cargo into NupX brushes. Secondly,

we explore the transport properties of NupX-functionalized solid-state nanopores and show that NupX-lined pores constitute a selective transport barrier. Similar to FG-Nups previously studied with the same technique [29, 31], the NPC-mimicking nanopores allow fast and efficient passage of Kap95 molecules, while blocking transport of BSA. Coarse-grained MD simulations of NupX-functionalized nanopores highlight the formation of a dense FG-rich meshwork with similar protein densities as in native NPCs, which excludes inert molecules but allows entry and passage of Kap95.

The current work provides the proof of concept that a designer FG-Nup can reconstitute NPC-like selectivity, and the results show that no specific spacer sequence nor a spatial segregation of different FG-motifs (as observed in recent work [4, 34]) are required for achieving selectivity. This work lays the foundation for multiple future directions in follow-up work as the approach opens the route to systematically study the essential microscopic motifs that underlie the unique selectivity of NPCs.

5.2. RESULTS

5.2.1. DESIGN OF THE SYNTHETIC NUPX

In the design of our synthetic NupX protein, we aim to reconstitute nuclear transport selectivity while operating under a minimal set of simple design rules. The design procedure that we outline below uses the following four rules: i) we design a protein that incorporates the physical properties of GLFG-Nups (a specific class of essential FG Nups that are particularly cohesive and contain many GLFG-motifs), ii) it comprises two parts, with a cohesive domain at one end and a repulsive domain at the other end, where each domain is characterized by the ratio C/H of the number of charged and the number of hydrophobic residues, iii) FG and GLFG motifs are present in an alternating and uniformly spaced fashion within the protein's cohesive domain, and iv) the protein is intrinsically disordered throughout its full length, similar to native FG-Nups.

We implemented our design rules in a step-wise design process as follows: First, we selected and analysed an appropriate set of native FG-Nups (design rule i), namely GLFG-Nups, which differ from other FG-Nups in terms of the type of FG repeats and the properties of the spacer regions¹¹. The emphasis on GLFG-Nups follows from their localization in the central channel [4] of the yeast NPC (Figure 5.1a), where they strongly contribute to the nuclear transport selectivity. Indeed, a small subset of GLFG-Nups (*e.g.*, either Nup100 or Nup116 in combination with Nup145N) was shown to be essential and sufficient for cell viability [22, 35]. To derive the amino acid content of NupX, we therefore characterized the archetypical GLFG-Nup sequence by determining the amino acid content of the disordered regions of Nup49, Nup57, Nup145N, Nup116, and Nup100 from yeast. Of these, the most essential GLFG-Nups (*i.e.* Nup100, Nup116, and Nup145N) comprise a collapsed domain with a low C/H -ratio and abundance of FG/GLFG repeats, and an extended domain with a high C/H -ratio and absence of FG repeats [6]5. This distinction is highlighted in Figures 5.1b, 5.2a, where non-FG/GLFG/charged residues are highlighted in light green and pink for the collapsed and extended domains in respectively – a colouring scheme used throughout this work. The division into two domains of these essential GLFG-Nups led us to phrase design rule ii in our design process of NupX, with each domain comprising ~150 amino acid residues (see Figures 5.1b,

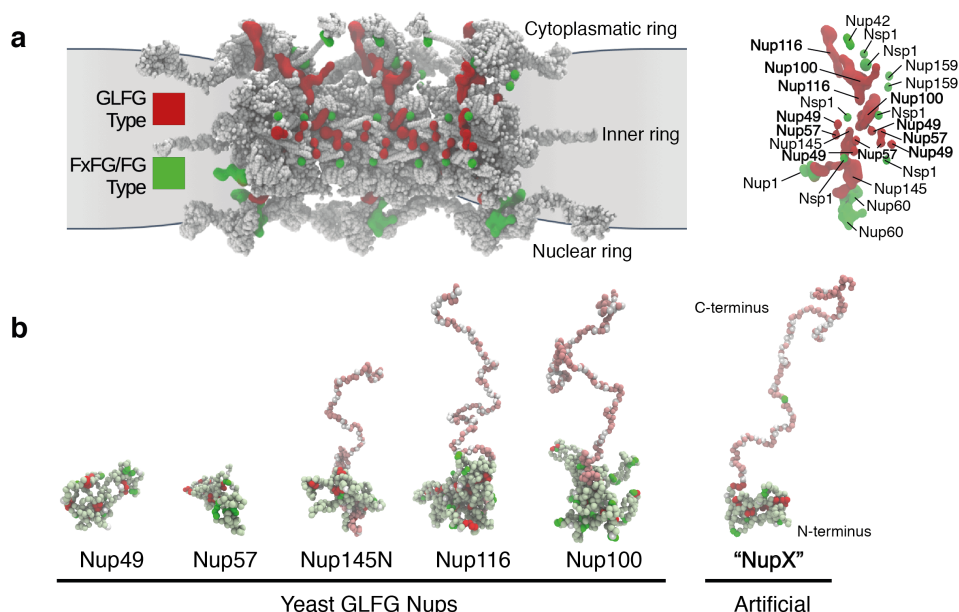


Figure 5.1: *De novo* design of an artificial FG-Nup. **a**, Left: Frontal view on three spokes of the *Saccharomyces cerevisiae* NPC (PDB-DEV, entries 11 and 12, Ref.[4]) that shows how the GLFG-Nups (red) are predominantly anchored in the inner ring, as opposed to the FxFG/FG-Nups (green). Right: Anchoring points of individual Nups in a single spoke. The GLFG-Nups Nup100, Nup116, Nup49, and Nup57 (red) contribute strongly to the permeability barrier of the NPC3, where Nup100 and Nup116 are known to be indispensable for NPC viability [22, 35]. This image and other visualizations of protein structures were rendered using VMD [36]. **b**, Simulation snapshots of isolated native yeast GLFG-Nups at one amino acid resolution. The conformations of Nup145N, Nup116, Nup100 highlight a bimodality of the Nups [6], with a collapsed and extended domain. FG repeats, GLFG repeats, and charged residues are displayed in bright green, red, and white, respectively. Other amino acids in the cohesive and extended domains are depicted in light green and pink, respectively. NupX adopts the same bimodal conformations as essential GLFG-Nups Nup100 and Nup116.

5.2a). Whereas the extended domain of NupX is of quite similar length to the corresponding extended domains of Nup100, Nup116 and Nup145N (190 residues on average), the cohesive domain is notably shorter than the collapsed domains of native GLFG-Nups (390 residues on average).

Assigning the amino acid (AA) content to NupX, as derived from the sequence information of the GLFG-Nups, was performed separately for the two domains: we computed the cumulative amino acid contents (excluding FG and GLFG motifs) for both the collapsed domains of all five GLFG-Nups, and for the extended domains of Nup100, Nup116 and Nup145N (design rule ii). Upon normalizing for the total length of the collapsed or extended domains of all native GLFG-Nups, this analysis resulted in the distributions presented in 5.2b, plotted separately for the collapsed (light green, top) and the extended (light red, bottom) domains. Based on these histograms, we assigned amino acids to the collapsed and extended domains of NupX separately. Following design rule iii, we then placed FG and GLFG repeats in the collapsed domain with a fixed spacer

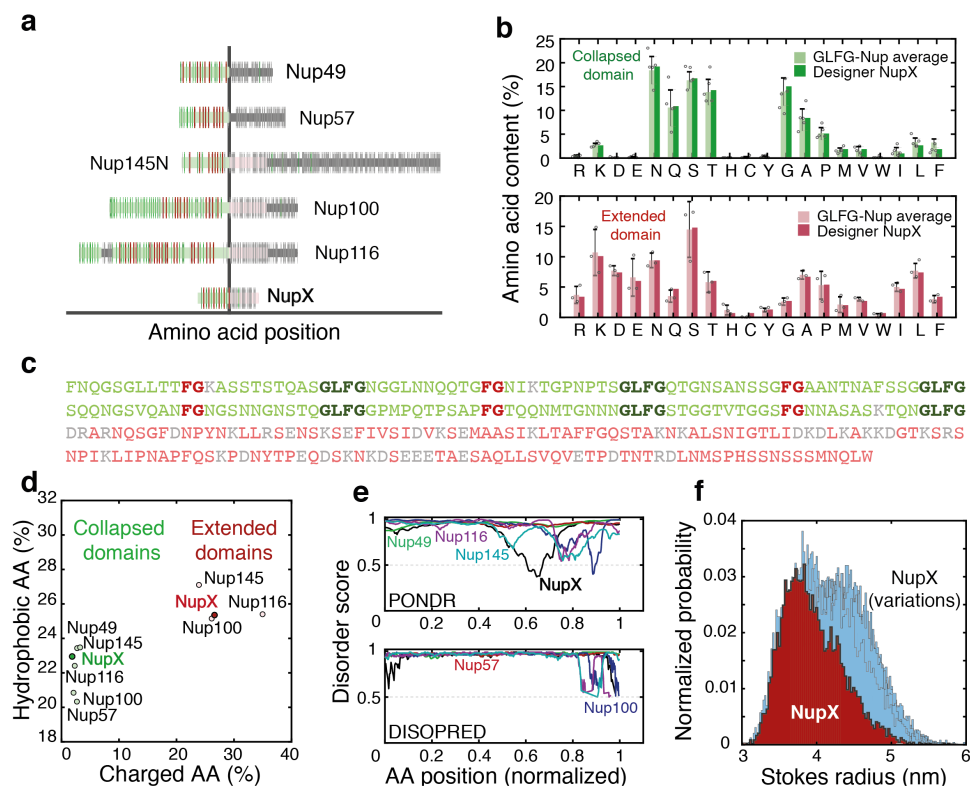


Figure 5.2: a, Comparison of the full-length sequences between yeast GLFG-Nups and NupX. Sequence highlights follow the colour-scheme of Fig.5.1b, folded domains are indicated in dark-grey. b, Amino acid contents of yeast GLFG-Nups (averaged) and NupX for the collapsed (top panel) and extended (bottom panel) domains. Bar heights denote the average amino acid fraction within GLFG-Nup domains, where N=5 (all GLFG-Nups) for the collapsed domain and N=3 (Nup100, Nup116, Nup145) for the extended domain. Error bars indicate standard deviations in the average occurrence of amino acids. FG and GLFG-motifs were excluded from this analysis. c, Sequence of NupX, following the colour scheme of figures 5.1b and panel a. FG and GLFG repeats are spaced by 10 residues in the cohesive domain. d, Charge-and-hydrophobicity plot of NupX and yeast GLFG-Nup domains. For both the collapsed (green shading) and extended (red shading) domains, the charged and hydrophobic amino acid contents of NupX agree with the properties of individual GLFG-Nups. e, Disorder prediction scores for the unfolded domains of GLFG-Nups (coloured lines) and full-length NupX (black curve) from two different predictors (see Materials and Methods). Disorder prediction scores higher than 0.5 (dashed line) count as fully disordered. f, Distribution of Stokes radii from 10 μ s of coarse-grained molecular dynamics simulations for NupX (red) and 25 design variations (light blue). NupX is, on average, slightly more compacted than other design variants.

length of 10 AAs. This value was chosen based on the spacer length of ~5-15 AAs in native GLFG-Nups. An analysis of the charged and hydrophobic amino acid content of the domains of NupX and native GLFG-Nups shows that the assigned sequence properties are indeed reproduced by our design method (Figure 5.2d). Finally, the sequences of the collapsed and extended domains of NupX were repetitively shuffled (except for the FG and GLFG motifs that we kept fixed) until a desirable level of disorder was achieved

(design rule iv), as predicted by PONDR[37] and DISOPRED [38, 39] (Figure 5.2e). This resulted in the NupX sequence shown in Figure 5.2c. Whereas PONDR predicts one short folded segment between residues 189 and 209 (normalized position of 0.65 in Figure 5.2e), additional structure prediction [40] (Materials and Methods) did not yield any high-confidence folded structures for this segment.

To assess the robustness of our design procedure, we tested how permutations of the NupX sequence (which shuffle amino acids while retaining the FG/GLFG sequences and the definition of both domains) affect the Stokes radius R_s , as computed from 1-bead-per-amino-acid MD-simulations developed for intrinsically disordered proteins (Figure 5.2f, see Materials and Methods). We found that over 25 different designs for NupX (Table S5.2) yielded an average R_s of 4.2 ± 0.2 nm (errors are S.D.). This is close to the simulated (3.9 ± 0.4 nm) and measured (3.7 ± 1.1 nm by DLS, Table S5.1) R_s value of the NupX protein design (Figure 5.2c).

Summing up, using a minimal set of rules, we designed a NupX protein that incorporates the average properties that characterize GLFG-Nups [6, 12]. Moreover, by creating 25 different designs that all showed similar behaviour in our simulations, we showed that the physical properties such as the Stokes radius and the division of NupX into a cohesive and repulsive domain are recovered in a reliable way.

5.2.2. QCM-D EXPERIMENTS AND MD SIMULATIONS SHOW SELECTIVE BINDING OF KAP95 TO NUPX BRUSHES

To assess the interaction between NupX and Kap95, we employed a Quartz-Crystal-Microbalance with Dissipation monitoring (QCM-D), with gold-coated quartz chips and phosphate-buffered saline (PBS, pH 7.4) as running buffer, unless stated otherwise. First, C-terminus-thiolated NupX molecules were injected into the chamber at a constant flow-rate ($20 \mu\text{L}/\text{min}$) where they chemically reacted with the gold surface. Binding of NupX to the gold surface could be monitored in real-time by measuring the shift in resonance frequency Δf of the quartz chip (Figure 5.3a). We applied the NupX coating by administering a protein concentration ranging from 100 nM to $2 \mu\text{M}$ (Figure S5.92) until a plateau in the frequency shift was reached, which typically occurred after ~ 1 hr of incubation. To gain insight into the areal mass density of the deposited layers, we employed Surface Plasmon Resonance (SPR) measurements (Figure S5.10), where we used the same coating protocol for consistency. From these measurements of the areal mass density, we found grafting distances of 7.7 ± 0.5 nm (mean \pm S.D.) for chips incubated with a 60 nM NupX solution, and 2.91 ± 0.02 nm (mean \pm S.D.) for $2 \mu\text{M}$. In determining the grafting density from the areal mass density, we assumed a triangular lattice (since an equilateral triangulated (sometimes also denoted as hexagonal) lattice is the densest type of packing that can be described by a unique length scale that sets the grafting density). Figure 5.3a shows a typical frequency shift over time for the binding of $1 \mu\text{M}$ NupX to a gold surface. After the Nup-layer was formed, a 1-mercapto-11-undecyltetra(ethyleneglycol) molecule (MUTEG), which is expected to form a ~ 2 nm thin passivating film [18], was added to passivate any remaining bare gold that was exposed in between NupX molecules (Figure S5.11). This minimizes unintentional interactions between Kap95 and gold for subsequent binding experiments (Figure S5.12) [18, 19, 41].

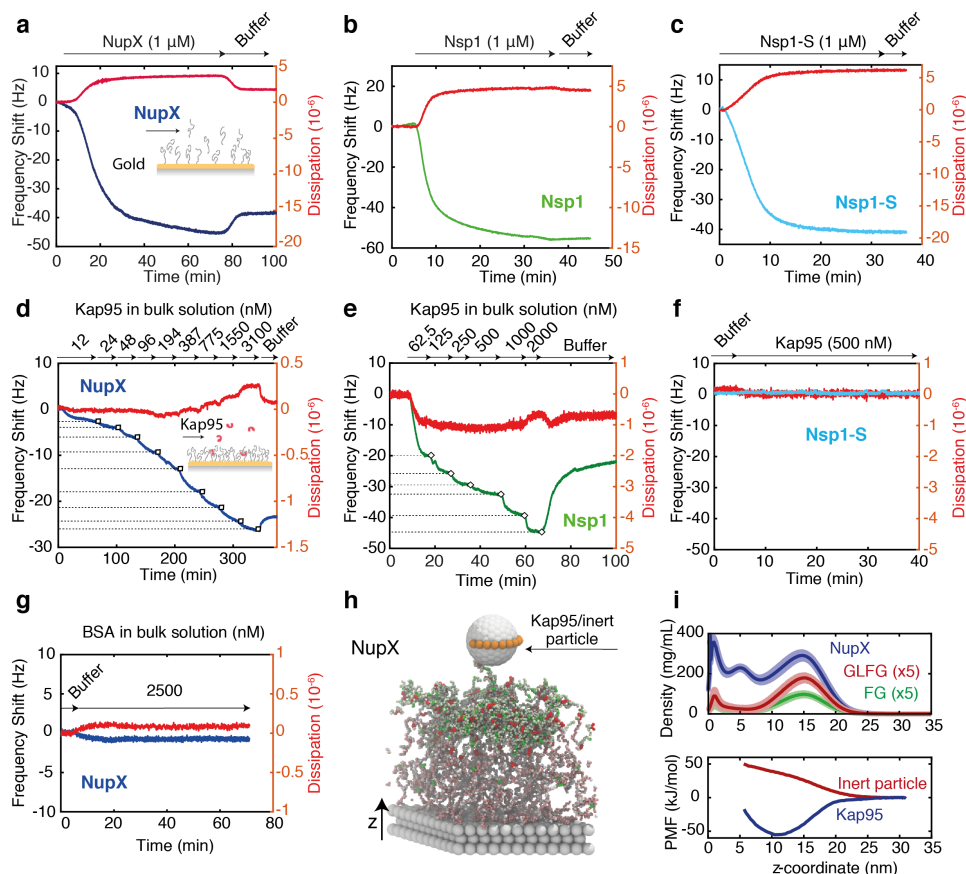


Figure 5.3: Binding affinity of Kap95 to NupX, Nsp1 and Nsp1-S brushes, using QCM-D and MD simulations. a-c, Change in frequency shift upon coating of gold surface with NupX (dark blue), Nsp1 (green), and Nsp1-S (light blue) proteins, respectively, at 1 μ M protein concentration. Red curves indicate the corresponding shift in dissipation. d-f, Change in frequency shift upon titration of Kap95 (with concentration in the range \sim 10-3000 nM) on NupX (dark blue), Nsp1 (green), and Nsp1-S (light blue) coated surfaces. Numbers indicate the concentration in nM of Kap95 for each titration step. Large changes in frequency shift are observed for NupX and Nsp1, whereas no detectable shift is measured for Nsp1-S. Red curves indicate the corresponding shift in dissipation. g, Frequency (dark blue) and dissipation (red) shift upon adsorption of 2.5 μ M BSA onto the NupX-coated sensor. h, Side-view snapshot of the umbrella sampling simulation setup for a NupX brush with 4.0 nm grafting distance, where a model Kap95 particle (8.5 nm diameter grey sphere with binding sites depicted in brown) or inert particle (7.5 nm diameter, not shown) is restrained along different z-coordinates. Scaffold beads are shown in grey, NupX proteins follow the same colour scheme as presented in Figure 5.1b. i, Top panel: Time and laterally averaged protein density distributions for the NupX brushes (blue) and for the FG-motifs (green) and GLFG-motifs (red) present inside the NupX brushes with a grafting distance of 4.0 nm. The density profiles of the GLFG and FG motifs within the NupX brush are multiplied by 5 for clarity. Dark central lines and light shades indicate the mean and standard deviation in density profiles, respectively. These measures were obtained by averaging over the density profiles of trajectory windows 50 ns in length ($N=60$). High-density regions (up to almost 400 mg/mL) form near the attachment sites ($z = 0$ to 2 nm) and near the free surface of the brush layer (at $z \sim 15$ nm). FG and GLFG-motifs predominantly localize near the free surface of the brush. Bottom: Free-energy profiles (PMF-curves) of the center of mass of the 8.5 nm-sized model Kap95 (blue) and inert particle (red) along the z-coordinate, where $z = 0$ coincides with the substrate. The difference in sign between the PMF-curves of both particles indicates a strong preferential adsorption of the model Kap95 to NupX brushes and a repulsive interaction with the inert particle.

After thus setting up a NupX-coated layer, we flushed in Kap95 at stepwise increasing concentrations (~ 10 – 3000 nM, Figure 5.3d) and monitored binding to the NupX-coated surface. We observed a clear concentration-dependent amount of Kap95 molecules bound to the NupX brush. For reference, we repeated the experiment on brushes of Nsp1 (a native FG-Nup from yeast), as well as Nsp1-S, a Nsp1-mutant where the hydrophobic amino acids F, I, L, V are replaced by the hydrophilic amino acid Serine (S) (Figure 5.3b,c). The latter was employed as a negative control since it is expected to not bind Kap95 due to the lack of FG repeats [15, 16]. Gold surfaces coated with Nsp1 or Nsp1-S were characterized with SPR under similar coating conditions as for QCM-D, yielding grafting distances of 4.9 ± 0.1 nm for Nsp1 and 5.8 ± 0.4 nm for Nsp1-S. Upon flushing Kap95, we found, consistent with previous studies [28, 41], a concentration-dependent adsorption to Nsp1 brushes (Figure 5.3e), whereas we did not observe any detectable interaction between Kap95 and Nsp1-S (Figure 5.3f). The latter is consistent with the lack of FG repeats in the Nsp1-S sequence which makes the Nsp1-S film devoid of binding sites for Kap95. We note that non-linear effects, *e.g.*, coverage-dependent changes in water entrapment within the layer [42], as well as mass transport limitations inherent to the QCM-D technique [41] are likely to affect the observed binding kinetics, which, together with a relatively slow dissociation of Kap95 from both the NupX and Nsp1 brushes, lead us to refrain from extracting a dissociation constant. Adsorbed molecules could be completely removed upon flushing 0.2 M NaOH however (Figure S5.13). Finally, we investigated whether the inert molecule BSA could bind to the NupX brush. Upon flushing 2.5 μ M of BSA (Figure 5.3g) we did not observe any appreciable change in the resonance frequency, indicating that the NupX brush efficiently excludes these inert molecules. This measurement was repeated for all the grafting conditions used in this study (Figure S5.14) showing that BSA did not produce any detectable shift in frequency, while Kap95 showed clear binding to the NupX films. Importantly, the data show that the NupX brush selectively interacts with Kap95 over a range of grafting densities.

In order to study the morphology and physical properties of NupX brushes at the microscopic level, we employed coarse-grained molecular dynamics (MD) simulations (see Materials and Methods), which resolved the density distribution within the NupX brush layer and the preferential adsorption of Kap95 over inert molecules of similar size such as BSA. 36 NupX proteins were tethered on a triangular lattice with a fixed spacing of 4.0 nm (Figure 5.3h) or 5.7 nm (Figure S5.18), well in the range of grafting distances from 2.9 nm to 7.7 nm as measured by SPR. Averaged over a simulation time of 3 μ s, we found that the NupX brushes with a 4.0 nm grafting distance form a laterally homogeneous meshwork with densities ranging from ~ 400 mg/mL near the substrate to around ~ 200 mg/mL in the central region and to ~ 300 mg/mL near the free surface of the brush (Figure 5.3i, top panel). The interface near the free surface of the brush contains the highest relative concentration of FG and GLFG motifs (see Figure 5.3i, top panel). Notably, the protein density throughout the brush is of the same order of magnitude as the density obtained in simulations of the yeast NPC [43]. Upon increase of the grafting distance to 5.7 nm, we find that the NupX brush attains different and less dense conformations: the density profile plateaus at a value of 170 mg/mL and slowly decays without showing a peak density near the free surface of the brush (Figure S5.18). We translated our density profiles into height estimates in a similar fashion as other computation efforts on FG-

Nup brushes [44, 45]. We consider the z -coordinates at which 90% of the protein mass is incorporated as the effective brush heights. This approach yields brush heights of 12 and 18 nm for the NupX brushes with 5.7 and 4.0 nm grafting distances, respectively. These values coincide quite well with the inflection point of the decaying tail of the density profiles in Figures 5.3l and Figure S5.18.

The simulated density profiles yield notably higher brushes than expected from the Sauerbrey equation: For example, assuming a density of the hydrated brush of ~ 1.05 g/mL45, one can estimate a brush height of 6.4 nm for the NupX brush in Figure 5.3a (that was incubated at 1 μ M, which we expect to have a grafting distance at the higher end of the values used in our simulations). Importantly, however, the Sauerbrey equation does not account for viscoelastic effects and only provides a lower limit to the brush height [42]. Indeed, given the dissipation-to-frequency ratio of $\sim 0.045 \times 10^{-6}$ Hz $^{-1}$ (Figure S5.16), one expects that the actual experimental brush height will be larger than 6.4 nm, an effect also seen in other QCM-D studies of FG-Nups [28, 46]. Notably, a quantitative difference between the NupX brush height estimations of the computational and experimental results does not affect the major conclusions of the study, namely the selective transport across biomimetic nanopores with a rationally designed artificial FG-Nup and the selective binding of Kap95 over BSA to NupX.

To assess the selective properties of the NupX brushes, we performed umbrella sampling simulations of the adsorption of Kap95 and an inert molecule to NupX brushes (Materials and Methods), again for two grafting densities of 4 nm and 5.7 nm. We modelled Kap95 (Figure S5.19) as an 8.5 nm sized sterically repulsive (*i.e.*, modelling only repulsive, excluded volume interactions) particle with 10 hydrophobic binding sites [9, 31, 47, 48] and a total net charge similar to that of Kap95 (−43e). The inert molecule was modelled as a sterically inert spherical particle of 7.5 nm diameter [11]. We obtained potential-of-mean-force (PMF) curves associated with the adsorption of Kap95 and inert particles by means of the weighted histogram analysis method (WHAM)[49]. We found that for the dense brush (4.0 nm grafting density), a significant (−52 kJ/mol) negative free energy is associated with the entry of Kap95 in the NupX brush, as is visible in Figure 5.3i (bottom panel). By contrast, the PMF curve of the inert particle steeply increased when the protein entered into the NupX meshwork, showing that adsorption of non-specific proteins of comparable size as Kap95 will not occur. The large free energy differences between Kap95 (corresponding to \sim nM binding affinity) and inert particle adsorption qualitatively support the experimental findings. When increasing the grafting distance to 5.7 nm, the inert particle and Kap95 protein are repelled and adsorbed less strongly (μ M binding affinity, similar to other *in vitro* works [19, 50]), respectively (Figure S5.18). The data indicate that dense brushes bind more strongly to Kap95 and that selectivity is maintained for less densely coated NupX brushes, which is in line with our experimental observation of selective adsorption in chips coated with NupX brushes of varying grafting densities (Figure S5.14).

5.2.3. SINGLE-MOLECULE TRANSLOCATION EXPERIMENTS WITH NUPX-COATED NANOPORES DEMONSTRATE SELECTIVITY

In order to test whether our synthetic FG-Nup do indeed form a transport barrier that mimics the selective properties of the NPC, we performed electrophysiological exper-

iments on biomimetic nanopores [29, 31]. These NPC mimics were built by tethering NupX proteins to the inner walls of a solid-state SiN_x nanopore [51] using Self-Assembled-Monolayer (SAM) chemistry (details in Materials and Methods). Solid-state nanopores of 10–60 nm in diameter were fabricated onto a glass-supported [52] SiN_x free-standing membrane by means of TEM drilling. A buffer with 150 mM KCl, 10 mM Tris, 1 mM EDTA, at pH 7.5 was used to measure the ionic conductance through the pores, while retaining near-physiological conditions. Coating bare SiN_x pores with NupX yielded a significant decrease in conductance (*e.g.* ~50% for ~30 nm diameter SiN_x pores) of the bare-pore values, as estimated by measuring the through-pore ionic current before and after the functionalization (Figure S5.20). Additionally, the current-voltage characteristic in the ± 200 mV range (Figure S5.20) is linear both for the bare and NupX-coated pores, indicating that the NupX meshwork is not affected by the applied electric field at the 100 mV operating bias. To obtain more information on the NupX-coating process of our SiN_x pores, we repeated the same functionalization procedure on silica-coated SPR chips (Figure S5.10), where APTES, Sulfo-SMCC, and NupX coatings were independently characterized using the same coating protocol as for the SiN_x nanopores, for consistency. From these experiments, we estimate an average grafting distance of 5.4 ± 1.1 nm between adjacent NupX molecules. Measurements of the ionic current through NupX-coated pores revealed a higher $1/f$ noise in the current (Figure S5.21) compared to bare pores, which we attribute to random conformational fluctuations of the Nups within the pore volume and access region [53, 54], similar to findings from previous studies on biomimetic nanopores [29, 31].

To test the selective behaviour of the biomimetic nanopore, we measured translocation rates of Kap95 and BSA through bare pores of ~30–35 nm in diameter (Figure 5.4a). Figure 5.4c shows examples of raw traces recorded for a 30 nm pore under 100 mV applied bias, when either only buffer (top), 450 nM Kap95 (middle), or 2.8 μ M BSA (bottom) were added to the cis-chamber. As expected, we observed transient dips in the current through the bare pore upon injection of the proteins, which we attribute to single-molecule translocations of the analyte molecules. As is typical in nanopore experiments, translocation events yield current blockades with a characteristic amplitude and dwell time, where the former relates to the size of the molecule occupying the pore and the latter generally depends on specific interaction between the translocating molecule and the pore wall[55]. Next, we repeated the experiment under identical conditions on the same pore after coating with NupX took place (Figure 5.4b). Examples of typical raw traces are shown in Figure 5.4d. Strikingly, Kap95 molecules could still translocate efficiently through the NupX-coated pore, whereas BSA molecules were practically blocked from transport.

Figures 5.4e–f show scatter plots of the event distributions, where the conductance blockade is plotted against dwell time for all translocation events. For the bare pore, we observe similar average amplitudes of 0.24 ± 0.09 nS and 0.20 ± 0.05 nS (errors are s.d.) for BSA and Kap95, respectively. For the NupX-coated pore, we found slightly larger but again mutually similar event amplitudes of 0.31 ± 0.03 nS and 0.27 ± 0.03 nS for BSA and Kap95, respectively. We found comparable translocation times through the bare pore of 0.66 ± 0.03 ms and 0.81 ± 0.02 ms (errors are s.e.m) for BSA and Kap95, respectively. For the coated pore, however, we measured longer dwell times of 5.0 ± 0.5 ms and $1.9 \pm$

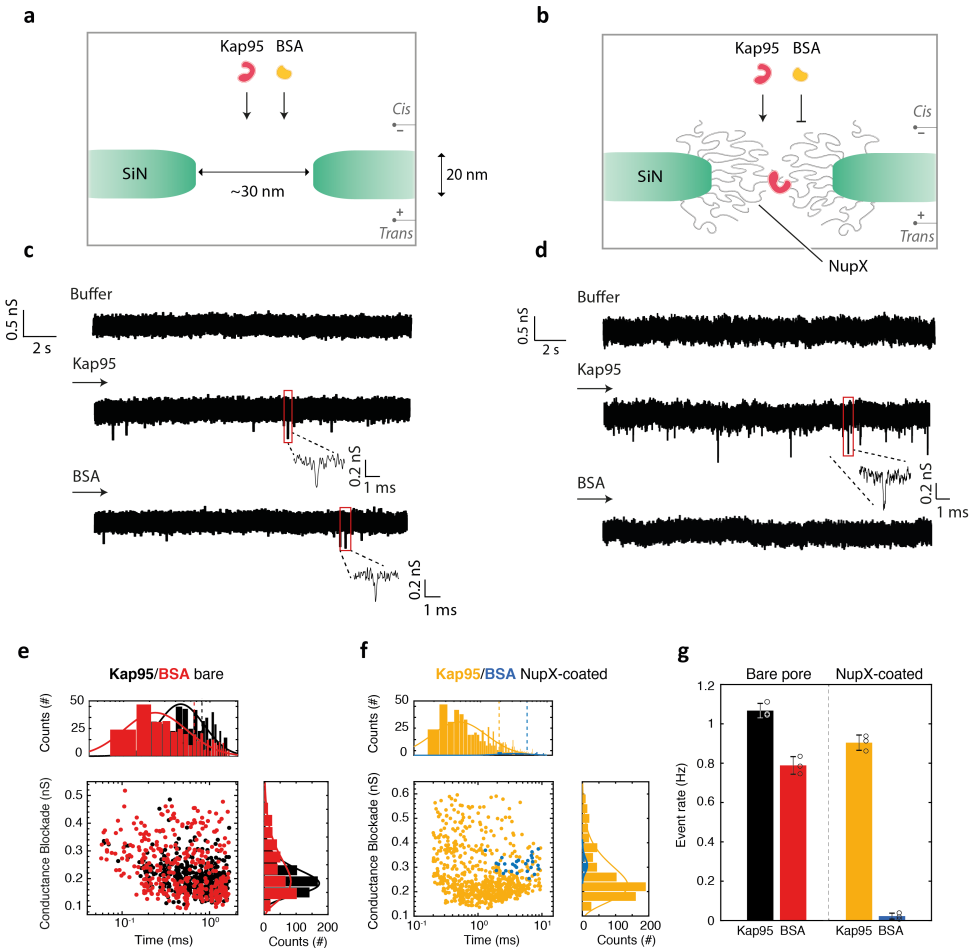


Figure 5.4: Electrical measurements on NupX-coated solid-state nanopores. a-b, Schematic of the nanopore system before (a) and after (b) NupX functionalization. c-d, Examples of raw current traces through bare (c) and NupX-coated (d) pores, recorded under 100 mV applied bias for different analyte conditions. Current traces are recorded in the presence of buffer only (top), upon addition of 450 nM Kap95 (middle), and 2.8 μ M BSA (bottom). Traces were filtered at 5 kHz. e, Scatter plot showing conductance blockades and dwell time distributions of translocation events of the analytes Kap95 (black, N=506) and BSA (red, N=387) through a bare 30 nm pore, recorded over the same time interval. f, Scatter plot showing conductance blockades and dwell time distributions of translocation events of the analytes Kap95 (yellow, N=686) and BSA (blue, N=28) through a NupX-coated 30 nm pore, recorded over the same time interval. Top and right panels in e and f show log-normal fits to the distribution of dwell times and conductance blockades, respectively. Dashed vertical lines in top panels indicate the mean values for the dwell time distributions. g, Average event rate of translocations for Kap95 through a bare pore (black), BSA through a bare pore (red), Kap95 through a NupX-coated pore (yellow), and BSA through a NupX-coated pore (blue). Error bars indicate standard deviations from independent measurements (circles) on three different pores, N=3.

0.1 ms for BSA and Kap95, respectively, which indicates that the presence of the NupX molecules in the pore significantly slows down the translocation process of the passing

molecules. Notably, BSA molecules were slower in translocating through the coated pore as compared to Kap95, which we attribute to the lower affinity between BSA and the NupX mesh as compared to Kap95. The transient and multivalent interactions between Kap95 and the FG-repeats in the NupX meshwork lead to a reduced energy barrier as compared to BSA permeation, which may explain the observed differences in dwelling times[11]. Repeating the same experiment on a larger 60 nm NupX-coated pore (Figure S5.22) yielded selective pores with faster translocations for both Kap95 (0.65 ± 0.05 ms) and BSA (1.6 ± 1.3 ms), consistent with the presence of an open central channel. Smaller pores (< 25 nm) did not result in any detectable signal for either Kap95 or BSA, due to the poor signal-to-noise ratio attainable at such low conductances.

Most importantly, these data clearly show selectivity of the biomimetic pores. Figure 5.4g compares the event rate of translocations for Kap95 and BSA through bare and NupX-coated pores under 100 mV applied bias. Event rates were 0.7 ± 0.04 Hz and 1.10 ± 0.04 Hz ($N=3$ different nanopores; errors are s.d.) for BSA and Kap95 through the bare pore, respectively, whereas upon coating the pore with NupX, the event rates changed to 0.02 ± 0.02 Hz and 0.90 ± 0.04 Hz ($N=3$ different nanopores) for BSA and Kap95, respectively. The sharp decrease in event rate for BSA upon NupX coating of the pores indicates that BSA molecules are strongly hindered by the NupX meshwork formed inside the pore. In contrast, the transport rate of Kap95 through the coated pore is nearly unaffected when compared to the bare pore. From these experiments, we conclude that the user-defined NupX does impart a selective barrier, very similar to native FG-Nups [27, 29, 31], by allowing efficient transportation of Kap95 while hindering the passage of BSA.

5.2.4. MD SIMULATIONS OF NUPX-LINED NANOPORES REVEAL THEIR PROTEIN DISTRIBUTION AND SELECTIVITY

We used coarse-grained MD simulations (Materials and Methods) to understand the selective properties of NupX-lined nanopores as obtained in our experiments. The 20 nm height of these nanopores is the same as the SiN_x membrane thickness, while we vary the diameter from 15 to 70 nm. Multiple copies of NupX are tethered to the nanopore lumen by their C-terminal domain in an equilateral triangular lattice with a spacing of 5.5 nm, based on estimates obtained from the SPR experiments (Figure S5.10, Materials and Methods). We note that the geometrical confinement by the nanopore may affect the grafting distance on the concavely curved interior pore wall (parallel to the pore axis) as compared to the planar geometry [56]. Based on 6 μs of coarse-grained MD simulations, we obtained the protein density distribution in the (r, z) -plane (averaged over time and angle θ) within a NupX-lined nanopore of 30 nm in diameter (Figure 5.5b), similar in size as the translocation experiments.

High-density regions form close to the attachment sites (*i.e.* the four dots at each wall in Figure 5.5b) and along the central axis of the nanopore. Since the triangulated lattice (comprising four rows) does not strictly exhibit a symmetry plane along the $z = 0$ axis, a slight asymmetry ($< 10\%$ in terms of protein density) occurs between the top and bottom of the density map. From these data, we obtained a radial protein density profile, averaged over the pore height for the pore region ($|z| < 10$ nm, Figure 5.5c), which exhibits a maximum of 230 mg/mL at the pore center for the 30 nm NupX nanopore system and is

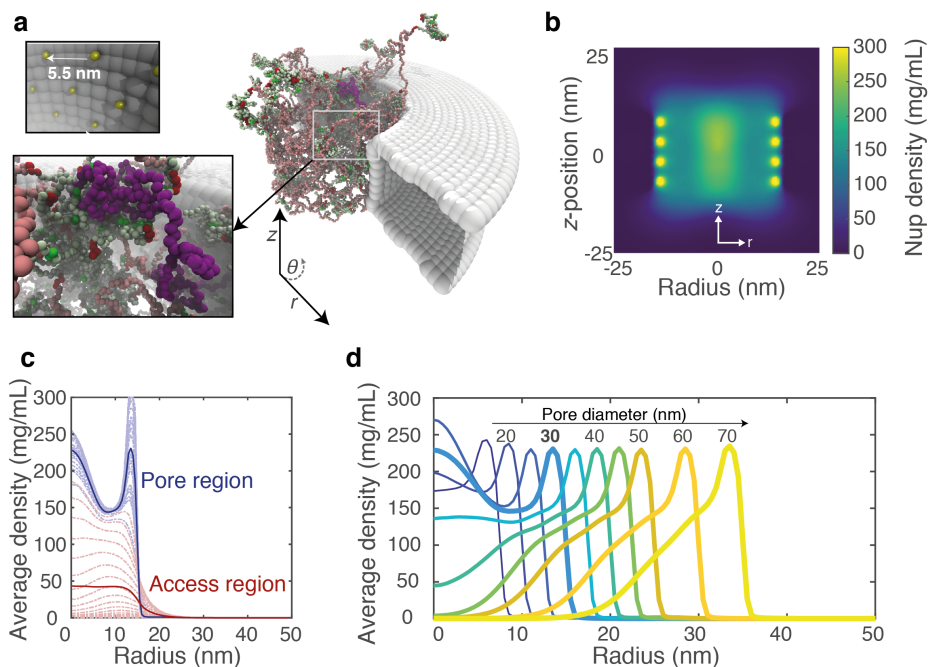


Figure 5.5: Protein distribution and conductance of NupX-coated pores. a, Snapshot of a biomimetic nanopore simulation. NupX proteins (following the colouring scheme of Figure 5.1) were tethered with a grafting distance of 5.5 nm (yellow, top inset) to a cylindrical occlusion made of inert beads (grey). Pore diameters ranged from 15-70 nm, where the pore thickness was 20 nm throughout. Bottom inset: highlight of a single NupX-protein (purple) within the NupX-meshwork. b, Axi-radial map (averaged over time and in the azimuthal direction) of the protein density within a 30 nm NupX-lined nanopore, from 6 μ s simulations. Dark colours indicate regions of low density, brighter colours indicate regions of high density. The collapsed domains of the NupX proteins form a high-density central plug. The high-density regions near the pore radius (15 nm) coincide with the anchoring sites of the NupX proteins. c, Density distributions (thick lines) for the pore (blue, $|z| < 10$ nm) and access (red, $10 \text{ nm} < |z| < 40$ nm) regions. Dashed curves indicate the average density within 1 nm thick slices in the z -direction. d, Radial density distributions (z-averaged) for NupX-lined nanopores with diameters ranging from 15 to 70 nm (darker and lighter colours denote smaller and larger diameters, resp.). The curve for 30 nm is emphasized. An increase in pore size beyond 30 nm leads to a decrease in the pore density along the pore's central channel.

insensitive to the aforementioned small asymmetry. This density agrees well with values in the range of 200-300 mg/mL observed in earlier computational studies of the yeast NPC central channel [34, 43]. We attribute the central localization of the NupX proteins to the combination of repulsion between the high C/H ratio extended domains near the pore wall and attraction between the cohesive, low C/H ratio collapsed domains of opposing NupX proteins. Since the average density in the access region ($10 \text{ nm} < |z| < 40$ nm, Figure 5.5c) is found to be low in comparison to the average density within the pore region, we conclude that the NupX proteins predominantly localize within the nanopore. When the grafting distance is perturbed by $\sim 10\%$ in either direction (Figure S5.24) to values of 5.0 or 6.0 nm, similar density profiles are obtained. So even though the experimental grafting distance might be somewhat larger for the nanopore compared to the

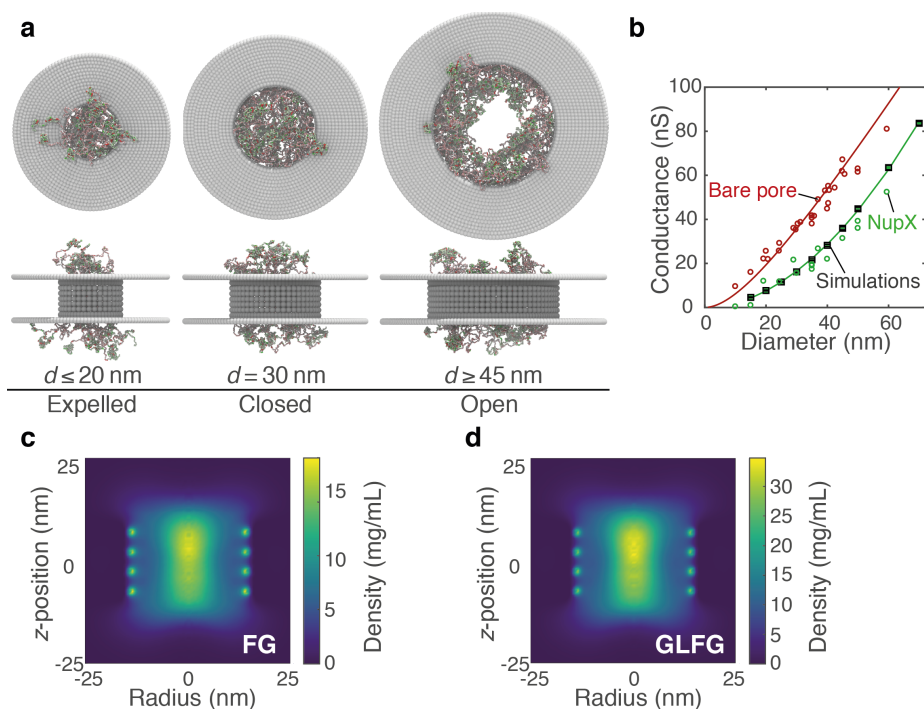


Figure 5.6: a, Side-view and top-view visualizations of 20 nm, 30 nm, and 45 nm diameter NupX-lined nanopores. For nanopores with diameters smaller than 25 nm, the pore region density decreases due to an expulsion of the collapsed NupX domains towards the access region. For nanopore diameters larger than 40 nm, the pore density decreases and a hole forms. For nanopore diameters of 25–30 nm, the pore region is sealed by the NupX cohesive domains. b, Conductance scaling for bare and NupX-coated nanopores. Open circles indicate conductance measurements for bare (red) and NupX-coated (green) pores. Squares indicate time-averaged conductance values obtained from MD simulations via a density-conductance relation (Materials and Methods). Error bars indicate the standard deviation in the conductance and are smaller than the marker. Second-order polynomial fits to the bare pore (experimental) and the simulated conductance values are included as a guide to the eye. c,d, Axi-radial density maps for FG and GLFG motifs, respectively. Both types of motif localize in the dense central region, indicating that there is no spatial segregation of different types of motif in NupX-coated nanopores.

planar brushes due to the different geometrical confinement, similar profiles would be expected for more sparsely coated pores.

The organization of the NupX proteins inside the nanopore geometry changes notably with pore diameter (Figures 5.5d, 5.6a). For large diameter pores, the density profile of NupX proteins protruding from the pore surface quite well resembles that of a planar brush (cf. Figure S5.18), resulting in a central opening for pores that are > 45 nm. When the pore diameter reaches values < 45 nm, NupX-coated nanopores are effectively sealed. This 45 nm length scale is remarkable, given the quickly decaying density profile of a planar NupX brush with a similar grafting distance (Figure S5.18). Upon further decreasing the pore diameter to values < 25 nm, we find that the NupX collapsed domains are being expelled from the pore region towards the access region, resulting in decreased

densities in the central pore region (Figures 5.5d, 5.6a). Interestingly, we find that these changes in NupX morphology as a function of pore diameter are in good qualitative agreement with predictions from earlier works on polymer-coated nanopores [57, 58], which point to a curvature-dependent modulation of the brush height. More specifically, an increase in curvature (*i.e.*, a decrease in pore diameter) of a concave brush substrate is expected to lead to a relative extension of the brush as compared to the planar geometry. Additionally, attractive interactions between the cohesive head groups of NupX anchored at opposing pore walls will also contribute to the sealing of NupX pores. Finally, we note that a central opening in the NupX nanopore meshwork, present for diameters from 45 nm upwards, is consistent with the increased event frequency and translocation speed observed in large (60 nm) NupX-coated pores (Figure S5.22).

Using a relation between the local protein density and the local conductivity separately for the pore and access regions [31], we calculated the conductance of the NupX nanopores for varying diameters (Figure 5.5d, Figure S5.25, Materials and Methods). The calculated conductance from the simulated NupX-lined pores is shown in Figure 5.6b (black squares) together with the experimental conductances for bare and NupX-coated pores (open circles). Note that we adopted a critical protein density of 85 mg/ml from the earlier work on Nsp1 [31] in our density-conductivity relation, but assume a different dependency of the local conductivity on the local protein density (Materials and Methods). Rather than assuming an abrupt complete blockage of conductance above the critical protein density of 85 mg/mL, we now use an exponential relation that provides a more gradual reduction in conductance with density. The necessity of a different density-conductance relationship indicates that the conductivity of the NupX nanopore meshwork depends non-linearly on the average protein density. Interestingly, the slope of the conductance-diameter curve for NupX-lined pores converges to that of bare pores already at relatively small pore sizes. This is due to the formation of a hole within the NupX meshwork (Figure 5.5d) already in pores with diameters over 40 nm, rendering these effectively similar to bare nanopores of smaller diameter.

A spatial segregation of different types of FG-motifs, as was observed in recent computational studies [4, 34], is not studied here explicitly. However, we find both types of FG-motifs localize similarly in the high-density central region within the NupX nanopore channel (Figures 5.6c, d). From these distributions and the observed selective transport of these pores (Figures 5.4e-g), we can infer that a spatial segregation of different FG-motifs is not required for selective transport.

Finally, in order to assess the selective properties of NupX-lined nanopores, we simulated a 30 nm diameter NupX-lined nanopore in the presence of 10 Kap95 or 10 inert particles. We released Kap95/inert particles in the access region at the top and recorded their location in over 5 μ s of simulation time (see Materials and Methods, Figures 5.7c, d). The Kap95 particles entered and left the NupX meshwork and sampled the pore lumen by traversing in the z -direction (Figure 5.7c). They localized preferentially at positions radially halfway between the central pore axis and the edge of the nanopore, where their time-averaged density distribution takes the shape of a concave cylindrical region, as is shown in Figure 5.7a. Kap95 was found to be capable of (re-)entering and leaving the meshwork on either side (Figure 5.7c). Since no external electric field was applied, exiting and subsequent re-absorption of Kap95 into the NupX meshwork occurred and there

was no directional preference for the motion of the Kap95 molecules, in contrast to the experiments.

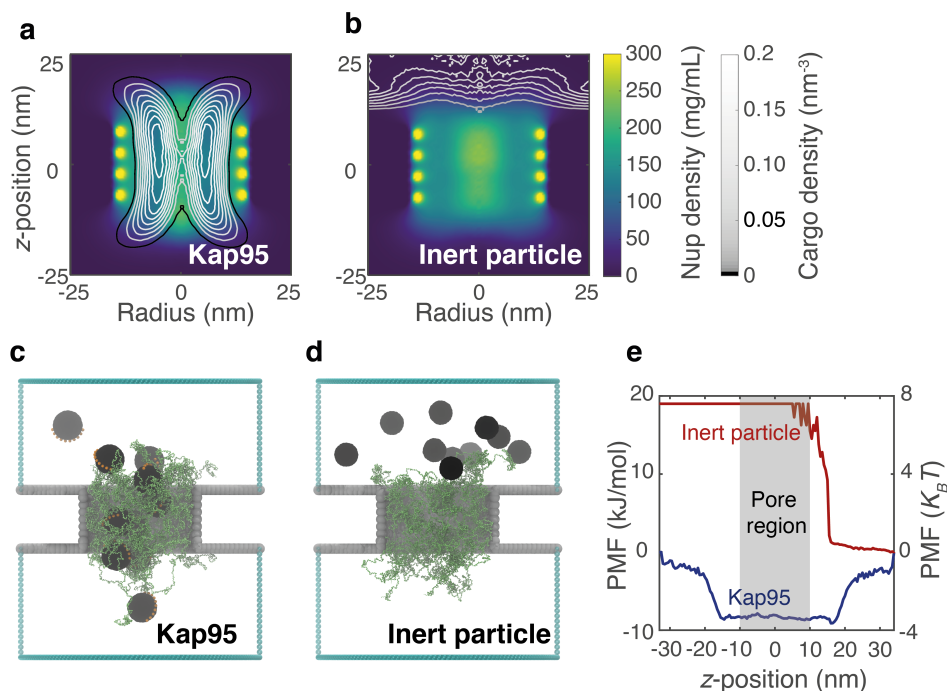


Figure 5.7: Effect of transporters on NupX-lined biomimetic pores. a, Contour graphs of the Kap95 number density (grey contours) superimposed on the NupX protein density distributions (in presence of Kap95) within a 30 nm NupX-lined nanopore (NupX-density follows the same colouring scheme as in Figure 5.5b and is shown separately in Figure S5.26). The protein meshwork adapts (as compared to the distribution in Figure 5.5b) to accommodate the permeating Kap95 particles. b, Density distribution of inert particles superimposed on the NupX protein density distribution in a 30 nm diameter NupX-lined nanopore. Inert particles remain in the top compartment and do not permeate the NupX-protein meshwork. c, d, Simulation snapshots of 30 nm NupX-lined nanopores in the presence of Kap95 particles (c, black spheres with orange binding spots) and inert particles (d, black spheres), which were released in the top compartment. Kap95 particles enter and exit the NupX meshworks at either side of the nanopore, whereas inert particles remain in the top compartment. e, PMF curves of Kap95 (blue) and inert particles (red) along the z -coordinate, obtained via Boltzmann inversion of the normalized density profile along the z -axis. The pore region coincides with an energy well of over $3 k_B T$ for Kap95, whereas inert particles experience a steep energy barrier of $\sim 7 k_B T$.

Interestingly, the NupX-meshwork adapted itself to the presence of the Kap95 particles by expanding towards the access region (compare Figures 5.5b and Figure S5.26): the protein density in the pore region decreased due to the presence of the Kap95, whereas the protein density increased in the access region. In contrast to the findings for Kap95, we observed that the inert particles, simulated under the same conditions, remained in the top compartment (Figure 5.7b,d) and did not permeate into the NupX-meshwork over the $5 \mu s$ time span of the simulation.

To quantify the selectivity of the 30 nm NupX-lined nanopores, we calculated PMF-curves along the z -axis for both cargo types (Figure 5.7e, see Materials and Methods).

Kap95 experienced a negative free energy difference of approximately 8 kJ/mol, which amounts to a binding energy of just over 3 $k_B T$ per Kap95. On the other hand, inert particles experience a steep energy barrier of approximately 18 kJ/mol, which corresponds to over 7 $k_B T$ per protein. The obtained Kap95 free energy profiles are similar to those found in other simulation studies of cargo permeation through NPCs [9, 48] or NPC mimicking systems [31, 59]. The Kap95 binding free energy differences along the nanopore axis are considerably smaller than the computed free energy profiles for NupX-brushes (Figure 5.3i). This most probably relates to the fact that the two studied reaction coordinates differ notably and cannot easily be compared: the reaction coordinate in Figure 5.3i describes orthogonal entry into a brush that extends infinitely in the lateral direction, whereas the coordinate in Figure 5.7e describes lateral entry and exit into the NupX assembly within the pore. As a result, one would not expect the free energy differences for transport through the nanopores to be similar to those obtained for entry into a brush geometry. Note that large free energy differences in our nanopores would also yield residence times that are orders of magnitude larger than the observed \sim ms dwell times in our nanopore experiments [60] (Figure 5.4f). From our combined experimental and simulation results, we conclude that NupX-lined nanopores indeed reproduce the NPC's remarkable selectivity towards Kap95.

5.3. CONCLUSION

In this work, we introduced a 311-residue long artificial FG-Nup, termed NupX, that we rationally designed *de novo* based on the average properties of GLFG-type Nups (Nup49, Nup57, Nup100, Nup116, Nup145N) and which faithfully mimics the selective behaviour of the nuclear pore complex. We experimentally found that substrates coated with NupX brushes of varying grafting densities bind selectively to Kap95, while they did not interact with the control BSA proteins – a finding confirmed through coarse-grained MD simulations of the adsorption of Kap95 and inert particles. Consistent with these results, we found that Kap95 translocates through both uncoated and NupX-lined nanopores on a physiological (\sim ms) timescale [61], whereas BSA passage through the NupX-coated pores was effectively excluded. Coarse-grained MD simulations revealed how the NupX proteins form a dense (> 150 mg/mL) phase that allows passage of Kap95 particles while excluding inert particles. Interestingly, we find that the high densities of the FG-rich NupX meshworks are comparable to those obtained in earlier simulation studies of yeast NPCs [43]. A comparison of the intrinsic protein density (*i.e.* the protein density of an individual molecule in solution, quantified by the mass per unit Stokes volume) of NupX (219 mg/mL) with that of Nsp1 (74 mg/mL) explains why our NupX-meshworks have the tendency to localize more compactly inside nanopore channels than Nsp1 in earlier work [31]. The increased conductance of the denser NupX-lined nanopores (as compared to Nsp1) required a non-linear relation between the average protein density and the local conductivity, and indicates that the average protein density is not the only factor that describes conductivity; the dynamics of the unfolded proteins and the local charge distribution might be important as well.

The design strategy presented in this work allows us to assess the role of the amino acid sequence of the spacer regions in GLFG-Nups. Spacer residues were reported to be involved in the interaction interface of Nup-NTR complexes [62–64], highlighting a

possible specific role of these domains in the binding of NTRs. In the current work, we assigned the positions of spacer residues along the NupX amino acid sequence entirely randomly, in both the collapsed, FG-rich low C/H ratio domain, and the extended high C/H ratio domain. This indicates that no specific spacer sequence motifs are required to facilitate the fast and selective transport of NTRs like Kap95. The consistency of the Stokes' radii of different NupX designs within our simulations (Figure 5.2f) supports this finding.

Furthermore, our results shed light on the functional role of the spatial segregation of FG and GLFG motifs that was observed in earlier work [4, 34]. Although these recent computational studies observed such a feature and suggested that it plays a role in selective transport, the coinciding distributions of FG and GLFG motifs (Figures 5.6c,d) show that no spatial segregation of different types of FG motifs exists within our selective nanopores. Notably, this does not rule out a different functional role for the spatial segregation of different types of FG-motifs, which can be explored in future work.

The combined design and characterization approach presented here, with brush-adsorption and nanopore-transport measurements on the one hand and coarse-grained MD simulations on the other, provides a powerful and exciting platform for future studies of artificial FG-Nups: one can now start to systematically examine the relation between FG-Nup amino acid sequence and size selectivity of the NPC. Such studies could, for example, entail the design of FG-Nups with radically different physicochemical properties (*i.e.* FG-spacing, FG motif type, spacer domain C/H ratios, sequence complexity) to assess the selective properties of nanopore systems functionalized with these designer FG-Nups. Indeed, solid-state nanopores modified with a single type of FG-Nup were shown in this and other works [27, 29, 31] to reproduce NPC selectivity, justifying the use of a single type of artificial Nups within an environment structurally similar to the NPC. Moreover, in view of the similarity [6] and redundancy [22, 35] of different FG-Nups within the NPC and the ability of our method to robustly reproduce FG-Nup properties (Figure 5.2f and Figure S5.27), we are confident that a single artificial FG-Nup can capture the selective barrier function the NPC. However, given that even minimally viable native NPCs [22, 35] contain several different FG-Nups, it is worth mentioning that NPC mimics with a heterogeneous set of (artificial) FG-Nups can be created as well: DNA origami scaffolds [33] potentially allow to position different artificial FG-Nups with great control, thus enabling systematic studies of how the interplay of different (artificial) FG-Nups gives rise to various transport properties of the NPC.

Finally, the design procedure that we introduced here is not limited to applications in nucleocytoplasmic transport. It may, for example, be possible to use a comparable approach to create *de novo* selective molecular filters (*e.g.* for use in artificial cells [65, 66]), systems that would rely on selective partitioning of molecules in meshworks of unfolded proteins with assigned properties. Control can be asserted over the composition and geometry of the meshwork *e.g.* by means of recently developed DNA-origami scaffolds [32, 33]. More generally, the approach illustrated here may enable future studies of the physical properties underlying phase separation of intrinsically disordered proteins [30]. One could, for example include degrees of freedom such as the proteins' second virial coefficient (B_{22}), or the charge patterning (κ), which have been linked to the phase behavior of intrinsically disordered proteins [67, 68]. We envision that just like the field

of de novo protein design has come to fruition with improved understanding of protein folding [69], the design of unstructured proteins like NupX will enable a versatile platform to study the intriguing functionality of intrinsically disordered proteins.

5.4. METHODS

5.4.1. ANALYSIS OF GLFG-NUPS AND DESIGN OF SYNTHETIC NUPS

Protein sequences of *Saccharomyces cerevisiae* GLFG-type Nups (*i.e.* Nup100, Nup116, Nup49, Nup57 and Nup145N) were analyzed using a script custom-written with *R* programming package (version 3.3.1). Following the definitions of high C/H-ratio and low C/H-ratio unfolded FG-Nup domains as given in Ref. [6], we obtained histograms of the amino acid frequencies in both the collapsed (low C/H-ratio) and extended (high C/H-ratio) domains. The collapsed / extended domain sequences of NupX were then assigned in three steps: First, the collapsed and extended domains of NupX were assigned equal lengths of 150 residues each. Then, by normalizing the distributions in Figure 5.2b to the number of available residues within each domain, the total pool of amino acids within each domain was obtained. Lastly, these amino acids were randomly assigned a sequence index within each domain, with a boundary condition of the presence of FG and GLFG repeats spaced by 10 residues within the low C/H-ratio domain. This approach was repeated iteratively in combination with disorder predictions using the on-line PONDR disorder prediction utility [37] until a sufficiently disordered design was obtained. The final version of the NupX amino acid sequence was also analyzed for secondary structure using DISOPRED [38, 39] and Phyre2 [40]. A 6-histidine tag was added to the N-terminus of the NupX sequence in order to facilitate protein purification (see Protein purification section). Finally, on the C-terminus a cysteine was included to allow the covalent coupling of the NupX protein to the surface.

5.4.2. EXPRESSION AND PURIFICATION OF NUPX AND KAP95

The synthetic NupX gene (Genscript), appended with codons for an N-terminal His6-tag and a C-terminal cysteine residue, was cloned into pET28a and expressed in *Escherichia coli* ER2566 cells (New England Biolabs, *fhuA2 lacZ::T7 gene1 [lon] ompT gal sulA11 R(mcr73::miniTn10-TetS)2 [dcm] R(zgb-210::Tn10-TetS) endA1 Δ(mcrCmrr)114::IS10*). To minimize proteolysis of NupX, the cells were co-transformed with plasmid pED4, a pGEX-derivative encoding GST-3C-Kap95 under control of the tac promoter. Kap95 was expressed as a C-terminal GST fusion protein in *Escherichia coli* ER2566 cells from plasmid pED4, a pGEX derived construct in which the thrombin cleavage site was replaced by a 3C protease cleavage site using primers ed7 and ed8 (Table S5.4). Cells were cultured in shake flasks at 37°C in Terrific Broth supplemented with 100 µg/mL ampicillin and 50 µg/mL kanamycin, and expression was induced at OD600~0.6 with 1 mM IPTG. After 3 hours of expression the cells were harvested by centrifugation, washed with PBS, resuspended in buffer A1 (50 mM Tris/HCl pH 7.5, 300 mM NaCl, 8 M urea, 5 mg/mL 6-aminohexanoic acid supplemented with one tablet per 50 mL of EDTA-free cOmplete ULTRA protease inhibitor cocktail) and frozen as “nuggets” in liquid nitrogen. Cells were lysed with a SPEX cryogenic grinder, after thawing 1,6-hexanediol was added to a final percentage of 5%, and the lysate was centrifuged for 30 minutes at 125000 xg in a Ti45 ro-

tor (Beckman Coulter). The supernatant was loaded onto a 5 mL Talon column mounted in an Akta Pure system, the column was washed with buffer A2 (50 mM Tris/HCl pH 7.5, 300 mM NaCl, 800 mM urea, 5 mg/mL 6-aminohexanoic acid, 2.5% 1,6-hexanediol) and NupX was eluted with a linear gradient of 0–200 mM imidazole. Peak fractions were pooled, diluted tenfold with buffer A2 lacking sodium chloride, loaded onto a 1 mL Hi-Trap SP sepharose HP column and NupX was eluted with a linear gradient of 0–1 M NaCl.

Kap95 was expressed as a C-terminal GST fusion protein in *Escherichia coli* ER2566 cells from plasmid pED4, a pGEX derived construct (kindly provided by Jaclyn Novatt) in which the thrombin cleavage site was replaced by a 3C protease cleavage site. Cells were grown in shake flasks at 30°C on LB medium supplemented with 100 µg/mL ampicillin, induction was induced at OD600~0.6 with 1 mM IPTG, and growth was continued overnight. Cells were harvested by centrifugation, washed with PBS, resuspended in TBT buffer (20 mM HEPES/NaOH pH 7.5, 110 mM KOAc, 2 mM MgCl₂, 0.1% (w/v) Tween20, 10 µM CaCl₂ and 1 mM β-mercaptoethanol), and lysed by a cell disruptor (Constant Systems) at 20 kpsi. Following centrifugation for 30 minutes at 125000 xg in a Ti45 rotor (Beckman Coulter), the supernatant was loaded onto a 2 mL GStrap 4B column mounted in an Akta Pure system. The column was washed with TBT buffer, TBT + 1 M NaCl and TBT + 0.1 mM ATP, and the fusion protein was eluted with TBT + 10 mM reduced glutathione. The GST moiety was cleaved off by overnight digestion with home-made 3C protease, and Kap95 was separated from GST and the protease by size exclusion chromatography on a Superdex S200 column pre-equilibrated with TBT buffer.

5.4.3. QCM-D SAMPLE PREPARATION AND DATA ACQUISITION

QSense Analyzer gold- and SiN-coated quartz QCM-D chips were purchased from Biolin Scientific, Västra Frölunda, Sweden. Prior to the experiment, chips were immersed in RCA-1 solution, which consisted of 30% Ammonium Hydroxide, 30% Hydrogen Peroxide, and deionized (DI) water in 1:1:5 ratio, for ~30 minutes at 75°C. This step was used to clean the surface from carbon species, as well as to enrich the surface with hydroxyl groups in case of the SiN-coated chips. Chips were further rinsed with DI water, sonicated for ~10 minutes in pure ethanol, and blow-dried with a nitrogen stream. Before each experiment, flow-cells were disassembled, cleaned by sonication for 20–30 minutes in freshly prepared 2% SDS, rinsed with DI water, and blow-dried with a nitrogen stream. For SiN-coated quartz sensors, the SiN surface was chemically engineered in order to add free maleimide groups (see Preparation of NupX-coated nanopores for details). Prior to the coating of the gold surface, protein solutions containing either NupX, Nsp1, or Nsp1-S, were incubated in PBS with 1mM TCEP for at least half an hour, which was also present during the coating step. Similarly, MUTEK solutions included also 10mM TCEP. QMC-D data were monitored and recorded with sub-second resolution using Qsoft, which was provided by the company together with Qsense Analyzer. Buffer was injected into the flow-cell chamber at constant flow-rate of 20 µL/min using a syringe pump. Experiments were all performed at room temperature. Shift in the resonance frequency (Δf) and dissipation (ΔD) can be, in first approximation, attributed to changes in deposited mass and viscoelastic properties of the film, respectively. Δf and ΔD were acquired at the fundamental tone ($n = 1$) and the 5 overtones ($n = 3, 5, 7, 9, 11$). The normalized second overtone $\frac{\Delta f_5}{5}$ was used for display and analysis. Data processing

and plotting were performed using a custom-written Matlab script.

5.4.4. SPR MEASUREMENTS AND ANALYSIS

All measurements were performed using a Bionavis MP-SPR Navi™ 220A instrument equipped with two 670 nm laser diodes focused on two different spots on the sample surface. Both gold and silicon dioxide coated sensor slides were used (Bionavis). Grafting of proteins or MUTEg to the gold and silica coated sensors was performed using the same protocol as for the gold-coated QCM-D chips and for the nanopore chips, respectively. After the final incubation step, the chips were rinsed with milliQ water, ethanol, and gently blow-dried with pure nitrogen. Immediately before measurements of the sensors in air, the backside of each sensor was cleaned by carefully rubbing lint-free lens tissue soaked in 2-propanol (Sigma Aldrich) followed by blow-drying both sides with nitrogen. At least two repeat measurements were performed for all sensor slides to verify no signal drifting occurred due to adsorption of moisture. The background signal from each sensor was measured before grafting the adlayers to the sensor surfaces and was used as a starting point for modelling the adlayer thickness, d . The silicon dioxide thin film thickness was evaluated to 15.1 ± 0.5 nm across the different samples and surface spots prior to surface grafting. Three replicate sensor slides were used for each type of adlayer (except for MUTEg which used 1 sensor slide per concentration measurement).

Adlayer thickness was determined from least-square fitting measurements with Fresnel models using an approach similar to those used in previous works [70, 71], which we briefly describe here. The following information was used to obtain adlayer thickness: a fit performed on the angular reflectivity spectra close to the resonance angle (see Figure S5.10), knowledge of the sensor layer thicknesses and refractive indices [72], the bulk refractive index of air in the measurement cell, as determined from the total internal reflection angle of each measurement, and the assumption that the adlayer refractive index n is the same as its dry bulk counterpart ($n_{protein} = 1.5373$, $n_{APTES} = 1.42$, $n_{MUTEg} = 1.45674$). The formed adlayers were further assumed to be homogeneous and not containing solvent and to be free of contaminants. Grafting densities, Γ , of MUTEg, Nsp1, Nsp1-S and NupX were obtained from the Fresnel model determined d using the relation:

$$\Gamma = \frac{\rho d N_A}{M} \quad (5.1)$$

where ρ is the density ($\rho_{MUTEg} = 1.09$ g/cm³, $\rho_{protein} = 1.35$ g/cm³; Ref. 70), N_A is Avogadro's constant, and M is the molecular weight ($M_{MUTEg} = 380$ Da, $M_{Nsp1} = 65.7$ kDa, $M_{Nsp1-S} = 62.1$ kDa, $M_{NupX} = 32.5$ kDa).

5.4.5. PREPARATION OF NUPX-COATED NANOPORES AND CURRENT DATA ACQUISITION

Solid-state nanopores with diameters from 10-60 nm were drilled using TEM in glass-supported SiN_x free-standing membranes. Glass chips were purchased from Goeppert. We refer to Ref. [52, 73] for details on the fabrication of the chip substrate and free-standing membrane. Freshly drilled solid-state nanopores were rinsed with ultrapure water, ethanol, acetone, and isopropanol, followed by 2-5 minutes of oxygen plasma

treatment, which was performed in order to further clean and activate the nanopore surface with hydroxyl groups. Next, chips were incubated in 2% APTES (3-aminopropyltriethoxysilane) (Sigma Aldrich) in anhydrous toluene (Alfa Aesar) for 45-60 min at room temperature, shaking at 400 rpm, followed by 15 minutes in anhydrous toluene for washing. These two steps were performed in a glove-box under constant nitrogen stream in order to prevent the APTES from polymerizing. Then, chips were further rinsed with ultrapure water, ethanol, and heated at 110°C for at least 30 minutes. This step was used to fixate the APTES layer by favouring further binding between the unreacted ethoxy groups.

The nanopore surface was thus covered with primary amines, which were subsequently reacted to Sulfo-SMCC (sulphosuccinimidyl-4-(N-maleimidomethyl)-cyclohexanecarboxylate) (2 mg no-weight capsules (Pierce)), a crosslinker that contains NHS-ester (reacts to amines) and maleimide (reacts to thiols) groups at opposite ends, for > 3 hrs at room temperature, shaking at 400 rpm. Chips were subsequently washed in PBS for 15 minutes and incubated with thiolated proteins for 2-3 hours, which were pretreated with 5 mM TCEP for ~30 minutes in order to reduce the thiol groups. Chips were further washed in PBS before the electrical measurement. Raw ionic current traces were recorded at 100 kHz bandwidth with an Axopatch 200B (Molecular devices) amplifier, and digitized (Digidata 1322A DAQ) at 250 kHz. Traces were monitored in real-time using Clampex software (Molecular devices). Data were digitally filtered at 5 kHz using a Gaussian low-pass filter and analysed using a custom-written Matlab script76.

5.4.6. DYNAMIC LIGHT SCATTERING (DLS) MEASUREMENT OF THE HYDRODYNAMIC DIAMETER

DLS experiments were performed using Zetasizer Nano ZS (Malvern). Cuvette of 100 μL (Brand GMBH) were used for the measurement. All protein hydrodynamic diameters were measured in 150 mM KCl, 10 mM Tris, 1mM EDTA, at pH 7.5, and averaged over three experiments. Mean value and standard deviation for each of the proteins used are reported in Table S5.1. Proteins which contained exposed cysteines (NupX, Nsp1, and Nsp1-S) were pre-treated with TCEP (present in at least 100 \times excess) in order to break disulfide bonds.

5.4.7. COARSE-GRAINED MODEL FOR UNFOLDED PROTEINS

All coarse-grained MD-simulations were performed using our earlier developed one-bead-per-amino acid (1BPA) model for unfolded proteins [43, 74]. This model maps complete amino acids to single beads with a mass of 124 amu placed on the C_α position, separated by an average bond length (modelled as a stiff harmonic potential) with an equilibrium distance of 0.38 nm. Backbone potentials were assigned via an explicit coarse-grained mapping of Ramachandran data of a library of the coil regions of proteins that distinguishes flexible (*i.e.* Glycine), stiff (*i.e.* Proline) and regular amino acids [74]. Non-bonded interactions between different amino acid residues are based on their respective hydrophobicity (normalized between 0 and 1 and based on the free energy of transfer between polar and apolar solvents) and obey the following interaction potential [43]:

$$\Phi_{HP} = \begin{cases} \epsilon_{rep} \left(\frac{\sigma}{r}\right)^8 - \epsilon_{ij} \left[\frac{4}{3} \left(\frac{\sigma}{r}\right)^6 - \frac{1}{3} \right], & r \leq \sigma \\ (\epsilon_{rep} - \epsilon_{ij}) \left(\frac{\sigma}{r}\right)^8, & \sigma \leq r \end{cases} \quad (5.2)$$

$$\quad (5.3)$$

where $\epsilon_{rep} = 10$ kJ/mol and $\epsilon_{ij} = 13 \cdot \sqrt{(\epsilon_i \epsilon_j)^\alpha}$ kJ/mol, with ϵ_i the normalized (between 0 and 1) hydrophobicity of a residue i and $\alpha = 0.27$ a scaling exponent. The electrostatic interactions within the 1BPA model are described by a modified Coulomb law:

$$\Phi_{EL} = \frac{q_i q_j}{4\pi\epsilon_0\epsilon_r(r)r} \exp(\kappa r), \quad (5.4)$$

where the electrostatic interactions are modulated via a Debye screening component. This form of electrostatics takes into account the salt concentration (set at 150 mM here, via a screening length $\kappa = 1.27$ nm⁻¹) together with a solvent polarity at short distances via a distance-dependent dielectric constant:

$$\epsilon_r(r) = 80 \left[1 - \frac{r^2}{z^2} \frac{e^{\frac{r}{z}}}{\left(e^{\frac{r}{z}} - 1\right)^2} \right], \quad (5.5)$$

where $z = 0.25$. Non-bonded interactions are cut-off at 2.5 nm (hydrophobic interactions) or 5.0 nm (electrostatic interactions). Since the 1BPA model operates without explicit solvent, we apply stochastic dynamics with a coupling frequency τ_T of 50 ps⁻¹. Stochastic dynamics handles temperature coupling implicitly, ensuring that the system operates within a canonical ensemble at a reference temperature of 300 K. We refer the reader to the original work for further details on the used 1BPA model [43, 74]. Unless otherwise mentioned, all simulations were performed using the above forcefield and corresponding settings, employing the GROMACS [75] molecular dynamics software (version 2016.1/2016.3) on a parallelized computer cluster. A complete overview of all simulations in this work is provided in Table S5.3.

5.4.8. CALCULATING STOKES RADIUS OF NUPX AND VARIATIONS

Intrinsically disordered proteins were modelled using the 1BPA model [43, 74], starting from an extended configuration. After energy minimization (steepest descent) and a brief (5 ns) equilibration step, we simulated the individual proteins for $5 \cdot 10^8$ steps using a timestep of 20 fs (total simulation time: 10 μ s). Conformations were extracted every 10000 frames (*i.e.*, every 200 ps). In order to calculate the Stokes radii (R_s) from the MD trajectories, we extracted protein conformations every 2 ns and applied the HYDRO++ software [76] in order to calculate the R_s -values. This procedure yields a total of 5000 Stokes radii per protein.

5.4.9. CALCULATING NUPX BRUSH DENSITY PROFILES AND PMF CURVES OF CARGO ADSORPTION

We modelled the brush substrate as a fully triangulated (sometimes denoted as hexagonally) closed-packed array of sterically inert beads with a diameter of 3 nm. NupX pro-

teins were tethered on top of the scaffold by their C-terminus, following an equilateral triangular lattice with a uniform grafting distance of 4.0 or 5.7 nm. A fully triangulated lattice is close-packed in two dimensions, meaning that a unique length scale sets the grafting density. The simulation box consisted of a $24 \times 24 \times 81.5 \text{ nm}^3$ triclinic and fully periodic unit cell (Figure 5.3h). In our simulation of a less dense brush (grafting distance of 5.7 nm), the simulation box size was accordingly scaled up to 34.2 nm in the lateral dimensions. The grafting pattern of the NupX proteins was placed such as to ensure homogeneity of the NupX-brush in the lateral plane throughout the periodic boundaries. Density profiles for the NupX brushes and FG/GLFG repeats were obtained by simulating the NupX brush systems for 1.75×10^8 steps ($3.5 \mu\text{s}$) using a timestep of 20 fs. The first 500 ns of the simulation trajectory was discarded as equilibration. We modelled Kap95 and inert particles in the following way: The Kap95 particle consists of sterically repulsive beads, arranged in a geodesic shell such that the particle has a diameter of 8.5 nm, consistent with the hydrodynamic dimensions of the Kap95 protein (Table S5.1). The Kap95 surface beads interact with the NupX amino acid beads through the repulsive term of Φ_{HP} (*i.e.*, volume exclusion), and the modified Coulomb potential Φ_{EL} , where we distributed the charge (total net charge of $-43e$) of Kap95 over the Kap95 surface beads. This modelling choice is based on the high degree to which charged residues are exposed on the surface of Kap95 [63]. We preserved the structure of the particle by applying a harmonic restraint of 40000 kJ/mol on bead pairs whenever the distance between beads within the reference structure was below a cut-off of 1 nm. A total of ten hydrophobic binding pockets were placed at a mutual distance of 1.3 nm along an arc (Figure S5.19) on the surface of the Kap95-particle [9, 47, 48]. The binding sites interact with NupX amino acid beads via the hydrophobic potential Φ_{HP} , where the hydrophobicity of these binding sites was set equal to that of Phenylalanine. In the same way as for the Kap95, we assembled an inert particle [11, 31, 48] with a diameter similar to inert control proteins (7.5 nm, Table S5.1). Other than steric repulsion, no specific interactions between the inert particle on one hand, and the amino acid or substrate beads on the other were assigned. Using a harmonic restraint of 100 kJ/mol, we generated umbrella sampling windows by pulling the cargo in the negative z -direction (while freezing the particle's movement in the xy -plane) with a pulling velocity of -0.001 nm/ps and a time step of 20 fs along the centre of the triclinic box. Starting configurations were extracted every 0.5 nm, yielding 51 umbrella windows per cargo. After energy minimization (removal of overlap between beads) via the steepest descent algorithm, we performed 100 ns (5×10^6 steps) of equilibration, and $1 \mu\text{s}$ (5×10^7 steps) of production MD per umbrella window, where the Kap particles were restrained using a harmonic umbrella potential of 100 kJ/mol in the z -direction, applied to the cargo's center of mass. Aside from this restraint, the particles were free to rotate and move in the xy -plane. Potential-of-mean-force (PMF) curves were obtained using the weighted histogram analysis method (WHAM) via the `g_wham` [49] utility of GROMACS.

5.4.10. COARSE-GRAINED MD SIMULATIONS OF NUPX-LINED NANOPORES

We modelled the SiN nanopores as cylindrically shaped occlusions in a membrane constituted entirely of sterically repulsive beads with a diameter of 3 nm. The height of the nanopore was 20 nm in all cases, with diameters ranging from 15 to 70 nm. NupX-

proteins were modelled using the 1BPA model described earlier and tethered to the inner surface of the cylinder in an equilateral triangular lattice with a grafting distance of 5.5 nm. This value was estimated from NupX immobilization on silica surfaces using the SPR technique and should be taken as a lower limit given that molecular adsorption in nanopores can be influenced by steric repulsion and geometric confinement [56]. Simulations were carried out for 2×10^8 steps using a timestep of 15 fs ($3 \mu\text{s}$), or 4×10^8 steps ($6 \mu\text{s}$) for the single case of a 30 nm diameter NupX-lined nanopore.

5.4.11. DENSITY DISTRIBUTIONS AND NANOPORE CONDUCTANCE FROM NANOPORE SIMULATIONS

Axi-radial density maps were obtained from NupX nanopore simulation trajectories using the 'gmxdensmap' utility of GROMACS, where a bin size of 0.5 nm was used to construct number densities within a cylinder centred on the nanopore. Average densities were extracted for the pore and access regions by averaging the axi-radial density distributions over the coordinate ranges $|z| \leq 10$ nm and $10 \text{ nm} < |z| < 40$ nm, respectively [31].

The conductance of NupX-lined nanopores was obtained by assuming that the conductance $G(d)$ is governed by a modified Hall-formula [31, 53]:

$$G(d) = \left(\frac{4l}{\sigma_{pore}\pi d^2} + \frac{1}{\sigma_{access}d} \right)^{-1}, \quad (5.6)$$

where $l = 20$ nm is the height of the nanopore, d denotes the diameter (15-70 nm), and σ_{pore} and σ_{access} denote the conductivities in the pore and access regions, respectively. The conductivities in both regions can be extracted from the axi-radial density distributions by integrating and normalizing the local conductivity over the pore diameter and corresponding height ranges:

$$\sigma_{pore} = \frac{1}{\pi l \frac{1}{4} d^2} \int_{z=-\frac{l}{2}}^{z=+\frac{l}{2}} \int_{r=0}^{r=\frac{d}{2}} 2\pi \sigma_{bulk} r \sigma(r, z) dr dz, \quad (5.7)$$

$$\sigma_{access} = \frac{1}{\pi l \frac{1}{4} d^2} \int_{z=\frac{l}{2}}^{z=\frac{l}{2}+h} \int_{r=0}^{r=\frac{d}{2}} 2\pi \sigma_{bulk} r \sigma(r, z) dr dz. \quad (5.8)$$

The local conductivity $\sigma(r, z)$ follows from the local axi-radial density distribution $\rho(r, z)$:

$$\sigma(r, z) = \exp \left(-\sqrt[3]{\frac{\rho(r, z)}{\rho_c}} \right), \quad (5.9)$$

where ρ_c is set to 85 mg/mL³¹. Whereas this relation is a zero-parameter fit, the dependency of the conductivity on the local protein density is different from the linear model with a strict cut-off used in earlier work [31]. Here, the conductivity drops quickly with protein density initially while decreasing only slowly at high protein densities. This change in dependence was necessary since NupX-lined pores show a higher conductance at higher densities than the NPC mimics in earlier work. Axi-radial density distributions and the corresponding conductance were calculated for 100 ns windows to

obtain an average conductance for each pore size. The sensitivity of this method was tested against the time averaging window of the density distributions and was found to only be marginally influenced by the window size, nor did the conductance change with time.

5.4.12. SELECTIVITY OF NUPX-LINED NANOPORES

We probed the selectivity of a NupX-lined nanopore with a diameter of 30 nm by inserting either 10 Kap95 molecules or 10 inert particles to the cis-side of the nanopore. To speed up sampling, Kap95 or inert particles were confined to the periphery of the nanopore using a cylindrical constraint that prevents Kap95 or inert particles from entering regions with $|z| > 40$ nm or $r > 35$ nm [77]. This occlusion consisted entirely of sterically repulsive beads with a diameter of 3 nm, which only interact with Kap95 or inert particles. The size of the cylindrical constraint was set such that Kap95 molecules or inert particles can only leave the access region by entering the NupX-lined nanopore. The total simulation time spanned 3.33×10^8 steps (5 μ s), where we discarded the first 10% (500 ns) of the trajectory as equilibration. Axi-radial density maps for the protein density and contour graphs for the Kap95 and inert particle densities were obtained using the 'gmx_densmap' utility using a bin size of 0.5 nm. We reported a cargo number density in lieu of a mass density, since the number of beads that constitute the Kap95 or inert particles does not necessarily correspond to the number of amino acids in either protein.

To calculate the PMF curve along the z -axis for Kap95 and inert particles, we integrated the axi-radial number density of the centre-of-mass of the particles in the radial direction, resulting in a one-dimensional axial number density $n(z)$. Normalizing $n(z)$ with the number of bins in the z -direction results in a probability distribution $p(z)$, from which the PMF can be calculated by using the inverse Boltzmann relation:

$$PMF(z) = -k_B T \ln p(z). \quad (5.10)$$

The PMF curves for both Kap95 and inert particles (Figure 5.7e) were shifted such that the curves were zero at $z = 35$ nm. Regions with zero density (leading to divergence of the $\ln p(z)$ -term) were set equal to the maximum of the PMF curve.

5.5. SUPPORTING INFORMATION

5.5.1. AMINO ACID SEQUENCES OF ALL PROTEINS USED IN THIS WORK (NupX, Nsp1, Nsp1-S, Kap95, BSA).

NupX:

MGHHHHHHFHNQGSGLLTTFGKASSTSTQASGLFGNGGLNNQQTGFGNIKTGPNPTSGL
FGQTGNSANSSSGFGAANTNAFSSGGLFGSQQNGSVQANFGNGSNNGNSTQGLFGGPMMP
QTPSAPFGTQQNMTGNNNGLFGSTGGTGTGGSFGNNASASKTQNGLFGDRARNQSGFD
NPYNKLLRSENSKSEFIVSIDVKSEMAASIKLTAFFGQSTAKNKALSNI GTLIDKDLKAKKD
TKSRNPIKLIPNAPFQSKPDNYTPEQDSKNKDSEEETAESAQLLSVQVETPDTNTRDLNM
SPHSSNSSSMNQLWC

Nsp1:

MSKHHHHHSGHHHTGHHHHHSGSHHHTGENLYFQGSNFNTPPQQNKTPFSFGTANNNSN
TTNQNSSTGAGAFGTGQSTFGFNNSAPNNTNNANSSITPAFGSNNTGNTAFGNSNPTSN
VFGSNNSTTNTFGSNSAGTSLFGSSAQQTksNGTAGGNTFGSSSLFNNSTNSNTTKPAFG
GLNFGGGNNTPSTGNANTSNNLFGATANANKPAFSFGATTNDDKKTEPDKPAFSFNS
SVGNKTDQAAPTTFGFSFSQLGGNKTVNEAAKPSLSFGSGSAGANPAGASQPEPTTNEPA
KPALSFGTATSDNKTTNTTPSFSFGAKSDENKAGATSKPAFSFGAKPEEKKDDNSSKPAFSF
GAKSNEDKQDGTAKPAFSFGAKPAEKNNNETSKPAFSFGAKSDEKKDGDASKPAFSFGAK
PDENKASATSKPAFSFGAKPEEKKDDNSSKPAFSFGAKSNEDKQDGTAKPAFSFGAKPAEK
NNNETSKPAFSFGAKSDEKKDGDASKPAFSFGAKSDEKKDSDSSKPAFSFGTKSNEKKDSG
SSKPAFSFGAKPDEKKNDEVSKPAFSFGAKANEEKESDESKSAFSFGSKPTGKEEGDGAKA
AISFGAKPEEQSSDTSKPAFTFGAQKDNEKKTETSC

Nsp1-S:

MSKHHHHHSGHHHTGHHHHHSGSHHHTGENLYFQGSNSNTPQQNKTPSSSGTANNNSN
TTNQNSSTGAGASGTGQSTSGSNNSAPNNTNNANSSSTPASGSNNTGNTASGNSNPTSN
SSGSNNSTTNTSGSNSAGTSSSGSSAQQTksNGTAGGNTSGSSSSNNSTNSNTTKPASG
GSNSGGNNTPSTGNANTSNNSSGATANANKPASSSGATTNDDKKTEPDKPASSNS
SGNKTDQAPTTGSSSGSQSGGNKTSNEAAKPSSSSGSGSAGANPAGASQPEPTTNEPAKP
ASSSGTATSDNKTTNTTPSSSSGAKSDENKAGATSKPASSSGAKPEEKKDDNSSKPASSSGA
KSNEDEKQDGTAKPASSSGAKPAEKNNNETSKPASSSGAKSDEKKDGDASKPASSSGAKPD
ENKASATSKPASSSGAKPEEKKDDNSSKPASSSGAKSNEDKQDGTAKPASSSGAKPAEKNN
NETSKPASSSGAKSDEKKDGDASKPASSSGAKSDEKKDSDSSKPASSSGTKSNEKKDSGSSK
PASSSGAKPDEKKNDESSKPASSSGAKANEEKESDESKSASSSGSKPTGKEEGDGAKAASS
GAKPEEQSSDTSKPASTSGAQKDNEKKTETSC

Kap95:

MSTAFAQLLENSILSPDQNI RL TSETQLKKLSNDNFLQFAGLSSQVLIDENTKLEGRILAA
LTLKNELVSKDSVKTQQFAQRWITQVSPEAKNQIKTNALTALVSI EPRIANAAAQLIAAIADI
ELPHGAWPELMKIMVDNTGAEQPENVKRASLLALGYMCESADPQS QALVSSSNILIAIVQ
GAQSTETSKAVRLAALNALADSLIFIKNNMEREGERNYLMQVVCEATQAEDIEVQAAAFGC
LCKIMSLYTFM KPYMEQALYALTIATMKSPNDKVASMTVEFWSTICEEIIDIA YELAQFPQ
SPLQSYNFALSSIKDVVPNLLNLLTRQNEDEPEDDDWNVMSAGACLQLFAQNCGNHILEP
VLEFVEQNITADNWRNREAAVMAFGSIMDGPDKVQRITYYVHQALPSILNLMNDQSLQVK
ETTAWCIGRIADSVAESIDPQQHLPGVVQACLIGLQDHPKVATNCSWTIINLVEQLAEATPS
PIYNFYPALVDGLIGANRIDNEFNARASAFSALTMMVEYATDTVAETSASISTFVMDKLGQ

TMSVDENQLTLEDAQSLQELQSNILTVLAAVIRKSPSSVEPVADMLMGLFFRLLLEKKDSAFI
EDDVFYAISALAASLGKGFEEKYLETFSPYLLKALNQVDSPPVSITAVGFIADISNSLEEDFRYS
DAMMNVL AQMISNPNARRELKPAVLSVFGDIASNIGADFIPYLN DIMALCVAAQNTKPEN
GTLEALDYQIKVLEAVL DAYVGIVAGLHDKPEALFPYVGTIFQFIAQVAEDPQLYSEDATSRA
AVGLIGDIAAMFPDGSIKQFYGQDWVIDYIKRTRSGQLFSQATKDTARWAREQQKRQLSL

BSA:

MKWVTFISLLLLFSSAYSRGVFRRDTHKSEIAHRFKDLGEEHFKGLVLIAFSQYLQQCPFDE
HVKLVNELTEFAKTCVADESHAGCEKSLHTLFGDELCKVASLRETYGDMADCCEKQEPER
NECFLSHKDDSPDLPKLPDPNTLCDEFKADEKKFWGKYLYEIARRHPYFYAPELLYYANK
YNGVFQECQAEDKGACLLPKIETMREKVLASSARQLRCASIQKFGERALKAWSVARLSQ
KFPKAEFVEVTKLVTDLT KVHKECCHGDLLECADDRADLAKYICDNQDTISSKLKECCDK
PLLEKSHCIAEVEKDAIPENLPPLTADFAEDKDVCKNYQEAQDAFLGSFLYEYSRRHPEYAV
SVLLRLAKEYEATLEECCA KDDPHACYSTVF DKLHLVDEPQNLIKQNC DQFEKLGEYGF
QNALIVRYTRKVPQVSTPTLVEVSRSLGKVGTRCCTKPESERMPCTEDYLSLILNRLCVLHE
KTPVSEKVTKCCTESLVNRRPCFSALTPDETYVPKAFDEKLFTFHADICTLPDTEKQIKKQT
ALVELLKHKPKATEEQ LKTVMENFVAFVDKCCAADDKEACFAVEGPKLVVSTQTALA

5

5.5.2. OVERVIEW OF MEASURED STOKES DIAMETERS FOR THE PROTEIN USED BY DLS.

Protein	Average Stokes diameter (nm)	Standard deviation (nm)
NupX	7.4	±2.2
Nsp1	14.9	±3.9
Nsp1-S	13.5	±3.1
Kap95	9.2	±1.2
BSA	8.5	±3.3

Table S5.1: Hydrodynamic diameter measured with Dynamic Light Scattering (DLS) of the proteins used. Data were all acquired in 150 mM KCl, 10 mM Tris, 1mM EDTA, at pH 7.5, room temperature.

5.5.3. SEQUENCES OF 25 NUPX VARIANTS.

Variant number	Sequence
1	HHHHHHTGGGNTPNGNF GGGSAGQANAFGLFGTANGSGQ QSGFGQNSNTGTNSNGLFGQNGNFVANASFGTQSGNSPSGS GLFGPKSIMPQPQSFGNAVSSNSTSTGLFGTTTLNQNTTLFG TGNNGTGTPKGLFGMAANNQGN NFGSGTSLQSQAKGLFG DGLMRKFKKPKQLPGLSNAMLNEHEPSNTLLAAQSPSFISSIK NNNSSKRKNSGEDIIQDNGRTDPNCVFSSINDRYANDDTAT ATMSPISSAQTYKDDNPAQEKSTSQKTD SKQESKLSFESEKRK LVAEAWLNLNKSPSIFDVLTEV

2	HHHHHHQTAGGQNPNAFGSGQNSLNNPKGLFGSNTNGNQ TSTFGPAGTQSSSGSGLFGGNGNQTMQLFGSGSAQGNSTG GLFGNSSQQVGTNAFGVSTNAGITNQGLFGGQFKNNGTAPF GTKLSSANATNGLFGTASGQPMNTSFGSNGSFNNPTTGLFG DSTLLWITSSLPSDKTPKLSKYRNEAVKDDSPATIVLNNKIVNEL KNDGNKNFDQTAKSLGIRLRDLPNRNEQNESNCAMIDQLF DDPSQSMKAFFSPSQETHAETKSFKELAIKTDSSSGSNAPKS KRSSIAQAGNSYAEKNPQMTE
3	HHHHHHNSGSPNNNQQFGASQTQNAKTGFLGQTKGATT QSNFGPGNPITQSNNGLFGGNAMGNSNSTFGSGQNTSLNN SGLFGTGANGSNNQAFGGSGLSSAFTQGLFGNASGVSTGGKF GPTSQNLNTAPNGLFGQMTTPGSSGNFGFSANGTVQGGGLFG QSDGRSSKSLNADSYLLNSSHLDNNSDKRNKFPIAFKTPFIKN SQTSSSALAEMFASNKDDPFEQINAQKVIKEIEKLALNMDCN KIQLAPVTSTIPQDSGSDSPSEMTDLKPTSKSKGYWLPGDQSE ENVKRNELSKATTRTRNNAVE
4	HHHHHHNVSGVGPSTNFGQGGGTNNTNGGLFGGFNNSSP LSSFGQNPATTSNASGLFGTNNAGTAGGAFGQQKMGMQNNQ QGLFGSGNNNNKASFGTNQTGITPSAGLFGSNNGGNTKLQ FGGPLQFTTQGGQLFGSSNSMNTTTTFGSASGPSASQAGLFG LLNMFSAANTFLTSHDQIQIKKPEMDNNGSVETSLNDSRKSrk ANPCDIISQTSRSNNIDILNQSSGPQNAKEAIVRNSFPESPDE KTLLEYKSFNKSEESPSRKSDDTLTLQLSKENWADGMAAGISK VYQKSLNPLKKPASFTEDVDA
5	HHHHHHSTGTTSKNTNFGQQSSLGNALTGLFGSSNPSSAMS SFGAAGNSGGATIGLFGSAGNTNNGQQFGTNPQAANPGMG LFGTTSQNPSKNTFGSQGPSNNGNNGLFGTFSTTTANQNFG LGSGVQNNPVGLFGGNSTSFQQAFGGNNGQQNKGGGLFG VPNNDESISQPQEEENFKDLEGFLSRKSLLANLEVATIKTEKKS QPVAAKYNSSIKPANPKDNGQISTALPMKFCGPLDSSKSDISSI DMTNDDRTSHWSRENSNTDSTIKALFKLSNVLSQNRAQPKS KDYEQAFLMAKDTNSTNGRE
6	HHHHHHGSAASGSSGNFGGNSAPFSSTQGLFGSSGGIVTNT KFGTNGNQATGTNGLFGFQQSQSNQGNKFGNQGMAAATKN GLFGTQTPPGTSNNFGNQSNTPNNGSGLFGTTLGNTTSAAF GAPMLNQSTSGGLFGQSNPQSNQGSFGTNVQGNNSLGGFL GKSQPSIWENSQMDRSPDNSNYEDLMGSPNFYPLKNSADIQ LPEKKRSLTSLKQAIESGFEDSLSDEFRPTDKMKTKNCEFND KDTKINVAAKIEPASNFKNLIQIAEGSDVSRNDRAASTTSLST LTVLHSGQSSPATNNKKASLVQ

7	HHHHHHHSGSGSPGSGNSFGGQPPQGQNGGPGLFGQAQNTSQ QAMFGATANMTNTASGLFGGGSNNSSGNTFGTKANNNGNVS PGLFGSNSTTNSLNSFGKQLTPNQSLNGLFGTIVTSGNNQTF GNTAGNTPSSQGLFGASSGNGNFGAFGTTTGKQAFNQGLFG DNNNSEIDSFQYFNPETKDVRMKNEEAKFPEPKDLLINPSWG RPKSTLSQSRKFTSNDISTCNEADSKSLSNLSEKQAMVLGRPK LKSNNLSSATEDGMGILAAVEDKSAQDYTSAIPKSQSRFHSND IKSLKTNNQTAQIPVSALDTN
8	HHHHHHHQATVNFNQNAFGAAQAGSMAGNGLFGGGMQSSS NKAFGTINGGGSQNAAGLFGTTSGSPNNSTFGTSQSQKGGNT GLFGFSPSQTQGSFGNGSSTVSNPNGLFGNGLPTNLQGF GNTSTTNQAGTGLFGTSSPQQPAGNFGNNGTKNSLNTGLFG GDNSDQDINHLISNSKLDLSAESNTLFMKQEEKAKYWKSNP DETLAEKTSNSDTPNINLSLPTSSNPARAQASSMRVILASTT SFKVLTGLKNSENKFKFQPLKQGKMNSINADRCQSPDSD PEYKSVRNSETIIVKDARAEPFG
9	HHHHHHHGGTASQNNSAFGSGSTTSAQNNGLFGTKSNTGQF PNFGSVGNNTPGSNGLFGSSATGTQQSNFGTNGTNKMPSSG LFGSGAMTLTFNSFGNQVTAGNNGAGLFGNQLTQTNPSSQFG GPSANNSNGTGLFGNGLSPQAIKQFGGQGGGQTASNGLFGA QKPKNAQNGQATDKIPIAAPLFDIWKNLKLRNSVLSEEKST FKAEPNNQSKKNCLAVPQNDHSSSTRNEVDTPSALTRISM SGGNMEKLFLRTNPEIYDESNSSSAESTSKNSDKDIFQNSDYT SQIDATSLSEFLMDLGSVPS
10	HHHHHHHFQTKNNGNNSFGTSQTGQGSATGLFGNNANSSPA STFGNSGLATTNNGGLFGGNGNSNNTLGFGSANSQQSQGM GLFGSGTSNPGQATFGNGQSFSAGTNGLFGPQVPGGAKNNF GITTATSQPQPGLFGSSTNTVQTQMFLAGNSGNSKGGFLFG NRDGTIDEAGDSTQKAPSLIELGSELLTESPAATIESLNREEKR TNPKSMMLSSYFNEKSKTKLDISNEFNNTKNVSTNSDVPAAAP RPCSKSSLFTNIMQFDKSKDRLFSKNVKLAKPAQDVMQNDQI DDKSKWIHQYLQANPSSSSGN
11	HHHHHHHTSGSSNGVNPFGQTNFQPNNVGGLFGGTGGSAP NKNFGAANSNNSTSNGLFGMGNSNQQGSFPGTAAQNSSGT TGLFGGNSNGTPSLSFGTSSSGTGLNGLFGNPSGNTAQGA FGQQNMSGFGQTGLFGQGTANLQNQIFGSATQTTTKAGLF GQNNELLSAHDKNKSPKNMAAESANRSFKSLEVQATIIKSNR YGNNSSKILLSRFEKEPIMQNPPKTNDPCVTVSLSSDNQLTSSS AEDPASGEFNRTDIWLTESLDKYGGDVATNQAQASSSIMLL KQDEFIRKDKPTSDDKNSFKPTK

12	HHHHHHHAQGQGKKAQSFGSLTSSNSSNGLFGQNNQTGN QTNFGTGQGGSTANSGLFGSGGNSNTQNGFGAGFPGSPMS VGLFGSNQNGNANGTFGGTSSLNLIPTGLFGNSGNANSMTT FGSTPQVFQATSGLFGNGAGTPPSGTFGGQNSATKNNAGLF GEMNTSVTIEQIDAKKNSDNSFEIESYQSTVRSTWNLKSLQD DNSNSNSPLDGDPIPIRNSQSSYSEDNTDSLKMKTAMKEGEL DSERSSGAVDFSNNFIDSNKPICTKKKSQFTFKVGAKQAPKNL AAQHAPLAFKSPKRLNRLLLPA
13	HHHHHHHSGGNNGGTSGFGLSVQSQGASPLFGVQPKTTNG NQFGQNQSQANTGSGLFGPGSSASNLSFGGNPTAANANAG LFGTGANNSSSIMFGAMTSLNPNNQGLFGKKGNSGTSSNFG QGFTGNNSTQGLFGPTNTQANGFNFGTTGQTQTGTSGLFG CGISNNIYRDESPQISFSSESSHADENKKNPPSIKMSDNKSI IVALDSVMVEPTPKATNKDKVFSQSLSQYTKINDSDLAALNEF GQLQKNSQLPNSQRLDESSLRPSRNELSRFDKGAQMGGKKD DNNATKWTALLKTANTFEPT
14	HHHHHHHGQQTTPSLTKNFGTGSTGTASGAGLFGTNNSTSVT TFGNGNALSQNNTGLFGGSSQGSPGNFNGANNNTGGIG LFGGTTNGMNGFTFGSQASQQSFSNGLFGNSGASSNASFGP QPQGNQAALGLFGNKSNNVQNPMTGTQGGGKTQASGLFGT SPLNNFPQPFQMNQVNNIRSDVLLKQPVWPKSSLSSCQTIDKS RSQNMIAELNDLLAKFDQSIKEFKSNMSANKTSAENASVRKT DDTSASLEGEYEDLTLSRYGIGNSDFNKTPPNATDPTNSKD KKLSEIHSAAAKPEERGKSS
15	HHHHHHHLNNSSGNGTNFGSSQSGANNQNGLFGQTNSSSL PQTFGQGTSSNTNGLFGGGGQMASFTGFGASAQGSATNV GLFGPQTQQPKNTSFGAGNKGPNPNNGLFGSGTAQGTAF GSQANGSSPTNGLFGQVGNTGMNLTFGSSSKTTINNPGLFGL ELSFKNKANISTLMWKDKALLKPNASTSQFEKIPDITDSDKFT EAAVKPDDERPKENISSDARLDSSQESHIAKLKSNRLNANLST GRSKNGVPQATNIQEITQSKSDDYSTPFKVQNNVKLATMSSN PSCSGQNNYRGFLPSMEEDS
16	HHHHHHHSMAMFSQTTTQGGQTTQNNPNIGLFGGAALTGAS NSFGGQAQSGGTNGGLFGSTNPSQSSKSFGNQSGSGSTNTG LFGQSQQNSNGAAFNNNNKSGNTAGLFGAGNVGGNSNPF GNTNKAQVTTGLFGQQTNNSGSTNFGPGPTNGLLTFGLFG PESTSLVSKKDISTIDLANKANNQHDPDNFNPVKVDKVQPN GDETQPQDLSMELSMRQKGANQKNASCQERSWKAFFSFKL KNANDTIFSILNKKPLSSLYETKKLSGTRAMTGKDFAESAPTS NDRSSTANLSNIDESIIRELEYS

17	HHHHHHTSNTQGGAGNFGGTPAGSNNSTGLFGITGQNQSG NQFGQGKMNTQPQGLFGQNSGGSTNNNFGNATSNTVFNS GLFGQNAASQGGNQFGTQNMTTKFANGLFGTNLNLVSPSSF GNGGSSSGNKLGLFGSPSGNSGGASFGAAATSPTQTTLGFE EQLTSDLNCVPTSDQNNSDIRFTTKQETLSNAGALMPKQSSS DDWNAENKAKYLEIDTEKEQFPINKTPSMDATSNRTVLKERS SFNPRKKASNSFSKDYFSKNIAPVISDISGRELKSHSSNDKL QALANINPPAQMDVKLGGS
18	HHHHHHQGGNQGPSSTFGSSGNQAGVTGLFGNPSNMNV NQFFGANSTSGAPNGGLFGNTAMNAQTGGFGTGNTSQSTP AGLFGKQSPNGKNATFGITSGGNQSNNGLFGNANGQQKNP FFGLGTSTASSGSLFGTGNSNTGNTSFGNALSTQSQTGGLF GNLNRNTQINEKSQRASLSSKAISDATSQENTQVNCLNNYNE SKSDQNHVPVEKKDSAWQKSGTSKTSSESSQKAERSIFDVISFL PLTRDVGSLAKKTPDFDGENMKFSDELGKSFRSKANPAPLIA PKNLSDITYDMNAMLPDKLEPI
19	HHHHHHHTTASFNNGGTFGSSNPNTSNKGGFGTSGQNSTS STFGNQAAQIGGGNGLFGMVQANSNQPPFGAQKNNTQNST GLFGSQFSGSPLASFGLTSNTNASTGLFGNATMVNSSSTFG AGQGGNQQQGGLFGQPNLTAGNNGFGPGKTTSGNGNGLF GIQANRSISPNSDQNEHKVKWESSITLDGKTAFDADQSAISAN DSNKNIGNKSLPQDGLSCSAAMNPLTSRESSTKLLFSNNKLI RYERSLFSDRLTENPDSEKDDTMKKNDQKFSKGTVVYQVFPT LPQKEAANPELESKPASITMDNK
20	HHHHHHPPSQNNQKQTFGNQNSTANNSSGLFGANNGTSSQ AANFGVNQNTGTQTSGLFGSSTSQAQSGGFGTTPAGQTNNT GLFGGNTNANNPGSFGTSKGNPIGQAGLFGGQGSFASKPAF GVMSGNGNSGGGLFGSSQSTFGNLLFGNGTLSTMTNGGLF GQSDKNSNSISDFNCTIDDKAITKVLAKALQNKEDVFRPNSSK KAVSPKSKSETINDDLVRTSPDGYTESLSILNSSSAMPRKGTTL LTAQFKSQLYEFDPDENSKDRKPKSMDWSNERGKNGENLISAF QLANQISMPAATSENLQPHNE
21	HHHHHHVQGNNGGQKTQFGTSSNNAGPNQGLFGQAKNTNS QGQFGAGPAGPTNSNGLFGTNGNSNAGGQFGKNMSFSNFG TGLFGSSNQALPASFGSTNVSNPTQPGLFGTNSIATAMSGF GQGGSSGTNANGLFGNGSTSNLTFTGTTSLQTSNGGGLFG KQARPSSADPQIKSSMDSSQVDPLQNKPEKLSHDEANLKPLS PDEEKFITYINTSRQNELKSSKELYIMNDGWGNRNKKFDSSTS KIFSNFTTEANRLNELDGD LAPKSNDKMPRTSVAKSNSFQVS AETSGNCKTTQIDNAASILVLA

22	HHHHHHPTSTTATSNTFGNTSNNNNNGNGGLFGTNQKTSQ NTSFGGGILTAGTSSGLFGFFNGNTTNKAFGPPPGNAQGASG LFGSPAPQKGSSGFGSGNTNMNSQTGLFGMQSGQTGQLSFG QSPANANNQNGLFGSGGANVSSALFGTNVSGQGNQQGLFG TGSRAFKRPINSSCDETPSNAIKNQLKSKDGKNDDRDNPDVQ TEANESSMAQSAELDTPAKYREDFIFQSELKTANALKTDASLG NSDLINQTSVDSPLLESIQSKKLTTPLSRMNFKLSMKKESSKN HGSPewVAFSQYINVNSINP
23	HHHHHHNNTTQPNQNNFGLSQGSTQTSSGLFGSQQMNG TNPFGGQNGTGSSAGLFGQGGNGSGTSTFGGAGKNNTGF PGLFGPKAAGSNLPsfGGNSLTQnatGGLFGTAISTPVQSTFG AMNNSTGASNGLFGKNTGNSTQVNFgfSSAQNNsAGLFG LEKSSensMTDKfSAKSSISKVAQeAVPVLGARPSDFAKFNPT YGPskLQLNTDQeAIRKNSKQqNTmSENDTFKTRVnELNDQ QSDWACPnRHDSKNEETKALILAPGSnASPTnYSILLIDLKfS EPKNISSMLSDKSNIGDTSRKD
24	HHHHHHASGLASSSNGFGTSQTTGTsqPGLFGANSKGGQAP AFGGAGSPNGNQTLFGQSMQSTAGTAFGNTNNMTSKGQG LFGGTNQSANQNSFGPVGNSNGNGPGLFGNGNQGTkQNSF GQLQATNTLNGGLFGTVNNTSPSNNFGITSfNSfGTSGLFGR NNISLSKYLRKLNCePAKGfSRKEAATTWPQSKSAKINDESSQ ASQTMITVNFSTSSVAETKkELSPNFsQSSLFDDIKHSYADTE DSSADGTIVPPVDLENLNQSGSMSAKNKGDLdkQKPKNKN NEFEARLLQDMINNSDITRPL
25	HHHHHHHAQGNTSQNAGFGQPTSTGTTNfGLFGTNSTAQQ NNNfGGQQAAPSGNNGLFGLSSNSTLTKTfGTNNIqNPSAS GLFGNKSASSAVSGFGMGLNVQSGGAGLFGQNPNsNGGTN FGSPNGKQGTsNGLFGNGTPMGANSSFGGTGTfTSQGQGLF GSLISPENTERSEIPTKVWSKVGSPKPIfNYLQTSLSLTlNQnKS YQSLQSSGRFNKNSKEPALELLRDFDGKEMENLTnKKDDSK DDNRNKTkSTCMQASPfASLASHFDNTKGDDPIEDASVSEV QAIAMSPRTKAakLSNIANQDSN

Table S5.2: Sequences of 25 NupX variants.

5.5.4. SIMULATION PARAMETERS USED FOR MD-SIMULATIONS

System description	System size (no. of beads)	No. of sim-ulations	Forcefield	Timestep (ps)	Simulation time (steps)	Temperature (K)
NupX protein	311	1	1-BPA	0.02	5.00E+08	300
NupX variants	311	25	1-BPA	0.02	5.00E+08	300
NupX brush, 5.7 nm spacing	12060	1	1-BPA	0.02	1.75E+08	300

NupX brush, PMF, Kap	12233	46	1-BPA	0.02	5.00E+07	300
NupX brush, PMF, Kap equilibration	12233	46	1-BPA	0.02	5.00E+06	300
NupX brush, PMF, inert particle	12223	47	1-BPA	0.02	5.00E+07	300
NupX brush, PMF, inert particle equilibration	12223	47	1-BPA	0.02	5.00E+06	300
NupX brush, 4 nm spacing	11991	1	1-BPA	0.02	1.75E+08	300
NupX brush, PMF, Kap	12164	51	1-BPA	0.02	5.00E+07	300
NupX brush, PMF, Kap equilibration	12164	51	1-BPA	0.02	5.00E+06	300
NupX brush, PMF, inert particle	12154	51	1-BPA	0.02	5.00E+07	300
NupX brush, PMF, inert particle equilibration	12154	51	1-BPA	0.02	5.00E+06	300
NupX nanopore, 15 nm	11407	1	1-BPA	0.015	2.00E+08	300
NupX nanopore, 15 nm, equilibration	11407	1	1-BPA	0.015	5.00E+06	270
NupX nanopore, 20 nm	15551	1	1-BPA	0.015	2.00E+08	300
NupX nanopore, 20 nm, equilibration	15551	1	1-BPA	0.015	5.00E+06	270
NupX nanopore, 25 nm	19694	1	1-BPA	0.015	2.00E+08	300
NupX nanopore, 25 nm, equilibration	19694	1	1-BPA	0.015	5.00E+06	270
NupX nanopore, 30 nm	23834	1	1-BPA	0.015	4.00E+08	300
NupX nanopore, 30 nm, equilibration	23834	1	1-BPA	0.015	5.00E+06	270
NupX nanopore, 35 nm	27977	1	1-BPA	0.015	2.00E+08	300
NupX nanopore, 35 nm, equilibration	27977	1	1-BPA	0.015	5.00E+06	270
NupX nanopore, 40 nm	32121	1	1-BPA	0.015	2.00E+08	300

NupX nanopore, 40 nm, equilibration	32121	1	1-BPA	0.015	5.00E+06	270
NupX nanopore, 45 nm	36260	1	1-BPA	0.015	2.00E+08	300
NupX nanopore, 45 nm, equilibration	36260	1	1-BPA	0.015	5.00E+06	270
NupX nanopore, 50 nm	39160	1	1-BPA	0.015	2.00E+08	300
NupX nanopore, 50 nm, equilibration	39160	1	1-BPA	0.015	5.00E+06	270
NupX nanopore, 60 nm	47443	1	1-BPA	0.015	2.00E+08	300
NupX nanopore, 60 nm, equilibration	47443	1	1-BPA	0.015	5.00E+06	270
NupX nanopore, 70nm	55726	1	1-BPA	0.015	2.00E+08	300
NupX nanopore, 70 nm, equilibration	55726	1	1-BPA	0.015	5.00E+06	270
NupX variants in nanopores, 30nm	23834	25	1-BPA	0.015	2.00E+08	300
NupX variants in nanopores, 30nm (equilibration)	23834	25	1-BPA	0.015	5.00E+06	270
30nm NupX nanopore with 10 Kap95p particles and cylindrical occlusion	38574	1	1-BPA	0.015	3.33E+08	300
30nm NupX nanopore with 10 inert particles and cylindrical occlusion	38474	1	1-BPA	0.015	3.33E+08	300

Table S5.3: Simulation parameters used for MD-simulations.

5.5.5. LIST OF PRIMERS FOR GST-3C-KAP95

Name	Sequence
ed7	5'-TTCCAGGGGGCCCGCATCTGTTGGATCCATGTCCACC-3'
ed8	5'-CAGAACTTCCAGATCCGATTTTGGAGGATGGTC-3'

Table S5.4: List of primers for GST-3C-Kap95.

5.5.6. NUPX AND KAP95 SDS-PAGE

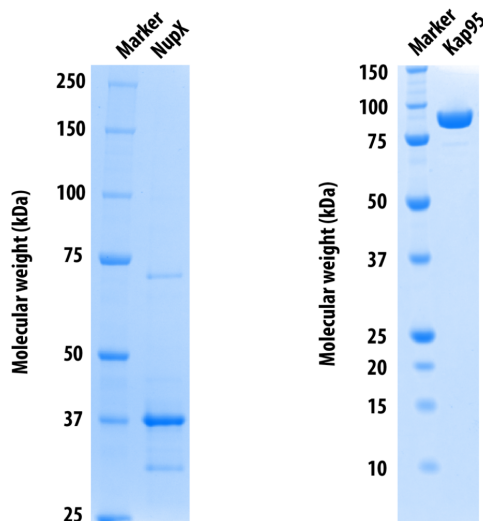


Figure S5.8: SDS-PAGE gel shows the band for the 32.5 kDa NupX molecule (left, thick bend running at ~37 kDa) and the 95kDa Kap95 molecule (right) after purification. This experiment was reproduced more than three times yielding similar results.

5.5.7. NUPX COATING OF GOLD SURFACES UNDER DIFFERENT CONCENTRATIONS

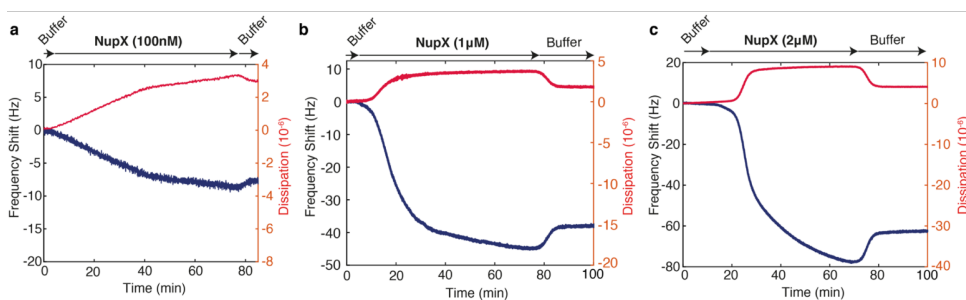


Figure S5.9: Real-time monitoring of NupX-coating of gold-coated quartz chips under concentrations of 100 nM (a), 1 μ M (b), and 2 μ M (c) at constant flow-rate (20 μ L/min), using QCM-D. The slight increase in frequency at the end of the incubation represents the washing step, which induces a subsequent release of non-specifically bound NupX molecules. The NupX solution included also 1 mM of TCEP in order to reduce the cysteines, which was present during the coating step.

5.5.8. SPR MEASUREMENTS OF PROTEIN- AND MUTEG-FUNCTIONALIZED CHIPS

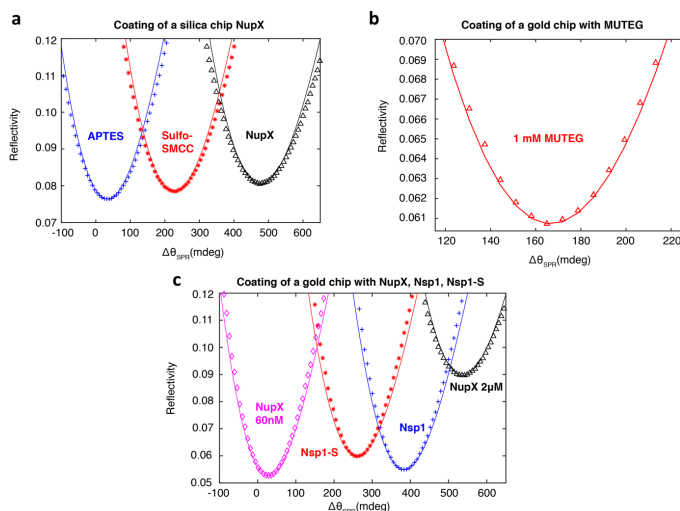


Figure S5.10: Angular reflectivity spectra of SPR measurements for dried samples in air. a Data for APTES (blue crosses), APTES + Sulfo-SMCC (red asterisks), and APTES + Sulfo-SMCC + NupX (black triangles) on silicodioxide-coated sensors. b Data for MUTEG (380 Da) on gold sensors grafted using 1 mM concentration. c Data for 1 μ M Nsp1 (blue crosses), 1 μ M Nsp1-S (red asterisks), 2 μ M (black triangles) and 60 nM NupX (pink diamonds) on gold sensors. $\Delta\theta_{SPR}$ denotes the angular shift in millidegrees of the resonance angle. Solid lines show Fresnel model fits (which are offset in the y -direction to match the measurement reflectivity minima), which are used to determine the thickness of each adlayer.

5.5.9. PASSIVATION OF NUPX-COVERED AU-SURFACES USING MUTEG

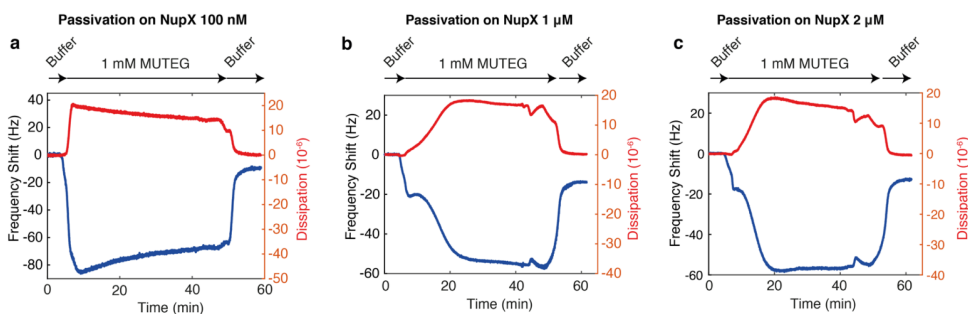


Figure S5.11: Real-time monitoring of 1 mM MUTEG binding to gold chips that were pre-functionalized with NupX at NupX concentrations of 100 nM (a), 1 μ M (b), and 2 μ M (c) at constant flow-rate (20 μ L/min), using QCM-D. Note that final dissipation shifts were all close to zero, while (negative) frequency shifts were found in the range of \sim 10-14 Hz, indicating the formation of a thin monolayer. The MUTEG solution included also 10 mM of TCEP in order to reduce the thiols, which was present during the coating step (same for Fig.S5.10a).

5.5.10. KAP95 BINDING TO PASSIVATED GOLD QCM-D CHIP

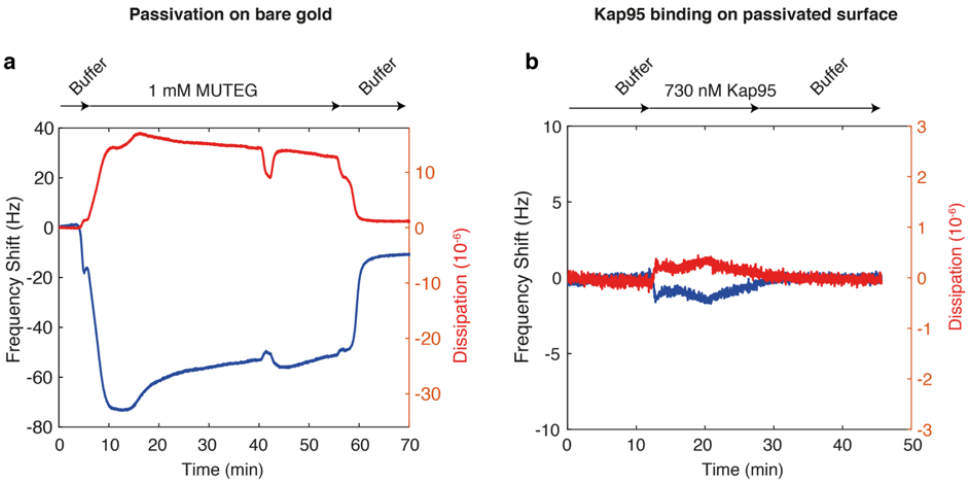


Figure S5.12: Real-time monitoring of Kap95 interacting with a MUTEG-passivated gold surface. a, Frequency shift over time upon flushing of 1 mM of 1-mercaptop-11-undecylte-tra(ethyleneglycol) (MUTEG) onto a gold surface. From an independent measurement using SPR (Fig.S5.10b) where the same incubation time and concentration were used, the MUTEG coating of a bare gold surface yielded a dense monolayer with a 0.59 ± 0.01 nm average grafting distance. b, Frequency shift over time upon flushing of 730 nM of Kap95 to a MUTEG-passivated gold layer. Only minor interactions (< 2 Hz) were detected.

5.5.11. KAP95 DISSOCIATION FROM NUPX BY 0.2 M NaOH

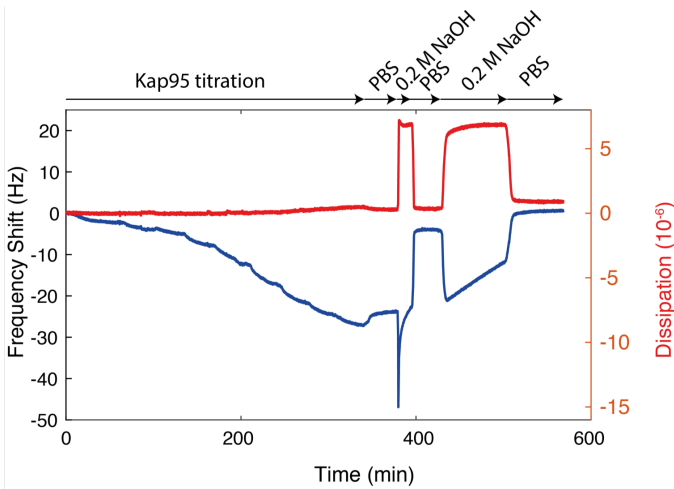


Figure S5.13: Real-time monitoring of Kap95 interacting with a NupX-coated surface with subsequent dissociation upon flushing of 0.2 M NaOH.

5.5.12. KAP95 VS BSA BINDING TO DIFFERENT NUPX-COATED GOLD SURFACES

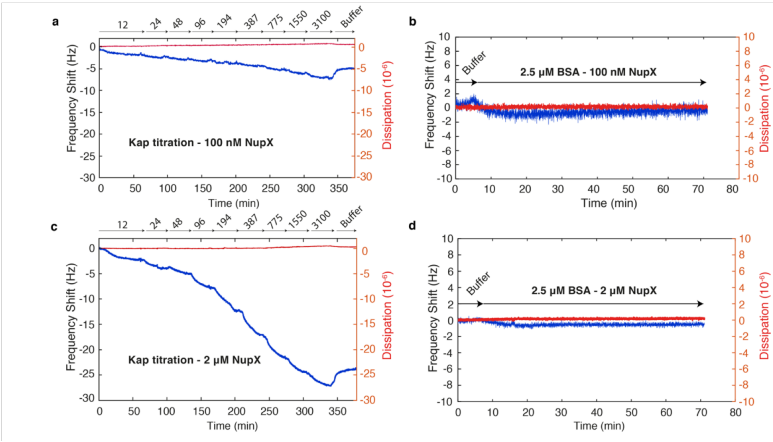


Figure S5.14: Real-time monitoring of ~10-3000 nM Kap95 and 2500 nM BSA binding to gold chips functionalized with NupX at a concentration of 100 nM (a-b, respectively) and 2 μM (c-d, respectively), at constant flow-rate (20 μL/min), using QCM-D.

5.5.13. TESTING THE STABILITY OF NUPX COATINGS AGAINST MILLIQ AND 50% PURE ETHANOL

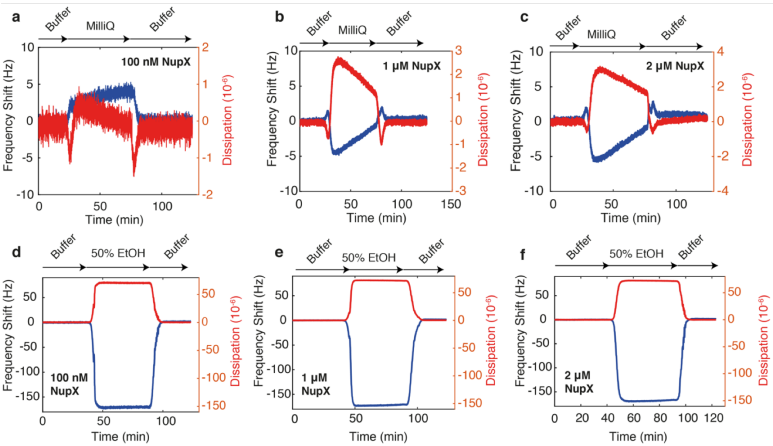


Figure S5.15: Real-time monitoring of milliQ and 50% pure ethanol rinsing of gold surfaces that were pre-coated with NupX and subsequently passivated with 1 mM MUTE_G, at different NupX concentrations of 100 nM (a,d, respectively), 1 μM (b,e, respectively), and 2 μM (c,f, respectively), at constant flow-rate (20 μL/min), using QCM-D. Note that final frequency and dissipation shifts are all close to zero, indicating that our protein and MUTE_G layers are stably bound to the gold surface.

5.5.14. DISSIPATION-TO-FREQUENCY RATIO CHANGE UPON QCM-D COATING

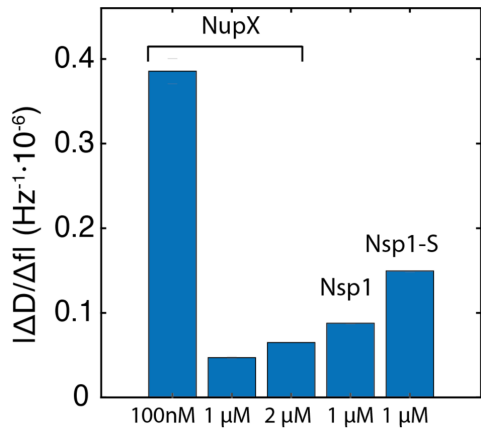


Figure S5.16: Dissipation-to-frequency ratio $\Delta D_5/\Delta f_5/5$ for NupX (with concentrations as in Figure ??), Nsp1, Nsp1-S coating of a gold-coated quartz chip. When comparing the 3 proteins (NupX, Nsp1, and Nsp1-S) for the same incubation concentration of 1 μM , NupX produced the lowest dissipation-to-frequency ratio, consistent with the higher hydrophobic character of GLFG-type Nups (*e.g.* Nup98 [1]), and hence of NupX, as compared to FXFG-Nups. Note that these $\Delta D_5/\Delta f_5/5$ values are for the FG-Nup films only, *i.e.* prior MUTEG passivation.

5.5.15. DISSIPATION-TO-FREQUENCY RATIO OF A NUPX LAYER UPON INCREASING KAP95 CONCENTRATION

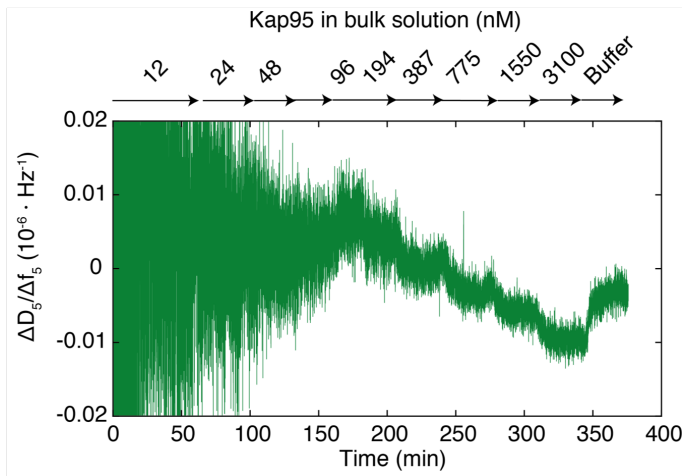


Figure S5.17: Dissipation-to-frequency ratio $\Delta D_5/\Delta f_5/5$ for Kap95 absorption to a NupX-coated surface for increasing concentrations (from 12 nM to 3100 nM).

5.5.16. COARSE-GRAINED SIMULATIONS OF CARGO ADSORPTION IN A NUPX BRUSH WITH A 5.7 NM GRAFTING DISTANCE

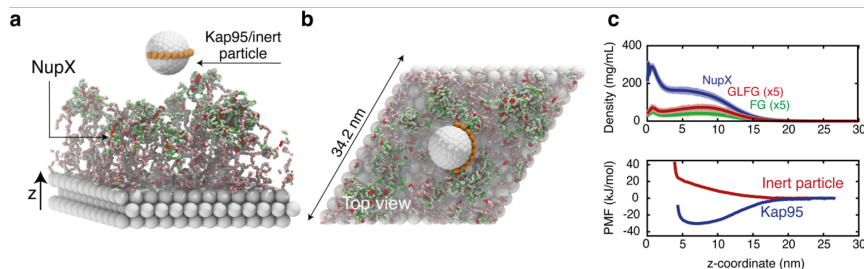


Figure S5.18: NupX brush system, simulated for a grafting distance of 5.7 nm. a,b Snapshots of the simulations (see also: Figure 5.3h). c, Top panel: Time and laterally averaged protein density distributions for the NupX brushes and for the two different types of FG motifs present inside the NupX brushes. The density profiles of the GLFG and FG motifs within the NupX brush are multiplied by 5 for clarity of display. Dark central lines and light shades indicate the mean and standard deviation in density profiles, respectively. These measures were obtained by averaging over the density profiles of trajectory windows 50 ns in length ($N=60$). A high-density region (up to a maximum of 300 mg/mL) forms near the attachment sites of the NupX to the surface ($z = 0$ to 2 nm). Further away from the scaffold, the protein density remains at a constant value of ~ 170 mg/mL up to a distance of ~ 8 nm, after which it decays. FG and GLFG motifs predominantly localize near the transitioning point (8 nm). Bottom panel: Free-energy profiles (PMF-curves) of the center of mass of the model Kap95 and inert particle along the z -coordinate, where $z = 0$ coincides with the substrate. The PMF-curves originate from a z -value where the distance between the center of mass of either particle and the substrate approaches one half of the former's diameter. The difference in sign between the PMF-curves of both particles indicates a strong preferential absorption of the model Kap95 to NupX brushes and a repulsive interaction of the inert particle. Compared to the brush with a lower grafting distance (see Figs. 5.3h,i in the main text), the repulsion and adsorption are less strong, which is due to the decrease in the density of the NupX brush and FG/GLFG-motifs, respectively (see c top panel).

5

5.5.17. MODEL KAP95 PARTICLE

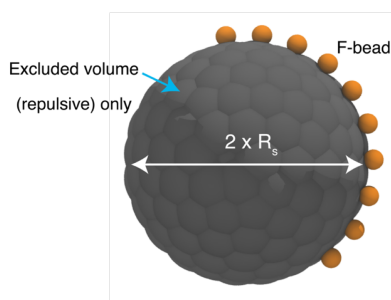


Figure S5.19: The computational model of the Kap95 particle used in this work, rendered using VMD2. The Kap95 (and the inert particle) consists of sterically repulsive beads (*i.e.*, only repulsive excluded volume interactions with its surroundings, here shown in dark grey) arranged in a geodesic shell. In the case of the Kap95 particle a strip of 10 hydrophobic binding sites (brown-orange) is placed on the surface, and the net charge ($-43e$) is distributed equally over all the surface beads. Binding sites are modeled as Phenylalanine beads and are spaced 1.3 nm apart on an arc. Phe-beads are the most hydrophobic particle type in our 1-BPA model. The diameter of Kap95 is equal to two times the Stokes radius (see Table S5.1).

5.5.18. CONDUCTANCE DECREASE UPON NUPX-COATING OF SOLID-STATE NANOPORES

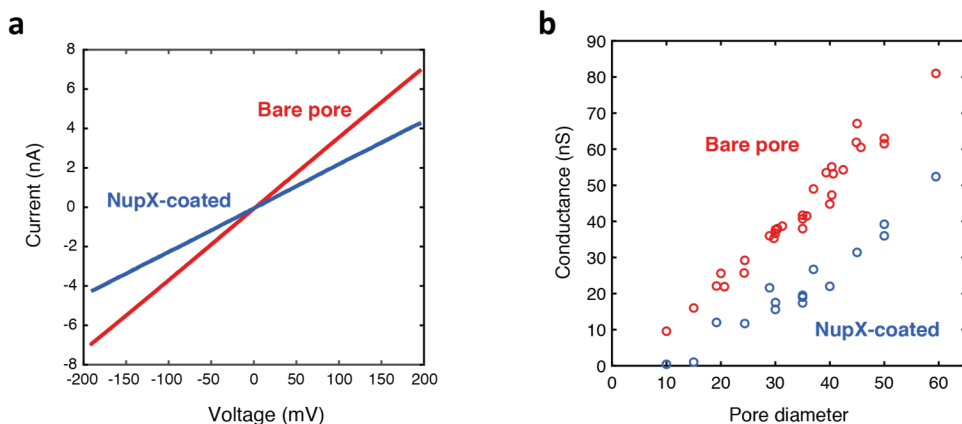


Figure S5.20: NupX-coating of solid-state nanopores. a, I-V characteristics for a bare (red) and NupX-coated (blue) 30 nm pore. b, Ionic conductance of differently sized nanopores over a range of 10-60 nm is plotted vs diameter for bare (red) and coated (blue) pores.

5.5.19. CURRENT POWER SPECTRAL DENSITY BEFORE AND AFTER NUPX-COATING

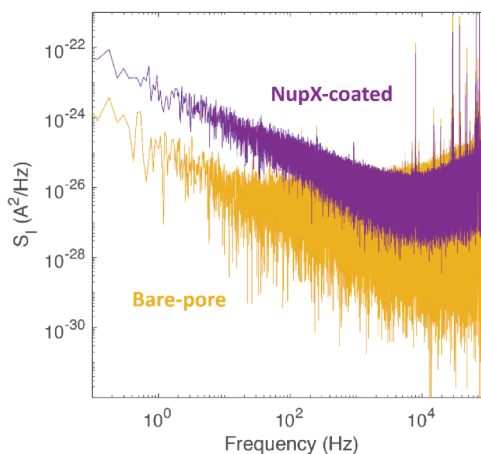


Figure S5.21: Power Spectral Density of the ionic current noise before (yellow curve) and after (purple) NupX-coating for a 30 nm pore.

5.5.20. SELECTIVITY MEASUREMENTS THROUGH DIFFERENT PORE SIZES (30 NM, 35 NM AND 60 NM)

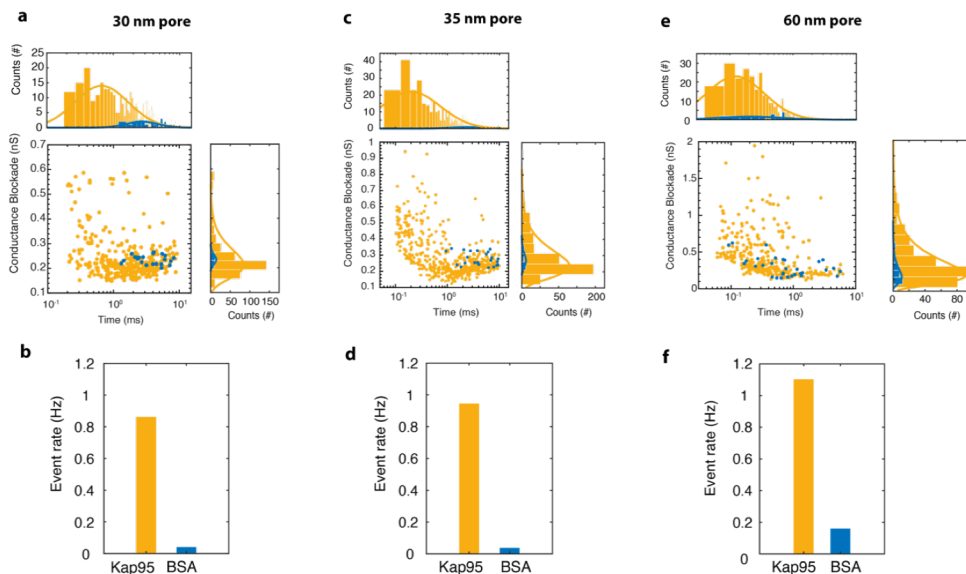


Figure S5.22: Selectivity measurements on NupX-coated pores of different sizes. Scatter plots show event distributions for translocations of $2.8 \mu\text{M}$ BSA and 450 nM Kap95 under 100 mV applied bias, in 150 mM KCl, $\text{pH } 7.4$ buffer. a-b, Scatter plot and bar plot showing (a) conductance blockades ($0.24 \pm 0.07 \text{ nS}$ for Kap95, $0.24 \pm 0.02 \text{ nS}$ for BSA; errors in s.d.) vs dwell times ($2.4 \pm 0.4 \text{ ms}$ for Kap95, $4.2 \pm 1.2 \text{ ms}$ for BSA; errors in s.e.m.) (b) and event rates (0.9 Hz for Kap95, 0.04 Hz for BSA) for translocations of Kap95 ($N=369$) and BSA ($N=22$) through a NupX-coated 30 nm pore. c-d, Scatter plot and bar plot showing (c) conductance blockades ($0.3 \pm 0.1 \text{ nS}$ for Kap95, $0.28 \pm 0.04 \text{ nS}$ for BSA; errors in s.d.) vs dwell times ($2.5 \pm 0.2 \text{ ms}$ for Kap95, $5.2 \pm 0.9 \text{ ms}$ for BSA; errors in s.e.m.) and (d) event rates (0.95 Hz for Kap95, 0.04 Hz for BSA) for translocations of Kap95 ($N=482$) and BSA ($N=23$) through a NupX-coated 35 nm . e-f, Scatter plot and bar plot showing (e) conductance blockades ($0.45 \pm 0.03 \text{ nS}$ for Kap95, $0.30 \pm 0.02 \text{ nS}$ for BSA; errors in s.d.) vs dwell times ($0.65 \pm 0.05 \text{ ms}$ for Kap95, $1.6 \pm 1.3 \text{ ms}$ for BSA; errors in s.e.m.) and (f) event rates (1.1 Hz for Kap95, 0.04 Hz for BSA) for translocations of Kap95 ($N=314$) and BSA ($N=32$) through a NupX-coated 60 nm pore.

5.5.21. EVENT RATE OF KAP95 TRANSLOCATION THROUGH NUPX-COATED PORES VS KAP95 CONCENTRATION

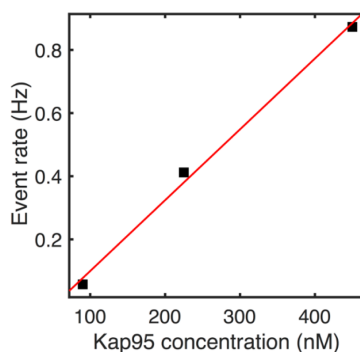


Figure S5.23: Event rate of translocation of Kap95 molecules through a NupX-coated pore, at increasing concentrations from 90 nM, 225 nM, to 450 nM. The translocation frequency increases linearly with concentration, as expected.

5.5.22. DENSITY DISTRIBUTIONS OF NUPX FOR DIFFERENT GRAFTING DENSITIES

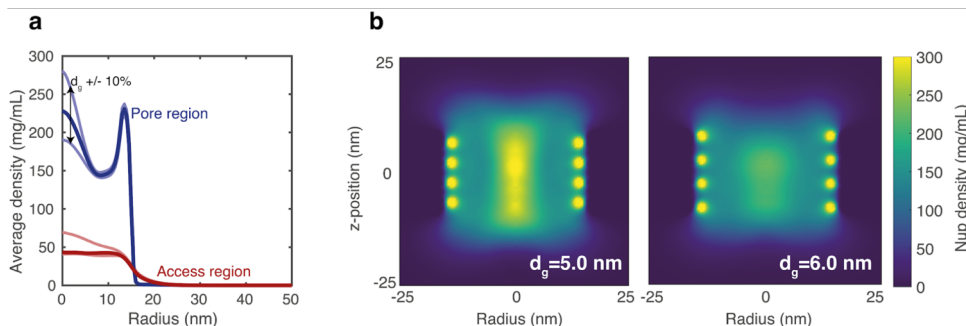


Figure S5.24: Sensitivity of the average pore and access region protein densities against a change in grafting distance d_g . a, Upon increase resp. decrease of the grafting distance with approx. 10% (6.0/5.0 nm as compared to 5.5 nm used for SiN in the main text), we observe a corresponding decrease (−17%) and increase (+22%) in the maximal pore region density (light blue and dark blue curves, resp.). The maximal access region density (red) is only sensitive to a decrease in grafting distance, where a 10% decrease in grafting distance yields a large density increase of +60% due to NupX proteins being expelled from the pore region (light red). b, Axi-radial density distributions of 30 nm NupX-lined nanopores upon an approximate 10% decrease (left panel) or increase (right panel) in grafting distance. The high-density region towards the central axis of the nanopore increases in density and extends over a larger range in the z -direction when the grafting distance is decreased, whereas the opposite occurs for an increase in grafting distance. The overall morphology of the NupX-meshwork in the nanopore remains consistent under an increase of approximately 10% in grafting distance.

5.5.23. DENSITY DISTRIBUTIONS OF NUPX IN THE ACCESS REGION

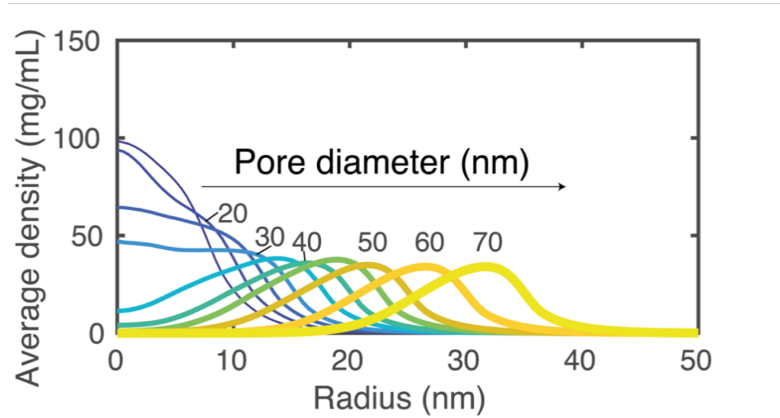


Figure S5.25: Access region densities for NupX-lined nanopores with diameters ranging from 15 nm to 70 nm. Lighter colors and increasing line thicknesses indicate larger diameter pores. A preferred localization of NupX proteins towards the central axis of the pore region occurs for a pore diameter of 30 nm and smaller.

5.5.24. DENSITY DISTRIBUTION OF NUPX IN A 30 NM PORE IN THE PRESENCE OF KAP95 MOLECULES

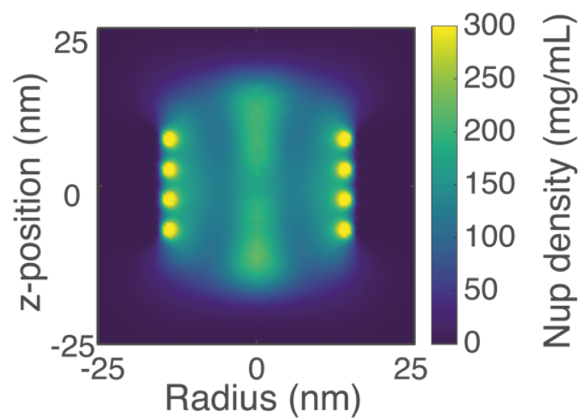


Figure S5.26: Axi-radial density map of the protein density distribution in a 30 nm NupX-lined nanopore that interacts with Kap95 particles. The density distribution shifts towards the interface between the pore and access regions, rather than focus centrally in the pore, which is the case when no Kap95 particles are present (as shown in Figure 5.5b).

5.5.25. DENSITY DISTRIBUTIONS OF NUPX VARIATIONS IN NANOPORES

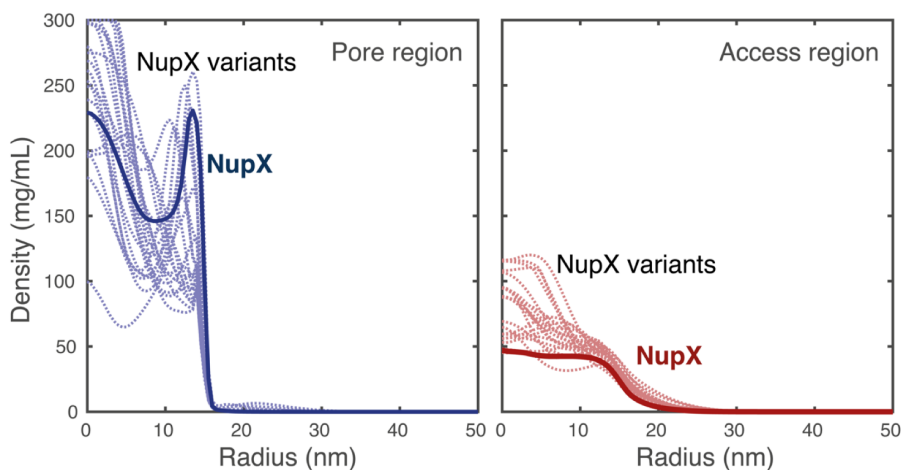


Figure S5.27: Density distributions in the pore (blue dotted lines, left) and access (red dotted lines, right) regions for 25 NupX variants from Table S5.22. NupX (bold lines) is shown for reference.

REFERENCES

- [1] A. Fragasso, H. W. de Vries, J. Andersson, E. O. van der Sluis, E. van der Giessen, A. Dahlin, P. R. Onck, and C. Dekker, *A designer FG-Nup that reconstitutes the selective transport barrier of the nuclear pore complex*, *Nature communications* **12**, 2010 (2021).
- [2] S. R. Wentz, *Gatekeepers of the Nucleus*, *Science* **288**, 1374 (2000).
- [3] S. R. Wentz and M. P. Rout, *The nuclear pore complex and nuclear transport*. Cold Spring Harbor perspectives in biology **2**, 1 (2010).
- [4] S. J. Kim, J. Fernandez-Martinez, I. Nudelman, Y. Shi, W. Zhang, B. Raveh, T. Hericks, B. D. Slaughter, J. A. Hogan, P. Upla, I. E. Chemmama, R. Pellarin, I. Echeverria, M. Shivaraju, A. S. Chaudhury, J. Wang, R. Williams, J. R. Unruh, C. H. Greenberg, E. Y. Jacobs, Z. Yu, M. J. de la Cruz, R. Mironska, D. L. Stokes, J. D. Aitchison, M. F. Jarrold, J. L. Gerton, S. J. Ludtke, C. W. Akey, B. T. Chait, A. Sali, and M. P. Rout, *Integrative structure and functional anatomy of a nuclear pore complex*, *Nature* **555**, 475 (2018).
- [5] R. Reichelt, A. Holzenburg, E. L. Buhle, Jr., M. Jarnik, A. Engel, and U. Aebi, *Correlation between structure and mass distribution of the nuclear pore complex and of distinct pore complex components*, *Journal of Cell Biology* **110**, 883 (1990).
- [6] J. Yamada, J. L. Phillips, S. Patel, G. Goldfien, A. Calestagne-Morelli, H. Huang, R. Reza, J. Acheson, V. V. Krishnan, S. Newsam, A. Gopinathan, E. Y. Lau, M. E.

- Colvin, V. N. Uversky, and M. F. Rexach, *A Bimodal Distribution of Two Distinct Categories of Intrinsically Disordered Structures with Separate Functions in FG Nucleoporins*, *Molecular & Cellular Proteomics* **9**, 2205 (2010).
- [7] L. J. Terry and S. R. Wentz, *Flexible Gates: Dynamic Topologies and Functions for FG Nucleoporins in Nucleocytoplasmic Transport*, *Eukaryotic Cell* **8**, 1814 (2009).
- [8] R. Bayliss, K. Ribbeck, D. Akin, H. M. Kent, C. M. Feldherr, D. Görlich, and M. Stewart, *Interaction between NTFP and xFxFG-containing nucleoporins is required to mediate nuclear import of RanGDP*, *Journal of Molecular Biology* **293**, 579 (1999).
- [9] A. Ghavami, E. van der Giessen, and P. R. Onck, *Energetics of Transport through the Nuclear Pore Complex*, *PLOS ONE* **11**, e0148876 (2016).
- [10] P. Popken, A. Ghavami, P. R. Onck, B. Poolman, and L. M. Veenhoff, *Size-dependent leak of soluble and membrane proteins through the yeast nuclear pore complex*, *Molecular Biology of the Cell* **26**, 1386 (2015).
- [11] B. L. Timney, B. Raveh, R. Mironska, J. M. Trivedi, S. J. Kim, D. Russel, S. R. Wentz, A. Sali, and M. P. Rout, *Simple rules for passive diffusion through the nuclear pore complex*, *The Journal of Cell Biology*, jcb.201601004 (2016).
- [12] R. Y. H. Lim, N.-P. Huang, J. Koser, J. Deng, K. H. A. Lau, K. Schwarz-Herion, B. Fahrenkrog, and U. Aebi, *Flexible phenylalanine-glycine nucleoporins as entropic barriers to nucleocytoplasmic transport*, *Proceedings of the National Academy of Sciences* **103**, 9512 (2006).
- [13] R. Bayliss, T. Littlewood, and M. Stewart, *Structural basis for the interaction between FxFG nucleoporin repeats and importin- β in nuclear trafficking*, *Cell* **102**, 99 (2000).
- [14] M. P. Rout, J. D. Aitchison, M. O. Magnasco, and B. T. Chait, *Virtual gating and nuclear transport: The hole picture*, *Trends in Cell Biology* **13**, 622 (2003).
- [15] S. Frey, *FG-Rich Repeats of Nuclear Pore Proteins with Hydrogel-Like Properties*, *Science (New York, N.Y.)* **314**, 815 (2006).
- [16] S. Frey and D. Görlich, *A Saturated FG-Repeat Hydrogel Can Reproduce the Permeability Properties of Nuclear Pore Complexes*, *Cell* **130**, 512 (2007).
- [17] R. Peters, *Translocation through the nuclear pore complex: Selectivity and speed by reduction-of-dimensionality*, *Traffic* **6**, 421 (2005).
- [18] L. E. Kapinos, R. L. Schoch, R. S. Wagner, K. D. Schleicher, and R. Y. Lim, *Karyopherin-centric control of nuclear pores based on molecular occupancy and kinetic analysis of multivalent binding with FG nucleoporins*, *Biophysical Journal* **106**, 1751 (2014).
- [19] L. E. Kapinos, B. Huang, C. Rencurel, and R. Y. Lim, *Karyopherins regulate nuclear pore complex barrier and transport function*, *Journal of Cell Biology* **216**, 3609 (2017).

- [20] K. D. Schleicher, S. L. Dettmer, L. E. Kapinos, S. Pagliara, U. F. Keyser, S. Jeney, and R. Y. Lim, *Selective transport control on molecular velcro made from intrinsically disordered proteins*, *Nature Nanotechnology* **9**, 525 (2014).
- [21] R. Y. H. Lim, B. Fahrenkrog, J. Köser, K. Schwarz-Herion, J. Deng, and U. Aebi, *Nanomechanical Basis of Selective*, *Science* **318**, 640 (2007).
- [22] R. L. Adams, L. J. Terry, and S. R. Wentle, *A Novel Saccharomyces cerevisiae FG Nucleoporin Mutant Collection for Use in Nuclear Pore Complex Functional Experiments*, *G3: Genes|Genomes|Genetics* **6**, 51 (2016).
- [23] W. Yang, J. Gelles, and S. M. Musser, *Imaging of single-molecule translocation through nuclear pore complexes*. *Proceedings of the National Academy of Sciences of the United States of America* **101**, 12887 (2004).
- [24] J. Ma, A. Goryaynov, and W. Yang, *Super-resolution 3D tomography of interactions and competition in the nuclear pore complex*, *Nature Structural & Molecular Biology* **23**, 239 (2016).
- [25] M. Beck and E. Hurt, *The nuclear pore complex: understanding its function through structural insight*, *Nature Reviews Molecular Cell Biology* **18**, 73 (2016).
- [26] D. H. Lin and A. Hoelz, *The Structure of the Nuclear Pore Complex (An Update)*, *Annual Review of Biochemistry* **88**, annurev (2019).
- [27] T. Jovanovic-Talisman, J. Tetenbaum-Novatt, A. S. McKenney, A. Zilman, R. Peters, M. P. Rout, and B. T. Chait, *Artificial nanopores that mimic the transport selectivity of the nuclear pore complex*, *Nature* **457**, 1023 (2009).
- [28] N. B. Eisele, S. Frey, J. Piehler, D. Görlich, and R. P. Richter, *Ultrathin nucleoporin phenylalanine-glycine repeat films and their interaction with nuclear transport receptors*, *EMBO Reports* **11**, 366 (2010).
- [29] S. W. Kowalczyk, L. Kapinos, T. R. Blosser, T. Magalhães, P. van Nies, R. Y. H. Lim, and C. Dekker, *Single-molecule transport across an individual biomimetic nuclear pore complex*, *Nature Nanotechnology* **6**, 433 (2011).
- [30] H. B. Schmidt and D. Görlich, *Nup98 FG domains from diverse species spontaneously phase-separate into particles with nuclear pore-like permselectivity*, *eLife* **2015**, 1 (2015).
- [31] A. N. Ananth, A. Mishra, S. Frey, A. Dwarkasing, R. Versloot, E. van der Giessen, D. Görlich, P. Onck, and C. Dekker, *Spatial structure of disordered proteins dictates conductance and selectivity in nuclear pore complex mimics*, *eLife* **7**, 1 (2018).
- [32] P. D. E. Fisher, Q. Shen, B. Akpinar, L. K. Davis, K. K. H. Chung, D. Baddeley, A. Šarić, T. J. Melia, B. W. Hoogenboom, C. Lin, and C. P. Lusk, *A Programmable DNA Origami Platform for Organizing Intrinsically Disordered Nucleoporins within Nanopore Confinement*, *ACS Nano* **12**, 1508 (2018).

- [33] P. Ketterer, A. N. Ananth, D. S. Laman Trip, A. Mishra, E. Bertosin, M. Ganji, J. Van Der Torre, P. Onck, H. Dietz, and C. Dekker, *DNA origami scaffold for studying intrinsically disordered proteins of the nuclear pore complex*, Nature Communications **9**, 1 (2018).
- [34] K. Huang, M. Tagliazucchi, S. H. Park, Y. Rabin, and I. Szleifer, *Nanocompartmentalization of the Nuclear Pore Lumen*, Biophysical Journal **118**, 219 (2020).
- [35] L. A. Strawn, T. Shen, N. Shulga, D. S. Goldfarb, and S. R. Wentz, *Minimal nuclear pore complexes define FG repeat domains essential for transport*, Nature Cell Biology **6**, 197 (2004).
- [36] W. Humphrey, A. Dalke, and K. Schulten, *VMD: Visual molecular dynamics*, Journal of Molecular Graphics **14**, 33 (1996).
- [37] K. Peng, P. Radivojac, S. Vucetic, A. K. Dunker, and Z. Obradovic, *Length-dependent prediction of protein intrinsic disorder*, BMC bioinformatics **7**, 208 (2006).
- [38] D. T. Jones and D. Cozzetto, *DISOPRED3: precise disordered region predictions with annotated protein-binding activity*, Bioinformatics **31**, 857 (2015).
- [39] J. J. Ward, J. S. Sodhi, L. J. McGuffin, B. F. Buxton, and D. T. Jones, *Prediction and Functional Analysis of Native Disorder in Proteins from the Three Kingdoms of Life*, Journal of Molecular Biology **337**, 635 (2004).
- [40] L. A. Kelley, S. Mezulis, C. M. Yates, M. N. Wass, and M. J. E. Sternberg, *The PyMol web portal for protein modeling, prediction and analysis*, Nature Protocols **10**, 845 (2015).
- [41] R. Hayama, M. Sorci, J. J. Keating, L. M. Hecht, J. L. Plawsky, G. Belfort, B. T. Chait, and M. P. Rout, *Interactions of nuclear transport factors and surface-conjugated FG nucleoporins: Insights and limitations*, PloS one **14**, e0217897 (2019).
- [42] I. Reviakine, D. Johannsmann, and R. P. Richter, *Hearing what you cannot see and visualizing what you hear: Interpreting quartz crystal microbalance data from solvated interfaces*, Analytical Chemistry **83**, 8838 (2011).
- [43] A. Ghavami, L. M. Veenhoff, E. Van Der Giessen, and P. R. Onck, *Probing the disordered domain of the nuclear pore complex through coarse-grained molecular dynamics simulations*, Biophysical Journal **107**, 1393 (2014).
- [44] R. Zahn, D. Osmanović, S. Ehret, C. Araya Callis, S. Frey, M. Stewart, C. You, D. Görlich, B. W. Hoogenboom, and R. P. Richter, *A physical model describing the interaction of nuclear transport receptors with FG nucleoporin domain assemblies*, eLife **5**, 1 (2016).
- [45] L. K. Davis, I. J. Ford, A. Šarić, and B. W. Hoogenboom, *Intrinsically disordered nuclear pore proteins show ideal-polymer morphologies and dynamics*, Physical Review E **101**, 22420 (2020).

- [46] N. B. Eisele, F. I. Andersson, S. Frey, and R. P. Richter, *Viscoelasticity of thin biomolecular films: A case study on nucleoporin phenylalanine-glycine repeats grafted to a histidine-tag capturing QCM-D sensor*, *Biomacromolecules* **13**, 2322 (2012).
- [47] T. A. Isgro and K. Schulten, *Binding Dynamics of Isolated Nucleoporin Repeat Regions to Importin- β* , *Structure* **13**, 1869 (2005).
- [48] M. Tagliazucchi, Y. Rabin, I. Szleifer, O. Peleg, and M. Kröger, *Effect of charge, hydrophobicity, and sequence of nucleoporins on the translocation of model particles through the nuclear pore complex*, *Proceedings of the National Academy of Sciences* **110**, 3363 (2013).
- [49] J. S. Hub, B. L. de Groot, and D. van der Spoel, *g_wham—A Free Weighted Histogram Analysis Implementation Including Robust Error and Autocorrelation Estimates*, *Journal of Chemical Theory and Computation* **6**, 3713 (2010).
- [50] R. S. Wagner, L. E. Kapinos, N. J. Marshall, M. Stewart, and R. Y. Lim, *Promiscuous binding of karyopherin β 1 modulates FG nucleoporin barrier function and expedites NTF2 transport kinetics*, *Biophysical Journal* **108**, 918 (2015).
- [51] C. Dekker, *Solid-state nanopores (Review Article)*, *Nature Nanotechnology*, 1 (2007).
- [52] A. Balan, C. C. Chien, R. Engelke, and M. Drndic, *Suspended Solid-state Membranes on Glass Chips with Sub 1-pF Capacitance for Biomolecule Sensing Applications*, *Scientific Reports* **5**, 1 (2015).
- [53] S. W. Kowalczyk, A. Y. Grosberg, and Y. Rabin, *Modeling the conductance and DNA blockade of solid-state nanopores*, **22** (2011), 10.1088/0957-4484/22/31/315101.
- [54] A. Fragasso, S. Pud, and C. Dekker, *1/F Noise in Solid-State Nanopores Is Governed By Access and Surface Regions*, *Nanotechnology* **30**, 395202 (2019).
- [55] N. Varongchayakul, J. Song, A. Meller, and M. W. Grinstaff, *Single-molecule protein sensing in a nanopore: a tutorial*. *Chemical Society reviews* **47**, 8512 (2018).
- [56] A. G. Koutsioubas, N. Spiliopoulos, D. L. Anastassopoulos, A. A. Vradis, and C. Toprakcioglu, *Formation of polymer brushes inside cylindrical pores: A computer simulation study*, *Journal of Chemical Physics* **131** (2009), 10.1063/1.3179686.
- [57] D. Dimitrov, A. Milchev, and K. Binder, *Polymer brushes in cylindrical pores: simulation versus scaling theory*, *J Chem Phys.* **125**, 34905 (2006).
- [58] O. Peleg, M. Tagliazucchi, M. Kröger, Y. Rabin, and I. Szleifer, *Morphology Control of Hairy Nanopores*, *ACS Nano* **5**, 4737 (2011).
- [59] S. Ro, A. Gopinathan, and Y. W. Kim, *Interactions between a fluctuating polymer barrier and transport factors together with enzyme action are sufficient for selective and rapid transport through the nuclear pore complex*, *Physical Review E* **98**, 12403 (2018).

- [60] J. Tetenbaum-Novatt, L. E. Hough, R. Mironska, A. S. McKenney, and M. P. Rout, *Nucleocytoplasmic transport: A role for nonspecific competition in karyopherin-nucleoporin interactions*, in *Molecular and Cellular Proteomics*, Vol. 11 (MCP Papers in Press, 2012) pp. 31–46.
- [61] K. Ribbeck and D. Görlich, *Kinetic analysis of translocation through nuclear pore complexes*, *The EMBO journal* **20**, 1320 (2001).
- [62] S. Milles, D. Mercadante, I. Aramburu, M. Jensen, N. Banterle, C. Koehler, S. Tyagi, J. Clarke, S. Shammas, M. Blackledge, F. Gräter, and E. Lemke, *Plasticity of an Ultrafast Interaction between Nucleoporins and Nuclear Transport Receptors*, *Cell* **163**, 734 (2015).
- [63] S. M. Liu and M. Stewart, *Structural Basis for the High-affinity Binding of Nucleoporin Nup1p to the Saccharomyces cerevisiae Importin- β Homologue, Kap95p*, *Journal of Molecular Biology* **349**, 515 (2005).
- [64] B. Raveh, J. M. Karp, S. Sparks, K. Dutta, M. P. Rout, A. Sali, and D. Cowburn, *Slide-and-exchange mechanism for rapid and selective transport through the nuclear pore complex*, *Proceedings of the National Academy of Sciences* **113**, E2489 (2016).
- [65] B. C. Buddingh' and J. C. M. van Hest, *Artificial Cells: Synthetic Compartments with Life-like Functionality and Adaptivity*, *Accounts of Chemical Research* **50**, 769 (2017).
- [66] W. K. Spoelstra, S. Deshpande, and C. Dekker, *Tailoring the appearance: what will synthetic cells look like?* *Current Opinion in Biotechnology* **51**, 47 (2018).
- [67] R. K. Das and R. V. Pappu, *Conformations of intrinsically disordered proteins are influenced by linear sequence distributions of oppositely charged residues*, *Proceedings of the National Academy of Sciences* **110**, 13392 (2013).
- [68] G. L. Dignon, W. Zheng, R. B. Best, Y. C. Kim, and J. Mittal, *Relation between single-molecule properties and phase behavior of intrinsically disordered proteins*. *Proceedings of the National Academy of Sciences of the United States of America* **115**, 9929 (2018).
- [69] P. S. Huang, S. E. Boyken, and D. Baker, *The coming of age of de novo protein design*, *Nature* **537**, 320 (2016).
- [70] G. Emilsson, R. L. Schoch, L. Feuz, F. Höök, R. Y. Lim, and A. B. Dahlin, *Strongly stretched protein resistant poly(ethylene glycol) brushes prepared by grafting-to*, *ACS Applied Materials and Interfaces* **7**, 7505 (2015).
- [71] G. Emilsson, R. L. Schoch, P. Oertle, K. Xiong, R. Y. Lim, and A. B. Dahlin, *Surface plasmon resonance methodology for monitoring polymerization kinetics and morphology changes of brushes—evaluated with poly(N-isopropylacrylamide)*, *Applied Surface Science* **396**, 384 (2017).

- [72] G. Ferrand-Drake Del Castillo, G. Emilsson, and A. Dahlin, *Quantitative Analysis of Thickness and pH Actuation of Weak Polyelectrolyte Brushes*, *Journal of Physical Chemistry C* **122**, 27516 (2018).
- [73] A. Balan, B. Machielse, D. Niedzwiecki, J. Lin, P. Ong, R. Engelke, K. L. Shepard, and M. Drndić, *Improving signal-to-noise performance for DNA translocation in solid-state nanopores at MHz bandwidths*, *Nano Letters* **14**, 7215 (2014).
- [74] A. Ghavami, E. van der Giessen, and P. R. Onck, *Coarse-Grained Potentials for Local Interactions in Unfolded Proteins*, *Journal of Chemical Theory and Computation* **9**, 432 (2013).
- [75] D. Van Der Spoel, E. Lindahl, B. Hess, G. Groenhof, A. E. Mark, and H. J. C. Berendsen, *GROMACS: Fast, flexible, and free*, *Journal of Computational Chemistry* **26**, 1701 (2005).
- [76] A. Ortega, D. Amorós, and J. García de la Torre, *Prediction of Hydrodynamic and Other Solution Properties of Rigid Proteins from Atomic- and Residue-Level Models*, *Biophysical Journal* **101**, 892 (2011).
- [77] A. Mishra, W. Sipma, L. Veenhoff, E. Van der Giessen, P. Onck, A. Mishra, W. Sipma, L. M. Veenhoff, E. Van der Giessen, and P. R. Onck, *The Effect of FG-Nup Phosphorylation on NPC Selectivity: A One-Bead-Per-Amino-Acid Molecular Dynamics Study*, *International Journal of Molecular Sciences* **20**, 596 (2019).

6

STUDYING KARYOPHERINS OCCUPANCY IN THE NUCLEAR PORE COMPLEX USING BIOMIMETIC NANOPORES

Nuclear Pore Complexes (NPCs) regulate all molecular transport between the nucleus and the cytoplasm in eukaryotic cells. Intrinsically disordered Phe-Gly nucleoporins (FG Nups) line the central conduit of NPCs and impart a selective barrier, where large proteins are excluded unless bound to a transport receptor (Karyopherin; Kap), which can freely pass the barrier. Two classes of models have been proposed to describe nuclear transport mechanistically, 'FG-centric', where FG Nups are the sole mediator of nuclear transport, and 'Kap-centric', where karyopherins participate in establishing the selective barrier. A consensus has not been reached yet. Here, we employ biomimetic nanopores, formed by tethering FG Nups to the inner wall of a solid-state nanopore, to show that a first population of Kaps are rapidly transported across the pore in \sim ms time, whereas a second population is stably assembled into the FG-mesh in the pore in a concentration-dependent manner. By analyzing the current noise fluctuations, we observe that such Kap binding induces an increase in rigidity of the FG-mesh as a function of concentration, a finding which we further corroborate with QCM-D experiments on FG Nup brushes. Our data show that Kaps do take part in forming the FG-barrier providing evidence for a 'Kap-centric' model of nuclear transport.

This chapter is based on a manuscript in preparation as: A. Fragasso, C.Dekker. Studying Karyopherins occupancy in the nuclear pore complex using biomimetic nanopores.

6.1. INTRODUCTION

Molecular traffic between nucleus and cytoplasm is exclusively controlled by the Nuclear Pore Complex (NPC), a large protein complex (52 MDa in yeast[1]) that forms a ~40nm-diameter pore across the nuclear envelope that encloses the nucleus[2, 3]. The NPC central channel is filled with a meshwork of intrinsically disordered FG-Nucleoporins (FG-Nups), that feature tandem phenylalanine-glycine (FG) amino acid sequences[4, 5]. Strikingly, such a FG-mesh appears to behave as a selective gate[4]: while molecules smaller than ~40kDa (~5 nm in size) can pass through the pore unhindered, macromolecules with size >40kDa are blocked, unless they are bound to specific nuclear transport receptors (NTRs), such as karyopherins (Kaps), which can actively interact, partition, and translocate through the FG-Nup barrier. Major NTRs involved in nuclear import are Importin- β in humans and Kap95 in yeast[6].

In an effort to describe nuclear transport mechanistically, many models have been proposed[7, 8] which can be broadly categorized into two major classes: ‘FG-centric’ and ‘Kap-centric’ models. The first class of FG-centric models, which include the ‘virtual-gate’[9], ‘selective-phase’[10, 11], and ‘forest’[5] models, regard the FG-Nup barrier as the sole important ingredient to achieve selective transport. In such scenario, Kaps act as mere transporters, *i.e.* they do not take part in establishing the selective barrier.

By contrast, Kap-centric models[12], such as the ‘reduction of dimensionality’[13], ‘reversible collapse’[14], and ‘molecular velcro’[15] models, predict that a part of the population of Kaps (‘slow-phase’) acts an integral, resident component of the NPC[12, 16], while a second population of Kaps consists of transporters (‘fast-phase’). According to this idea[8], Kaps that feature binding affinities (K_D) to the FG-mesh $<1 \mu\text{M}$, would bind strongly and occupy most of the available FG-repeats as a result of multivalent interactions, hence forming the slow-phase population. Notably, each Kap can bind multiple FG-repeats (up to ~10 FG-binding sites in Kap β 1[17]), while at the same time a single FG-Nup can bind multiple Kaps, thus giving rise to a complex multivalent-binding condensate. Saturation of available FG-repeats by the slow-phase Kaps would then result in a lowered affinity between the Kap-laden FG-mesh and additional free Kaps (fast-phase) down to $K_D > 10 \mu\text{M}$. Importantly, such a decreased affinity would explain the exceptionally fast transit times of Kaps (~5 ms) observed *in vivo*[18].

While experimental evidence has been provided in support of both classes of models, a general consensus has not yet been achieved. The difficulty in settling the debate stems from the complexity of the NPC in its physiological state, featuring a central mesh of ~200 unstructured FG-Nups that are confined into a ~40nm pore that is constantly being crossed by NTR-cargo molecules (~1000 molecules per second) in both directions, combined with the limited spatiotemporal resolution of current imaging techniques[1, 2, 19].

To probe nuclear transport through the FG-mesh, artificial mimics of the NPC have been successfully reconstituted that recapitulate the selective binding and transport behavior observed *in vivo*[20–25]. Prominent examples are the biomimetic nanopores, where ~30–50 nm solid-state nanopores are chemically functionalized using a single type of FG-Nup (*e.g.* Nsp1 or Nup98) and translocations of Kaps through the reconstituted FG-mesh are monitored in real-time optically[20] or electrically[21, 26, 27]. Although much knowledge has been gained in terms of a physical understanding of the FG-mesh and its ability to impart a selective barrier, a direct assessment is still lacking

of the properties of such pore-confined FG-mesh as a function of Kap concentration in light of the various transport models.

Here, we employ biomimetic nanopores to obtain experimental evidence on the interaction between Kaps and Nsp1 in nanopores, in an attempt to discriminate between the two major theories of transport. Building on previous work from Ananth *et al.*[26], which established that Nsp1-coated pores behave selectively, *i.e.* allowing Kap95 through while blocking other inert molecules of similar size, we investigate here the behavior of Nsp1-coated pores against increasing concentrations of Kaps.

Our data are found to support a Kap-centric model. Measurements of the ionic current through the biomimetic nanopores show that fast translocations of Kaps are observed, consistent with previous findings[26], but on top of that, a population of Kaps is found that resides permanently in the pore, and this population grows as a function of Kap concentration. By studying the noise spectra of the current traces, we observe a gradual decrease in $1/f$ noise as more Kaps are incorporated into the pore, consistent with a decrease in the collective fluctuations of the FG-Nups and an increase in the rigidity of the Nsp1 mesh. We complement our nanopore data with QCM-D affinity experiments that show a similar concentration-dependent occupancy of Kap95 into Nsp1 brushes as well as an increase in layer rigidity. By thus showing that a population of Kaps is stably bound to the Nsp1 mesh in a biomimetic nanopore at any given concentration, these data support the idea that Kaps do take part in establishing the NPC barrier, which should be accounted for in any mechanistic modeling of nuclear transport.

6.2. RESULTS

6.2.1. ELECTRICAL TRANSPORT THROUGH NSP1-COATED PORES SHOWS AN INCREASE IN KAP95 OCCUPANCY AS A FUNCTION OF KAP95 CONCENTRATION

To perform ion current measurements through Nsp1-coated pores (Fig.6.1a), solid-state nanopores were fabricated onto glass-supported freestanding 20nm-thick SiN_x membranes using a transmission electron microscope (TEM, see 'Methods' section). Chips were mounted in a custom-built Teflon flow-cell system to allow for quick exchange of bulk solution from the two opposite compartments surrounding the chip. Conductance measurements were initially performed on freshly drilled nanopores, which, as expected, exhibited fully ohmic behavior, *i.e.* linear current-voltage (I-V) characteristics. Figure 6.1a shows the I-V plot of a bare 55 nm pore. Subsequently, pores were functionalized with Nsp1 using a 3-step self-assembled-monolayer chemistry (SAM) as described in previous work[27] (see 'Methods'), which yielded a $\sim 50\%$ decrease in conductance (Fig.6.1b).

Next, Kap95 was flushed on the *cis*-chamber which resulted in a further decrease of the pore conductance. This in itself directly provides a first sign that Kap95 was incorporated within the pore volume. Figure 6.1c (bottom) compares the three (I,V) characteristics of a bare pore (black), Nsp1-coated (red), and Nsp1-coated pore with $1.9 \mu\text{M}$ of Kap95 present in bulk solution (green), where the latter shows a further $\sim 50\%$ decrease in conductance compared to the Nsp1-coated pore, indicating the presence of Kap95 molecules in the pore.

To assess the pore-occupancy of Kap95 as a function of concentration, we titrated Kap95 from about 100-2000 nM (Figure 6.2a), finding the pore conductance to decrease monotonously in a step-wise manner as higher concentrations of Kaps were flushed into the *cis*-chamber, which clearly indicates that additional Kaps are being incorporated into the Nsp1-mesh for increasing Kap95 concentration. Interestingly, we found that transient dips in the current, corresponding to fast Kap95 translocation events, were simultaneously present as well on top of the decreased current baseline, which occurred only when the bulk concentration was ~ 100 nM, in line with previous measurements[26]. We attribute the absence of current spikes at higher Kap95 concentrations to excessive pore crowding which negatively affects the SNR in such current-based detection system.

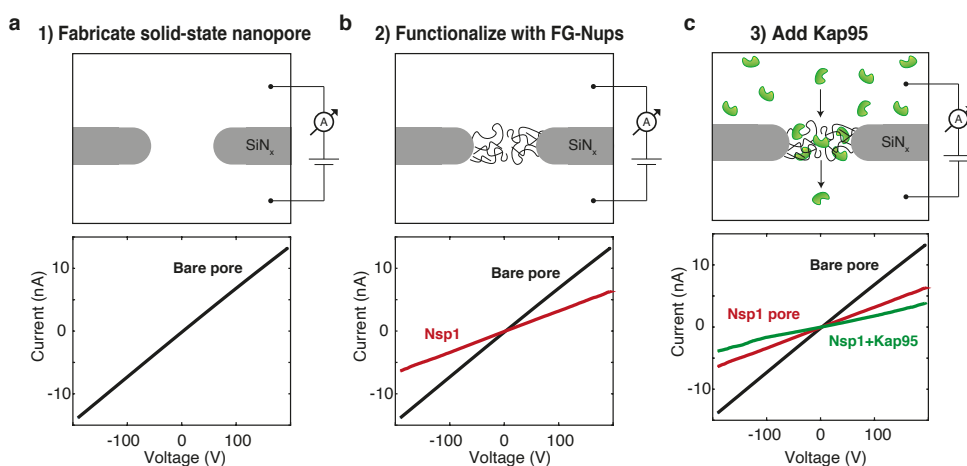


Figure 6.1: Current measurements of Nsp1-coated pores as a function of Kap95 concentration. a, Top: schematic showing the bare pore measurement system. Bottom: (I,V) characteristics of a bare 55 nm pore. b-c, Same as (a) but for a Nsp1-coated pore without (b) and with (c) $1.9\mu\text{M}$ Kap95 present in the *cis*-chamber (top part).

As a control, we repeated the same experiment by injecting increasing concentrations of BSA (Bovine Serum Albumine) in the *cis*-chamber from ~ 2 - $20\mu\text{M}$ (Figure 6.2c). Here we found that, unlike for Kap95, no significant change in the current baseline was observed. Importantly, this indicates that the interaction observed between Kap95 and Nsp1 is a result of specific protein-protein interactions, and not merely due to, *e.g.*, electrostatic pulling of the protein into the Nsp1-mesh. Repeating the experiment on different pore sizes resulted in a similar decreasing trend of the pore conductance as a function of Kap95 concentration (Fig.6.2d).

Next, we analyzed the power spectral density (PSD) of the ionic current as a function of Kap95 concentration, *i.e.* the frequency spectrum of the power of the current signal. For biomimetic nanopores, the increase in low-frequency (1-100 Hz) $1/f$ noise upon addition of the Nups has been typically associated to spatiotemporal fluctuations of FG-Nup proteins in the pore channel[21, 26, 27]. Indeed we also report an increase in $1/f$ noise when comparing the bare vs Nsp1-coated pore (Fig.S6.6). More interestingly, we furthermore observe an overall decreasing trend in the $1/f$ noise as a func-

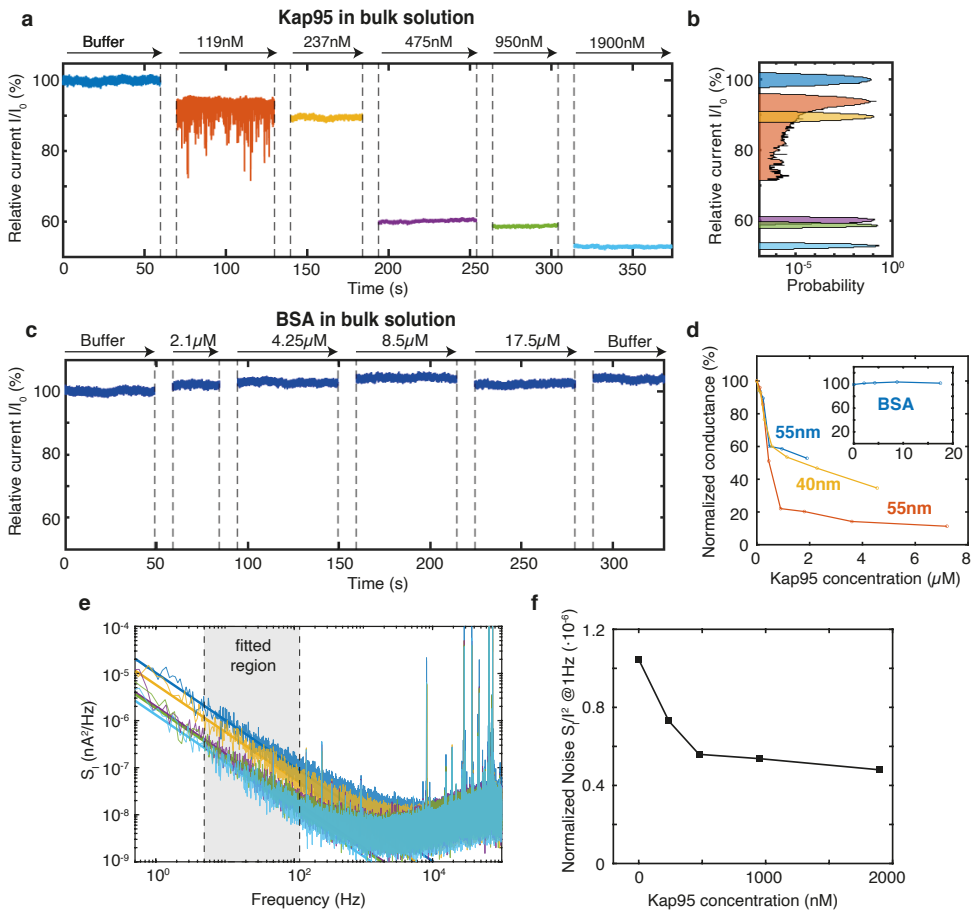


Figure 6.2: a, Concatenated current traces representing a Kap95 titration from 119-1900 nM, revealing a decrease of the nanopore current up to almost ~50% of the initial value. b, Histogram of the current traces illustrated in (a). c, Concatenated current traces representing a BSA titration from 2-20 μ M, showing no sign of current decrease. d, Normalized conductance for different nanopores vs Kap95 concentration. Inset: normalized conductance for a 55 nm pore vs BSA concentration (same units as in d applies). e, PSD spectra of the current traces shown in (a), same color coding as in (a) applies. f, Normalized noise $A = S_I(1\text{Hz})/I^2$, as a function of Kap95 concentration. Fit to the noise data for 119 nM concentration was excluded due to the presence of a pronounced Lorentzian component originating from the Kap95 translocations (see Refs.[28, 29]) which yielded a poor fit of Hooge's model to the data.

tion of Kap concentration (Fig.6.2e,f). To properly compare the magnitude of $1/f$ noise for different current traces, we fitted the low-frequency region (5-100 Hz) of the PSD (grey area in Fig.6.2e) using Hooge's model[30], which is commonly used to describe $1/f$ noise in solid-state nanopores[28, 31–33], where the current PSD (S_I) is expressed as $S_I = \alpha_H I^2 / N_c f = A I^2 / f$, where, α_H is the Hooge parameter that quantifies the strength of the $1/f$ noise, I is the through-pore current, N_c is the number of charge carriers within the pore volume which depends on salt concentration and pore geometry, f is the frequency, and $A = \alpha_H / N_c = S_I(1Hz) / I^2$ is the fit parameter, which is a measure of the noise magnitude normalized by the square of the current. Figure 6.2f shows a clear decreasing trend for A as a function of Kap95 concentration, indicating that a higher Kap occupancy resulted in a decrease of the $1/f$ noise. This is suggestive of an increase in overall rigidity of the Nsp1-mesh in the pore. This finding is in line with the observed increase in rigidity of Nsp1 brushes grafted on a planar geometry upon Kap95 binding as reported in our QCM-D measurements (see below), as well as in previous works[22, 34].

6.2.2. ANALYSIS OF FAST KAP95 TRANSLOCATIONS THROUGH AN NSP1 PORE

6

We then characterized the translocation events of Kap95 (fast phase) when increasing the applied voltage from 50 to 200mV. For each event, we measured the current blockade, which to a first approximation is proportional to the volume of the translocating molecule, and dwell time, which corresponds to the time the translocating protein spends in the pore which depends on the specific protein-pore interactions. In Figure 6.3a we show examples of current traces where each current spike correspond to a single Kap95 translocation event. Figure 6.3b illustrates some characteristic translocation events at different voltages in higher resolution.

As expected, conductance blockades at different voltages are found to be comparable: 76 ± 2 nS at 50mV ($N=310$, errors are S.E.M.), 80 ± 2 nS at 100mV ($N=1206$), 77 ± 3 nS at 150mV ($N=687$), and (64 ± 3) nS at 200mV ($N=820$). By contrast, for values of the applied bias >50 mV we observed a drastic decrease of the resident time of the protein being in the pore due to a stronger electrophoretic force driving the protein, which goes from 7.8 ± 0.8 ms for 50mV ($N=310$, errors are S.E.M.) to about ~ 1 ms at higher voltages: 1.2 ± 0.1 ms for 100mV ($N=1206$), 0.8 ± 0.2 ms for 150mV ($N=687$), and 1.1 ± 0.1 ms for 200mV ($N=820$). Notably, the translocation events that are the least affected by the applied bias, namely acquired under 50mV, result in dwell times of ~ 8 ms that are remarkably close to the ~ 5 ms observed in vivo. Additional examples of current traces are show in Fig.S6.7.

Lastly, the event rate of translocations, calculated as number of translocation events per second, was observed to increase as a function of applied voltage by almost an order of magnitude when increasing the bias from 50mV to 200mV (Fig.6.3d). This is indicative of an increase in the capture radius as a function of voltage[35], defined as the radius of the hemisphere surrounding the pore wherein the electrostatic force driving the protein to the pore overtakes simple diffusion.

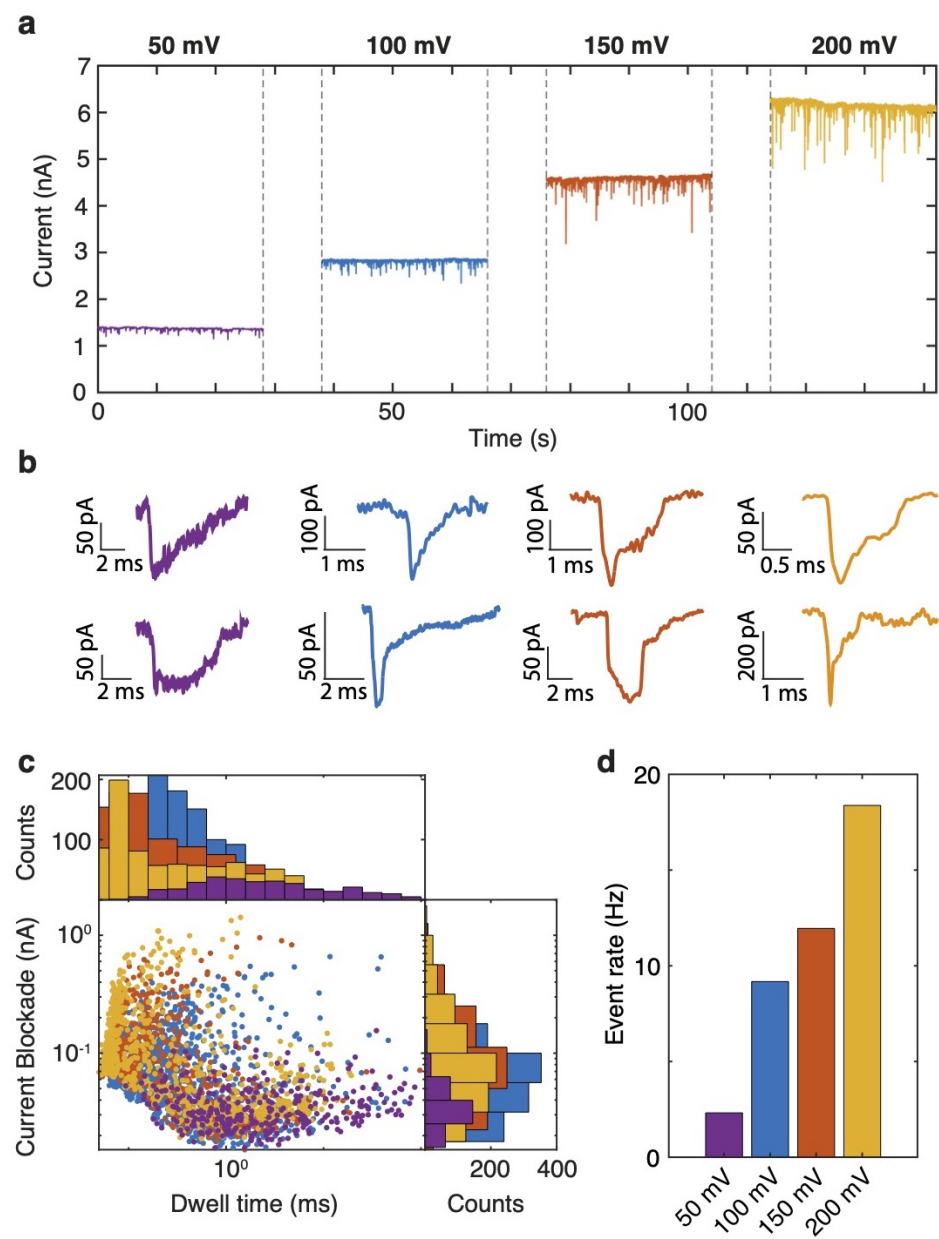


Figure 6.3: Event analysis of Kap95 translocations. a, Current traces showing single-molecule translocations of Kap95 through a Nsp1-coated pore under 50mV (purple), 100mV (blue), 150mV (red), 200mV (yellow). Additional examples are shown in Figure S6.7. b, Characteristic Kap95 translocation events at different voltages. c, Scatter plot of the current blockade vs dwell time of the translocation events for different voltages. Histograms for both dwell time and current blockade are logarithmically binned. d, Event rate of the translocations, defined as number of events per second, for increasing applied voltage. Color coding of b-d are the same as for a.

6.2.3. KAP95 OCCUPANCY IN A Nsp1 BRUSH INCREASES WITH KAP95 CONCENTRATION

To assess the binding of Kap95 to Nsp1 brushes, we complemented our nanopore data with measurements using a quartz-crystal-microbalance with dissipation monitoring (QCM-D). For this, we monitored the resonance frequency shift (Δf) of the crystal, which is proportional to amount of adsorbed mass, and the dissipation shift (ΔD), which depends on the viscoelastic properties of the adsorbed layer.

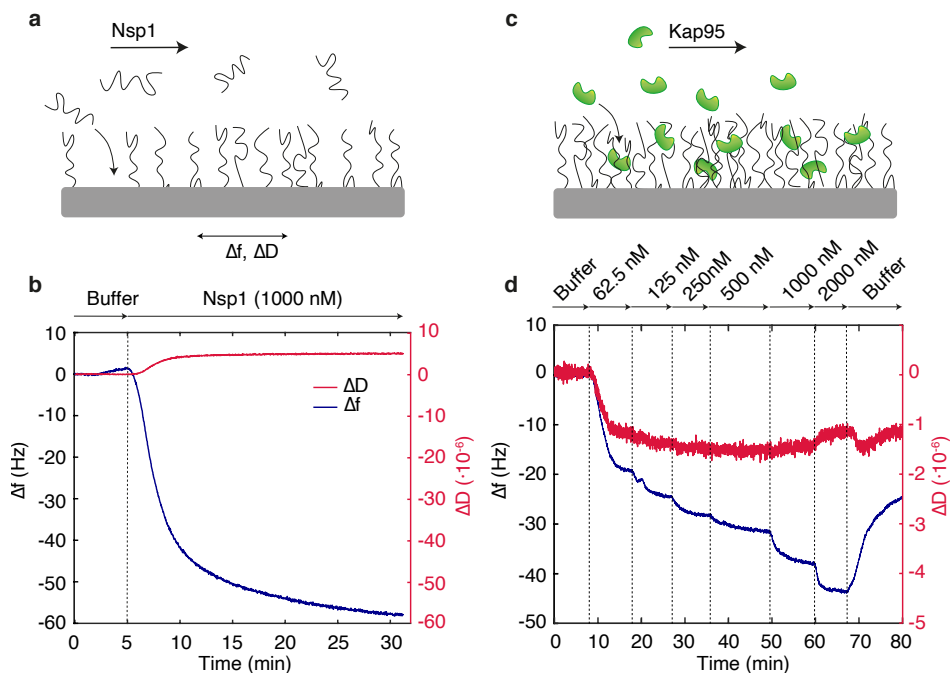


Figure 6.4: Probing Kap95 binding to Nsp1 with QCM-D. a,c, Schematics showing Nsp1 coating (a) and Kap95 injection (b) onto the quartz chip. b, Recordings of frequency (blue) and dissipation (red) shifts vs time when injecting 1000 nM Nsp1 onto the gold-coated chip surface. Binding of the molecule is revealed by the negative shift in resonance frequency, whereas the increase in dissipation is consistent with the formation of a hydrated Nsp1 brush. d, Frequency and dissipation shifts vs time upon Kap95 injection onto a Nsp1-coated surface at increasing concentrations from 62.5-2000 nM.

After a cleaning routine (see Methods), gold-coated chips were first functionalized with Nsp1 (Fig.6.4a,b) which features a cysteine on its C-terminus that is used for conjugation to the gold surface. Incubation of the Nsp1 protein with the gold surface resulted in a $\Delta f \sim -58\text{Hz}$, indicating the formation of a dense Nsp1-brush (cf. Ref.[36]). Subsequently we passivated the remaining gold exposed in between Nsp1 molecules using 1-mercapto-11-undecyltri(ethyleneglycol) (MUTEG) (see details in Ref.[27]).

Kap95 was flushed in at increasing concentrations in the range (62.5-2000 nM), which resulted in a step-wise decrease in frequency shift – indicating a concentration-dependent Kap95 adsorption onto the Nsp1-brush (Fig.6.4c,d). This observation is perfectly in line

with previous reports[22, 34], as well as our nanopore data where we report a concentration-dependent incorporation of Kap95 into the Nsp1 pore mesh.

Additionally, we observed a striking decrease in dissipation $\Delta D \sim -1 \times 10^{-6}$ as soon as the lowest Kap95 concentration (62.5 nM) was injected, which indicates an increase of the layer rigidity[22, 37, 38]. This finding is in line with the notion of ‘collapse’ of the Nsp1 brush, consistent with a decrease in brush height upon Kap binding, reported by Wagner *et al.*[34], where the interaction between Nsp1 and Kap β 1 was monitored optically by surface-plasmonic-resonance (SPR). Importantly, such an increase in layer rigidity measured by QCM-D is consistent with the decrease in $1/f$ noise observed in our nanopore experiments.

6.2.4. SUPPORT FOR THE KAP-CENTRIC MODEL OF NUCLEAR TRANSPORT

It is of interest to discuss these data in the context of the various models for nuclear transport. Most importantly, our nanopore data show that while a population of fast Kaps are rapidly translocating through the pore in a timescale of milliseconds, a second population of quasi-permanent Kaps is also present (Fig.6.5a) which appears in the ion current data as a stable, concentration-dependent, decrease of the current baseline. Moreover, binding of Kap95 appears to have a ‘stiffening’ effect on the Nsp1-mesh, as observed by the overall decrease of the $1/f$ noise in the nanopore and the dissipation in QCM-D.

A possible arrangement of the two Kap95 populations (fast vs slow) within the nanopore was suggested by Kapinos *et al.* 2014[12] and illustrated in Figure 6.5b. Here, slow Kaps that bind the Nsp1 mesh with high avidity ($<1\mu\text{M}$) would induce a collapse of the Nsp1-mesh towards the pore rim, resulting in the opening of a central channel (Fig. 6.5b, red dashed lines), through which fast Kaps can rapidly diffuse through in $\sim\text{ms}$ time. This is in line with our data showing a stable drop of the baseline due to slow Kaps binding to the FG-mesh while increasing its stiffness (Fig.6.2a,f), which may be associated with the formation of a central opening for the fast-diffusing Kaps resulting in the observed fast ($\sim 7.8\text{ ms}$ at 50mV, Fig.6.4) translocation events. Our data are also compatible with the ‘reduction-of-dimensionality’[13] and ‘molecular velcro’[15] models, where translocating Kaps would cross the pore following a 2D-random walk on the collapsed, Kap-saturated layer of FG-Nups. Formation of a channel opening upon Kap binding is also consistent with *in vivo* super-resolution data from Ma *et al.*[39], where increasing the concentration of Imp β from 1 nM to 15 μM in human cells resulted in higher NPC permeability to large 70 kDa Dextran molecules.

6.3. CONCLUSION

In this work, we investigated the interaction between the yeast transporter Kap95 and FG-nucleoporin Nsp1 using biomimetic nanopores. We identified two distinct Kap95 populations: slow Kaps that bind stably to the Nsp1 mesh causing a permanent decrease in the current baseline, and fast Kaps that rapidly translocate the pore on a $\sim\text{ms}$ timescale. The population of slow Kaps was found to increase in a concentration-dependent manner as revealed by the step-wise decrease of the pore conductance. The net decrease in $1/f$ noise in the current signal, together with the decrease in dissipation measured by QCM-D, for increasing Kap95 concentrations points to an increased rigidity of the Nsp1-

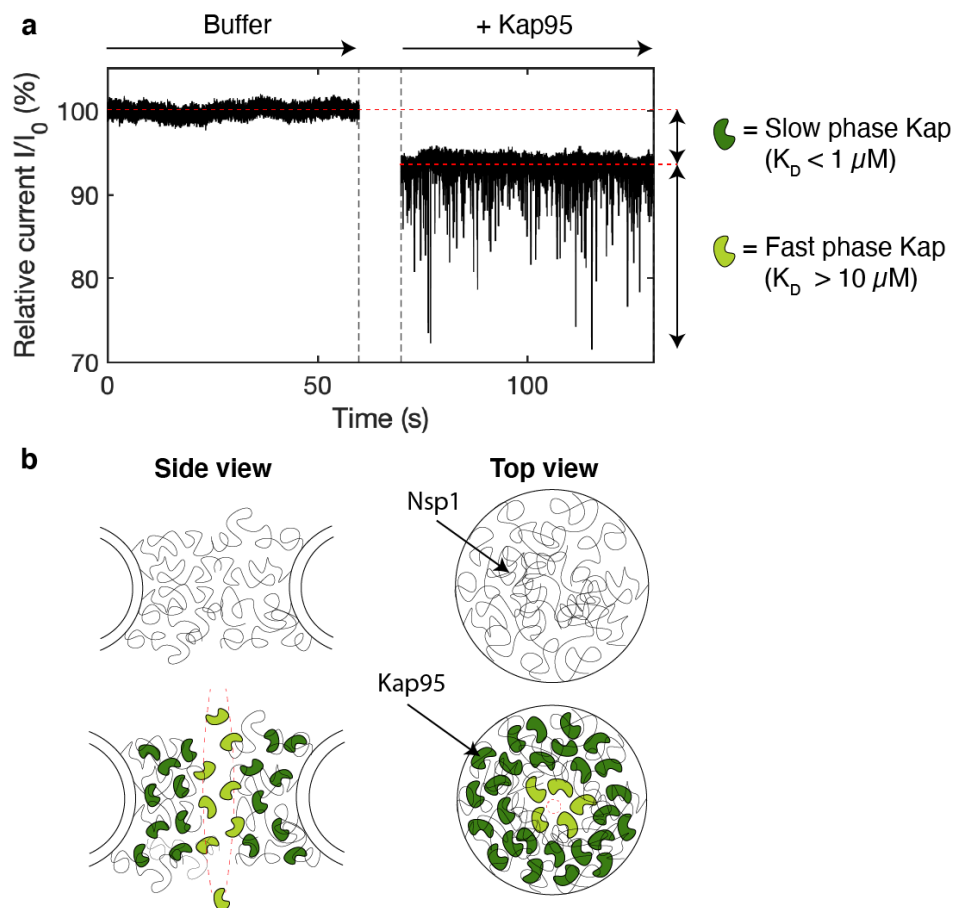


Figure 6.5: Kap-centric transport model. a, Nanopore current traces showing baseline decrease, associated with 'slow-phase' Kaps bidding stably to Nsp1, as well as transient spikes, which indicate 'fast-phase' (~ms) Kap95 translocations through the pore. b, Schematics of the coated pore side (left) and top (right) views in the absence (top) and presence (bottom) of Kaps, picturing the Kap-centric model (as in Kapinos et al.[12]). 'Slow-phase' Kaps (dark green) reside towards the pore rim and cause the opening of a central channel where 'fast-phase' Kaps (light green) are allowed to rapidly translocate by weakly interacting with the saturated FG-mesh.

mesh for increased Kap occupancy.

Taken together, our data are in agreement with the Kap-centric model for nuclear transport. It opens the way to further studies using more physiological scenarios by, *e.g.*, introducing the Kap95 binding partner, Kap60, and studying RanGTP-assisted dissociation when this is added on the *trans*-side of the pore. Other platforms that avoid the use of an applied voltage could also be envisioned, *e.g.* by using zero-mode-waveguides (ZMW[40]), where translocating molecules are freely diffusing (*i.e.* not driven by an electrical field) and optically detected. Finally, probing the spatial localization of Kap95 within Nsp1-coated pores could be achieved by labelling Kap95 with gold nanoparticles and performing CryoEM imaging of the pores.

6.4. METHODS

6.4.1. PREPARATION OF SOLID-STATE NANOPORES

Pores with sizes ~ 40 -55 nm were fabricated onto freestanding 20nm-thick SiN_x membranes supported on a glass substrate for low-noise recordings (purchased by Goepert). Drilling of the pores was performed by means of a transmission electron microscope (see Ref.[41] for details). Pore functionalization was performed as reported previously[27]. Briefly, freshly drilled nanopores were rinsed in milliQ water, ethanol, acetone, isopropanol, and treated with oxygen plasma for 2 min to further clean the chip and enrich the nanopore surface with hydroxyl (-OH) groups. Next, the chip was incubated with 2% APTES (Sigma Aldrich) in anhydrous toluene (Sigma Aldrich) for 45 min, at room temperature, shaking at 400 rpm, in a glove-box filled with pure nitrogen, which prevented APTES molecules from polymerizing. The chip was subsequently rinsed in anhydrous toluene, milliQ water, and ethanol, blow-dried with nitrogen, and heated at 110°C for ~ 30 -60min. Following the curing, the chip was incubated with Sulfo-SMCC (sulphosuccinimidyl-4-(N-maleimidomethyl)-cyclohexane-1-carboxylate) (2 mg no-weight capsules (Pierce)) for >3 hrs, a bifunctional crosslinker that binds amine groups of the APTES through a NHS-ester group, while providing a free maleimide group on the other end. Chips were then rinsed in PBS for 15 min and incubated with Nsp1 for ~ 1 hr, which reacted with the maleimides through the cysteine present on its C-terminus, forming stable covalent bonds. The chips were finally rinsed with PBS to remove unspecifically bound proteins

6.4.2. ELECTRICAL ION-CURRENT MEASUREMENTS

The buffer employed in nanopore experiments was 150 mM KCl, 10mM Tris, 1mM EDTA, pH 7.4. Current data were recorded in real-time using a commercial amplifier (Axopatch200B, Molecular devices), which applies a 100kHz low-pass filtering, and digitized at 250kHz (Digidata 1322A DAQ). Raw traces were further filtered digitally at 5kHz, and processed using a custom-written Matlab script[42].

6.4.3. QCM-D SAMPLE PREPARATION AND DATA ACQUISITION

QSense Analyzer chips were treated as in Ref.[27]. Briefly, gold-coated quartz chips (Biolin Scientific, Sweden) were cleaned with RCA-1 protocol, consisting of 30% H₂O₂, 30% NH₄OH, and deionized water in 1:1:5 ratio, at 75°C for ~ 15 -30 min. Subsequently, chips

were rinsed with deionized water, sonicated in pure ethanol for ~ 10 min, and blow-dried with nitrogen. QCM-D flow-cells were sonicated in 2% SDS for ~ 30 min, rinsed in deionized water, and blow-dried with nitrogen. Prior to the experiment, Nsp1 proteins were incubated with $100\times$ TCEP to break disulfide bonds. QCM-D data were recorded at sub-ms temporal resolution using Qsoft (Biolin scientific), and analysed using a custom-written Matlab script. Plotted dissipation and normalized frequency shifts correspond to the 5th harmonic, namely ΔD_5 and $\Delta f_5/5$, respectively.

6.4.4. PURIFICATION OF KAP95

We refer to Ref.[27] for details on the purification of Kap95.

6.5. SUPPORTING INFORMATION

6.5.1. 1/F NOISE COMPARISON OF BARE PORE VS Nsp1-COATED PORE

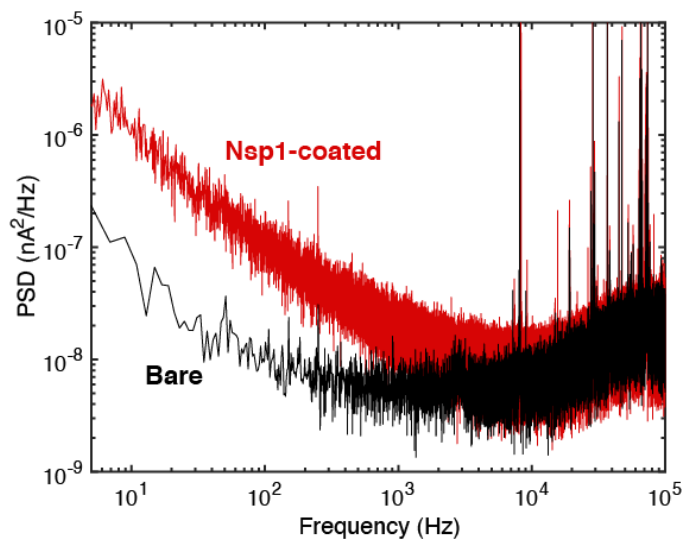


Figure S6.6: Current PSD spectra for a bare pore (black) vs a Nsp1-coated pore (red), illustrating the pronounced increase in 1/f noise upon coating the pore with Nsp1.

6.5.2. ADDITIONAL TRACES OF FAST KAP95 TRANSLOCATIONS

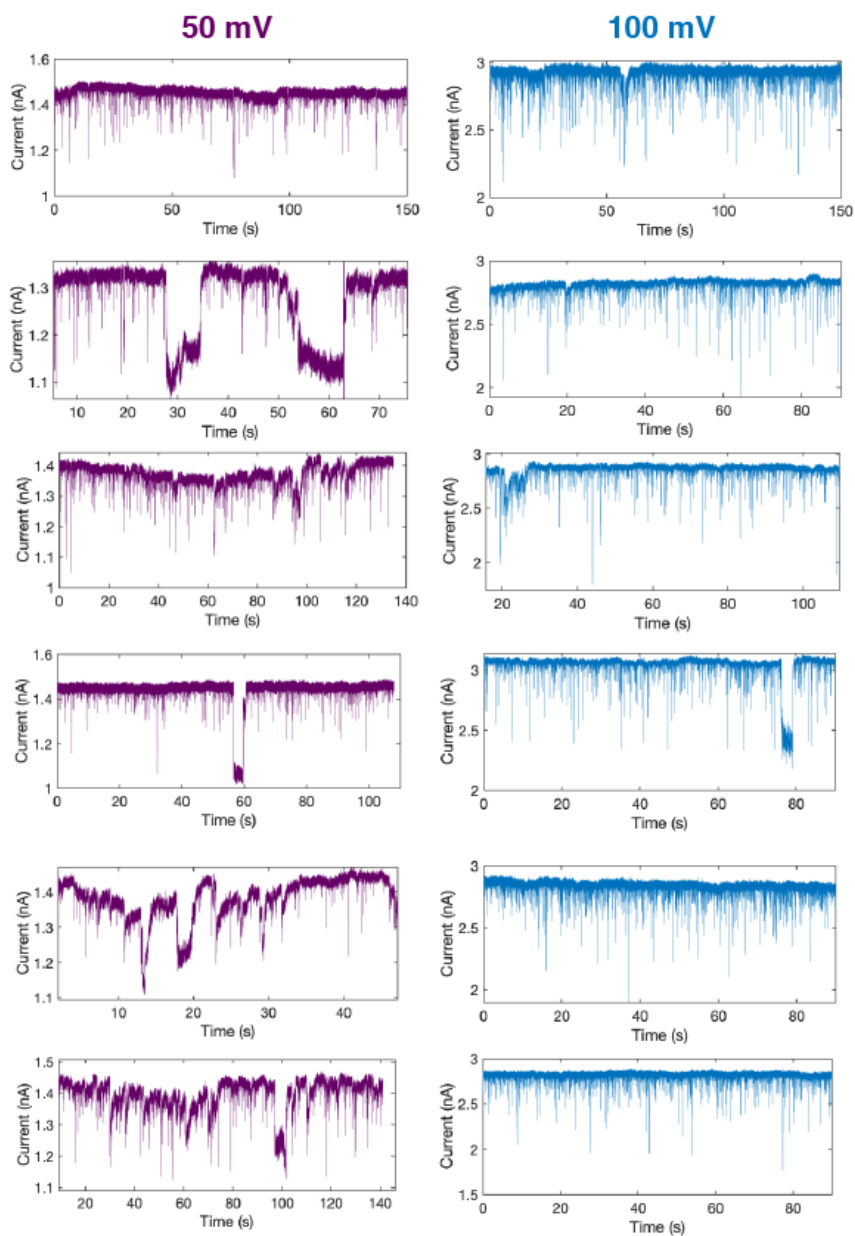


Figure S6.7: Additional current traces showing fast Kap95 translocation events through a Nsp1-coated pore under 50mV (left, purple) and 100mV (right, blue).

REFERENCES

- [1] S. J. Kim, J. Fernandez-Martinez, I. Nudelman, Y. Shi, W. Zhang, B. Raveh, T. Hericks, B. D. Slaughter, J. A. Hogan, P. Upla, I. E. Chemmama, R. Pellarin, I. Echeverria, M. Shivaraju, A. S. Chaudhury, J. Wang, R. Williams, J. R. Unruh, C. H. Greenberg, E. Y. Jacobs, Z. Yu, M. J. de la Cruz, R. Mironska, D. L. Stokes, J. D. Aitchison, M. F. Jarrold, J. L. Gerton, S. J. Ludtke, C. W. Akey, B. T. Chait, A. Sali, and M. P. Rout, *Integrative structure and functional anatomy of a nuclear pore complex*, *Nature* **555**, 475 (2018).
- [2] L. M. Veenhoff, J. Kipper, O. Karni-Schmidt, S. Dokudovskaya, W. Zhang, A. Sali, D. Devos, M. P. Rout, A. Suprpto, F. Alber, R. Williams, and B. T. Chait, *Determining the architectures of macromolecular assemblies*, *Nature* **450**, 683 (2007).
- [3] S. R. Wentz, *Gatekeepers of the Nucleus*, *Science* **288**, 1374 (2000).
- [4] L. J. Terry and S. R. Wentz, *Flexible Gates: Dynamic Topologies and Functions for FG Nucleoporins in Nucleocytoplasmic Transport*, *Eukaryotic Cell* **8**, 1814 (2009).
- [5] J. Yamada, J. L. Phillips, S. Patel, G. Goldfien, A. Calestagne-Morelli, H. Huang, R. Reza, J. Acheson, V. V. Krishnan, S. Newsam, A. Gopinathan, E. Y. Lau, M. E. Colvin, V. N. Uversky, and M. F. Rexach, *A Bimodal Distribution of Two Distinct Categories of Intrinsically Disordered Structures with Separate Functions in FG Nucleoporins*, *Molecular and Cellular Proteomics* **9**, 2205 (2010).
- [6] M. Stewart, *Molecular mechanism of the nuclear protein import cycle*, *Nature Reviews Molecular Cell Biology* **8**, 195 (2007).
- [7] G. David, S. R. H, and M. P. Rout, *Nuclear export dynamics of RNA-protein complexes*, *Journal of Chemical and Pharmaceutical Research* **6**, 504 (2014).
- [8] R. Y. Lim and L. E. Kapinos, *How to operate a nuclear pore complex by kap-centric control*, *Nucleus* **6**, 366 (2015).
- [9] M. P. Rout, J. D. Aitchison, M. O. Magnasco, and B. T. Chait, *Virtual gating and nuclear transport: The hole picture*, *Trends in Cell Biology* **13**, 622 (2003).
- [10] S. Frey, *FG-Rich Repeats of Nuclear Pore Proteins with Hydrogel-Like Properties*, *Science (New York, N.Y.)* **314**, 815 (2006).
- [11] S. Frey and D. Görlich, *A Saturated FG-Repeat Hydrogel Can Reproduce the Permeability Properties of Nuclear Pore Complexes*, *Cell* **130**, 512 (2007).
- [12] L. E. Kapinos, R. L. Schoch, R. S. Wagner, K. D. Schleicher, and R. Y. Lim, *Karyopherin-centric control of nuclear pores based on molecular occupancy and kinetic analysis of multivalent binding with FG nucleoporins*, *Biophysical Journal* **106**, 1751 (2014).
- [13] R. Peters, *Translocation through the nuclear pore complex: Selectivity and speed by reduction-of-dimensionality*, *Traffic* **6**, 421 (2005).

- [14] R. Y. H. Lim, B. Fahrenkrog, J. Köser, K. Schwarz-Herion, J. Deng, and U. Aebi, *Nanomechanical basis of selective gating by the nuclear pore complex*, *Science* **318**, 640 (2007).
- [15] K. D. Schleicher, S. L. Dettmer, L. E. Kapinos, S. Pagliara, U. F. Keyser, S. Jeney, and R. Y. Lim, *Selective transport control on molecular velcro made from intrinsically disordered proteins*, *Nature Nanotechnology* **9**, 525 (2014).
- [16] L. E. Kapinos, B. Huang, C. Rencurel, and R. Y. Lim, *Karyopherins regulate nuclear pore complex barrier and transport function*, *Journal of Cell Biology* **216**, 3609 (2017).
- [17] R. Bayliss, T. Littlewood, and M. Stewart, *Structural basis for the interaction between FxFG nucleoporin repeats and importin- β in nuclear trafficking*, *Cell* **102**, 99 (2000).
- [18] T. Dange, D. Grünwald, A. Grünwald, R. Peters, and U. Kubitschek, *Autonomy and robustness of translocation through the nuclear pore complex: A single-molecule study*, *Journal of Cell Biology* **183**, 77 (2008).
- [19] K. Ribbeck and D. Görlich, *Kinetic analysis of translocation through nuclear pore complexes*, *The EMBO journal* **20**, 1320 (2001).
- [20] T. Jovanovic-Talisman, J. Tetenbaum-Novatt, A. S. McKenney, A. Zilman, R. Peters, M. P. Rout, and B. T. Chait, *Artificial nanopores that mimic the transport selectivity of the nuclear pore complex*, *Nature* **457**, 1023 (2009).
- [21] S. W. Kowalczyk, L. Kapinos, T. R. Blosser, T. Magalhães, P. van Nies, R. Y. H. Lim, and C. Dekker, *Single-molecule transport across an individual biomimetic nuclear pore complex*, *Nature Nanotechnology* **6**, 433 (2011).
- [22] N. B. Eisele, S. Frey, J. Piehler, D. Görlich, and R. P. Richter, *Ultrathin nucleoporin phenylalanine-glycine repeat films and their interaction with nuclear transport receptors*, *EMBO Reports* **11**, 366 (2010).
- [23] B. Malekian, L. E. Kapinos, R. L. Schoch, G. Ferrand -Drake del Castillo, K. Xiong, R. Y. H. Lim, G. Emilsson, A. Dahlin, and T. Robson, *Detecting Selective Protein Binding Inside Plasmonic Nanopores: Toward a Mimic of the Nuclear Pore Complex*, *Frontiers in Chemistry* **6** (2018), 10.3389/fchem.2018.00637.
- [24] R. L. Schoch, L. E. Kapinos, and R. Y. Lim, *Nuclear transport receptor binding avidity triggers a self-healing collapse transition in FG-nucleoporin molecular brushes*, *Proceedings of the National Academy of Sciences of the United States of America* **109**, 16911 (2012).
- [25] H. B. Schmidt and D. Görlich, *Nup98 FG domains from diverse species spontaneously phase-separate into particles with nuclear pore-like permselectivity*, *eLife* **2015**, 1 (2015).

- [26] A. N. Ananth, A. Mishra, S. Frey, A. Dwarkasing, R. Versloot, E. van der Giessen, D. Görlich, P. Onck, and C. Dekker, *Spatial structure of disordered proteins dictates conductance and selectivity in nuclear pore complex mimics*, *eLife* **7**, 1 (2018).
- [27] A. Fragasso, H. W. de Vries, J. Andersson, E. O. van der Sluis, E. van der Giessen, A. Dahlin, P. R. Onck, and C. Dekker, *A designer FG-Nup that reconstitutes the selective transport barrier of the nuclear pore complex*, *Nature communications* **12**, 2010 (2021).
- [28] A. Fragasso, S. Schmid, and C. Dekker, *Comparing Current Noise in Biological and Solid-State Nanopores*, *ACS Nano*, acsnano.9b09353 (2020).
- [29] S. Machlup, *Noise in semiconductors: Spectrum of a two-parameter random signal*, *Journal of Applied Physics* **25**, 341 (1954).
- [30] F. Hooge, *1/F Noise*, *Physica B+C* **83**, 14 (1976).
- [31] R. M. M. Smeets, N. H. Dekker, and C. Dekker, *Low-frequency noise in solid-state nanopores*, *Nanotechnology* **20** (2009), 10.1088/0957-4484/20/9/095501.
- [32] R. M. M. Smeets, U. F. Keyser, N. H. Dekker, and C. Dekker, *Noise in solid-state nanopores*, *Proceedings of the National Academy of Sciences of the United States of America* **105**, 417 (2008).
- [33] A. Fragasso, S. Pud, and C. Dekker, *1/F Noise in Solid-State Nanopores Is Governed By Access and Surface Regions*, *Nanotechnology* **30**, 395202 (2019).
- [34] R. S. Wagner, L. E. Kapinos, N. J. Marshall, M. Stewart, and R. Y. Lim, *Promiscuous binding of karyopherin β 1 modulates FG nucleoporin barrier function and expedites NTF2 transport kinetics*, *Biophysical Journal* **108**, 918 (2015).
- [35] O. Otto and U. F. Keyser, *DNA Translocation*, in *Engineered Nanopores for Bioanalytical Applications: A Volume in Micro and Nano Technologies* (2013) pp. 31–58.
- [36] A. Ananth, M. Genua, N. Aissaoui, L. Díaz, N. B. Eisele, S. Frey, C. Dekker, R. P. Richter, and D. Görlich, *Reversible Immobilization of Proteins in Sensors and Solid-State Nanopores*, *Small* **14**, 1703357 (2018).
- [37] I. Reviakine, D. Johannsmann, and R. P. Richter, *Hearing what you cannot see and visualizing what you hear: Interpreting quartz crystal microbalance data from solvated interfaces*, *Analytical Chemistry* **83**, 8838 (2011).
- [38] N. B. Eisele, A. A. Labokha, S. Frey, D. Görlich, and R. P. Richter, *Cohesiveness tunes assembly and morphology of FG nucleoporin domain meshworks - Implications for nuclear pore permeability*, *Biophysical Journal* **105**, 1860 (2013).
- [39] J. Ma, A. Goryaynov, A. Sarma, and W. Yang, *Self-regulated viscous channel in the nuclear pore complex*, *Proceedings of the National Academy of Sciences of the United States of America* **109**, 7326 (2012).

- [40] N. Klughammer and C. Dekker, *Palladium zero-mode waveguides for optical single-molecule detection with nanopores*, *Nanotechnology* **32**, 18LT01 (2021).
- [41] M. Van Den Hout, A. R. Hall, M. Y. Wu, H. W. Zandbergen, C. Dekker, and N. H. Dekker, *Controlling nanopore size, shape and stability*, *Nanotechnology* **21** (2010), 10.1088/0957-4484/21/11/115304.
- [42] C. Plesa and C. Dekker, *Data analysis methods for solid-state nanopores*, *Nanotechnology* **26**, 84003 (2015).

7

RECONSTITUTION OF ULTRAWIDE DNA ORIGAMI PORES IN LIPOSOMES FOR TRANSMEMBRANE TRANSPORT OF MACROMOLECULES

Molecular traffic across lipid membranes is a vital process in cell biology that involves specialized biological pores with a great variety of pore diameters, from fractions of a nanometer to >30 nm. Creating artificial membrane pores covering similar size and complexity will aid the understanding of transmembrane molecular transport in cells, while artificial pores are also a necessary ingredient for synthetic cells. Here, we report the construction of DNA origami nanopores that have an inner diameter as large as 30 nm. We developed methods to successfully insert these ultrawide pores into the lipid membrane of giant unilamellar vesicles (GUVs) by administering the pores concomitantly with vesicle formation in an inverted-emulsion cDICE technique. The reconstituted pores permit the transmembrane diffusion of large macromolecules such as folded proteins, which demonstrates the formation of large membrane-spanning open pores. The pores are size selective as dextran molecules with a diameter up to 28 nm can traverse the pores, whereas larger dextran molecules are blocked. By FRAP measurements and modelling of the GFP influx rate, we find that up to hundreds of pores can be functionally reconstituted into a single GUV. Our technique bears great potential for applications across different fields from biomimetics, synthetic biology, to drug delivery.

This chapter has been published as: Alessio Fragasso, Nicola De Franceschi, Pierre Stömmmer, Eli O. van der Sluis, Hendrik Dietz, Cees Dekker. *Reconstitution of ultrawide DNA origami pores in liposomes for transmembrane transport of macromolecules*. ACS Nano 15(8), 12768-12779 (2021) [1].

7.1. INTRODUCTION

In the last decade, advancements in the field of DNA nanotechnology have enabled the fabrication of a great variety of ‘DNA origami’ nanostructures[2, 3], including transmembrane structures that resemble the biological pores found in cells[4]. Drawing inspiration from protein pores such as alpha-hemolysin[5], artificial pores have been engineered with DNA origami[2, 3] that can insert into lipid bilayers and allow for transmembrane diffusion of ions[6, 7] and small molecules such as fluorophores[8, 9], DNA oligomers[6, 8], short PEG[10], and dextran[9, 11]. To favor partitioning into the lipid bilayer, a popular strategy relies on the chemical modification of the outer nanopore surface with hydrophobic groups, *e.g.* cholesterol, that anchor and stabilize the strongly hydrophilic DNA-based nanopores into the lipid membrane[4]. As DNA origami structures can be designed with virtually any shape or size[12] up to the dimensions comparable to those of viruses[13], the approach bears great potential for various applications, from recapitulating the function of complex enzymes like flippase[14], to mimicking large protein transporters such as the nuclear pore complex[15, 16].

However, so far only small pores with an inner diameter of a few nm have been realized[9, 11], which is because wider pores are increasingly difficult to insert into a membrane. A commonly used strategy to reconstitute pores into a bilayer relies on spontaneous insertion into a preformed lipid membrane[4]. This method relies on transient membrane instabilities[17] and becomes quickly ineffective for larger size objects. This is because the work required to open up a hole in a membrane grows quadratically with the diameter of the hole[7, 9, 18], and spontaneous creation of such a hole occurs in a Boltzmann weighted fashion, which exponentially decreases the chances of success for inserting large pores into spontaneously occurring membrane defects. Scaling up the size of artificial pores thus requires an alternative insertion process that can circumvent the barriers associated with spontaneous insertion.

Here, we overcome these challenges by employing a continuous droplet interface crossing encapsulation (cDICE) technique[19] to incorporate ultrawide (~30 nm inner diameter, ~55 nm outer diameter) DNA origami pores into the membrane of giant unilamellar vesicles (GUVs). As we show below, by administering the pores concomitantly with vesicle formation, the pores can be localized efficiently at the membrane. To demonstrate the transmembrane transport through the pores, we measured the influx of multiple fluorescent macromolecules with different sizes using confocal microscopy. We find that the origami pores indeed support the transit of large (up to 28 nm) molecular structures, consistent with the 30 nm inner diameter of the pores. Using fluorescence recovery after photobleaching (FRAP), we estimate that up to hundreds of pores can be functionally reconstituted in a single liposome. These ultrawide pores represent an exciting tool for various applications, from the mimicking of large biological pores such as the nuclear pore complex, to applications in synthetic biology and drug delivery.

7.2. RESULTS

7.2.1. DESIGN AND ASSEMBLY OF ULTRAWIDE DNA ORIGAMI PORES

Using DNA origami folding of a template strand[2, 3], we designed and assembled a rigid octagonal ring-like structure, see Fig. 7.1. A multi-layer DNA origami object was designed

in square-lattice helical packing and folded from a 7560 bases long scaffold single strand with 240 individual oligonucleotide single strands, arranged in a 4×4 double-helical pattern. It was designed to form a closed-loop octagonal shape, formed by 8 corner design motifs[20] with single-stranded poly-T strands at the corner sites.

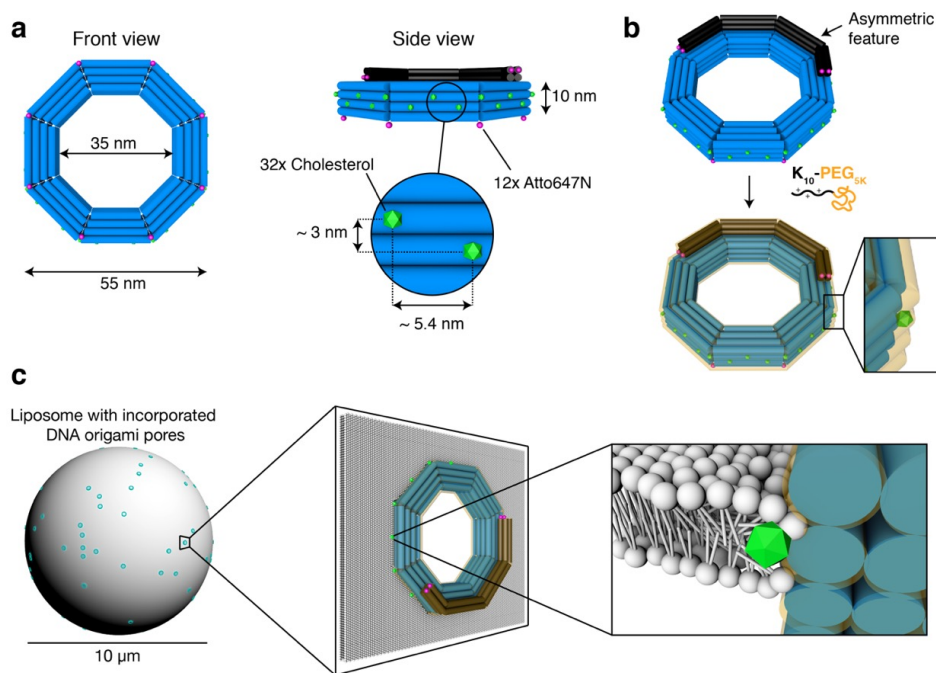


Figure 7.1: DNA origami pore design and incorporation approach. a, DNA origami pore in front (left) and side view (right). Blue cylinders represent DNA double helices. The outer diameter is 55 nm, the inner diameter is 35 nm. Green objects along the outer side of the DNA origami pore indicate the 32 cholesterol modifications. They vertically span over a width of ~ 3 nm (purposely slightly less than the hydrophobic thickness of ~ 3.7 nm of a DOPC-lipid bilayer[21]). Black cylinders represent an asymmetric feature that was introduced for class averaging of single particles from TEM. Violet spots along the outer surface of the DNA origami pore indicate the positions of 12 Atto647N dye modifications. The pore is designed with a height of 10 nm. b, Schematic representation of K_{10} -PEG_{5k} coating of the origami pore. c, Schematic representation of the DNA origami pore incorporated into the lipid bilayer of a GUV. Left: a GUV with pores incorporated in the lipid bilayer; middle: zoom-in on one of the incorporated origami pores resulting in a 30 nm diameter hole; right: a further zoom-in showing individual lipid molecules of the bilayer; white spheres represent lipid heads, white strokes represent lipid tails, the green object represents a cholesterol.

Deletions were introduced every 32 bases to correct for global twist[22]. The origami pore was designed with a nominal outer diameter of 55 nm, an inner diameter of 35 nm, and a height of 10 nm (Fig.7.1a) which represents the channel length. The design includes 48 single stranded handles that were distributed evenly on the interior surface facing the central cavity, as sites for future functionalization purposes (Fig.S7.24). The octagon furthermore included 32 cholesterol modifications on the outer surface that were arranged evenly with a ~ 5.5 nm horizontal spacing and ~ 3 nm vertical distance between neighboring cholessterols (Fig.7.1a). An asymmetric feature was added (Fig.7.1b)

consisting of four additional double helices on top of the octagon, arranged in a 2×2 double helical pattern on the top side of the octagon, spanning over 3 corners. The octagon further features 12 Atto647N dyes for fluorescence imaging, one at each corner on the bottom side of the octagon and four more on both ends of the asymmetric feature (Fig. 7.1a). We iteratively refined the octagon design using gel-electrophoretic mobility analysis as read-out, in order to minimize the occurrence of higher order aggregates and improve the folding quality of the octagon object (Figs.S7.12-S7.19).

The origami pore was coated with K_{10} -PEG_{5k} molecules, which consist of 10 positively charged lysine amino acids (K) linked to a short polyethylene glycol chain (PEG, 5 kDa) (Fig. 7.1B) as described in Ponnuswamy *et al.*[23] This coating serves two purposes: (i) it stabilizes the octagon in low-ionic strength environments, where uncoated DNA origami structures would otherwise disassemble; and (ii) it prevents the cholesterol-modified origami pores from aggregating in bulk. Figure 7.1c shows a schematic illustration of the incorporation of origami pores into the lipid membrane of a liposome (left). The zoom-ins highlight the interaction of the cholesterol-modified origami pores with the lipid molecules.

Characterization of the proper folding and verification of the intended dimensions of the structure were performed using negative-stain TEM imaging and subsequent class averaging of single particles (Figure 7.2). Figure 7.2a shows a high-pass-filtered image of a typical field of view with several octagon pores. The overall shape of the majority of the particles matches the intended design, without obvious defects, in which 8 straight edges and 8 corners form an octagonal ring-like structure with a ~ 35 nm inner diameter and a ~ 11 nm thickness. Most of the structures are oriented in a flat orientation on the surface, while a few can be seen in their side view.

We computed 2D class averages from single particle micrographs (Figure S7.21), which resulted in two distinct images (Figure 7.2b), corresponding to front and side view transmission projections of the particles. The front view displays four distinct layers of double-stranded DNA. The asymmetric feature is visible on the outer two helices on the top side (Figure 7.2b top). The class averaged image of the side view shows less detail of the expected 4 layers of DNA and the asymmetric feature. This is likely due to the staining with uranyl-formate and the tendency of the structures to adhere to the grid surface predominantly with their front side up resulting in less side-view particles. From these images, we measured an inner diameter of ~ 35 nm and a thickness of ~ 11 nm (Fig.S7.22). Accounting for the K_{10} -PEG_{5k} coating by including a layer with thickness 2.4 ± 1.3 nm, as measured by Ponnuswamy *et al.*[23] would result in an effective inner diameter of ~ 30 nm, and an effective height of ~ 16 nm including the unstructured PEG brushes. Class-averaged images of K_{10} -PEG_{5k}-coated and bare octagons match well (Figure S7.23), which shows that the coating preserves the global shape of the octagon pore.

Liposomes with octagons were imaged using negative-stained EM tomography, showing that the octagons can be well incorporated within the lipid membrane (Movie 4 and Movie 5). The tomograms were calculated from EM tilt series. Slices through the tomograms show octagons located at different heights on the surface of the liposomes (Figure ??). The top slices of the tomograms show octagons embedded in the lipid membrane on top of liposomes (Figure 7.2c). The global shape and the inner diameter of these octagons remained intact.

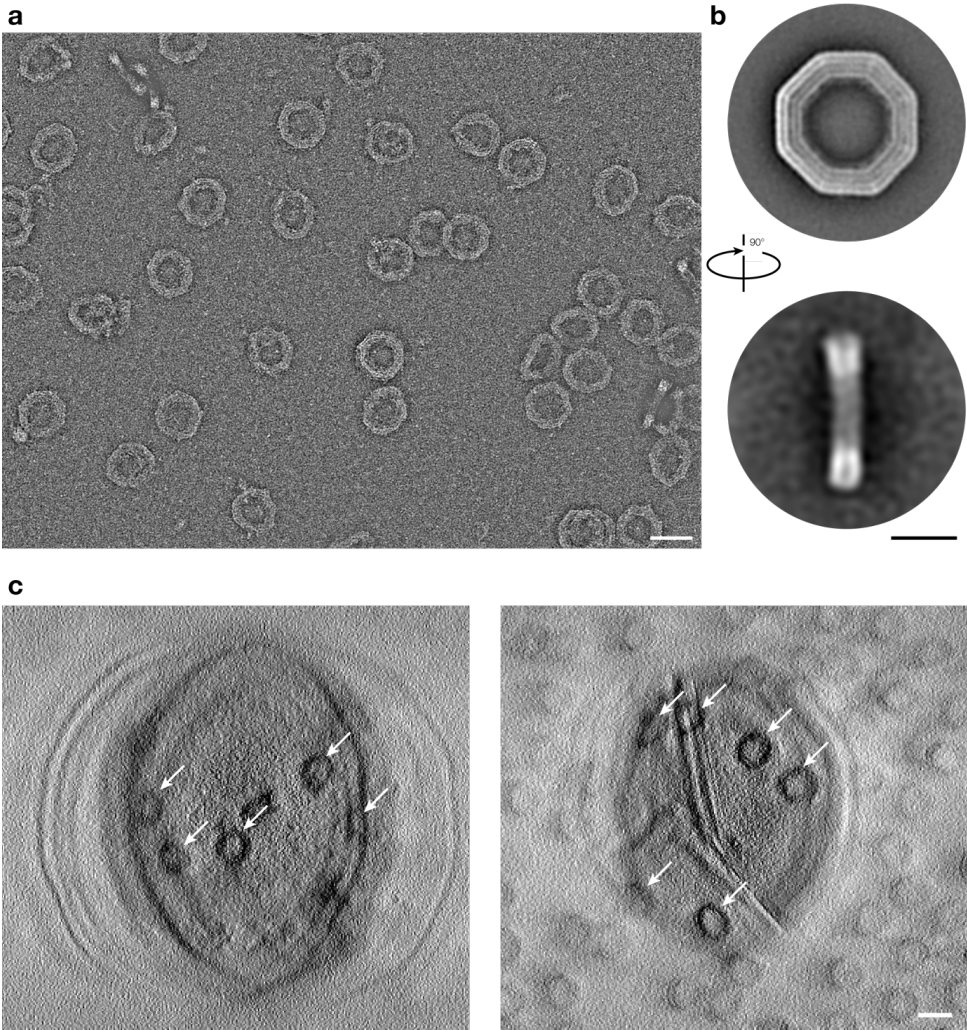


Figure 7.2: Negative-staining TEM and class averaging of the DNA origami pores. a, Typical field of view of a negative-stained DNA-origami sample. The pores in this image were prepared as described in the Methods section. The image is high-pass filtered with a radius of 20 nm and auto leveled in Photoshop. Scale bar: 50 nm. b, Top: Front view class average of N=682 single particles (Fig.S7.21, left). Bottom: Side view class average of N=80 single particles (Fig.S7.21, right). Scale bar: 25 nm. c, Two exemplary slices of negative-stained TEM tomograms calculated from EM tilt series, showing octagons (indicated by white arrows) embedded in the membrane of liposomes at a z-height away from the TEM support surface. See SI Fig.?? for a z-stack of the TEM tomography data. Scale bar: 50 nm.

7.2.2. DNA ORIGAMI PORE RECONSTITUTION IN LIPOSOMES BY cDICE

We first tested spontaneous insertions observed for our 55 nm (outer diameter) large DNA origami pores into free-standing planar lipid bilayers or into pre-formed GUVs, under various conditions and with different nanopore versions with either 32 or 64 cholesterol. As expected, these attempts were unsuccessful. While membrane interactions drove the DNA origami objects to adhere on the GUVs (Fig.S7.25), there was a total lack of influx of molecules (Fig.S7.27), indicating that no actual pores were created with a functional transmembrane opening.

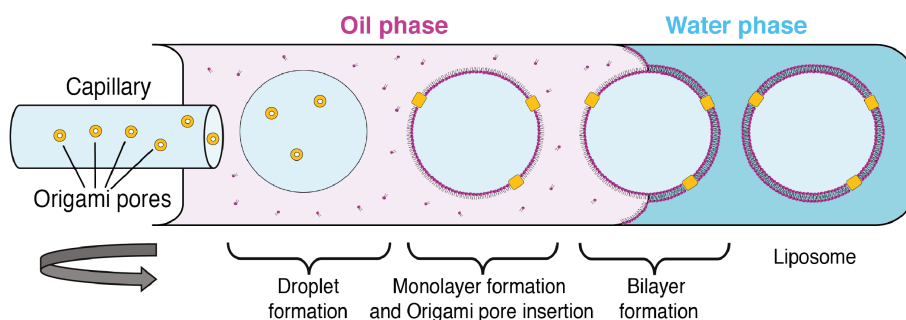


Figure 7.3: Reconstitution of wide DNA origami pores in GUVs by cDICE. Schematics of the cDICE workflow. A section of the rotating chamber is depicted, including the oil and outer buffer phases. Origami pores are indicated in yellow.

7

We therefore used an alternative approach where we incorporate the DNA origami pores during the process of the formation of the GUVs. We employed an inverted emulsion technique called cDICE[19] which yields unilamellar liposomes with good encapsulation of a large variety of macromolecules[24]. Briefly, in cDICE, layers of buffer solution and lipid-in-oil suspension are deposited subsequently in a rotating chamber. As illustrated in Fig.7.3, an inner buffer solution containing the origami pores is then injected through a capillary into the rotating lipid-in-oil suspension at a constant flow rate. Shear forces due to the rotation result in detachment of droplets from the capillary orifice. While travelling through the oil phase, these droplets acquire a first monolayer of lipids where the origami pores can insert. A second monolayer is subsequently formed when the droplets cross the oil-water interface, resulting in GUVs that are eventually collected from the outer buffer solution. In this cDICE process, we thus aimed to reconstitute the pore within the lipid monolayer that is formed in the water-in-oil droplets during the first step of cDICE. Whereas the origami rings with 64 cholesterol mainly resulted in formation of large aggregates at the droplet interface (Fig.S7.28), the rings with 32-cholesterol appeared to interact with the lipid monolayer without inducing significant aggregation, suggesting a more promising route. Hereafter, we report the results for the 32-cholesterol version of the DNA origami rings.

In a standard cDICE protocol[24], the inner buffer solution that is injected contains either sucrose or Optiprep[24] to obtain an optimal density of the inner GUV solution. We found, however, that in these conditions the reconstitution of 32-cholesterol origami rings was inefficient, with most of the origami pores remaining in solution after vesicle

formation (Fig.7.4a). When we included high molecular weight dextran (~2 MDa) in the inner buffer, we found that 32-cholesterol origami rings could be fully localized at the membrane (Fig.7.4a). Note that the choice of such a large dextran molecule (2 MDa) was also motivated by the high diameter of gyration (~76 nm; Ref.23) which makes it large enough to stay in the vesicle despite the presence of the 30 nm wide DNA origami pores. The origami pores appeared to be evenly distributed on the GUV surface, only oc-

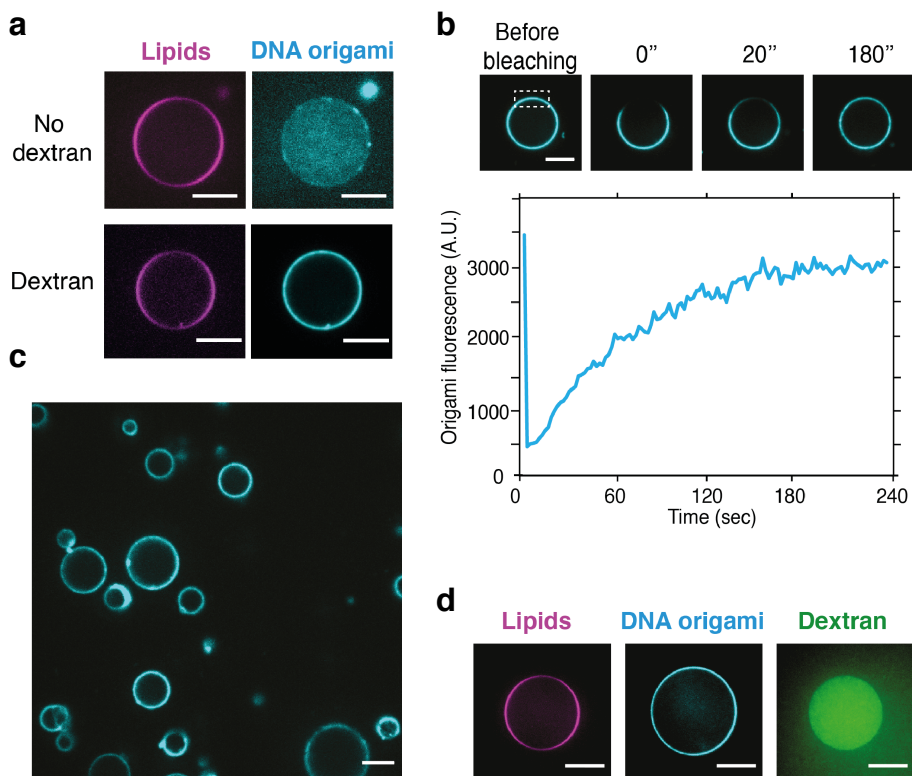


Figure 7.4: Reconstitution of wide DNA origami pores in GUVs by cDICE. a, Comparison of the efficiency of DNA origami pore localization at the membrane by addition of 2 MDa dextran in the inner buffer. Without dextran, origami pores were observed to remain dispersed in bulk, whereas inclusion of dextran drove the origami pores to the lipid surface. b, FRAP analysis of origami pores reconstituted in GUV that shows that the pores are mobile within the lipid bilayer. The dashed rectangle indicates the bleached area, which recovers within a few minutes. c, Example of large field of GUVs with reconstituted origami pores. d, Example of a GUV retaining the 2 MDa dextran in the lumen after 24 hours incubation in buffer. Scale bars: 10 μ m.

casional forming clusters, which then were also enriched in lipids (Movie 1 and Movie 2: z-stack and 3D rendering). Moreover, Fluorescence Recovery After Photobleaching (FRAP) analysis revealed that DNA origami pores could freely diffuse within lipid bilayer of the vesicle membrane (Fig.7.4b). Hundreds of GUVs could be obtained from a single preparation (Fig.7.4c). The resulting GUVs retained the 2 MDa dextran over prolonged periods of time (> 24hrs, Fig.7.4d) and were remarkably stable, remaining spherical in spite of osmotic changes, suggesting that the origami pores were very well able to equili-

brate osmotic differences by allowing osmolytes to rapidly cross the membrane. All in all, the data indicate the successful insertion of wide DNA origami pores in the membrane of GUVs.

7.2.3. PROTEIN INFLUX THROUGH THE PORES DEMONSTRATES THEIR TRANSMEMBRANE TRANSPORT CAPABILITIES

To assess whether the DNA origami pores were functional, *i.e.*, inserted in the intended orientation that allows for transmembrane transport through the central cavity of the octagon, we tested the influx of IBB-mEGFP-Cys, a 34.6 kDa variant of the soluble green fluorescent protein that includes an importin β binding domain[25] (see supporting information 7.5.23), henceforth referred to as ‘GFP’ for simplicity.

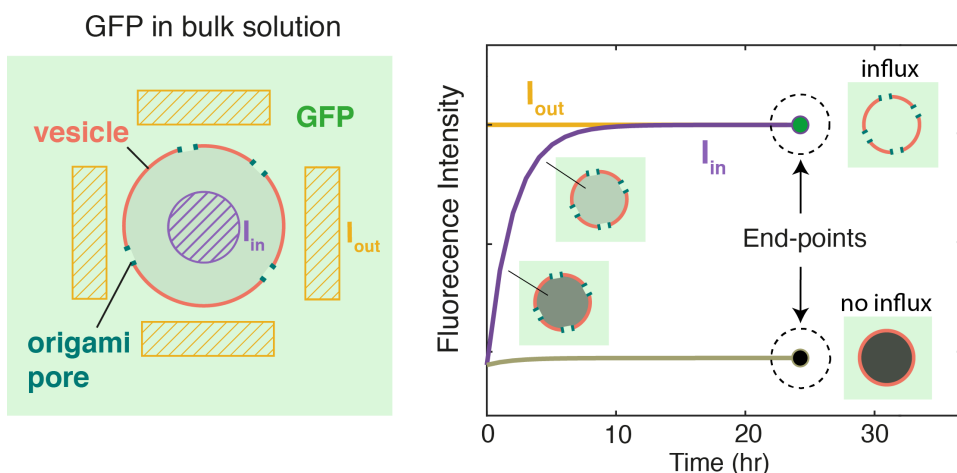


Figure 7.5: Schematic of the influx experiment. Left: Sketch of a vesicle (red) containing pores (blue), that is incubated with GFP (green). Right: Fluorescence intensities I_{in} and I_{out} that are expected to be measured in a time-lapse experiment on the dashed purple and yellow areas, respectively. The right part of the graph illustrates the end-point intensities after ~ 24 hrs, after an initial transient.

We measured the normalized fluorescence intensity difference $I_{n,diff} = (I_{out} - I_{in}) / I_{out}$ of the vesicles, *i.e.*, the difference between in-vesicle intensity (I_{in}) and the outer bulk (I_{out}) divided by I_{out} (Fig.7.5) after overnight incubation of the GUVs in an outer solution with $2.3\mu M$ of GFP. While pore-less vesicles (control, Fig.7.6a) remained empty yielding a finite value $I_{n,diff} = 0.13 \pm 0.05$ (errors are S.D., $N=34$), the pore-containing liposomes showed influx of GFP for about 50% of the vesicles (Fig.7.6b): Half of the vesicles exhibited an almost complete saturation to $I_{n1,diff} = 0.01 \pm 0.03$ ($N=45$), while the other half yielded $I_{n2,diff} = 0.09 \pm 0.03$ ($N=45$), *i.e.*, no significant change compared to the control. We note that heterogeneity in GUV samples is a widely reported phenomenon[26], that here apparently is associated with variations in the efficiency of pore insertion during vesicle formation in cDICE. Most importantly, a clear fraction of the liposomes unambiguously showed transmembrane transport of the folded proteins, indicating transport through the ultrawide DNA origami pores.

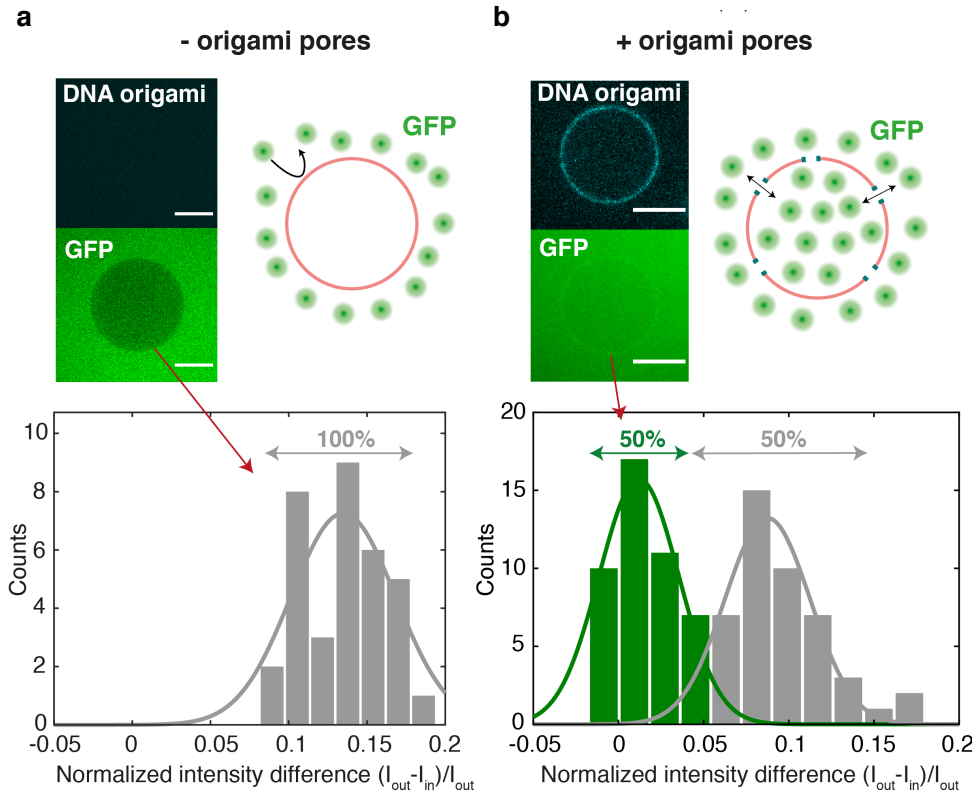


Figure 7.6: a, Influx experiment with vesicles that were not subjected to DNA-pore insertion. Top right: sketch of a pore-less vesicle that excludes GFP. Top left: example of fluorescence image for a pore-less vesicle (cyan) that prevents GFP (green) from entering the vesicle, showing up as a darker area signifying the absence of GFP. Bottom: histogram of the normalized end-point intensity difference $(I_{out} - I_{in})/I_{out}$ for the pore-less vesicles, verifying that no vesicles showed GFP influx. b, Influx experiment with vesicles that were functionalized with origami pores. Top right: sketch of a pore-containing vesicle filled with GFP. Top left: example of fluorescence image for a pore-containing vesicle (cyan) that allows GFP to diffuse (green) into the vesicle, resulting in $I_{out} - I_{in} \approx 0$. Bottom: histogram showing normalized end-point intensity difference $(I_{out} - I_{in})/I_{out}$ for the pore-less vesicles. We find that ~50% of the vesicle population manifested GFP influx. Scale bars: $10\mu m$.

Next, we characterized the GFP influx rate quantitatively using a FRAP assay (Fig. 7.7a). In this experiment, we selected pore-containing vesicles that showed that influx occurred during the overnight incubation (*i.e.*, those with $I_{n,diff} \approx 0$), then photobleached the inner part, and subsequently measured the recovery of the fluorescence signal. An example of FRAP experiment is shown in Fig. 7.7b (top) and Movie 3. Starting from an equilibrium state where $I_{in} \approx I_{out}$ (Fig. 7.7b, left), the vesicle fluorescence drops upon photobleaching to a level comparable to the one of an empty vesicle, to subsequently fully recover within a few minutes (Fig. 7.7b, right). Notably this timescale is much faster compared to those of previously reported fluorescence recovery with DNA origami pores [8, 9]. A control with vesicles lacking pores (Fig. 7.7b, bottom) resulted in no appreciable recovery upon photobleaching. Figure 7.7c displays I_{in} and I_{out} for a pore-containing GUV as a function of time where, after initial transient behavior (grey area), I_{out} is constant, whereas I_{in} continues to slowly increase over time, which represents the influx of GFP through the ultrawide DNA origami pores.

To obtain the number of functional pores, we model the influx rate using a diffusion model derived from the Fick's first law [27]

$$\Phi = -D \frac{dc}{dx}, \quad (7.1)$$

which describes the flux Φ of GFP molecules with diffusion constant D , as a result of the concentration gradient $\frac{dc}{dx}$ between the outer (c_{out}) and inner (c_{in}) environment of the GUV. The flux Φ is defined as number of molecules dN crossing a membrane area dA in a time dt . Since the vesicle volume V is constant over time, the in-vesicle concentration $c_{in}(t)$ is a time-dependent variable that reflects the fact that the vesicle is filling up over time, *i.e.*, $\frac{dc_{in}(t)}{dt} = \frac{1}{V} \frac{dN}{dt}$.

The outside concentration c_{out} instead is assumed to be constant over time, which is reasonable given the large volume ($\sim 200 \mu\text{L}$) of the bulk solution as compared to the $\sim \text{pL}$ volume of the vesicle. Assuming that the diffusion occurs through a number N_p of DNA origami pores that each have a length L_p and an area A_p , yielding a total integrated area $A = A_p N_p$, we can rewrite 7.1 as the first order differential equation

$$\frac{dc_{in}(t)}{dt} = \frac{AD}{V} \frac{c_{out} - c_{in}(t)}{L_p}, \quad (7.2)$$

which, with $c_{in}(t=0) = c_{in,start}$, has a solution

$$c_{in}(t) = c_{out} - (c_{out} - c_{in,start}) e^{-\frac{D_{eff} A}{V L_p} t}. \quad (7.3)$$

Note, however, that for the transport through the pores, we need to employ an effective diffusion constant D_{eff} which is reduced compared to the bulk diffusion constant D to account for the confined transport through the pores, as reported by Dechadilok and Deen [28]. For our pore dimensions, this results in almost a factor of 2 decrease of the GFP diffusivity, *i.e.*, $D_{eff} = 0.54 D_{bulk}$. Upon rearranging Equation 7.3, we then finally obtain

$$\frac{c_{out} - c_{in}(t)}{c_{out}} = \left(1 - \frac{c_{in,start}}{c_{out}}\right) e^{-\frac{D_{eff} A_p N_p}{V L_p} t}. \quad (7.4)$$

As the measured fluorescence intensities are a good measure for the protein concentrations of the fluorescent GFP, we can use Equation 7.4 to fit the $I_{n,diff}(t)$ data, with $c_{in,start}/c_{out}$ and N_p as fit parameters. Figure 7.7d provides an example, showing an excellent fit to the FRAP data. From fitting FRAP curves acquired from different vesicles, we find that the estimated number of pores N_p varies between a few to a few hundred per GUV. Despite the substantial scatter in the extracted N_p (grey circles in Fig.7.7e), which we attribute to the stochasticity inherent to the vesicle production and origami insertion during cDICE, we do observe an overall increase of N_p with the vesicle diameter. Assuming that all origami pores would move from the volume into the membrane during GUV formation, N_p should scale with the cube of the vesicle diameter, which is consistent with the behavior observed (black line in Fig.7.7e).

7.2.4. THE ULTRAWIDE DNA ORIGAMI PORES ACT AS A MOLECULAR SIEVE WITH ~ 30 NM CUT OFF.

To provide evidence that our DNA origami pores indeed form open channels with an effective size of the order of the inner pore diameter of 30 nm, we tested the influx of dextran-FITC molecules with a variety of sizes, *viz.* $D_g \approx 15$ nm (70 kDa), 22 nm (150 kDa), 28 nm (250 kDa), 39 nm (500 kDa), and 76 nm (2 MDa), see Fig.7.8, where D_g is the diameter of gyration as measured by Hanselmann and Burchard[29].

As in the GFP influx experiment, we incubated the pore-containing vesicles with $2 \mu\text{M}$ of dextran-FITC, and measured the normalized intensity difference $I_{n,diff}$ after ~ 24 hrs. This was done independently for each of the 5 molecules, keeping the same molar concentration of dextran-FITC molecules in bulk solution. Similar to the GFP experiments (Fig. 7.6b), $I_{n,diff}$ of pore-containing vesicles yielded two populations when incubated with 70kDa dextran-FITC (Fig.7.9, left), where 58% manifested influx ($I_{n1,diff,70k} = 0.02 \pm 0.03$, errors are S.D., $N=47$), while 42% remained empty ($I_{n2,diff,70k} = 0.13 \pm 0.02$, $N=34$). Incubation with 150 kDa dextran-FITC (Fig.7.9, center-left) led to a similar result, with 47% GUVs that were filled ($I_{n1,diff,150k} = 0.03 \pm 0.03$, $N=24$), against 53% of empty vesicles ($I_{n2,diff,150k} = 0.11 \pm 0.03$, $N=27$). Influx of the larger 250 kDa dextran-FITC (Fig.7.9, center) resulted in a reduced (19%), yet present, population of filled vesicles ($I_{n1,diff,250k} = 0.01 \pm 0.02$, $N=8$), while 79% ($I_{n2,diff,250k} = 0.10 \pm 0.02$, $N=34$) showed no sign of influx. Importantly, this demonstrates that very large (250 kDa; 28 nm) macromolecules can be transported across the ultrawide DNA origami nanopores. By contrast, incubation with the even larger 500 kDa and 2 MDa dextran-FITC (Fig.7.9, center-right and right) resulted in only one population of empty vesicles, with $I_{n,diff,500k} = 0.13 \pm 0.03$ ($N=49$), and $I_{n,diff,2M} = 0.09 \pm 0.04$ ($N=98$), respectively, indicating a lack of any transmembrane transport during 24 hours. This is fully consistent with expectations as their size clearly exceeds the 30 nm size of the origami pore. It is also consistent with the use of 2 MDa dextran as a macromolecular crowder, *cf.* Fig. 7.4d.

7.3. CONCLUSION

In this work, we achieved functional reconstitution of ultrawide DNA origami pores in giant liposomes, obtaining stable transmembrane pores of 30 nm inner diameter within the lipid bilayer. We successfully achieved the pore reconstitution by inserting of the

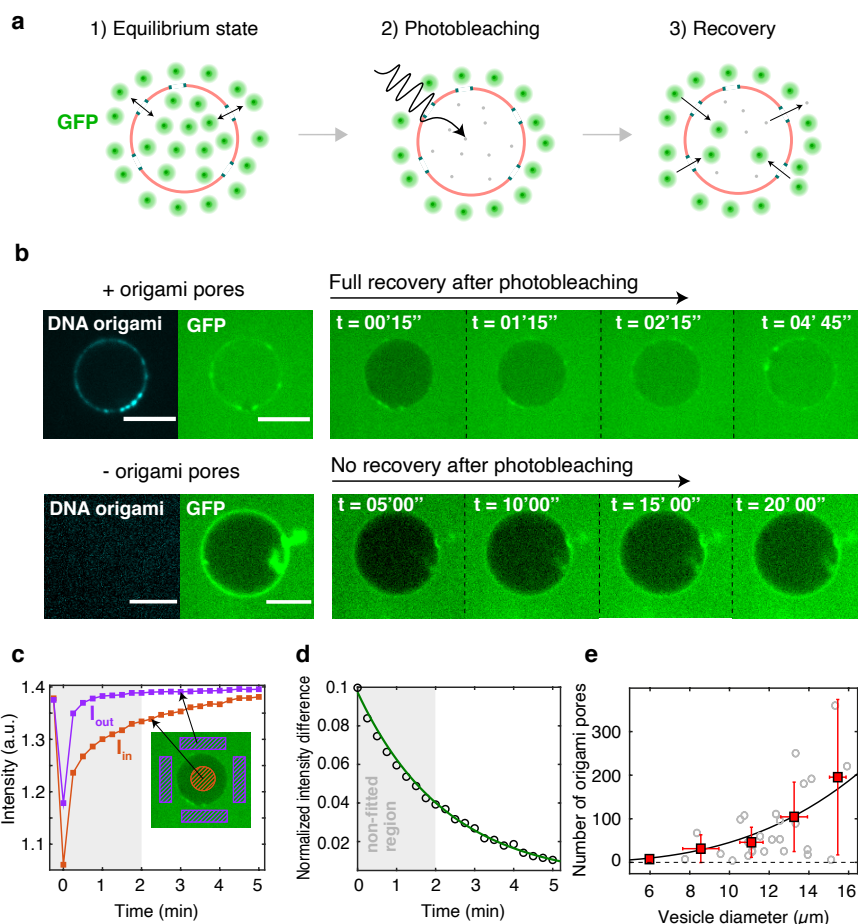


Figure 7.7: FRAP assay, modelling, and extraction of number of functional pores. **a**, Schematic of the FRAP assay: 1) the vesicle is left to equilibrate with bulk solution containing GFP; 2) GFP molecules inside the vesicle are photobleached; 3) new GFP molecules are driven through the ultrawide origami pores from the outer solution, causing a recovery of the fluorescence signal. **b**, Example of a FRAP experiment. Top: (left) image showing the pore-containing vesicle (origami pores in cyan) at equilibrium with the outer GFP (green) solution. Right: series of frames showing recovery (within minutes) of the GFP signal after photobleaching. Bottom: (left) image showing a pore-less vesicle (cyan) that excludes GFP (green) present in the outer solution. Right: series of frames showing the absence of a signal increase after photobleaching. **c**, Fluorescence intensities I_{in} (red) and I_{out} (purple) that reduce and recover after photobleaching for the vesicle shown in **b**. Grey area denotes the initial transient, after which I_{out} can be considered constant. Inset: highlight of the regions where I_{in} (red) and I_{out} (purple) were measured. **d**, Normalized intensity difference $I_{\text{n,diff}}$ over time for the vesicle illustrated in **b**. Data are fitted by Equation 7.4. Grey area was excluded from the fit as the model assumes a constant I_{out} . For such $13.3 \mu\text{m}$ diameter vesicle we estimated a number of functional pores $N_p = 250$. **e**, Number of origami pores extracted from fits for different vesicles, as a function of vesicle diameter (grey circles). Averaged data over $2.5 \mu\text{m}$ bins (red squares, error bars are S.D.) show an increase of the number of pores as a function of vesicle diameter. Black line represents a cubic fit to the data. Scale bars: $10 \mu\text{m}$.

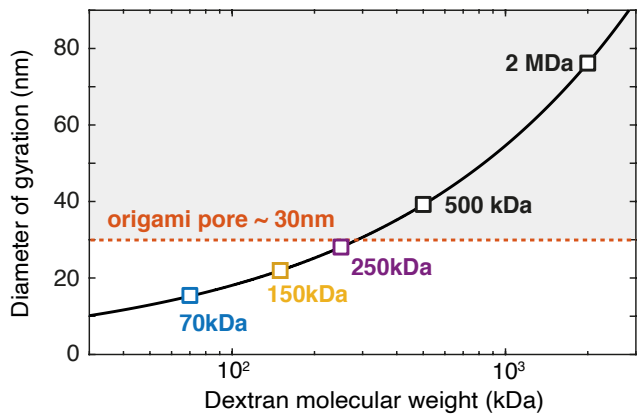


Figure 7.8: Diameter of gyration of dextran D_g vs molecular weight M_w . Black line is a fit of $D_g = 0.072 \cdot M_w^{0.48}$ (Ref.[29]). Dextran sizes of 70 kDa, 150 kDa, 250 kDa, 500 kDa, and 2 MDa employed in our study are highlighted in blue, yellow, magenta, and black, respectively. Grey area underlies dextran sizes larger than the origami pore (red) which are not expected to translocate.

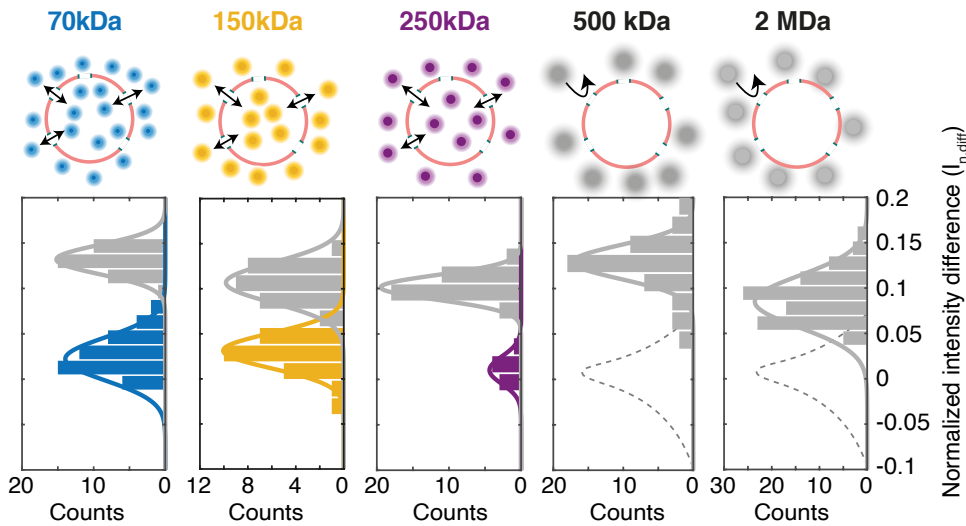


Figure 7.9: Size selectivity of DNA origami nanopores. Histograms showing normalized intensity difference of pore-containing vesicles after overnight incubation the dextran molecules. Blue indicate vesicles that showed influx of 70 kDa, yellow bars for 150 kDa, magenta bars for 250 kDa, whereas grey bars represent empty vesicles. Dashed lines represent hypothetical populations of vesicles that would have been present if influx of 500 kDa or 2 MDa through the origami pores had occurred.

origami pore into a lipid monolayer followed by bilayer formation. This methodology lowers the energy barrier for pore insertion, allowing functional reconstitution of pores with much larger diameter than previously possible.

Our results open the way to a number of biomimetic applications. For example, future efforts can be directed towards the functionalization of the origami pore with FG-nucleoporins from the Nuclear Pore Complex (NPC), the macromolecular complex mediating transport across the nuclear envelope in eukaryotes[30], as reported in previous works[15, 16]. This will enable the creation of selective biomimetic pores that permit the exclusive transport of specific transport receptor proteins. While such biomimetic pores constitute an exciting platform for investigating nucleocytoplasmic transport *in vitro*, it may also be employed as a building block for synthetic cells, thus paving the way towards the *in vitro* reconstitution of an artificial model of a nucleus. This will, for example, aid the study of emergent properties of liposome-confined genomes[31], by allowing the controlled injection of genome-processing proteins. Indeed, our DNA origami pores may be a great asset for building a synthetic cell as they provide a stable portal that is large enough for biological macromolecules like proteins and RNAs to enter a liposome. The long-term stability and functionality of these liposomes is a particularly useful feature in such synthetic-biology applications. Finally, responsive drug-delivery systems that release clinically relevant macromolecules such as antibodies upon stimulation by specific biomolecules could be envisioned as well. We expect that the ultrawide DNA origami nanopores may thus find a broad variety of different applications.

7.4. METHODS

7.4.1. DESIGN OF SCAFFOLDED DNA ORIGAMI OBJECTS

The objects were designed using caDNAno v0.2[32].

7.4.2. OPTIMAL FOLDING CONDITIONS OF THE OCTAGON

The folding reaction mixture for the octagon contained scaffold DNA[33] at a final concentration of 10 nM and oligonucleotide strands (IDT Integrated DNA Technologies) at 300 nM each. The folding reaction buffer contained 5 mM TRIS, 1 mM EDTA, 5 mM NaCl (pH 8) and 24 mM MgCl₂. The folding reaction mixtures were subjected to the following thermal annealing ramp using TETRAD (MJ Research, now Biorad) thermal cycling devices: 15 minutes at 65°C, followed by 16 hours at 50°C, followed by incubation at 20°C before further sample preparation steps.

7.4.3. PURIFICATION OF DNA ORIGAMI NANOSTRUCTURES

Excess oligonucleotides were removed *via* ultrafiltration (Amicon Ultra 0.5 ml Ultracel filters, 50K) with FoB5 (5 mM TRIS, 1 mM EDTA, 5 mM NaCl and 5 mM MgCl₂) buffer[20]. All centrifugation steps were performed at 10 kG for 3 minutes at 25°C. Step 1: 0.5 ml of FoB5 buffer was added to the filters and centrifuged. Step 2: 0.1 ml of folded object sample and 0.4 ml of FoB5 buffer was added to the filters and centrifuged. Step 3: 0.45 ml FoB5 buffer was added to the filters and centrifuged. Step 3 was repeated 3 times before a final retrieving step: the filter insets were turned upside down, placed into a new tube and centrifuged. This concludes one round of ultrafiltration.

7.4.4. COATING OF THE OCTAGON

Different volumes of purified octagons were mixed with PEG-oligolysine (K_{10} -PEG_{5k}). The optimal amount of K_{10} -PEG_{5k} added was determined based on the ratio of nitrogen in amines to the phosphates in DNA (Ponnuswamy *et al.*[23]), to a final ratio of 0.75:1 (N:P).

7.4.5. NEGATIVE-STAIN TEM

A carbon Formvar grid (Electron Microscopy Sciences) was plasma-treated (45 s, 35 mA) right before use. 5 μ L of uncoated octagon sample (10-50 nM DNA object concentrations, 5–20 mM $MgCl_2$ concentration) was pipetted onto the grid. Coated octagon samples were pipetted onto the grids without plasma-treatment, in order to reduce positive staining effects. The sample droplets were incubated for 30-120 s on the grids and then blotted away with filter paper. A 5 μ L droplet of 2% aqueous uranyl formate (UFO) solution containing 25 mM sodium hydroxide was pipetted onto the grid and immediately blotted away. A 20 μ L UFO droplet was then pipetted onto the grid, incubated for 30 s and blotted away. The grids were then air dried for 20 minutes before imaging in a Philips CM100 and an FEI Tecnai 120 microscope. Particles were picked automatically using crYOLO[34] and subsequently class averaged using Relion3.0[35].

Negative stain EM tomography was used to visualize octagons at the surface of liposomes. The samples (5 μ L) containing liposomes with incorporated octagons were incubated on the grid surface until the liquid evaporated (~15 min). The sample was not blotted away using filter paper in an effort not to damage the liposomes through shear forces. All other grid preparation steps were the same as described before.

The tilt series were acquired at a magnification of 30000 \times using an FEI Tecnai 120. The stage was tilted from -50° to 50° and micrographs were acquired every 2°. The tilt series were then processed using Etomo (IMOD)[36] to acquire tomograms. The micrographs were first aligned by calculating a cross correlation of the consecutive images. The tomograms were then generated using a filtered back projection. The Gaussian-Filter used a cutoff of 0.35 and a fall-off of 0.035.

7.4.6. GEL ELECTROPHORESIS OF OCTAGON SAMPLES

Octagon samples were electrophoresed on 1.5 and 2.0% agarose gels containing 0.5 \times tris-borate-EDTA and 5 mM $MgCl_2$ (unless noted otherwise) for around 1-2 hours at 70 or 90 V bias voltage in a gel box, cooled in a water or ice water bath. The loaded samples contained final monomer concentrations of 10 nM (unless otherwise noted). The gels were scanned with a Typhoon FLA 9500 laser scanner (GE Healthcare) at a resolution of 25 or 50 μ m/pixel. Further enhancing resulting images or parts of images was performed using Photoshop CS5.

7.4.7. DNA ORIGAMI SAMPLE PREPARATION PROTOCOL

1. Folding of DNA origami samples at previously described optimal folding conditions.
2. Three rounds of ultrafiltration to purify the samples of excess oligonucleotides.

3. Addition of Atto647N modified oligonucleotide at a final oligonucleotide:DNA origami ratio of 48:1 (12 handles per DNA origami; effective 4:1 ratio).
4. One round of ultrafiltration to purify the samples of excess Atto647N oligonucleotides.
5. Addition of PEG-oligolysine at N:P ratio of 0.75:1, incubate at room temperature overnight.
6. Addition of cholesterol modified oligonucleotide at a final oligonucleotide: DNA origami ratio of 128:1 (32 handles per DNA origami; effective 4:1 ratio).
7. One round of ultrafiltration to purify the samples of excess cholesterol oligonucleotides.

7.4.8. REAGENTS

The 2MDa dextran (D5376), MgCl₂ (M8266), glucose (G7021), Optiprep (60% (w/v) iodixanol in water, D1556), Silicon oil (317667) and Mineral oil (M3516-1L) were purchased from Sigma Aldrich. Tris-HCl (10812846001) was purchased from Roche. DOPC (1,2-dioleoyl-sn-glycero-3-phosphocholine) (850375) and DOPE-Rhodamine (1,2-dioleoyl-sn-glycero-3-phosphoethanolamine-N-(lissamine rhodamine B sulfonyl) (ammonium salt)) (810150C) were purchased from Avanti Lipids. Lipids were stored and resuspended in anhydrous chloroform (288306, Sigma Aldrich). Sodium dodecyl sulfate (SDS) employed for cleaning steps was purchased from Sigma Aldrich. UltraPure Bovine Serum Albumine (BSA) used for passivation of the glass coverslips was purchased by ThermoFisher. For the influx experiments, we employed 70kDa dextran-FITC (FITC:Glucose (mol/mol) = 0.004) (Sigma Aldrich), 150kDa dextran-FITC (FITC:Glucose (mol/mol) = 0.004) (Sigma Aldrich), 250kDa dextran-FITC (FITC:Glucose (mol/mol) = 0.003-0.020) (Sigma Aldrich), 500kDa dextran-FITC (FITC:Glucose (mol/mol) = 0.003-0.020) (Sigma Aldrich), and 2MDa dextran-FITC (FITC:glucose (mol/mol) = 0.001-0.004) (Sigma Aldrich).

7.4.9. EXPRESSION AND PURIFICATION OF IBB-eGFP

For the expression of His14-TEV-IBB-mEGFP-Cys ('IBB-GFP') plasmid pSF807 (Eisele *et al.*[37]) was transformed into *Escherichia coli* BLR cells. Cultures were grown in TB medium supplemented with 50 µg/mL kanamycin, and expression was induced with 0.5 mM IPTG during overnight incubation at 18°C, shaking at 150 rpm in baffled flasks. Cells were harvested by centrifugation (10 min 4000 rpm, JLA8.1000 rotor), washed in 1×PBS buffer and lysed using a French Press (Constant Systems) at 20 kpsi at 4°C in buffer A (2 M NaCl, 50 mM Tris/HCl pH 8.0, 5 mM MgCl₂). Unbroken cells, debris and aggregates were pelleted in a Ti45 rotor (30 min, 40,000 rpm, 4°C), and the lysate resulting from 1 liter cell culture was applied to 2 mL (bed volume) of Ni-NTA matrix pre-washed with buffer A. After 60 min incubation while slowly inverting the tube in a cold room (4°C) the matrix was washed extensively with buffer A supplemented with 60 mM imidazole, and buffer B (50 mM Tris/HCl pH 7.5, 300 mM NaCl, 5 mM MgCl₂, 1 mM βME, 10% glycerol). Following overnight elution by homemade TEV protease in buffer B, the eluate was concentrated by ultracentrifugation and further purified by size exclusion chromatography on a Superdex 200 column (GE Healthcare) pre-equilibrated with buffer B supplemented with

0.5 mM EDTA. The final IBB-GFP sample with a concentration of 138 μM was aliquoted, snap frozen in liquid nitrogen, and stored at -80°C .

7.4.10. CDICE BUFFERS AND SOLUTIONS

The encapsulated inner solution contains 50mM Tris-HCl pH 7.4, 5mM MgCl_2 , 15 μM 2MDa dextran, 2 nM DNA origami pores. The outer solution contains glucose in milliQ water and is osmotically matched to the inner solution. The oil phase is a mixture of silicone and mineral oil (4:1 ratio) and contains lipids dissolved at 0.2mg/mL. The lipid-in-oil suspension was prepared as in Van de Caeter *et al.*[24] and used immediately.

7.4.11. PREPARATION OF LIPID-IN-OIL SUSPENSION

DOPC and DOPE-Rhodamine lipids solubilized in chloroform were mixed at 99.9:0.1 ratio and blow-dried with pure nitrogen. Inside a glove-box filled with pure nitrogen, lipids were subsequently resolubilized with anhydrous chloroform. The freshly prepared mixture of silicon and mineral oil was added to the lipids dropwise while vortexing at 1400 rpm. The lipid-in-oil solution was finally vortexed at 2800 rpm for two minutes, further sonicated in an ice bath for 15 minutes.

7.4.12. CDICE EQUIPMENT AND GUV PRODUCTION

The rotating component of the cDICE device is built from a Magnetic stirrer L-71 (Labinco). A Teflon adaptor connects the rotating shaft with the cDICE chamber, assembled from a standard 3.5 cm cell culture dish (corning) modified to decrease the height. The chamber has an inner height of 8 mm and a circular opening of 10 mm on the top to allow insertion of the capillary and collection of the GUVs. The detailed protocol for GUV production is reported in Van de Caeter *et al.*[24], while here we describe it briefly. First, the cDICE chamber is set to rotate at 300 rpm. 350 μL of outer aqueous solution is injected into the rotating the chamber, followed by 1 mL of lipid-in-oil solution, resulting in the two phases being stacked as depicted in Fig.7.3. The tip of a 100 μm PEEK capillary tube (211633-3, BGB) is then inserted into the oil phase of the rotating chamber, allowing for a continuous supply of inner aqueous solution into the oil phase by a pressure pump (MFCS-EZ, Fluigent) set at 900 mbar. After 15 min, the rotating speed is set to zero, and GUVs are collected from the outer aqueous solution and moved to a pre-passivated imaging well to carry out the fluorescence experiments.

7.4.13. DATA COLLECTION AND ANALYSIS

Fluorescence images were acquired using spinning disk confocal laser microscopy (Olympus IXB1/BX61 microscope, 60 \times objective, iXon camera) with Andor iQ3 software. To induce GFP photobleaching, we employed raster scanning 491 nm laser (at 9.8 mW) over the region of interest. To measure the recovery signal, frames were collected every 15 seconds, starting right after the photobleaching event. Fluorescence images were analyzed and processed using ImageJ (v2.1.0). The extracted fluorescence data were plotted and fitted using MATLAB.

7.4.14. DIFFUSION MODEL

Fluorescence recovery data were fitted with a diffusion model, described by Equation 7.4, derived from the Fick's law of diffusion. While $\frac{c_{in,start}}{c_{out}}$ and N_p were free parameters of the fit, all the other parameters were known or could be calculated. More particularly, the area of the pore $A_p = 745.6 \text{ nm}^2$ was calculated from assuming an octagonal pore with an effective radius of 15 nm (as discussed in the text). The effective diffusion constant $D_{eff} = 47 \text{ } \mu\text{m}^2/\text{s}$ of GFP was calculated using the formula provided by Dechadilok and Deen[28]

$$\begin{aligned} \frac{D_{eff}}{D_{bulk}} = & 1 + \frac{9}{8} \left(\frac{R_g}{R_p} \right) \ln \left(\frac{R_g}{R_p} \right) - 1.56034 \left(\frac{R_g}{R_p} \right) + 0.528155 \left(\frac{R_g}{R_p} \right)^2 + 1.91521 \left(\frac{R_g}{R_p} \right)^3 \\ & - 2.81903 \left(\frac{R_g}{R_p} \right)^4 + 0.270788 \left(\frac{R_g}{R_p} \right)^5 + 1.10115 \left(\frac{R_g}{R_p} \right)^6 - 0.435933 \left(\frac{R_g}{R_p} \right)^7, \end{aligned} \quad (7.5)$$

where R_g is the molecule radius of gyration (for GFP, $R_g = 1.77 \text{ nm}$), R_p is the pore radius (here 15 nm), and D_{bulk} is the diffusion constant of the molecule in free solution (for GFP, $D_{bulk} = 87 \text{ } \mu\text{m}^2/\text{s}$, Ref.[38]). The channel length $L = 16 \text{ nm}$ was assumed to equal the effective height of the origami, which was measured by TEM imaging (Fig.S7.22b). Finally, V was the volume of the vesicle which was estimated from the fluorescence images.

7.5. SUPPORTING INFORMATION

7.5.1. OLIGONUCLEOTIDE SEQUENCES OF THE DNA ORIGAMI NANOPORE STRUCTURE

core_1	ACGGATTTTTTGATTTGTATCATGACAATGTATGATA
core_2	GTTACTTTTTTTTAGCCGGAACGTCGGTTTAACTAAA
core_3	ACTTTTTTTTTGAAAGAGGACAGTAATAATGAGTAGA
core_4	TTCATTTTTTTTCAAGAGTAATCTAAACAACCTTTTCAT
core_5	ACGGATTTTTTAATTATTCATTAGATCTAAATCCAAT
core_6	CGACTTGTAAGTATCGCTATATTTTGTAGTGTTG
core_7	CGGGAGGTTTTTTTTTTGAAGCCTTTTTTCGAGGGGATGAT AAGCATATTAAA
core_8	CACCCAGACAACGCAACGCCAATCAGAAGCGAAAA
core_9	CTACAATTTTTTTTTTATCCTGAATGCTTAATCGTTGTAAGC ATGTCTACGTG
core_10	TCCAGAGTACCAGTCTCAGGAAAGAGAATGGGGTC
core_11	CCTAATTTGCTTTTTTTCAGTTACAAGTATCATCTTCTAATCA GGTCGAACCTT
core_12	CTTCAAAGGAATCAACGCTGAGTAGCTATGACGGG
core_13	TATCGCGTTTTTTTTTTAATTCGAGAAGGCGTTTATCAACGT TCTAAGGAAGG
core_14	CGAACCAGACCGGAAGGTTGGAATCGAAATCCGCGACCT CTTAAAAATGCTG
core_15	CAAACCTCAATTGCTTTTTTAACTATATTTTAGGGCG
core_16	CAACAGGTCATTTTTTGGATTAGAGCATTTTTATATAAAAG ACAACGCGTAA
core_17	TAATTGCTCCAAGAACTGAATTACTCATAAGGGAACCGAAA AAAGGCATATAA
core_18	GGGTATTTCTTTCCTCGTAACTCACGTTCCGCCGCT
core_19	AAACCAAGTATTTTTTCCGCACTCAGTAGAAAAGGGGACAC AAACGTGACGAG
core_20	AAGCAAGCCGTTTTTAAACGAGTAGCCAGGCGCATAGGCTAA TAGAATCGCAAA
core_21	TTTTCATAAAATAAATCGCACCGAGTAAAGAATCA
core_22	CGTAGGAATCTTTTTTATTACCGCGAACAATAACCGCTTGTA GCCAATTAAAG
core_23	CAAGCAAATCAGATATCAAAGCTGTTCAATACCCAAATCAGT AAATCATCAAT
core_24	AGAAGGCGTTCAGCGCCATTCCCATCAACAGAATC
core_25	TTATCCGGTATTTTTTTTCTAAGAATCCAGACCTGTTGGAAA TCAGGAGGCCA
core_26	GTTTTAGCGAACCTCCAAAGACAAGTCACCGA
core_27	CTCAGAGCGTACAAAC

core_28	GAGAAGCCCGGCTACA
core_29	ATGCCTGAGGCCGCTT
core_30	ACCATCAAACAACAAC
core_31	AAATATGCATCAGCTT
core_32	CTGCGAACTTTTTAC
core_33	TAGCTATATTTCAACA
core_34	GCATTAACAGTTTTGT
core_35	GCGCAAAGTAATTACTAGAAAAAGAGCGATTAAGAAAGAT
core_36	TAAGTGTGCGCATATTATTTAAGATTACAGGT
core_37	ATGCGGCCCTTCGTTCGTTTTTAGTCCACAATATTTA
core_38	ATGCGGCCCTTCGTTCGTTTTTGGCCCACAATCATA
core_39	ATGCGGCCCTTCGTTCGTTTTTAAATCGATTGCCTG
core_40	ATGCGGCCCTTCGTTCGTTTTTGCGAGAAGCTGATAA
core_41	ATGCGGCCCTTCGTTCGTTTTTCACGCTGAGAACGCG
core_42	ATGCGGCCCTTCGTTCGTTTTGTGTGCTTGCGGATTG
core_43	ATGCGGCCCTTCGTTCGTTTTTGAGGCCGGCTTTCAT
core_44	ATGCGGCCCTTCGTTCGTTTTTAATCAGTCTCATTTT
asym_1	AATTATTTTTTGAGCCAGCAATTTTCACCGGAGTTTTTCAT
asym_2	AATACTTTTTTGTAATCCACCTTTACCCTCAGGGGTCAGT
asym_3	ACTAATTTTTTAACACGAGGTTTTTGACAGGATCCAGTAA
asym_4	TACCAAGCTAGCCCGGCCCTTGATGAATGGAA
asym_5	ATTAGTTGCTATTTTTGTAAGTTTAGGAAGTTTCAAGCCCACT CCCTCAAAACAGTT
asym_6	CGCTAACGAGCGTCTTTAATGCAGAAACGAAAACCGCCACC CAGAACCTACAGGAG
asym_7	ACCAATGCTTGAGCTTCCACATTAGCAA
asym_8	AGCACCATTACCATTAGCAAAAGTCACCAATAAAGC
asym_9	GGGATAGCCATTA AAAAGACTTATGACCC
asym_10	CTCAGAGGCCACTAGTAGCAATTTATTT
asym_11	CCTCAGAGAGGCAACTCAGCAAACCCCTC
asym_12	TATCACCGTACTCAGTCATCTTAGTTAAAGTAATGT
asym_13	ATGCGGCCTTCGTTCGTTTTTTGATATAAGTAGCGAAACCCG ATATGAAAGGC
asym_14	ATGCGGCCTTCGTTCGTTTTTAAACCATAGCCCCCTTATT
asym_15	TTGTAATCAGTAGCGTAGCGCACCAGAG
asym_16	AATGCCCCCTGCCTACCCGTATGAGCCGC
asym_17	TTTATTCTGAAACATTTAACGAGCCACC
asym_18	CTGAGACTCCTCAAGTTGATGAACCACCA
asym_19	TTTTAGCGGGGTTTTTACCGTGTTGAG
asym_20	ATGCGGCCTTCGTTCGTTTTTATCCTCATTAAGCCAATTCA CAAACAATAA
asym_21	ATGCGGCCTTCGTTCGTTTTTAGCGTTTGCCATCTTTTCATC TGTAGCACATTTGGGAGAGAATA

handle_1	CGACGAAGGCCGCATCATTTTTTTAAGCAACTCTTCCACTT TGGGGAACAGGATTAGCAGAGCGAGG
handle_2	CGACGAAGGCCGCATATTTTTTTAACCTTATGATATACATTT GGGGAACAGGATTAGCAGAGCGAGG
handle_3	CGACGAAGGCCGCATATTTTTTTTGCTTCTGTAAGCGAATTT TGGGGAACAGGATTAGCAGAGCGAGG
handle_4	CGACGAAGGCCGCATGATTTTTTTGAGTAAACAGATAAAGTT TGGGGAACAGGATTAGCAGAGCGAGG
handle_5	TTTTGTCAATCAATCTGGCATGGAGAATTATTTGGGGAA CAGGATTAGCAGAGCGAGG
handle_6	TCATCAGTCATAGTAAAGAAACGTTTGGGGAACAGGATTA GCAGAGCGAGG
handle_7	CTTATGCGATTTTAAGCCAGAGGGAATCAGGTTTTGGGGAA CAGGATTAGCAGAGCGAGG
handle_8	CTCATTCAGTGAATAACCCTTTTTATAATAAGTTTGGGGAAC AGGATTAGCAGAGCGAGG
handle_9	AAAGAAAGAAAATTCTTTTTATATGGTTTACATACCCTTTGG GGAACAGGATTAGCAGAGCGAGG
handle_10	CAAACGAAAAGAAACTTTTTTGCAAAGACACATGTTAGTTAA CATAATTTGGGGAACAGGATTAGCAGAGCGAGG
handle_11	ACGAGGTGAGATTTATTTTTTGGAATACCACAGGAATTTTG GGGAACAGGATTAGCAGAGCGAGG
handle_12	GACGACTAAAACGAATTTTTTCTAACGGAACCTTACCATTTT AAGAGTTTGGGGAACAGGATTAGCAGAGCGAGG
handle_13	GTTTTGAACTGGCTCTTTTTTATTATACCAGAAAAGATTTGG GGAACAGGATTAGCAGAGCGAGG
handle_14	GTCCAATGGTTTAATTTTTTTTTCACTTTAGGATAGCTTTT CAGAATTTGGGGAACAGGATTAGCAGAGCGAGG
handle_15	CCGAAGGGCTTGCCCTTTTTTTGACGAGAAATATCTTTTTG GGGAACAGGATTAGCAGAGCGAGG
handle_16	TACCAGCGATTGAGGTTTTTTGAGGGAAGGTACAAAGTTTA GATAACTTTGGGGAACAGGATTAGCAGAGCGAGG
handle_17	AAATCAAGTGCGGCCACGAGCCGGCCAACGCTTTGGGGA ACAGGATTAGCAGAGCGAGG
handle_18	CTTACCAAGCTTCTAATGAGCTTTGGGGAACAGGATTAGCA GAGCGAGG
handle_19	AATAAACACTTAGTGCTACCTTTTAATTGCGTTTTGGGGAAC AGGATTAGCAGAGCGAGG
handle_20	CTTCAAAGCCTTAGAATTTGATTTGGGGAACAGGATTAGCA GAGCGAGG
handle_21	AGTACCTTTGTGAGTGTTCAATTACAGAAGATTTTGGGGAA CAGGATTAGCAGAGCGAGG

handle_22	TCGAGAACATTTTCATTAAACATTTGGGGAACAGGATTAGCA GAGCGAGG
handle_23	CCCAATAGCTCCTGGTATCCCCGGGACAATATTTTGGGGAA CAGGATTAGCAGAGCGAGG
handle_24	CGCGAGGCCCTTGAATTTTCCTTTGGGGAACAGGATTAGCA GAGCGAGG
handle_25	AACGCTCACCAACCTAAAAGGTGGCAACATATTAGAATTTG GGGAACAGGATTAGCAGAGCGAGG
handle_26	CGACCGTGAAATTGTGGAAAAATCTACGTTAAGATAATTTG GGGAACAGGATTAGCAGAGCGAGG
handle_27	CCTAATTTTGTACAGATAAATTGGGCCTTGAGATACTGTTTG GGGAACAGGATTAGCAGAGCGAGG
handle_28	AGGTAAAGTTATCACCAAGGGCGACATTCAACAAGGATTTG GGGAACAGGATTAGCAGAGCGAGG
handle_29	TCTATTTACTTTTTTGCTCGCCCTGGGTGCCTTTACCTGTC TTTGGGGAACAGGATTAGCAGAGCGAGG
handle_30	TCCTTGAAATTTTTTACATAGCGATTTTCGCCTTTAATTATTT TTGGGGAACAGGATTAGCAGAGCGAGG
handle_31	TGAATTACCTTTTTTTTTTTAATGACAAACATTCGCCATTT TTGGGGAACAGGATTAGCAGAGCGAGG
handle_32	CGGCTGACGTTTTTTCATTTACATATGGTCATTCCAGTGA TTTGGGGAACAGGATTAGCAGAGCGAGG
handle_33	CCCCTTTATTAGAGGCGGTTTTCGTATTTTGGGGAACAGGA TTAGCAGAGCGAGG
handle_34	CCCCTTTAAGTGTAAGAAGCGCATTAGACGGATTAAGACTT TGGGGAACAGGATTAGCAGAGCGAGG
handle_35	CCCCTTTGTTTCAGGTTTAACGTCTGCTTTGGGGAACAGGA TTAGCAGAGCGAGG
handle_36	CCCCTTTAGAAACAAGAATCCCAATCCAAATGAGCAACATTT GGGGAACAGGATTAGCAGAGCGAGG
handle_37	CCCCTTTTTTGAGGTGAGGCGGTCAGTTTTGGGGAACAGG ATTAGCAGAGCGAGG
handle_38	CCCCTTTAAAGAAGAATGACCATAAATCAAAGGTAATAGTTT GGGGAACAGGATTAGCAGAGCGAGG
handle_39	CCCCTTTATTATGGCTATTAGTCTTTATTTGGGGAACAGGA TTAGCAGAGCGAGG
handle_40	CCCCTTTCTCGAATTAATTGAGTTAAGCCCAAAGAAAAGTTT GGGGAACAGGATTAGCAGAGCGAGG
handle_41	CCCCTTTGTGCCAGCTGCATTAATGAATCGGAAGCATATTT GGGGAACAGGATTAGCAGAGCGAGG
handle_42	CCCCTTTGCTCACTGCCCCGCTCACATTAATTGCGTAATTT TGGGGAACAGGATTAGCAGAGCGAGG

handle_43	CCCCTTTTGCACGTAAAAACAGAAATAAAGAACATCGGGTTT GGGGAACAGGATTAGCAGAGCGAGG
handle_44	CCCCTTTATTAACACCGCCTCCAAGTTACAAAATCGTCATTT GGGGAACAGGATTAGCAGAGCGAGG
handle_45	CCCCTTTAAAAATACCGAACGAACCACCAGCCTGAGCATTT GGGGAACAGGATTAGCAGAGCGAGG
handle_46	CCCCTTTATGCGCGAACTGATTAATTACGTGCTTGTTCATTT TGGGGAACAGGATTAGCAGAGCGAGG
handle_47	CCCCTTTGACGGGCAACAATACGTGGCACAGTACCGAGTTT GGGGAACAGGATTAGCAGAGCGAGG
handle_48	CCCCTTTTGGGCGCCAGGGTGTGAAATTGTTATCCGTCATT TGGGGAACAGGATTAGCAGAGCGAGG
handle_49	CCCCTTTATTACCCCTGAACAAAGCTCACAAGTCGGTGGCT GGTTCGAGATA
handle_50	CCCCTTTTCTTATTACGCAGTCACGGAA
handle_51	CCCCTTTAATTTTACAGAGAGAATTTAATGAG
handle_52	CCCCTTTTTTTGTTTAACGTCAAAAGATGAACAATGTCAGAT GATCAATTTCG
handle_53	CCCCTTTCTATCATAACCCTCGAACATTA
handle_54	CCCCTTTAAATTGCATCAAAAAGATTGATTGC
handle_55	CCCCTTTATTCTGACTATTATAGCGCAGAGATCGTCGTGA AAAAAAAGGAA
handle_56	CCCCTTTTAAATGTTTAGACTATCATTG
handle_57	CCCCTTTCGGAATGCTTTAAACAGTTTCAAGA
handle_58	CCCCTTTATTAACAATGAAATAGTACCTCGGGCTTAAACAT TCTACAATAT
handle_59	CCCCTTTTAAGCAGATAGCCGAAACGTAA
handle_60	CCCCTTTAACCGCTAATATCAGAGTTTAGCTG
handle_61	CCCCTTTACTGAATTCAACATTGCCATCTGTTT
handle_62	CCCCTTTAAACAGGAGCCTGGGAGTGACACAAAGAGAGTAA C
handle_63	CCCCTTTGAAAATAGCAGCCACATACATATACATAACGCCAA AATTCAAC
handle_64	CCCCTTTATTTTTTTTTAACAGTGAATTGTCCTTT
handle_65	CCCCTTTGAAGCCCTAACGGAAGCTTAGAATAATGTTAGAG C
handle_66	CCCCTTTGAAGCAAAAGCGGACCAAAATAGCGAGAGGCTTTT GCTCAGGAC
handle_67	CCCCTTTCTTTACTTATTCATAATAACCTTTTT
handle_68	CCCCTTTAACGAGATGATGAAGAAACAGGATTATTTTGACG C
handle_69	CCCCTTTTGAATCCCCCTCAAATCGTCATAAATATTCAATAG CCACCAGA

handle_70	CCCCTTTAGCAAGTTCGGAGGTGGTGTAAATTT
handle_71	CCCCTTTCACAAGCGTAATCAAATCATTGATTGCCATCACT
handle_72	CCCCTTTGAGGGTAATTGAGCGAGGAAACGCAATAATAACG GACAGCGCC
handle_73	CCCCTTTTAATTTCCAGTCGGGAA
handle_74	CCCCTTTATAGCAACAGTTATCAA
handle_75	CCCCTTTAAATAGCCCTAAAACAT
handle_76	CCCCTTTTGTGGTTTTTCTTTTCA
handle_77	CCCCTTTGCGGGGAAAATTCCCTTATAAATTT
handle_78	CCCCTTTAGATTTTATAATCATTTAGAAGTATTT
handle_79	CCCCTTTAAACACTTGCTTGGTCAGTTGGCTT
handle_80	CCCCTTTTTTTGAAGAACCATCGGCCTTGCTTT
core2_1	ATGGTGGTTTTGCGGATCTATGATAGTTGGGTCAACATGTA ATTTAGGCCATGTAC
core2_2	GATTTTTTAGGAGCGGACGAACGTTATTATT
core2_3	TTGGATTATACTTCTGATTGCACT
core2_4	AGTTTTTTAACCTACCATTTAGGAGCACTTT
core2_5	AATATCAACTGAAATGTACATAAATGGGCGCATTATCATTCC TTTTGAACGGTCAA
core2_6	CATTTTTTGATTACACAAAACGCTCATGGTT
core2_7	CTGAAAGCGTAAGAGCTTCTCCGAGGCAAAGCTAATGCAGA ACGCGCCACCGGATA
core2_8	GCTTTTTTCTGGCCCTGGCAATACTTCTTTT
core2_9	GGGTCACGGTCCATTGTAAAATTC
core2_10	ATTATCATGTCAAAGGAAGCCCCA
core2_11	ACAACCTCGAAGTTTTTTTCGATGAA
core2_12	CGTCAATATTAGAGCTTTTTTGAG
core2_13	TTGAGGAAGCGGGCGCTAGTTAAT
core2_14	TCAATCGTGCTTAATGGGTGTAGA
core2_15	TACCGCCATCCTCGTTCAACCCGT
core2_16	TGCCTGAGCGGTACGCAAATAATT
core2_17	CGGCATTTTCGGTCATCGATAGCAGAAACGTC
core2_18	CCTTTAGCGTCAGACTGACAGAAT
core2_19	GCCTTGAGTAACAGTGTTTCGGAACATTTTCA
core2_20	TGTACTGGTAATAAGTTGAAAGTACCGCCACC
core2_21	GCGTCATACATGGCTTAGAAGGATACCGCCAC
core2_22	AGCGCAGTCTCTGAATTGCTCAGT
core2_23	CCACCACCTGAGTTTCTCACCAGTCAGAGGCA
core2_24	CACCCTCAGAGGACTAACGGGTAACATATTTA
core2_25	ACCCTCAGGAACGAGGCGAAGGCAACAGTAGG
core2_26	GAGCCGCCTCGTCACCAAGAATACCAAATTTCT
core2_27	GCAGGTCATTGCAGGGTGACCCCCCTGTTTA
core2_28	CATATTCCTGATTATCCCGCCAAACAAGCTTTATAAAGCC

core2_29	GAGAGCCAGCAGCAAACCTATTAATGACTACCTGAAAATAC
core2_30	ACCAGTAATAAAAAGGGGCTACGTGTCAGGAAGTATCCCAT
core2_31	GCAGCAAGCGGTCCACGGCACGAAGGGCCTCTCCGACAAA
chol_anchor_1	TTTTTTTTTTAATTAAGCACGTTAATTACGCCAGGAATAGCC TGCCCCAG
chol_anchor_2	TTTTTTTTTTTAAATCGGAAGATTGTTGCTGCAACGGCAAAA CCTGTTTG
chol_anchor_3	TTTTTTTTTTTGTAAATACGGTTGATAGGGTTTTCAAAAGTTT AACCACCA
chol_anchor_4	TTTTTTTTTTTCAACGCAAGTAAACCTAAACGACGCCTTTGCC ATTATCAT
chol_anchor_5	TTTTTTTTTTTATATATTTGAGCAAACGAAGCCAGTTTACAAA GGCAATTC
chol_anchor_6	TTTTTTTTTTTGTAGGTAAAAAGGCTAGTGTTGTATTTGAG GCTGATTGT
chol_anchor_7	TTTTTTTTTTTCGGAGACACGGAGAGGGAAGAGTCCTAATAG AGAAGGGTT
chol_anchor_8	TTTTTTTTTTTTCCTAAATTTAATGGTTTGATATCAGCTTGA
chol_anchor_9	TTTTTTTTTTTAGCTCAATTTCAAACCTCCGGCTAACAGTTG TCTAAAGC
chol_anchor_10	TTTTTTTTTTTGTACGGTGCCAATCGCCTATATGTTCAATATC GAACCTCA
chol_anchor_11	TTTTTTTTTTTCAGTTGATGGGATAGGCGTGCATCCCTACAT TTACATTGG
chol_anchor_12	TTTTTTTTTTTTTAGTTTCCGTGGGAGACGACAGAACAGGA AGTCACACG
chol_anchor_13	TTTTTTTTTTTGGTCAATAATGTGAGTCCAGCCATATCCAGA GGCCAACA
chol_anchor_14	TTTTTTTTTTTGGGGCGGCCTTCCTCTGGTGCCCTCAAAC TCTTCTGAC
chol_anchor_15	TTTTTTTTTTTCTACTAATAGGAACGGCCATTCAAGTAATAA CCTTCACC
chol_anchor_16	TTTTTTTTTTTAAATCATATTTTTTTTTTGTGAAGGGCGCCG TTGTAAGAGAGTT
chol_anchor_17	TTTTTTTTTTAATTGTAAAATAAAGCTTTTAATA
chol_anchor_18	TTTTTTTTTTTAAACAGGTTGTACCAAAAACATTTTTTTTTTC ATGA
chol_anchor_19	TTTTTTTTTTTGTACCCCTTTTGCGGTTTATCGC
chol_anchor_20	TTTTTTTTTTTCGGTAATCGGATAAAAATTTTTTTTTTTAGGCG AAAGA
chol_anchor_21	TTTTTTTTTTTAGAGTCTGTAAATGCATTTTTTTTTTTATA
chol_anchor_22	TTTTTTTTTTTAGATCTACAGATTCAAAAGGGTGAATTCGGTC
chol_anchor_23	TTTTTTTTTTTATTAATGCGTCAAATCTTTAAGAA

chol_anchor_24	TTTTTTTTTTTCATCTTCTGACAACAATCATAGAAAATATC GCCACGCT
chol_anchor_25	TTTTTTTTTTAGAAAACATGTTTTTTTTTTTTTTGGCT
chol_anchor_26	TTTTTTTTTTATGCAAATCTGGAAGTTTCATTCCTCCAAAA
chol_anchor_27	TTTTTTTTTTACCGTAATCCCAATTTTTTTTTTCAATA
chol_anchor_28	TTTTTTTTTTCGGATTCTGACCATTAGATACATTAGGAACAA
chol_anchor_29	TTTTTTTTTTCACATTAAACCTGTTTTTTTTTGTCTT
chol_anchor_30	TTTTTTTTTTCGCGTCTGCGAGCTGAAAAGGTGGGAATTTT C
chol_anchor_31	TTTTTTTTTTTTTAACCAATAGTAGTATTTCAATA
chol_anchor_32	TTTTTTTTTTTGCATTAAACAGGCAAGGCAAAGAAGACAGCC C
core3_1	TACAACGCAATCAAAATTTGGCCGGCACCTT
core3_2	CGTAACACGGAACCGCATAGGAACCAAGTTTG
core3_3	GAGGCTTTGAACCGCCTTTACCCTCCTATTT
core3_4	CAGCATCGAGCCGCCACCTCAGAATTAAGAGG
core3_5	TTGCGGGAGCCAGCATTTTTTAGTTAGGATT
core3_6	GCTGAGGCGACGATTGAATAGGTGACCAGGCGGATAAGTG CCGTCGAGAGG
core3_7	CATCGCCACGCATAAAAAAGTACATAAACACC
core3_8	TACCGATAGTTGCGCCCGCCTGATTGATAAAT
core3_9	GCTTTCGAGGTGAATTTGCTCCATTAGAGCTT
core3_10	GGAGCCTTTAATTGTAAGGCGCAGTAAGAGGT
core3_11	GTTGAAAATCTCCAAAACGACCAATCGGCTG
core3_12	CTAAAGGAATTGCGAAATGAACGGACGAGCAT
core3_13	GTTTCAGCGGAGTGAGGGCTGACCGAACAAGA
core3_14	TGTATGGGATTTTGCTTGACAAGATGTTTATC
core3_15	CGTCTTTCCAGACGTTAAATATTGAACAACAT
core3_16	TCATAGTTAGCGTAACAAGGTGAATAATTCTG
core3_17	TTCCAGTTTGGAACAATTTCAAAACTGGCTTTTTTGAAAGGC CAGTTT
core3_18	GAACGTGGACTCCAACTCCGAAATGGCGATTAAACCGACAG
core3_19	ACCGTCTATCAGGGCGTTTATTTTCCAGTTTTTTTCACGAT GAGATTT
core3_20	AACCATCACCCAAATCTATTAAATGCCAGTGCATAACCCC
core3_21	GAGGTGCCGTAAAGCATTTTAGACGGTGGTTTTTATGTTA TGCGTTT
core3_22	AAAGGGAGCCCCCGATGATAATACGAATTCAT
core3_23	GAAAGCCGGCGAACGTTTTAACAAAATAGTTTTTTTGAATTA AATTTT
core3_24	GAAGAAAGCGAAAGGAGGTTATCTGTCTGAGATAATTTTC
core3_25	CTGGCAAGTGTAGCGGTTTAAATCTAGGTTTTTTTTTGGGTG CGGATTT

core3_26	CCACCACACCCGCCGCACCCTCAAAAATGCTGTCAATATA
core3_27	ACAGGGCGCGTACTATTTTAAATATGCCATTTTTTGTTCG CAATTTT
core3_28	CACGTATAACGTGCTTGCCATTGCTATCGGCCATTTAACA
core3_29	GAGCGGGAGCTAAACATTTGGTAAGCTTTTTTTTTCCGGCG ATAATTT
core3_30	GGATTTTAGACAGGAATAGAAGAAGGAAACCAACTCTGAC
core3_31	CTGAGAAGTGTTTTATTTTGATTGGCTGTTTTTCGCAAGA CGATTT
core3_32	CCGAGTAAAGAGTCTCAAATTAAATCGGTGCTATAGGGG
cholesterol-oligo	AAAAAAAAAA-TEG-Chol
ATTO-dye-oligo	CGACGAAGGCCGCA/3ATTO647NN/

Table S7.1: Oligonucleotide sequences employed for the DNA origami nanopore structure.

7.5.2. SEQUENCE OF THE 7560 BASE LONG SCAFFOLD

TGATAGACGGTTTTTCGCCCTTTGACGTTGGAGTCCACGTTCTTTAATAGTGGACTCTT
GTTCCAAACTGGAACAACACTCAACCCTATCTCGGGCTATTCTTTTGATTATAAGGGA
TTTTGCCGATTTGGAACCAACCATCAAACAGGATTTTCGCCTGCTGGGGCAAACCAGC
GTGGACCGCTTGCTGCAACTCTCTCAGGGCCAGGCGGTGAAGGGCAATCAGCTGTTGC
CCGTCTCACTGGTGAAAAAGAAAAACCACCCTGGCGCCCAATACGCAAACCGCCTCTCC
CCGCGCGTTGGCCGATTCATTAATGCAGCTGGCAGCAGAGGTTCCCGACTGGAAAGC
GGGCAGTGAGCGCAACGCAATTAATGTGAGTTAGCTCACTCATTAGGCACCCAGGCT
TTACAGTTTATGCTTCCGGCTCGTATGTTGTGTGGAATTGTGAGCGGATAACAATTTCA
CACAGGAAACAGCTATGACCATGATTACGAATTCGAGCTCGGTACCCGGGGATCCTCC
GTCTTTATCGAGGTAACAAGCACACGTAAGCTTAAGCCCTGTTTACTCATTACACCAAC
CAGGAGGTCAGAGTTTCGGAGAAATGATTTATGTGAAATGCGTCAGCCGATTCAAGGCC
CCTATATTCGTGCCACCGACGAGTTGCTTACAGATGGCAGGGCCGCACTGTCGGTAT
CATAGAGTCACTCCAGGGCGAGCGTAAATAGATTAGAAGCGGGTTATTTTGCGGGGA
CATTGTCATAAGGTTGACAATTCAGCACTAAGGACACTTAAGTCGTGCGCATGAATTCA
CAACCACTTAGAAGAACATCCACCCTGGCTTCTCCTGAGAAAGCTTGGCACTGGCCGT
CGTTTTACAACGTCGTGACTGGGAAAAACCCTGGCGTTACCCAACCTAATCGCCTTGCAG
CACATCCCCCTTTCGCCAGCTGGCGTAATAGCGAAGAGGCCCGCACCGATCGCCCTTC
CCAACAGTTGCGCAGCCTGAATGGCGAATGGCGCTTTGCCTGGTTCCGGCACCAGAA
GCGGTGCCGGAAGCTGGCTGGAGTGCGATCTTCTGAGGCCGATACTGTCGTCGTC
CCCTCAAACCTGGCAGATGCACGGTTACGATGCGCCCATCTACACCAACGTGACCTATC
CCATTACGGTCAATCCGCCGTTTGTTCACGAGGAATCCGACGGGTTGTTACTCGCT
CACATTTAATGTTGATGAAAGCTGGCTACAGGAAGGCCAGACGCGAATTATTTTGATG
GCGTTCTTATTGGTTAAAAAATGAGCTGATTTAACAAAAATTTAATGCGAATTTAACA
AATATTAACGTTTACAATTTAAATATTTGCTTATACAATCTTCCTGTTTTTGCGGCTTT
CTGATTATCAACGGGGTACATATGATTGACATGCTAGTTTTACGATTACCGTTTCATCG
ATTCTCTGTTTGCTCCAGACTCTCAGGCAATGACCTGATAGCCTTTGTAGATCTCTCA
AAAATAGCTACCCTCTCCGGCATTAAATTTATCAGCTAGAACGGTTGAATATCATATTGAT
GGTGATTGACTGTCTCCGGCCTTCTCACCCTTTGAATCTTTACCTACACATTACTC
AGGCATTGCATTTAAAATATATGAGGGTTCTAAAAATTTTTATCCTTGCGTTGAAATAAA

GGCTTCTCCCGCAAAAGTATTACAGGGTCATAATGTTTTTGGTACAACCGATTTAGCTT
TATGCTCTGAGGCTTTATTGCTTAATTTTGCTAATTCCTTGCCTTGCCTGTATGATTTAT
TGGATGTTAATGCTACTACTATTAGTAGAATTGATGCCACCTTTTCAGCTCGCGCCCCA
AATGAAAATATAGCTAAACAGGTTATTGACCATTTGCGAAATGTATCTAATGGTCAAACCT
AAATCTACTCGTTTCGAGAAATTGGGAATCAACTGTTATATGGAATGAACTTCCAGACA
CCGTACTTTAGTTGCATATTTAAAACATGTTGAGCTACAGCATTATATTCAGCAATTAAG
CTCTAAGCCATCCGCAAAAATGACCTCTTATCAAAAAGGAGCAATTAAGGTACTCTCTA
ATCCTGACCTGTTGGAGTTTGCTTCCGGTCTGGTTCGCTTTGAAGCTCGAATTAACG
CGATATTTGAAGTCTTTCGGGCTTCCTCTTAATCTTTTGATGCAATCCGCTTTGCTTC
TGACTATAATAGTCAGGGTAAAGACCTGATTTTTGATTTATGGTCATTCTCGTTTTCTGA
ACTGTTTAAAGCATTTGAGGGGGATTCAATGAATATTTATGACGATTCCGCAGTATTGG
ACGCTATCCAGTCTAAACATTTTACTATTACCCCTCTGGCAAACTTCTTTTGCAAAAG
CCTCTCGCTATTTTGGTTTTTATCGTCGTCTGGTAAACGAGGGTTATGATAGTGTTGCT
CTTACTATGCCTCGTAATTCCTTTTGGCGTTATGTATCTGCATTAGTTGAATGTGGTATT
CCTAAATCTCAACTGATGAATCTTCTACCTGTAATAATGTTGTTCCGTTAGTTTCGTTTT
ATTAACGTAGATTTTCTTCCCAACGTCCTGACTGGTATAATGAGCCAGTTCTTAAATC
GCATAAGGTAATTCACAATGATTAAAGTTGAAATTAACCATCTCAAGCCCAATTTACTA
CTCGTTCTGGTGTTTCTCGTCAGGGCAAGCCTTATTCAGTGAATGAGCAGCTTTGTTAC
GTTGATTTGGGTAATGAATATCCGGTTCCTGTCAAGATTACTCTTGATGAAGGTCAGCC
AGCCTATGCGCCTGGTCTGTACACCGTTCATCTGTCTCTTTCAAAGTTGGTCAGTTTCG
GTTCCCTTATGATTGACCGTCTGCGCCTCGTTCCGGCTAAGTAACATGGAGCAGGTCG
CGGATTTTCGACACAATTTATCAGGCGATGATACAAATCTCCGTTGTACTTTGTTTCGCG
CTTGGTATAATCGCTGGGGGTCAAAGATGAGTGTTTTAGTGATTCTTTTGCCTCTTTC
GTTTTAGGTTGGTGCCCTCGTAGTGGCATTACGTATTTTACCCGTTTAAATGGAAACTTC
CTCATGAAAAAGTCTTTAGTCCTCAAAGCCTCTGTAGCCGTTGCTACCCTCGTTCCGAT
GCTGTCTTTTCGCTGCTGAGGGTGACGATCCCGCAAAAAGCGGCCTTTAACTCCCTGCAA
GCCTCAGCGACCGAATATATCGGTTATGCGTGGGCGATGGTTGTTGTCATTGTGCGCG
CAACTATCGGTATCAAGCTGTTTAAAGAAATTCACCTCGAAAGCAAGCTGATAAACCGAT
ACAATTAAGGCTCCTTTTGGAGCCTTTTTTTTGGAGATTTTCAACGTGAAAAAATTATT
ATTGCAATTCCTTTAGTTGTTCTTTCTATTCTCACTCCGCTGAACTGTTGAAAGTTG
TTTAGCAAAATCCCATACAGAAAATTCATTTACTAACGTCTGGAAAGACGACAAAACCTT
AGATCGTTACGCTAACTATGAGGGCTGTCTGTGGAATGCTACAGGCGTTGTAGTTTGTA
CTGGTGACGAAACTCAGTGTTACGGTACATGGGTTCCCTATTGGGCTTGCTATCCCTGAA
AATGAGGGTGGTGGCTCTGAGGGTGGCGGTTCTGAGGGTGGCGGTTCTGAGGGTGGC
GGTACTAAACCTCCTGAGTACGGTGATACACCTATTCGGGGCTATACTTATATCAACCC
TCTCGACGGCACTTATCCGCCTGGTACTGAGCAAAACCCCGCTAATCCTAATCCTTCTC
TTGAGGAGTCTCAGCCTCTTAATACTTTCATGTTTCAGAATAATAGGTTCCGAAATAGG
CAGGGGGCATTAACTGTTTATACGGGCACTGTTACTCAAGGCACTGACCCCGTTAAAC
TTATTACAGTACACTCCTGTATCATCAAAAGCCATGTATGACGCTTACTGGAACGGTA
AATTCAGAGACTGCGCTTTCCATTCTGGCTTTAATGAGGATTTATTTGTTTGTAATATC
AAGGCCAATCGTCTGACCTGCCTCAACCTCCTGTCAATGCTGGCGGCGGCTCTGGTGG
TGTTTCTGGTGGCGGCTCTGAGGGTGGTGGCTCTGAGGGTGGCGGTTCTGAGGGTGG
CGGCTCTGAGGGAGGCGGTTCCGGTGGTGGCTCTGGTTCGGTGATTTTGATTATGAA
AAGATGGCAACGCTAATAAGGGGGCTATGACCGAAAATGCCGATGAAAACGCGCTAC
AGTCTGACGCTAAAGGCCAACTTGATTCTGTGCTACTGATTACGGTGCTGCTATCGAT

GGTTCATTGGTGACGTTTCCGGCCCTTGCTAATGGTAATGGTGCTACTGGTGATTTTGC
 TGGCTCTAATTCCCAAATGGCTCAAGTCGGTGACGGTGATAATTCACCTTTAATGAATA
 ATTTCCGTCAATATTTACCTTCCCTCCCTCAATCGGTTGAATGTCGCCCTTTTGTCTTTG
 GCGCTGGTAAACCATATGAATTTTCTATTGATTGTGACAAAATAAACTTATTCGGTGGTG
 TCTTTGCGTTTCTTTTATATGTTGCCACCTTTATGTATGTATTTTCTACGTTTGCTAACA
 TACTGCGTAATAAGGAGTCTTAATCATGCCAGTTCCTTTGGGTATTCCGTTATTATTGC
 GTTTCCTCGGTTTCTTCTGTTAACTTTGTTCCGGCTATCTGCTTACTTTTCTTAAAAAGG
 GCTTCGGTAAGATAGCTATTGCTATTTTATTGTTTCTTGCTCTTATTATTGGGCTTAACT
 CAATTCTTGTGGGTATCTCTCTGATATTAGCGCTCAATTACCCCTCTGACTTTGTTTCTAG
 GGTGTTTCTAGTTAATTCTCCCGTCTAATGCGCTTCCCTGTTTTATGTTATTCTCTCTGTA
 AAGGCTGCTATTTTCAATTTTACGTTAAACAAAAATCGTTTCTTATTGATTGTTGGGAT
 AAATAATATGGCTGTTTATTTTGTAACTGGCAAAATTAGGCTCTGGAAGACGCTCGTTA
 GCGTTGGTAAGATTACAGGATAAAATTGTAGCTGGGTGCAAAATAGCAACTAATCTTGAT
 TTAAGGCTTCAAAACCTCCCGCAAGTCGGGAGGTTGCTAAAAACGCCCTCGCGTTCTTA
 GAATACCGGATAAGCCTTCTATATCTGATTTGCTTGCTATTGGGCGCGGTAATGATTCC
 TACGATGAAAATAAAAACGGCTTGCTTGTCTCGATGAGTGCGGTACTTGGTTTAAATAC
 CCGTTCTTGAATGATAAGGAAAGACAGCCGATTATTGATTGGTTTCTACATGCTCGTA
 AATTAGGATGGGATATTATTTTCTTGTTCAGGACTTATCTATTGTTGATAAACAGGCGC
 GTTCTGCATTAGCTGAACATGTTGTTTATTGTCGTCGCTGGACAGAATTACTTTACCT
 TTTGTCGGTACTTTATATTCTTATTACTGGCTCGAAAATGCCTCTGCCTAAATTACAT
 GTTGGCGTTGTTAAATATGGCGATTCTCAATTAAGCCCTACTGTTGAGCGTTGGCTTTA
 TACTGGTAAGAATTTGTATAACGCATATGATACTAAACAGGCTTTTTCTAGTAATTATGA
 TTCCGGTGTTTATTCTTATTTAACGCCTTATTTATCACACGGTCGGTATTTCAAACCATT
 AAATTTAGGTCAGAAGATGAAATTAATAAAATATATTTGAAAAAGTTTTCTCGCGTTCT
 TTGTCTTGCATTGGATTTGCATCAGCATTTACATATAGTTATATAACCCAACCTAAGCC
 GGAGGTTAAAAAGGTAGTCTCTCAGACCTATGATTTTGATAAATTCATATTGACTCTTC
 TCAGCGTCTTAATCTAAGCTATCGCTATGTTTTCAAGGATTCTAAGGGAAAAATTAATTAA
 TAGCGACGATTTACAGAAGCAAGGTTATTTCACTCACATATATTGATTTATGTACTGTTTC
 CATTAAAAAGGTAATTCAAATGAAATTGTTAAATGTAATTAATTTTGTCTTCTGATGTT
 TGTTTCATCATCTTCTTTTGCTCAGGTAATTGAAATGAATAATTCGCCTCTGCGCGATTT
 TGTAACCTTGGTATTCAAAGCAATCAGGCGAATCCGTTATTGTTTCTCCCGATGTAAAAG
 GTACTGTTACTGTATATTCTGACGTTAAACCTGAAAACTACGCAATTTCTTTATTT
 CTGTTTTACGTGCAATAATTTTGATATGGTAGGTTCTAACCCCTCCATTATTGAGAAGT
 ATAATCCAAACAATCAGGATTATATTGATGAATTGCCATCATCTGATAATCAGGAATATG
 ATGATAATTCGCTCCTTCTGGTGGTTTCTTTGTTCCGCAAAATGATAATGTTACTCAA
 CTTTTAAATTAATAACGTTCCGGGCAAAGGATTTAATACGAGTTGTGCAATTGTTTGTA
 AGTCTAATACTTCTAAATCCTCAAATGTATTATCTATTGACGGCTCTAATCTATTAGTTG
 TTAGTGCTCCTAAAGATATTTTAGATAACCTTCTCAATTCCTTTCACTGTTGATTGTC
 CAACTGACCAGATATTGATTGAGGGTTTGATATTGAGGTTGAGCAAGGTGATGCTTTA
 GATTTTTCATTGCTGCTGGCTCTCAGCGTGGCACTGTTGCAGGCGGTGTTAATACTGA
 CCGCCTCACCTCTGTTTTATCTTCTGCTGGTGGTTCGTTCCGGTATTTTAAATGGCGATG
 TTTTAGGGCTATCAGTTGCGGCATTAAAGACTAATAGCCATTCAAAAATATTGTCTGTGC
 CACGATTCTTACGCTTTCAGGTCAGAAGGGTCTATCTCTGTTGGCCAGAATGTCCCT
 TTTATTACTGGTCGTGTGACTGGTGAATCTGCCAATGTAAATAATCCATTTACAGACGAT
 TGAGCGTCAAAATGTAGGTATTTCCATGAGCGTTTTTCTGTTGCAATGGCTGGCGGTA

ATATTGTTCTGGATATTACCAGCAAGGCCGATAGTTTGAGTTCTTCTACTCAGGCAAGT
GATGTTATTACTAATCAAAGAAGTATTGCTACAACGGTTAATTTGCGTGATGGACAGAC
TCTTTTACTCGGTGGCCTCACTGATTATAAAAACACTTCTCAGGATTCTGGCGTACCGT
TCCTGTCTAAAATCCCTTTAATCGGCCTCCTGTTTAGCTCCCGCTCTGATTCTAACGAG
GAAAGCACGTTATACGTGCTCGTCAAAGCAACCATAGTACGCGCCCTGTAGCGGCGCA
TTAAGCGCGGCGGGTGTGGTGGTTACGCGCAGCGTGACCGCTACACTTGCCAGCGCC
CTAGCGCCCGCTCCTTTCGCTTTCCTCCCTTCCTTCTCGCCACGTTGCGCGGCTTTC
CCGTCAAGCTCTAAATCGGGGGCTCCCTTTAGGGTTCCGATTTAGTGCTTTACGGCAC
CTCGACCCCAAAAACTTGATTTGGGTGATGGTTCACGTAGTGGGCCATCGCCC

7.5.3. CADNANO STRAND DIAGRAM OF THE ORIGAMI PORE

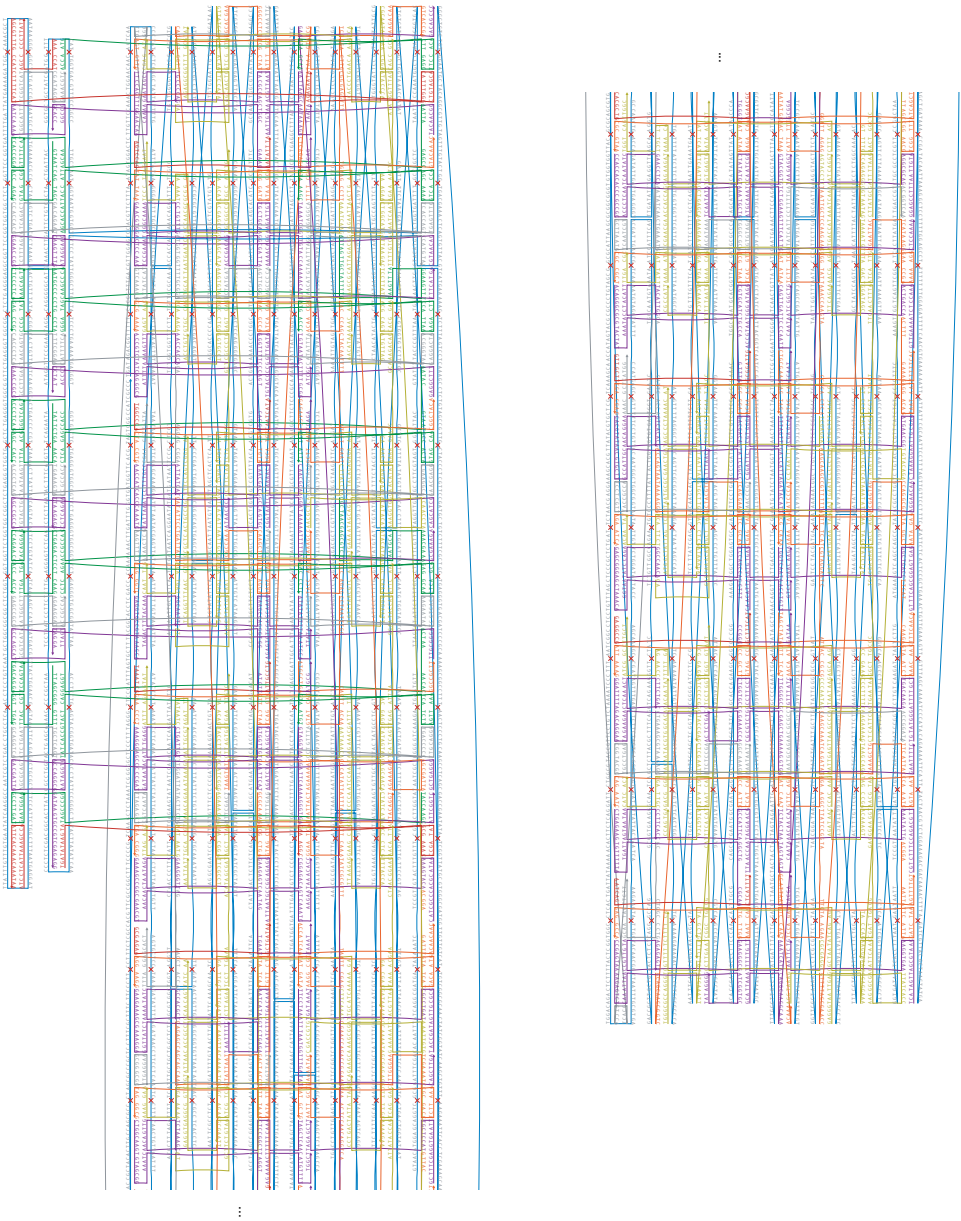


Figure S7.10: CaDNAno diagram of the DNA origami nanopore.

7.5.4. INITIAL FOLDING SCREEN OF THE ORIGAMI PORE

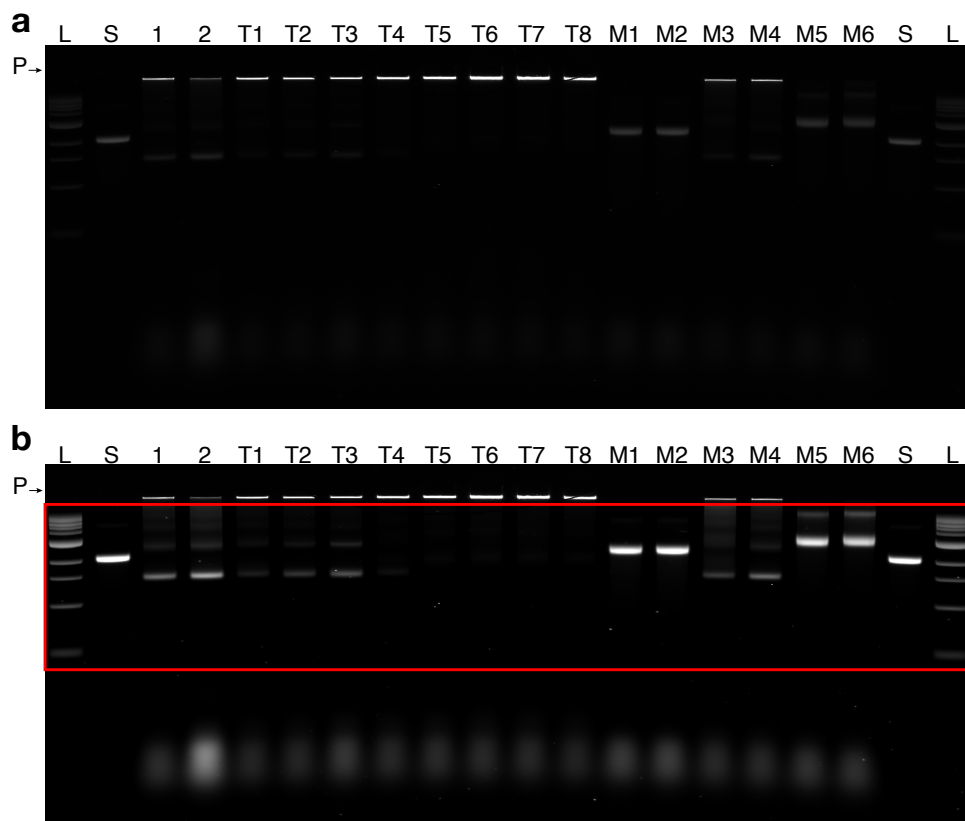


Figure S7.11: Initial folding screen of the DNA origami nanopore. a and b show the same laser-scanned image of a 2% agarose gel with 5.5 mM MgCl_2 run on a water bath. b, The red box indicates that this region was auto-leveled. The following samples were electrophoresed at 90 V for 90 min: L, 1kb ladder; S, 7560 bases long scaffold; 1, folding interval 60–44°C, 20 mM, 5× staple-to-scaffold excess; 2, 60–44°C, 1 h/°C, 20 mM MgCl_2 , 10× staple-to-scaffold excess; lanes T1–T8: 20 mM MgCl_2 ; T1, folding interval 50–47°C; T2, folding interval 52–49°C; T3, folding interval 54–51°C; T4, folding interval 56–53°C; T5, folding interval 58–55°C; T6, folding interval 60–57°C; T7, folding interval 62–59°C; T8, folding interval 64–61°C; lanes M1–M6, folding interval 60–44°C; M1, 5 mM MgCl_2 ; M2, 10 mM MgCl_2 ; M3, 15 mM MgCl_2 ; M4, 20 mM MgCl_2 ; M5, 25 mM MgCl_2 ; M6, 30 mM MgCl_2 . P: Pocket.

7.5.5. ADVANCED FOLDING SCREEN 1

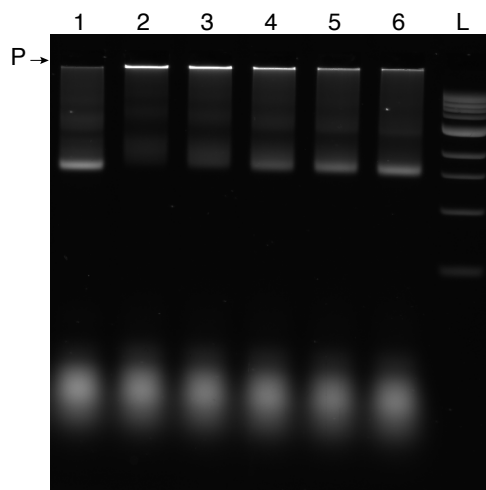


Figure S7.12: Temperature folding screen of the DNA origami nanopore. Laser-scanned image of a 2% agarose gel with 5.5 mM MgCl₂ run on a water bath on which the following samples were electrophoresed at 90 V for 90 min: lanes 1-6: 20 mM MgCl₂; 1, 60-44°C, 1 h /°C; 2, folding interval 42-39°C; 3, folding interval 44-41°C; 4, folding interval 46-43°C; 5, folding interval 48-45°C; 6, folding interval 50-47°C; L, 1kb ladder. P: Pocket.

7.5.6. ADVANCED FOLDING SCREEN 2

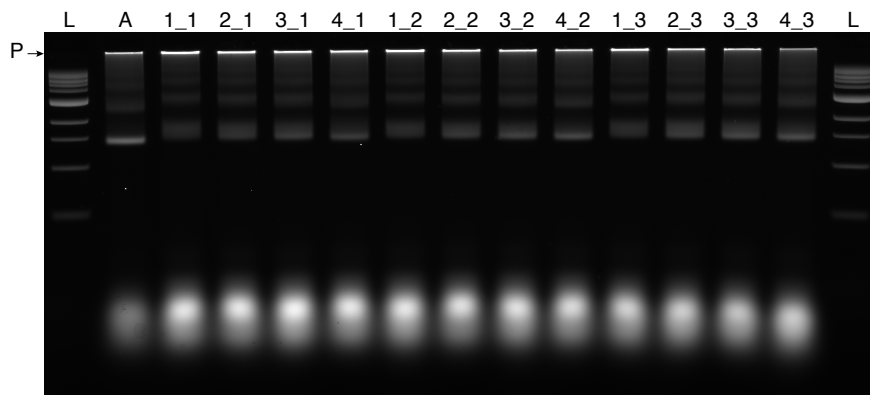


Figure S7.13: Temperature folding screen of the DNA origami nanopore. Laser-scanned image of a 2% agarose gel with 5.5 mM MgCl₂ run on a water bath on which the following samples were electrophoresed at 90 V for 90 min: L, 1kb ladder; all other lanes: 20 mM MgCl₂; A, 60-44°C, 1 h /°C; lanes 1_1 - 4_1, 1h /°C; 1_1, 44-41°C; 2_1, 46-43°C; 3_1, 48-45°C; 4_1, 50-47°C; lanes 1_2 - 4_2, 1h /°C; 1_2, 44-41°C; 2_2, 46-43°C; 3_2, 48-45°C; 4_2, 50-47°C; lanes 1_3 - 4_3, 1h /°C; 1_3, 44-41°C; 2_3, 46-43°C; 3_3, 48-45°C; 4_3, 50-47°C. P: Pocket.

7.5.7. ADVANCED FOLDING SCREEN 3

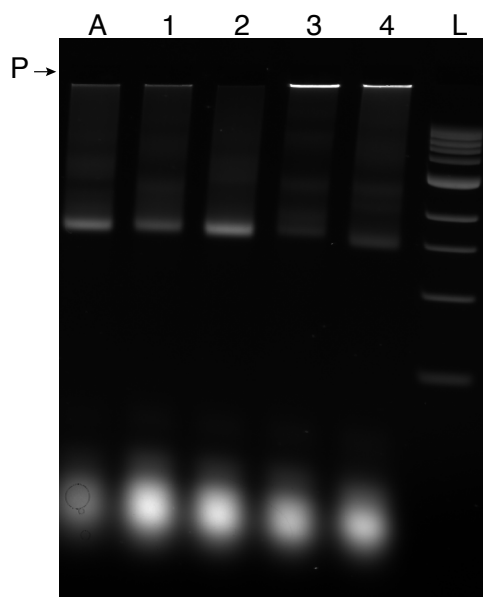


Figure S7.14: Folding screen of the DNA origami nanopore. Laser-scanned image of a 2% agarose gel with 5.5 mM MgCl₂ run on a water bath on which the following samples were electrophoresed at 70 V for 90 min: all lanes except L: 20 mM MgCl₂; A, 60–44°C, 1 h/°C; 1, 5h at 50°C; 2, 10h at 50°C; 3, 5h at 52°C; 4, 10h at 52°C; L, 1kb ladder. P: Pocket.

7

7.5.8. ADVANCED FOLDING SCREEN 4

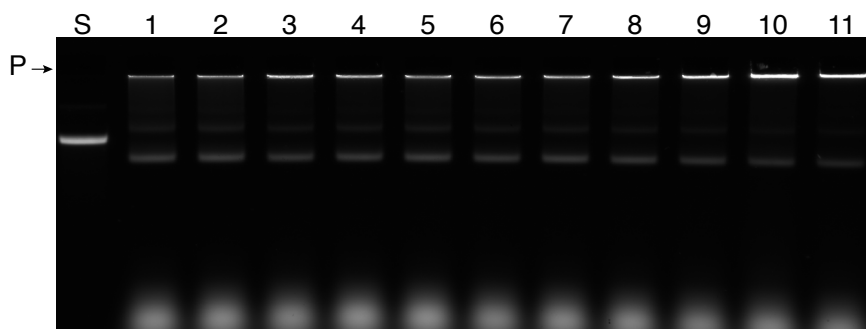


Figure S7.15: Magnesium folding screen of the DNA origami nanopore. Laser-scanned image of a 2% agarose gel with 5.5 mM MgCl₂ run on a water bath on which the following samples were electrophoresed at 70 V for 60 min: S, 7560 bases long scaffold; lanes 1–11, 60–44°C, 1 h/°C; 1, 20 mM MgCl₂; 2, 21 mM MgCl₂; 3, 22 mM MgCl₂; 4, 23 mM MgCl₂; 5, 24 mM MgCl₂; 6, 25 mM MgCl₂; 7, 26 mM MgCl₂; 8, 27 mM MgCl₂; 9, 28 mM MgCl₂; 10, 29 mM MgCl₂; 11, 30 mM MgCl₂. P: Pocket.

7.5.9. ADVANCED FOLDING SCREEN 5

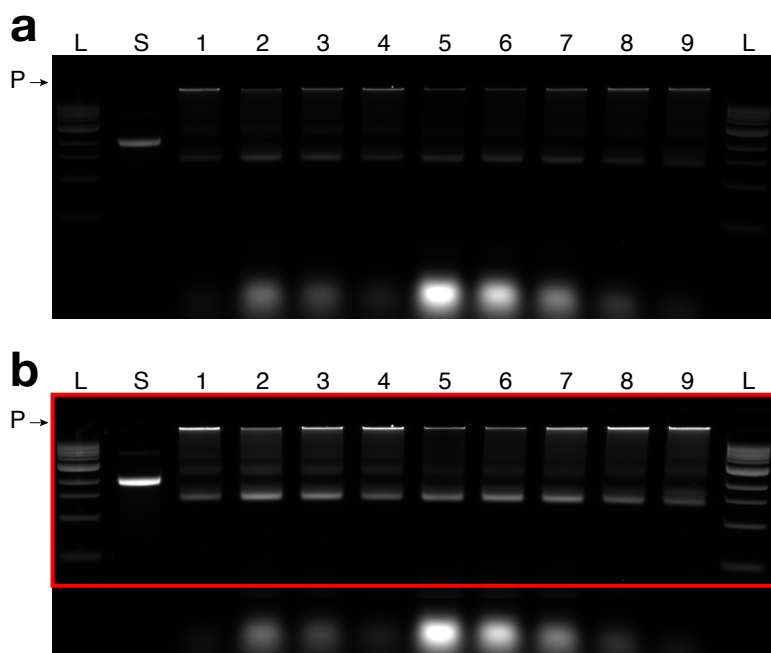


Figure S7.16: Scaffold to oligo ratio folding screen of the DNA origami nanopore. a and b show the same laser-scanned image of a 2% agarose gel with 5.5 mM MgCl_2 run on a water bath. b, The red box indicates that this region was auto-leveled. The following samples were electrophoresed at 70 V for 60 min: L, 1kb ladder; S, 7560 bases long scaffold; lanes 1-9, 24 mM MgCl_2 , 60-44°C, 1 h/°C; 1, 50 nM scaffold, 175 nM oligos; 2, 20 nM scaffold, 300 nM oligos; 3, 20 nM scaffold, 200 nM oligos; 4, 20 nM scaffold, 100 nM oligos; 5, 10 nM scaffold, 400 nM oligos; 6, 10 nM scaffold, 300 nM oligos; 7, 10 nM scaffold, 200 nM oligos; 8, 10 nM scaffold, 100 nM oligos; 9, 10 nM scaffold, 50 nM oligos. P: Pocket.

7.5.10. ADVANCED FOLDING SCREEN 6

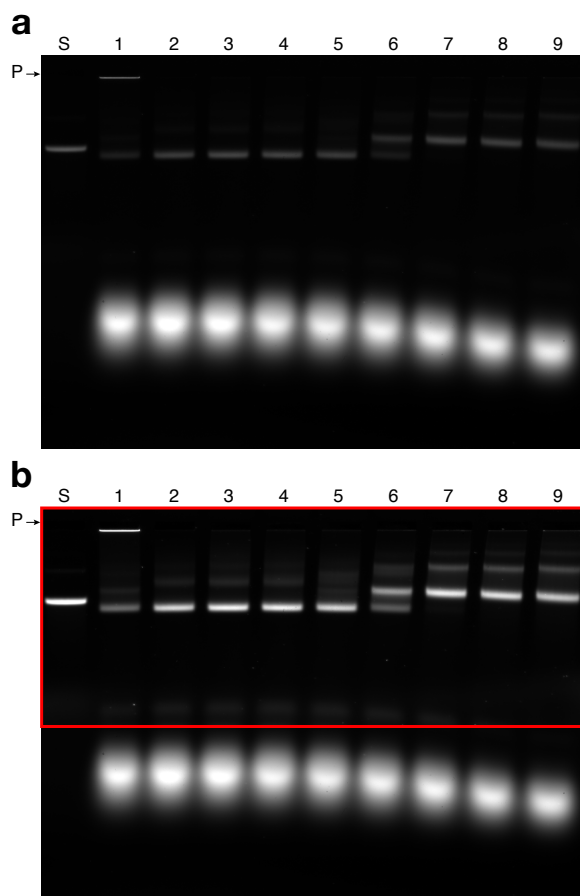


Figure S7.17: Scaffold to oligo ratio folding screen of the DNA origami nanopore. a and b show the same laser-scanned image of a 2% agarose gel with 5.5 mM MgCl_2 run on a water bath. b, The red box indicates that this region was auto-leveled. The following samples were electrophoresed at 70 V for 90 min: S, 7560 bases long scaffold; lanes 1-9, 24 mM MgCl_2 , 10 nM scaffold, 300 nM oligos, 15min at 56°C followed by different temperatures; 1, 24h at 54°C, 24h at 53°C; 2, 15h at 49°C; 3, 15h at 50°C; 4, 15h at 51°C; 5, 15h at 52°C; 6, 15h at 53°C; 7, 15h at 54°C; 8, 15h at 55°C; 9, 15h at 56°C. P: Pocket.

7.5.11. ADVANCED FOLDING SCREEN 7

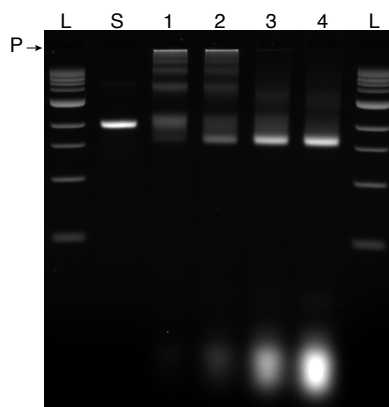


Figure S7.18: Scaffold to oligo ratio folding screen of the DNA origami nanopore. Laser-scanned image of a 2% agarose gel with 5.5 mM MgCl_2 run on a water bath on which the following samples were electrophoresed at 70 V for 90 min: L, 1kb ladder; S, 7560 bases long scaffold; lanes 1-4, 15min at 65°C, 24h at 50 °C, 10 nM scaffold, 24 mM MgCl_2 ; 1, 50 nM oligos; 2, 100 nM oligos; 200 nM oligos, 300 nM oligos. P: Pocket.

7.5.12. ADVANCED FOLDING SCREEN 8

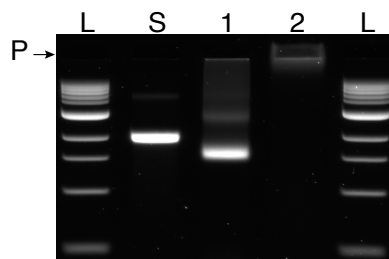


Figure S7.19: Scaffold to oligo ratio folding screen of the DNA origami nanopore. Laser-scanned image of a 2% agarose gel with 5.5 mM MgCl_2 run on an ice water bath on which the following samples were electrophoresed at 70 V for 90 min: L, 1kb ladder; S, 7560 bases long scaffold; 1, filter purified, uncoated DNA origami nanopore; 2, filter purified, K_{10} -PEG_{5k} coated DNA origami nanopore. P: Pocket.

7.5.13. SINGLE PARTICLE MONTAGE FOR CLASS AVERAGING OF THE UNCOATED ORIGAMI PORE

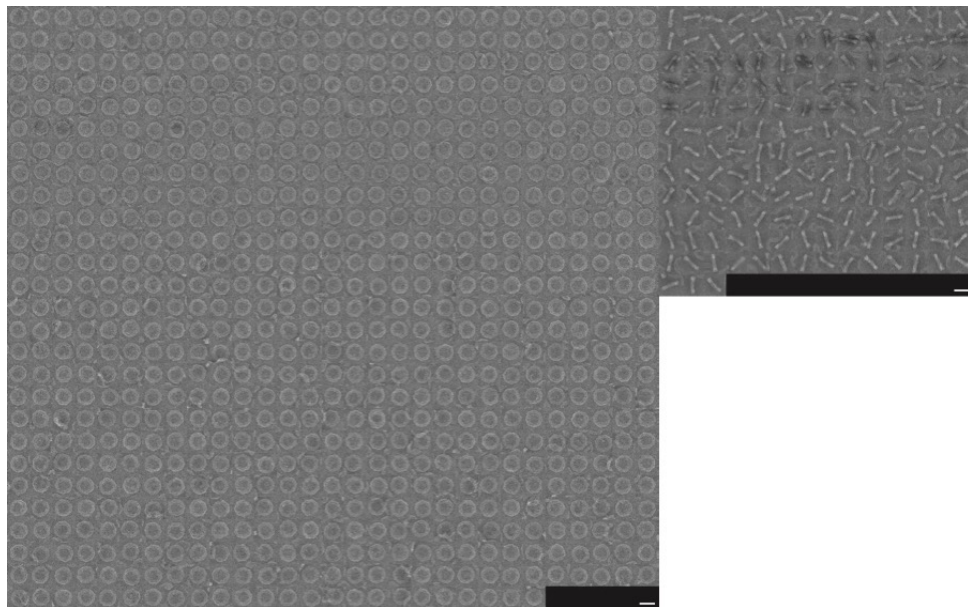


Figure S7.20: Library of negative-stain TEM particles for class averaging of the uncoated DNA origami nanopore in the front (left) and side (right) view. Scale bar: 50 nm.

7.5.14. SINGLE PARTICLE MONTAGE FOR CLASS AVERAGING OF THE COATED ORIGAMI PORE

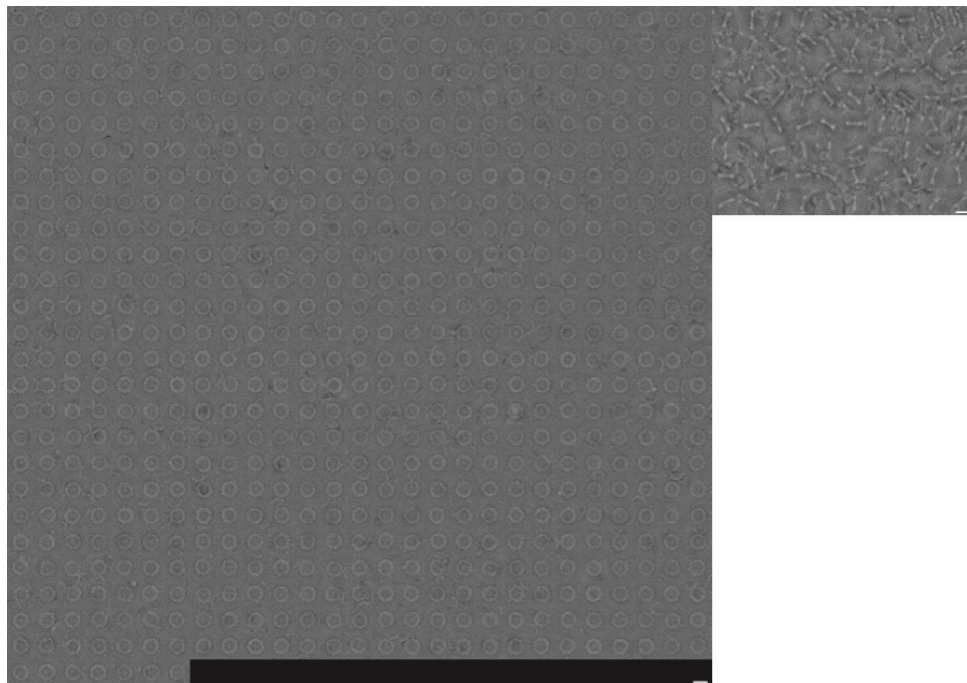
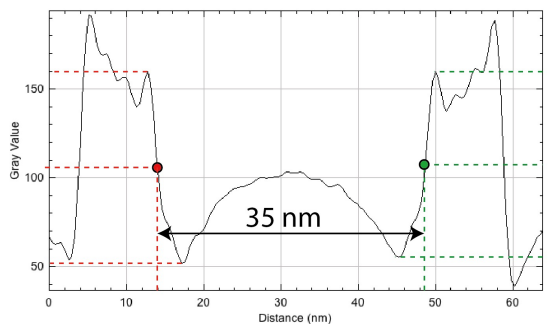
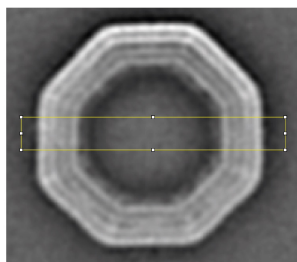


Figure S7.21: Library of negative-stain TEM particles for class averaging of the PEG-oligolysine-coated DNA origami nanopore in the front (left) and side (right) view. Scale bar: 50 nm.

7.5.15. INNER DIAMETER AND HEIGHT ESTIMATES FROM NEGATIVE-STAINING TEM AND CLASS AVERAGING OF THE PEG-OLIGOLYSINE-COATED DNA ORIGAMI NANOPORES

a



b

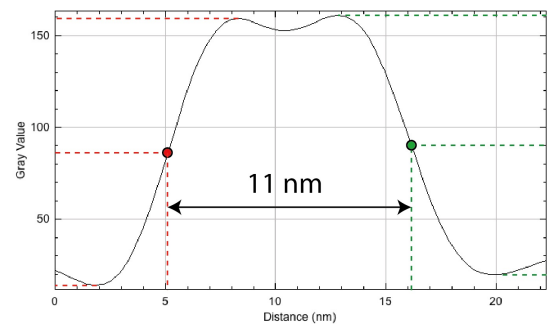
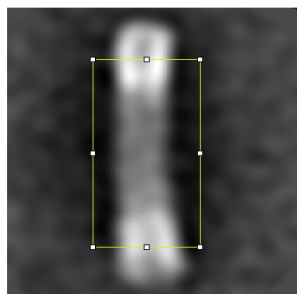


Figure S7.22: a, Front view class averaged image of the DNA origami nanopore (sample preparation as mentioned in methods section). The yellow box indicates the region of interest for the cross-section plot. A diameter of ~35 nm was estimated from the full-width-half maximum (FWHM) as indicated by the dashed lines. b, Side view class averaged image of the DNA origami nanopore (sample preparation as mentioned in methods section). The yellow box indicates the region of interest for the cross-section plot. A height of ~11 nm was estimated from the full-width-half maximum (FWHM) as indicated by the dashed lines.

7.5.16. COMPARISON OF COATED AND UNCOATED DNA ORIGAMI NANOPORES

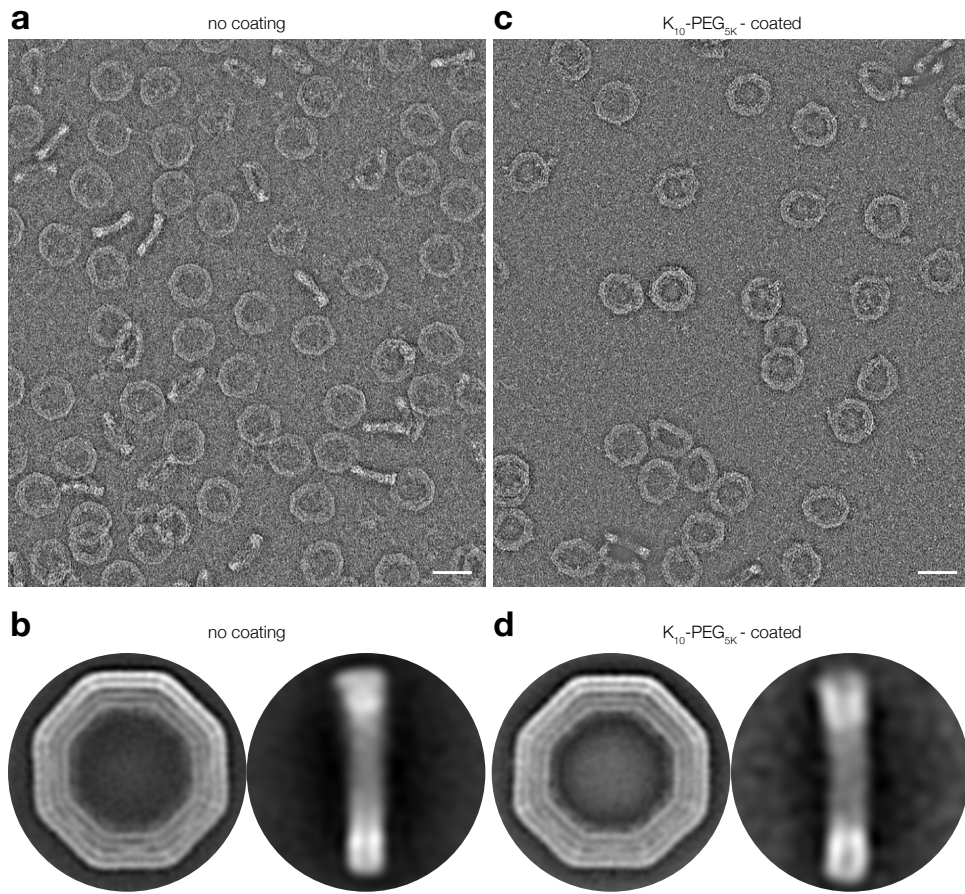


Figure S7.23: a, Typical field of view of a negative-stained DNA origami sample without coating and without cholesterol modifications. Scale bar: 50 nm. b, Front (left) and side (right) view class averaged image of uncoated DNA origami nanopores. Scale bar: 20 nm. c, Typical field of view of a negative-stained DNA origami sample with coating and cholesterol modifications. Scale bar: 50 nm. d, Front (left) and side (right) view class averaged image of coated DNA origami nanopores. Scale bar: 20 nm.

7.5.17. ILLUSTRATION OF SINGLE-STRANDED DNA HANDLES ON THE INSIDE WALL OF THE DNA ORIGAMI NANOPORE

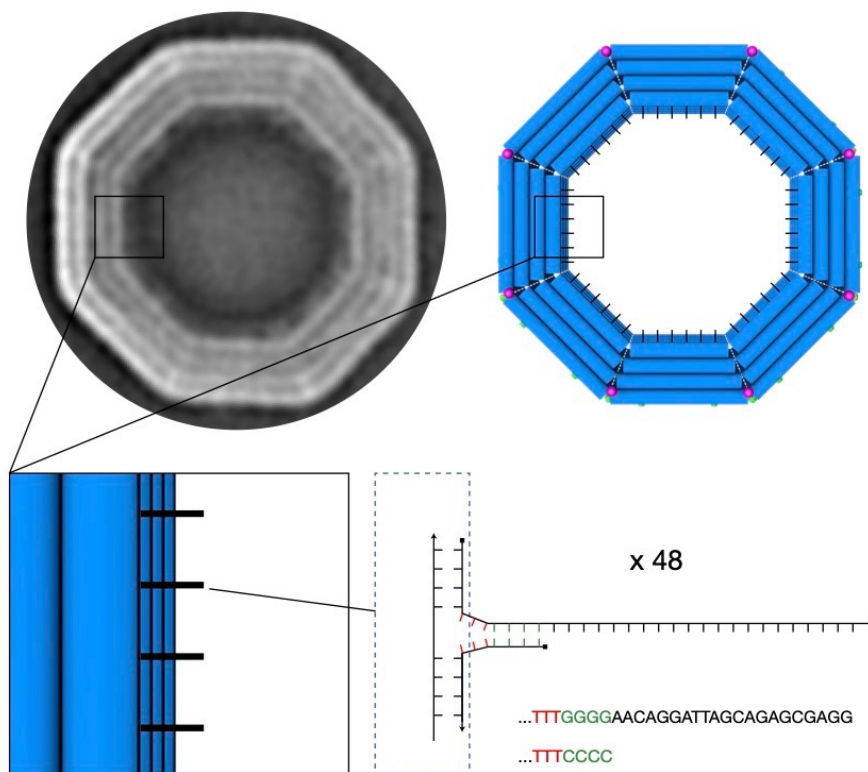


Figure S7.24: Top left: Front view class averaged image of coated DNA origami nanopores. The black box highlights density on the inner wall of the DNA origami nanopore. Top right: Front view model of the DNA origami nanopore. Black stripes on the inside wall resemble single-stranded DNA handles. Bottom left: Zoom in on the single-stranded handles. Bottom right: Illustration of the single-stranded handle sequence, which can be used in the future to attach macromolecules inside of the pore.

7.5.18. EFFECT OF THE AMOUNT OF CHOLESTEROLS THAT ARE ATTACHED TO THE DNA ORIGAMI NANOPORES

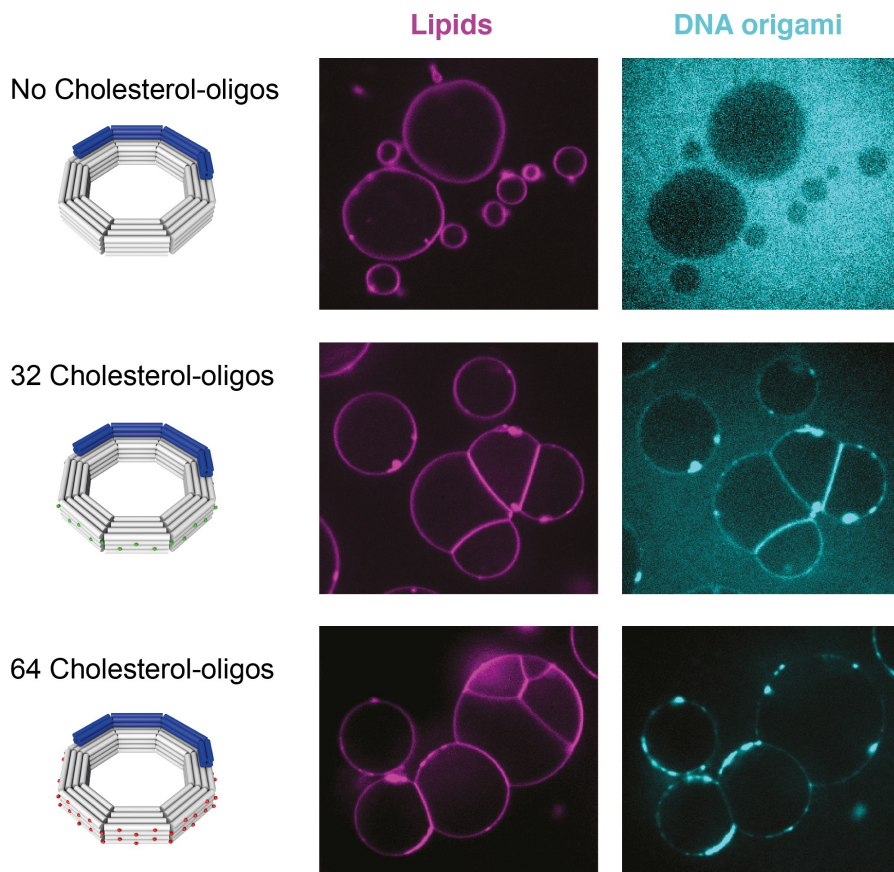


Figure S7.25: DNA origami pores were added from the outside to preformed GUVs. Top: DNA origami without any cholesterol anchor did not show detectable membrane localization. Center: 32-cholesterol DNA-origami pores showed increased localization at the membrane, resulting in a relatively homogeneous signal. The presence of bulk fluorescence in the origami channel indicates that some origami pores remained in solution and did not precipitate. Bottom: 64-cholesterol DNA-origami pores showed strong interaction with the lipid membrane, resulting in the formation of large aggregates.

7.5.19. TEST INFLUX OF GFP THROUGH DNA ORIGAMI PORES ADDED FROM THE OUTSIDE TO PREFORMED GUVS

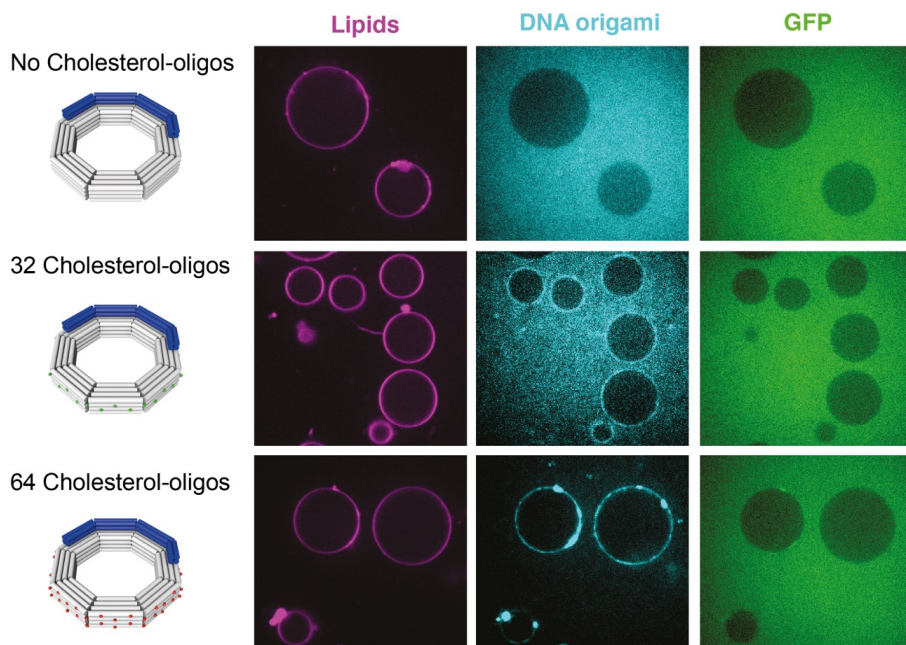


Figure S7.26: For both cholesterol-less origami pores (top), 32-cholesterols (center), and 64-cholesterols (bottom), administration of GFP from the bulk solution at the outside did not result in influx, indicating that addition of DNA origami pores to preformed vesicles does not result in formation of functional pores that embed within the membrane to create open pores that allow transmembrane diffusion of GFP.

7.5.20. RECONSTITUTION OF DNA ORIGAMI PORES INTO THE LIPID MONOLAYER OF WATER-IN-OIL DROPLETS

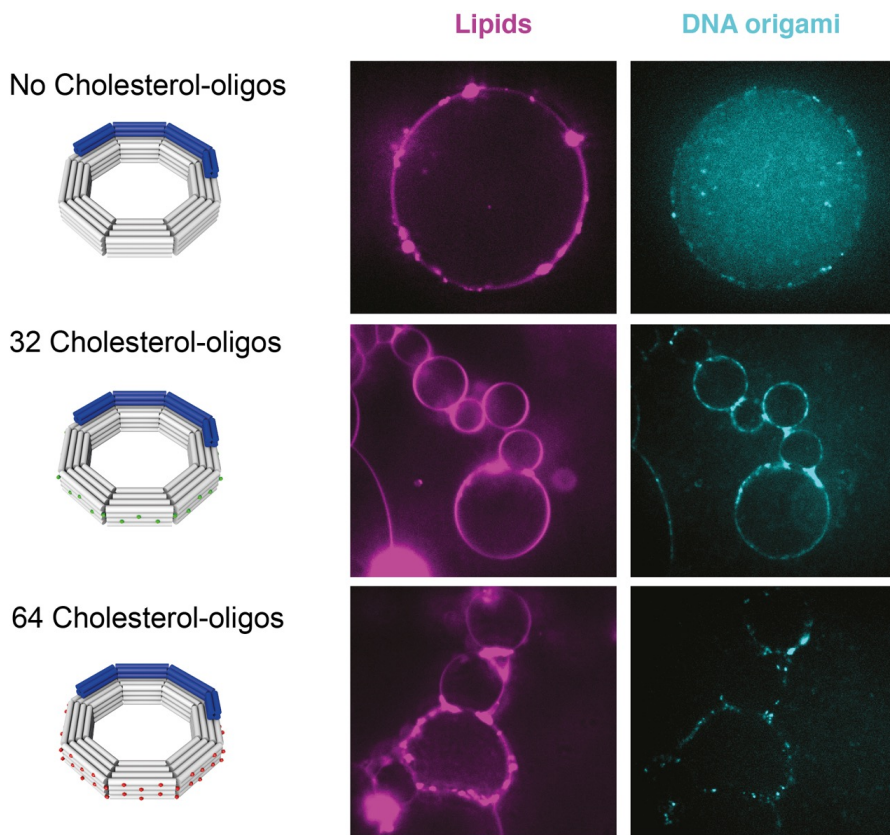


Figure S7.27: Top: cholesterol-less origami pores did, as expected, not result in localization to the monolayer lipid membrane in water in oil droplets, as indicated by the homogeneous fluorescence origami signal in the bulk of the vesicle and the absence of an increased intensity at the lipid membrane. Center: 32-cholesterol origami pores, by contrast, showed clear localization at the droplet membrane. Bottom: 64-cholesterol origami pores resulted in aggregates localized at the membrane, which we attribute to the higher hydrophobicity caused by the relatively large number of cholesterol groups.

7.5.21. CDICE WITH CHOLESTEROL-LESS DNA ORIGAMI PORES

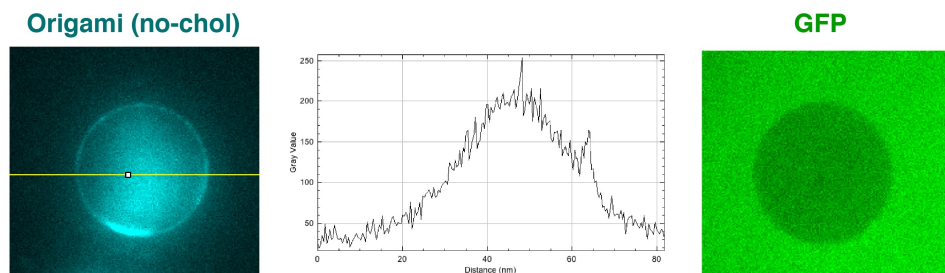


Figure S7.28: Example of a GUV with cholesterol-less origami pores that manifested poor membrane localization, while a large amount of origami signal was present in the bulk of the vesicle.

7.5.22. AMINO ACID SEQUENCE OF THE His₁₄-TEV-IBB-mEGFP-CYS PROTEIN

(MSKHHHHS~~GH~~HHTGHHHHSGSHHHTGENLYFQ)cleavedHis14-tag

GSDNGTDSSTSKFVPEYRRTNFKNKGRFSADELRRRRDQTQQVELRKAKRDEALAKRR
 NFIPPTDGTSGEELFTGVVPILVELDGDVNGHKFSVSGEGGDATYGKLT~~LK~~FICTTGKLP
 VPWPTLVTTLT~~Y~~GVQCFSRYPDHMKQHDFFKSAMPEGYVQERTIFFKDDGNYKTRAEVK
 FEGDTLVNRIELKGIDFKEDGNILGHKLEYN~~Y~~NSHN~~V~~YIMADKQKNGIKVNF~~K~~IRHNIED
 GSVQLADHYQQNTPIGDGPVLLPDNHYLSTQSALSKDPNEKRDHMLKEFVTAAGITLG
 MDELYKTGC

7.5.23. SDS-PAGE OF THE IBB-mEGFP-CYS PROTEIN

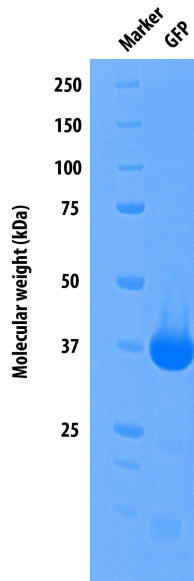


Figure S7.29: SDS-PAGE shows the band for the 34.6 kDa IBB-mEGFP-Cys protein (right, thick band running at ~37 kDa).

7.5.24. DNA ORIGAMI PORE SIGNAL ESTIMATION

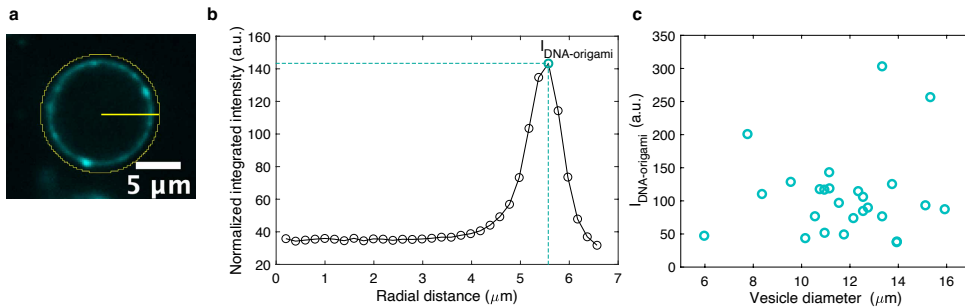
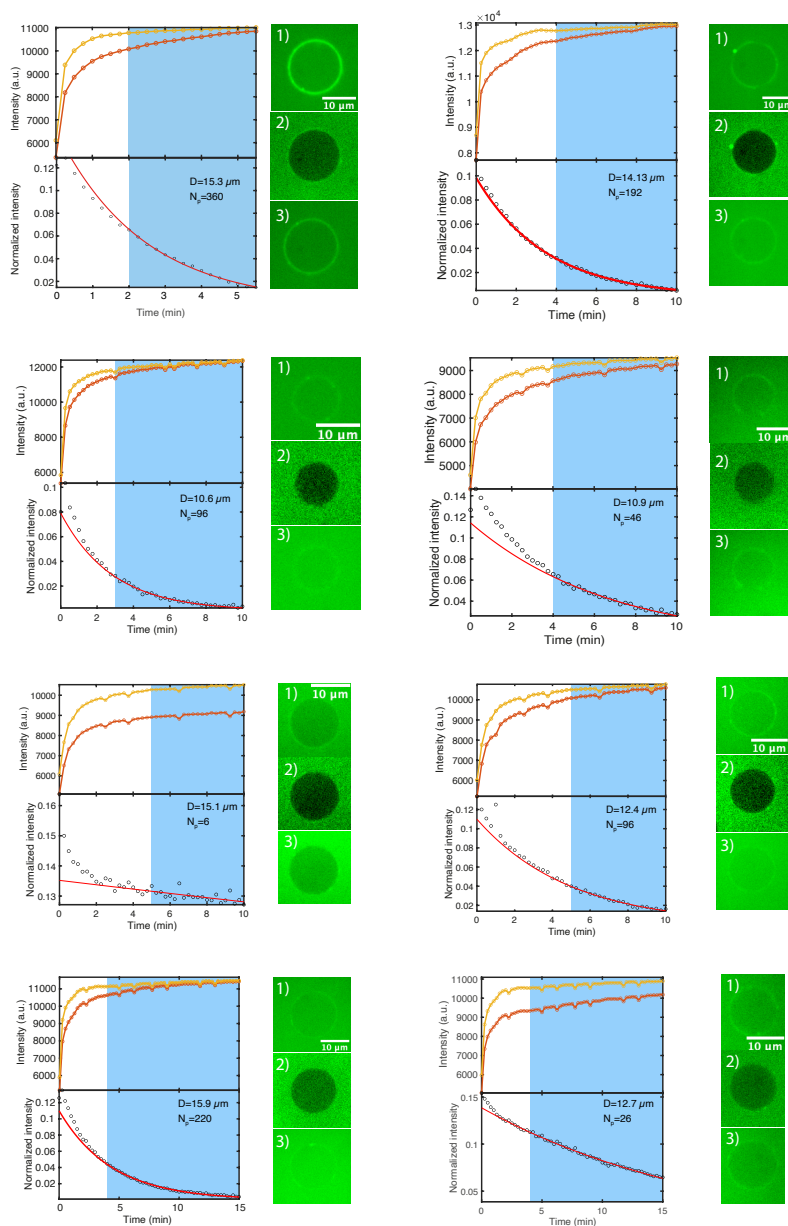
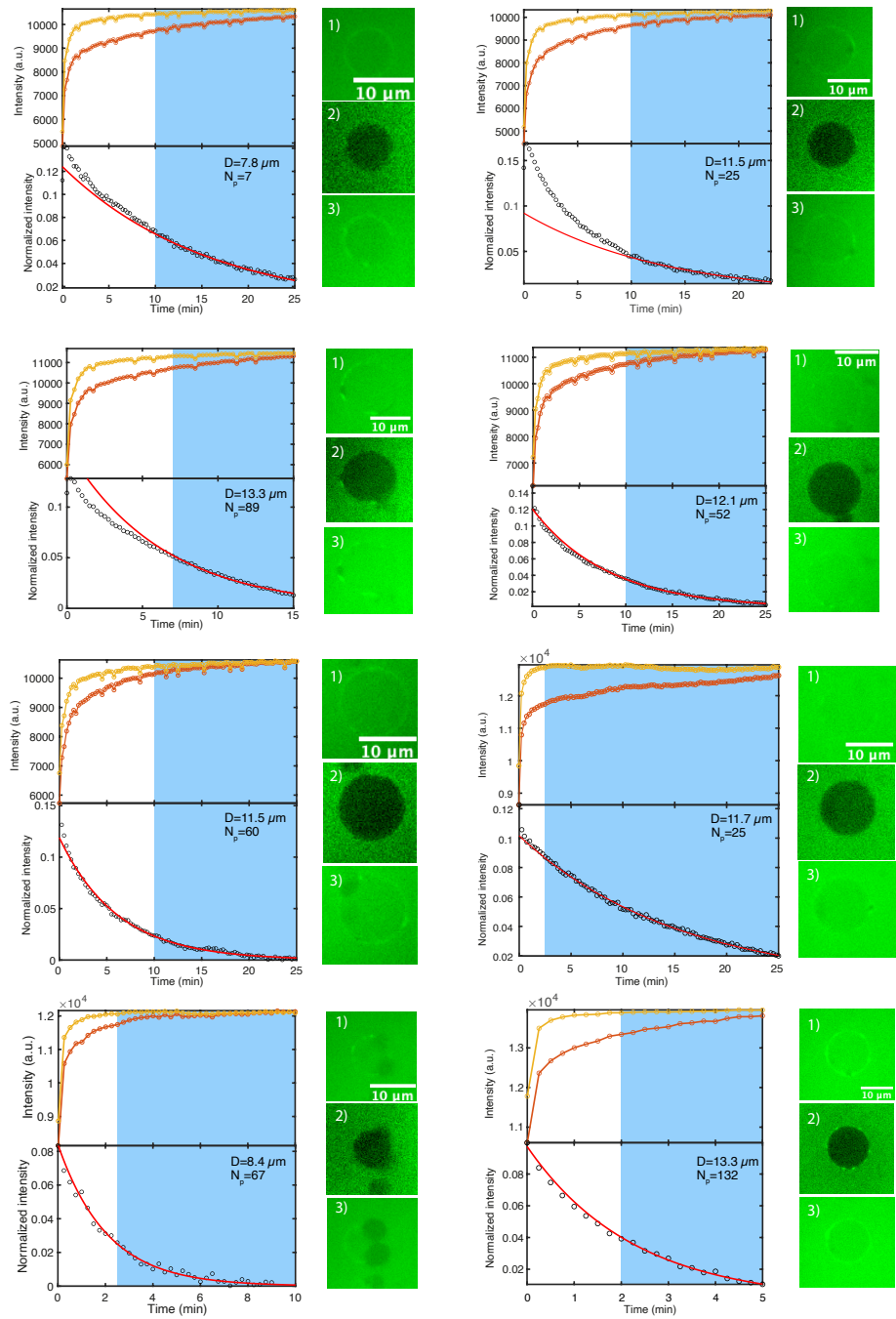
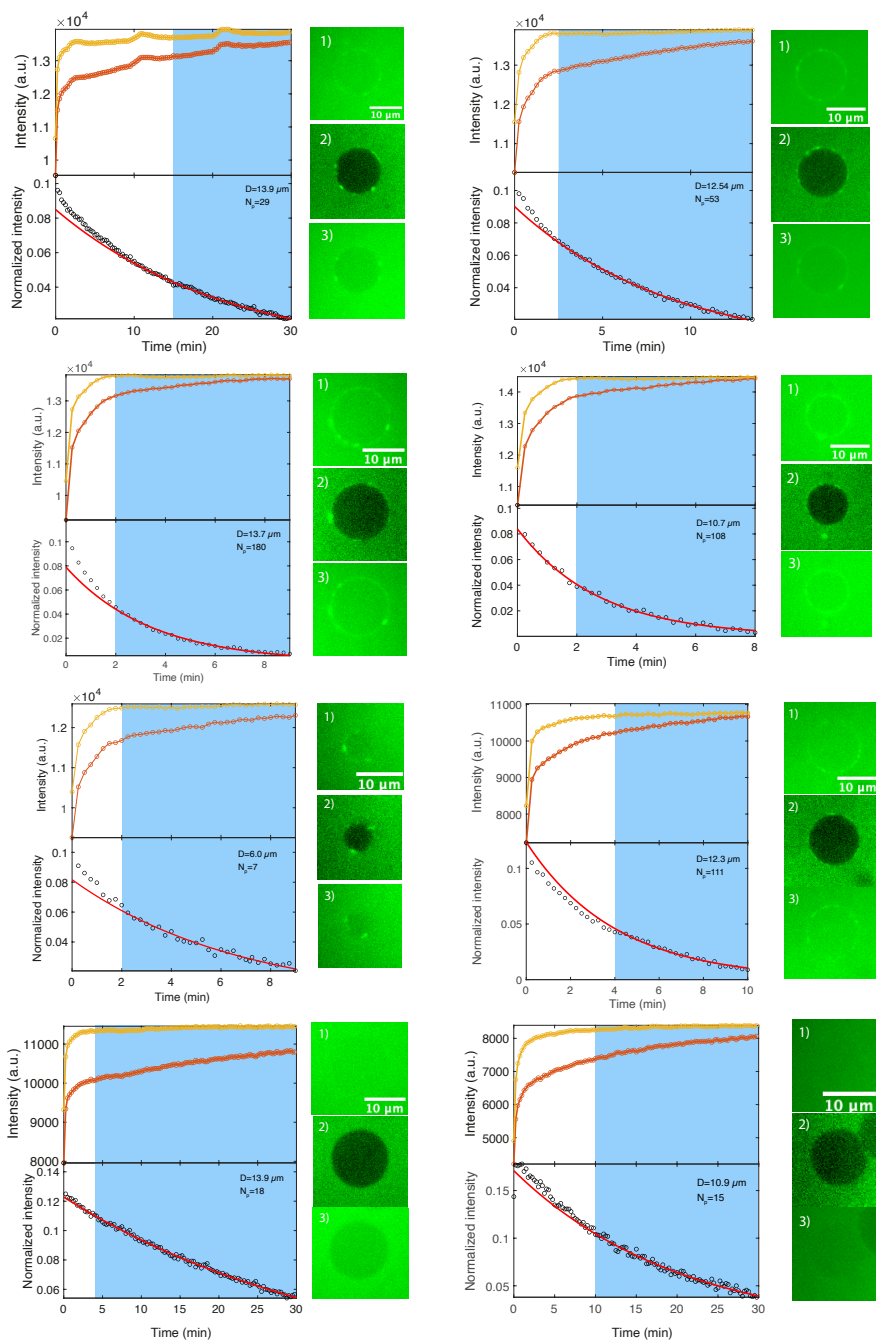


Figure S7.30: a, Fluorescence image showing DNA origami (cyan) at the vesicle membrane. Yellow circle and straight line indicate the area and corresponding radius where the radial profile was computed. b, Normalized integrated intensity measured over the radial distance for the vesicle shown in (a), calculated as the integrated intensity over concentric circles starting from the center of the vesicle divided by the number of pixels in the circle. The peak intensity, marked as $I_{\text{DNA-origami}}$, was taken as the measure of interest for quantifying the DNA origami signal intensity at the membrane. Intensity values were further normalized by the laser power used during acquisition. c, $I_{\text{DNA-origami}}$ calculated as described in (b) as a function of vesicle diameter, measured for all vesicles where FRAP was performed. Notably, $I_{\text{DNA-origami}}$ does not show any apparent correlation with the vesicle diameter.

7.5.25. RAW DATA AND FITS USED IN THE ESTIMATION OF N_p FOR EACH VESICLE IN FIG.7.7E







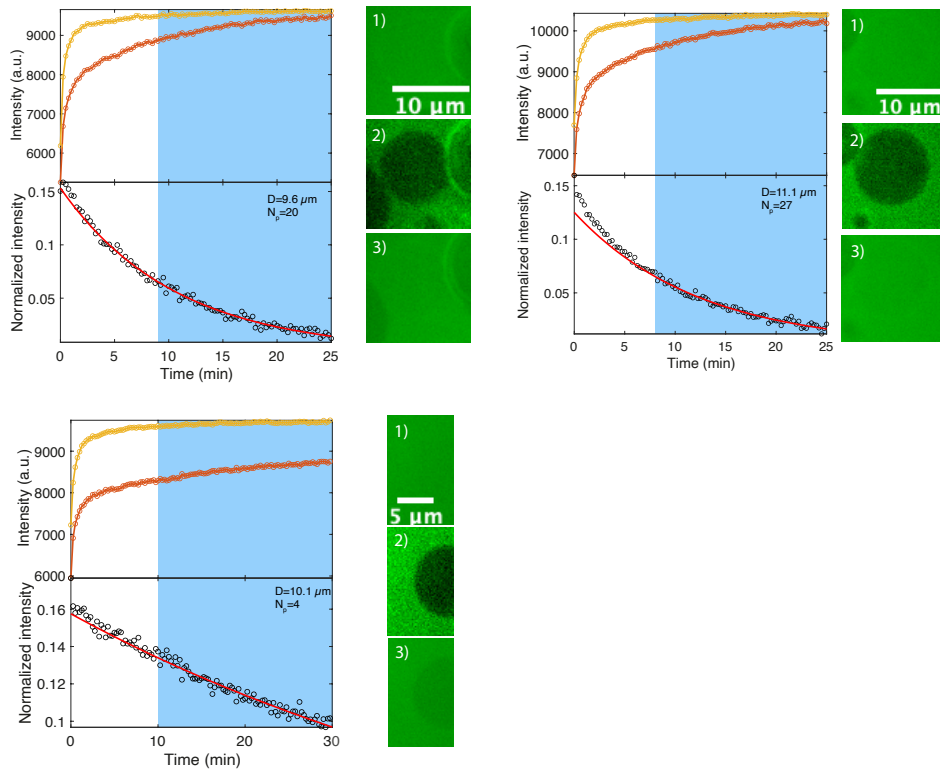


Figure S7.31: For each vesicle, 5 panels are shown: Top left: Yellow and red curves indicate the outer (I_{out}) and inner (I_{in}) vesicle intensities, respectively. Light blue area denotes the fitted region. Bottom left: Black circles indicate the normalized intensity difference $(I_{out} - I_{in}) / (I_{out})$. Red line shows a fit to the data points using Eq. 7.4. Vesicle diameter (D) and extracted number of pores (N_p) are reported. Right: Fluorescence images showing the vesicle before photobleaching (1, top), right after photobleaching (2, center), and at the end of recovery (3, bottom).

7.5.26. SLICES THROUGH TOMOGRAMS OF LIPOSOMES WITH INCORPORATED OCTAGONS

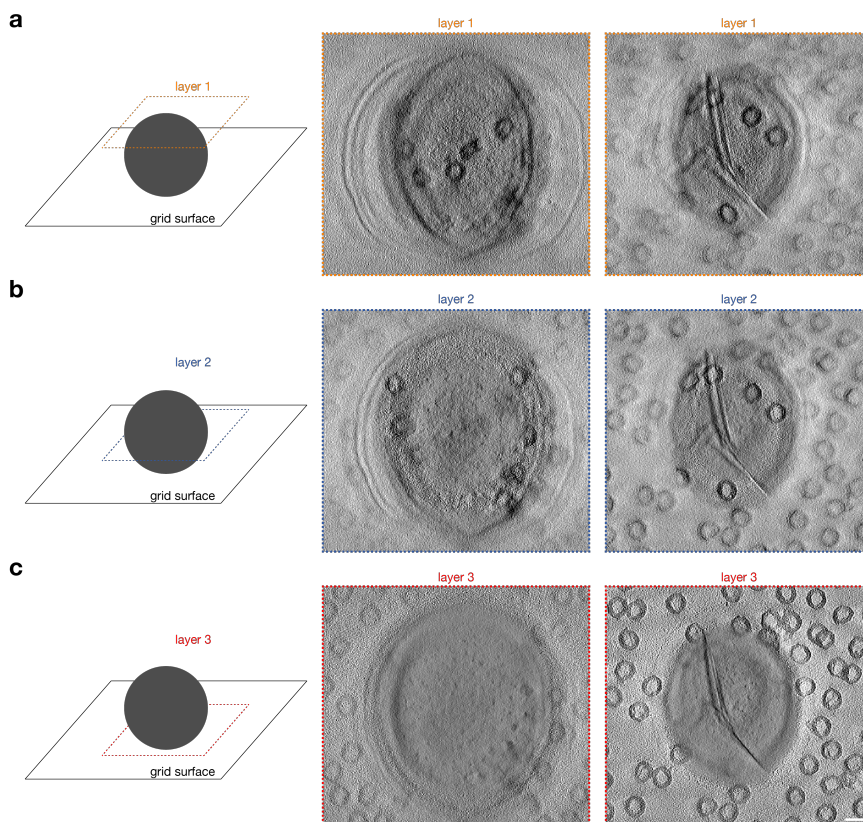


Figure S7.32: Left: Slices through a model, representing liposomes on a grid surface. The grey spheres represent liposomes, black lines represent the borders of a grid surface, colored (a, top slice; b, middle slice; c, bottom slice) dotted lines represent different slices through the liposomes at different heights. Middle and right: negative-stained TEM tomogram slices (a, top slice; b, middle slice; c, bottom slice) of vesicles with incorporated octagons.

REFERENCES

- [1] A. Fragasso, N. De Franceschi, P. Stömmmer, E. O. Van Der Sluis, H. Dietz, and C. Dekker, *Reconstitution of Ultrawide DNA Origami Pores in Liposomes for Transmembrane Transport of Macromolecules*, ACS Nano **15**, 12768 (2021).
- [2] P. W. Rothemund, *Folding DNA to create nanoscale shapes and patterns*, Nature **440**, 297 (2006), arXiv:0202466 [cond-mat] .
- [3] S. M. Douglas, H. Dietz, T. Liedl, B. Högberg, F. Graf, and W. M. Shih, *Self-assembly of DNA into nanoscale three-dimensional shapes*, Nature **459**, 414 (2009).
- [4] S. Hernández-Ainsa and U. F. Keyser, *DNA origami nanopores: Developments, challenges and perspectives*, Nanoscale **6**, 14121 (2014).
- [5] T. Sugawara, D. Yamashita, K. Kato, Z. Peng, J. Ueda, J. Kaneko, Y. Kamio, Y. Tanaka, and M. Yao, *Structural basis for pore-forming mechanism of staphylococcal α -hemolysin*, Toxicon **108**, 226 (2015).
- [6] T. G. Martin, F. C. Simmel, V. Arnaut, M. Mayer, H. Dietz, M. Langecker, S. Renner, and J. List, *Synthetic Lipid Membrane Channels Formed by Designed DNA Nanostructures*, Science **338**, 932 (2012).
- [7] B. Gyenes, K. Göpfrich, M. Winterhalter, C.-Y. Li, A. Ohmann, J. Yoo, A. Aksimentiev, M. Ricci, S. P. Bhamidimarri, and U. F. Keyser, *Large-Conductance Transmembrane Porin Made from DNA Origami*, ACS Nano **10**, 8207 (2016).
- [8] S. Krishnan, D. Ziegler, V. Arnaut, T. G. Martin, K. Kapsner, K. Henneberg, A. R. Bausch, H. Dietz, and F. C. Simmel, *Molecular transport through large-diameter DNA nanopores*, Nature Communications **7**, 1 (2016).
- [9] R. P. Thomsen, M. G. Malle, A. H. Okholm, S. Krishnan, S. S. Bohr, R. S. Sørensen, O. Ries, S. Vogel, F. C. Simmel, N. S. Hatzakis, and J. Kjems, *A large size-selective DNA nanopore with sensing applications*, Nature Communications , 1.
- [10] J. R. Burns, A. Seifert, N. Fertig, and S. Howorka, *A biomimetic DNA-based channel for the ligand-controlled transport of charged molecular cargo across a biological membrane*, Nature Nanotechnology **11**, 152 (2016).
- [11] S. Iwabuchi, I. Kawamata, S. Murata, and S.-i. M. Nomura, *Large, square-shaped, DNA origami nanopore with sealing function on giant vesicle membrane*, Chemical Communications (2021), 10.1039/d0cc07412h.
- [12] H. Ramezani and H. Dietz, *Building machines with DNA molecules*, Nature Reviews Genetics **21**, 5 (2020).
- [13] K. F. Wagenbauer, C. Sigl, and H. Dietz, *Gigadalton-scale shape-programmable DNA assemblies*, Nature **552**, 78 (2017).

- [14] A. Ohmann, C. Y. Li, C. Maffeo, K. Al Nahas, K. N. Baumann, K. Göpfrich, J. Yoo, U. F. Keyser, and A. Aksimentiev, *A synthetic enzyme built from DNA flips 107 lipids per second in biological membranes*, Nature Communications **9** (2018), 10.1038/s41467-018-04821-5.
- [15] P. Ketterer, A. N. Ananth, D. S. Laman Trip, A. Mishra, E. Bertosin, M. Ganji, J. Van Der Torre, P. Onck, H. Dietz, and C. Dekker, *DNA origami scaffold for studying intrinsically disordered proteins of the nuclear pore complex*, Nature Communications **9**, 1 (2018).
- [16] P. D. E. Fisher, Q. Shen, B. Akpinar, L. K. Davis, K. K. H. Chung, D. Baddeley, A. Šarić, T. J. Melia, B. W. Hoogenboom, C. Lin, and C. P. Lusk, *A Programmable DNA Origami Platform for Organizing Intrinsically Disordered Nucleoporins within Nanopore Confinement*, ACS Nano **12**, 1508 (2018).
- [17] D. Exerowa, D. Kashchiev, and D. Platikanov, *Stability and permeability of amphiphile bilayers*, Advances in Colloid and Interface Science **40**, 201 (1992).
- [18] S. A. Akimov, P. E. Volynsky, T. R. Galimzyanov, P. I. Kuzmin, K. V. Pavlov, and O. V. Batishchev, *Pore formation in lipid membrane I: Continuous reversible trajectory from intact bilayer through hydrophobic defect to transversal pore*, Scientific Reports **7**, 1 (2017).
- [19] M. Abkarian, E. Loiseau, and G. Massiera, *Continuous droplet interface crossing encapsulation (cDICE) for high throughput monodisperse vesicle design*, Soft Matter **7**, 4610 (2011).
- [20] K. F. Wagenbauer, F. A. Engelhardt, E. Stahl, V. K. Hecht, P. Stömmmer, F. Seebacher, L. Meregalli, P. Ketterer, T. Gerling, and H. Dietz, *How We Make DNA Origami*, ChemBioChem **18**, 1873 (2017).
- [21] D. Marquardt, F. A. Heberle, D. V. Greathouse, R. E. Koeppe, R. F. Standaert, B. J. Van Oosten, T. A. Harroun, J. J. Kinnun, J. A. Williams, S. R. Wassall, and J. Katsaras, *Lipid bilayer thickness determines cholesterol location in model membranes*, Soft Matter **12**, 9417 (2016).
- [22] H. Dietz, S. M. Douglas, and W. M. Shih, *Folding DNA into twisted and curved nanoscale shapes*, Science **325**, 725 (2009), arXiv:9910002 [quant-ph] .
- [23] N. Ponnuswamy, M. M. Bastings, B. Nathwani, J. H. Ryu, L. Y. Chou, M. Vinther, W. A. Li, F. M. Anastassacos, D. J. Mooney, and W. M. Shih, *Oligolysine-based coating protects DNA nanostructures from low-salt denaturation and nuclease degradation*, Nature Communications **8**, 1 (2017).
- [24] L. Van de Cauter, F. Fanalista, L. van Buren, N. De Franceschi, E. Godino, S. Bouw, C. Danelon, C. Dekker, G. Koenderink, and K. Ganzinger, *Optimized cDICE for efficient reconstitution of biological systems in giant unilamellar vesicles*, bioRxiv preprint (2021).

- [25] D. Görlich, P. Henklein, R. A. Laskey, and E. Hartmann, *A 41 amino acid motif in importin- α confers binding to importin- β and hence transit into the nucleus*, EMBO Journal **15**, 1810 (1996).
- [26] E. Baykal-Caglar, E. Hassan-Zadeh, B. Saremi, and J. Huang, *Preparation of giant unilamellar vesicles from damp lipid film for better lipid compositional uniformity*, Biochimica et Biophysica Acta - Biomembranes **1818**, 2598 (2012).
- [27] A. Fick, *Über Diffusion [Translated: (1995) "On liquid diffusion". Journal of Membrane Science]*, Poggendorff's Annalen der Physik und Chemie **94**, 59 (1855).
- [28] P. Dechadilok and W. M. Deen, *Hindrance factors for diffusion and convection in pores*, Industrial and Engineering Chemistry Research **45**, 6953 (2006).
- [29] R. Hanselmann, W. Burchard, R. Lemmes, and D. Schwengers, *Characterization of DEAE-dextran by means of light scattering and combined size-exclusion chromatography/low-angle laser light scattering/viscometry*, Macromolecular Chemistry and Physics **196**, 2259 (1995).
- [30] S. R. Wente and M. P. Rout, *The nuclear pore complex and nuclear transport*. Cold Spring Harbor perspectives in biology **2**, 1 (2010).
- [31] A. Birnie and C. Dekker, *Genome-in-a-Box: Building a Chromosome from the Bottom up*, ACS Nano (2021), 10.1021/acsnano.0c07397.
- [32] S. M. Douglas, A. H. Marblestone, S. Teerapittayanon, A. Vazquez, G. M. Church, and W. M. Shih, *Rapid prototyping of 3D DNA-origami shapes with caDNAno*, Nucleic Acids Research **37**, 5001 (2009).
- [33] B. Kick, F. Praetorius, H. Dietz, and D. Weuster-Botz, *Efficient Production of Single-Stranded Phage DNA as Scaffolds for DNA Origami*, Nano Letters **15**, 4672 (2015).
- [34] T. Wagner, F. Merino, M. Stabrin, T. Moriya, C. Antoni, A. Apelbaum, P. Hagel, O. Sitsel, T. Raisch, D. Prumbaum, D. Quentin, D. Roderer, S. Tacke, B. Siebolds, E. Schubert, T. R. Shaikh, P. Lill, C. Gatsogiannis, and S. Raunser, *SPHIRE-crYOLO is a fast and accurate fully automated particle picker for cryo-EM*, Communications Biology **2**, 1 (2019).
- [35] J. Zivanov, T. Nakane, B. Forsberg, D. Kimanius, W. J. Hagen, E. Lindahl, and S. H. Scheres, *New tools for automated high-resolution cryo-EM structure determination in RELION-3*, bioRxiv, 1 (2018).
- [36] J. R. Kremer, D. N. Mastronarde, and J. R. McIntosh, *Computer visualization of three-dimensional image data using IMOD*, Journal of Structural Biology **116**, 71 (1996).
- [37] N. B. Eisele, S. Frey, J. Piehler, D. Görlich, and R. P. Richter, *Ultrathin nucleoporin phenylalanine-glycine repeat films and their interaction with nuclear transport receptors*, EMBO Reports **11**, 366 (2010).

- [38] E. O. Potma, W. P. De Boeij, L. Bosgraaf, J. Roelofs, P. J. Van Haastert, and D. A. Wiersma, *Reduced protein diffusion rate by cytoskeleton in vegetative and polarized Dictyostelium cells*, Biophysical Journal **81**, 2010 (2001).

8

FUTURE DIRECTIONS

In this thesis, I presented new approaches to study nuclear transport, from creating synthetic FG-Nups bottom up using a rationally designed sequence that mimic NPC selectivity (Chapter 5), to studying the interaction between a reconstituted FG-mesh and Kap transporters at varying Kap concentrations (Chapter 6), to embedding large DNA-origami pores into the membrane of giant liposomes as a potential new platform to mimic nuclear transport (Chapters 7). In this final chapter, I explore new possibilities for follow-up studies that aim to resolve some remaining open issues in the field of nuclear transport, as well as present a brief overview of current outstanding questions in the field.

There are multiple ways that one can follow to achieve a mechanistic description of nuclear transport. While taking a bottom-up approach may seem far from providing a complete representation of the complex *in vivo* system, it allows us to study, dissect, inspect, and play around with all various components that take part in the intriguing transport process. Upon measuring and understanding how a few selected components interact together, one can scale up the complexity and the number of components to reach a scenario that is progressively closer to the native biological system.

In this thesis, I made steps towards a bottom-up reconstitution of the nuclear pore complex, starting from single molecules to building up fully functional synthetic proteins that can mimic the NPC selectivity. Furthermore, the last two chapters introduced novel ways to study and mimic transport through the Nuclear Pore Complex (NPC). I will now discuss some possible future directions that I consider feasible to achieve in the short term, while bearing great potential for new insights and discoveries.

8.1. DESIGNER FG-NUPS – A PLAYGROUND FOR STUDYING NPC SELECTIVITY

In Chapter 5, we showed how it is possible to create an artificial protein ‘NupX’ that mimics the selectivity of native FG-Nups by following a few simple design rules [1]. In essence, we modelled FG-Nups following the stickers-and-spacers model that describes the formation of multivalent protein condensates [2], where intrinsically disordered proteins (IDPs) feature short attractive motifs (stickers), interspaced by flexible linkers (spacers) (Fig.8.1).

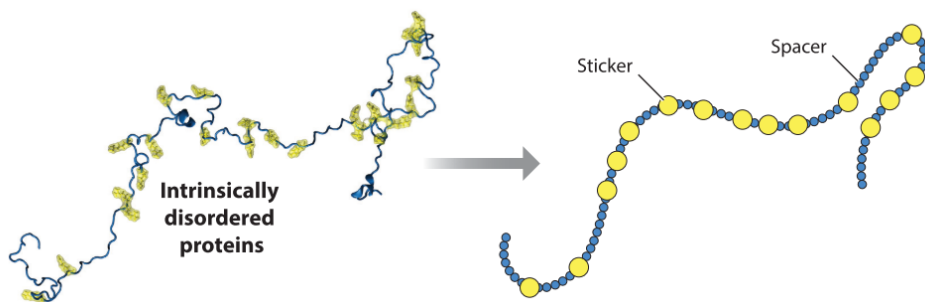


Figure 8.1: Stickers-and-spacers model of condensate-forming intrinsically disordered proteins. Adapted from [2].

While the notion of phase separation has recently become relevant in biology to describe the behavior of associative polymers found in the cell [3], such as proteins and RNAs, it appears to also fit well in modelling the behavior of FG-Nups. Both native and artificial FG-Nups have been shown to phase separate when present in physiological buffer above a certain critical concentration. Remarkably, the resulting droplets featured NPC-like selectivity [4–6].

Given such promising indications that a relatively simple framework can describe the complex multivalent interactions of FG-Nups, while conferring them with NPC-like

selectivity, a few questions arise: (1) Can we pinpoint all the necessary and sufficient conditions that are needed for a protein to impart a NPC-like selective barrier? (2) Can we tune the ‘selective power’ of a designer FG-mesh by varying simple parameters, such as the composition or distribution of the spacers and stickers? (3) How robust is the set of properties incorporated into the NupX sequence?

To answer such questions, a possible approach could be to systematically vary some key parameters of a starting amino acid sequence and study the effects on its selective properties. From analysing the amino acid sequence of native FG-Nups it can be observed that, just like in the stickers-and-spacers model, short sticky FG-motifs are separated by flexible, disorder spacers [7]. Having proven in Chapter 5 that such a simple scheme is sufficient for building a selective protein, one may start altering parameters such as the spacer length, namely the distance between consecutive FG-repeats, or the physicochemical properties of the spacers by changing, *e.g.*, their charge-to-hydrophobicity ratio (C/H) (Fig.8.2).

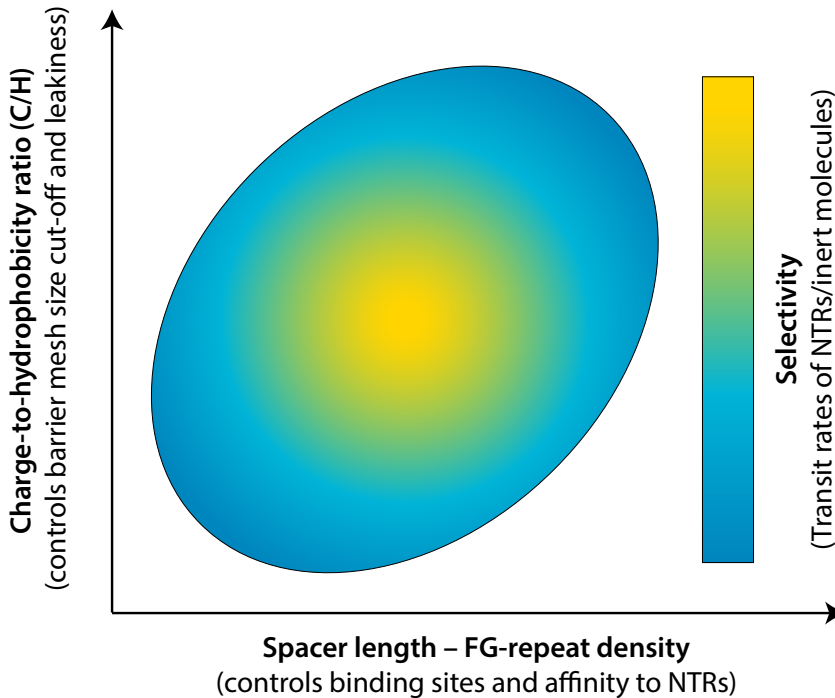


Figure 8.2: Phase diagram for NPC selectivity as a function of spacer length and charge-to-hydrophobicity ratio (C/H).

Increasing the spacer length while keeping the C/H the same would result in a reduction of overall FG-repeats, namely a depletion of binding sites for transporter proteins like Kaps, which would, in principle, render the Kap partitioning into the FG-mesh less and less favorable. In this way, it would be possible to understand what spacer length is needed to achieve an efficient, energetically favorable permeation of transporters into

the NPC. At the same time, changing the C/H of the spacers while keeping a fixed spacer length will modulate the overall cohesiveness of the FG-mesh. Increasing the C/H would indeed result in a looser mesh-size due to the more repulsive nature of the spacers, thereby diminishing the blocking capability of the FG-mesh while increasing the leakiness to larger cargoes. Acting independently on these two parameters may thus shed light on how the NPC central channel carries out its twofold function of transport facilitator (of cargo-bound NTRs) and size-selective molecular sieve (of inert molecules), ultimately explaining why FG-Nups have naturally evolved into their final sequences.

Ultimately, the capability to rationally design new proteins with tunable selective properties may enable the creation of molecular nanofilters for sample purification or selection and identification of specific biomarkers for diagnostics.

8.2. STUDY HOW THE KAPS REGULATE THE FG-NUP BARRIER

In Chapter 6 we provided new compelling evidence that supports a recent model for nuclear transport, namely the Kap-centric model [8]. Employing biomimetic nanopores reconstituted by grafting a native FG-Nup from yeast, Nsp1, to a solid-state nanopore, we explored the behavior of transporter Kap95 at increasing concentrations, finding that while a 'slow-phase' population of Kaps permanently resides in the pore, a 'fast-phase' is also present causing transient dips in the ionic current that correspond to fast (\sim ms) translocation events.

While such observations are insightful, we are left now with yet other questions: (1) Is there a preferential spatial localization/segregation of slow-phase *vs* fast-phase Kaps within the NPC channel? (2) Would Kaps behave the same in a more 'physiological' FG-mesh, composed by different types of FXFG- and GLFG-Nups, with the correct stoichiometry and positioning within the pore? (3) How do other transport factors (such as NTF2 or Mex67) enter into the Kap-centric picture? (4) While FG-Nups have been shown to phase separate in bulk solution forming micrometer-size gel-like particles, how does the presence of Kaps affects such phase state? Although the ideal platform to answer all

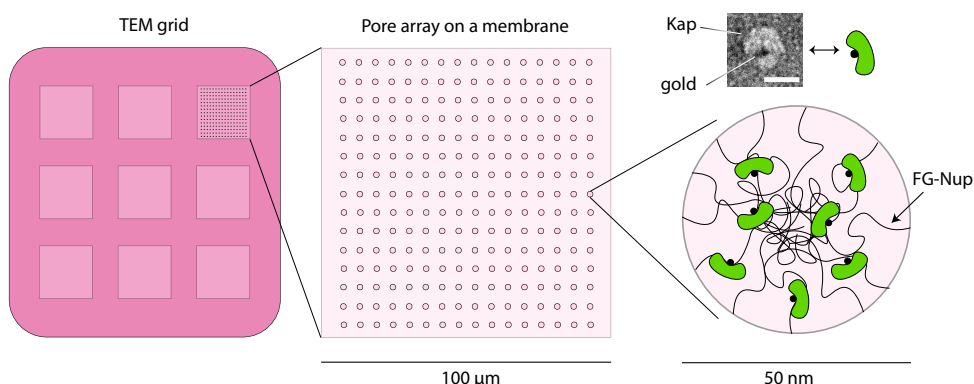


Figure 8.3: CryoEM approach for resolving Kap localization within biomimetic nanopores. TEM micrograph on the top right shows a negative-staining image of a single Kap (white) bound to a 1.4 nm gold nanocluster. Scale bar: 10nm.

such questions would always be the real NPC, the astounding complexity of the cellular environment makes biomimetic NPCs still very attractive tools to probe the interaction between FG-Nups and NTRs. For instance, to test whether slow- and fast-phase Kaps are spatially segregated within the FG-mesh it would be possible to perform transmission electron microscopy in cryogenic conditions (cryoEM) of biomimetic nanopores, and resolve where Kaps reside in the pore (Fig.8.3). Detection of Kaps could be achieved by labelling them with tiny gold nanoclusters ($\sim 1\text{-}2\text{ nm}$), whereas focused ion beam (FIB) [9] or reactive ion etching (RIE) [10] could be employed as high-throughput techniques to fabricate large pore arrays achieving thousands of pores in one single membrane. Given that slow-phase Kaps are expected to be constantly residing within the pore (nearly 100% of the time), such population would result in a much higher signal (higher amount of gold particles) compared to the fast population which, in our biomimetic nanopores (Chapter 6), statistically occupies the pore for only $<0.02\%$ of the time. By class-averaging over thousands of pores it would then be possible to build 2D (or even 3D by tilting the grid in TEM) probability distributions of where Kaps preferentially reside within the pore.

An alternative approach where the positioning and stoichiometry of FG-Nups can be achieved programmatically consists in using a DNA-origami scaffold (similar to the structure presented in Chapter 7) to spatially organize FG-Nups in a similar octagonal arrangement to the NPC (Fig.8.4) [11, 12]. By combining such platform with cryoEM

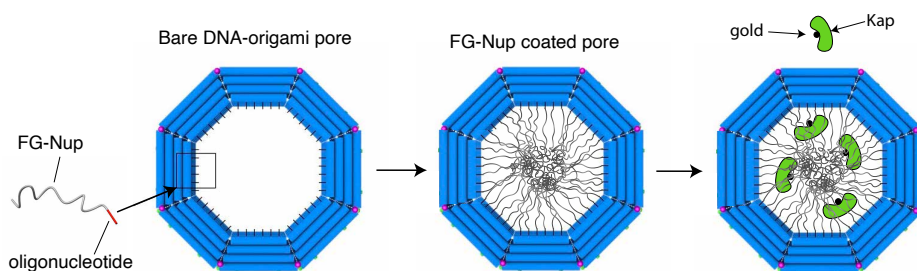


Figure 8.4: Reconstitution of the FG-mesh using a DNA-origami scaffold and oligo-conjugated FG-Nups. Addition and localization of gold-labelled Kaps can be resolved with cryoEM imaging.

it would be possible to resolve the localization of gold-labelled Kaps within the reconstituted FG-mesh and study how they spatially organize within the pore when different types of FG-Nups, and combinations thereof, are present (Fig.8.5). This would provide new insights into how Kaps interact with a more physiological FG-mesh.

Probing how different transport factors such as NTF2 participate in such Kap-centric picture could be achieved with both suggested approaches by, for instance, labelling NTF2 with gold nanoparticles while leaving Kaps unlabelled in the background at physiological concentrations. By doing the reverse configuration (labelled Kaps, unlabelled NTF2) and subsequently overlaying the reconstructed spatial localization maps of both Kaps and NTF2 from independent experiments it would then be possible to observe whether a spatial segregation of different transporters occurs, as predicted in previous studies [14, 15].

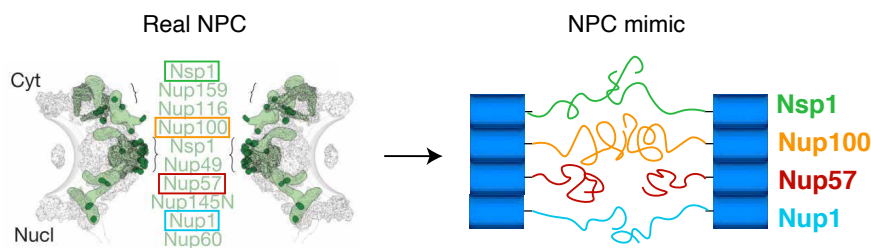


Figure 8.5: Left: Illustration of the NPC scaffold (grey) with highlighted FG-Nup anchor domains (light green) and emanating points (dark green). Adapted from [13]. Right: Side view of a FG-Nup coated DNA-origami scaffold with four different types of FG-Nups to mimic the FG-Nup distribution of the real NPC (left).

Another interesting approach may involve the use of biomimetic zero-mode-waveguide (ZMW) nanopores [16] that are built by attaching FG-Nups to a nanopore made into a metal membrane (*e.g.* gold or palladium). With this technique it would be possible to measure translocations through a biomimetic pore of fluorescently labelled proteins with different colors at single-molecule resolution, thus allowing, unlike for standard electrical measurements, for parallel detection (multiplexing) of the various proteins within the same experiment. A number of key experiments could be performed on biomimetic ZMWs: (1) test how the presence of Kaps affects the transport efficiency of other transporters such as NTF2 or Mex67, hence addressing the hypothesis that Kaps can facilitate partitioning while speeding up transit times of the other NTRs through the NPC; (2) measure transport efficiency of differently sized inert molecules in the absence or presence of Kaps to assess whether and how Kaps play a role in strengthening the selective barrier; (3) Mimic the Kap-guided import process of cargo molecules and characterize the effect of RanGTP-induced cargo dissociation on the *trans*-side of the pore with single-molecule resolution. Similarly, minimal export machineries based, *e.g.*, on Mex67-RNA complexes could be tested as well.

Finally, characterizing FG-Nups condensates in the presence of Kaps and in the physiological FG-Nup-to-Kap stoichiometry, may shed light on the actual *in vivo* phase state of the FG-mesh. Even better would be to characterize the phase of confined FG-Nups using biomimetic DNA-origami pores (built as in Fig.8.4 and 8.5), which could be achieved by fluorescently labelling different parts of the FG-Nup chain and measure the chain dynamics in real time using a Förster resonance energy transfer (FRET) assay. Importantly, studying the behavior of FG-mesh dynamics and phase separation as a function of Kap concentration will bring new insights that may resolve the current discrepancies between the models of transport.

8.3. TOWARDS BUILDING AN ARTIFICIAL NUCLEUS

In Chapter 7 we presented a novel approach to insert large DNA-origami objects in the membrane of giant unilamellar vesicles using an inverted-emulsion technique (cDICE) [17]. The creation of large 30nm-passageways that span the membrane of a vesicle represents a significant step forward compared to previous works, where the largest DNA-origami pores ever formed across a lipid bilayer were at most 10nm-wide [18, 19].

In the context of this thesis, an exciting application of this new development consists in functionalizing the origami pores with FG-Nups to reconstitute a NPC-like selective FG-mesh within the origami pore (Figures 8.4 and 8.5), as it was similarly reported in previous works [11, 12]. By combining the exquisite versatility and control that DNA-origami pores offer in terms of FG-Nup anchors positioning and distribution, together with our newly developed platform for embedding DNA-origami pores into a lipid membrane, it will be possible to recapitulate nuclear transport selectivity in a much more well-defined system.

A number of experiments that are of interest for the field of nuclear transport can be envisioned: (1) Characterizing how different combinations of FG-Nups impact the transport of NTRs and selectivity; (2) Testing whether the positioning of the different FG-Nups within the lumen, as is found in the real NPC, serves a particular task, such as creating an affinity gradient to impart a certain transport directionality for specific NTRs [20]; (3) Reconstitute a minimal nucleocytoplasmic transport cycle *in vitro* by including NTRs, RanGTP/GDP gradient, together with cytoplasmic (RanGAP1) and nucleoplasmic (RanGEF) factors in the outer and inner compartment of the vesicle, respectively (Fig.8.6). Importantly, this would represent the first model of an artificial nucleus that may be used as an *in vitro* mimic for studying nucleocytoplasmic transport.

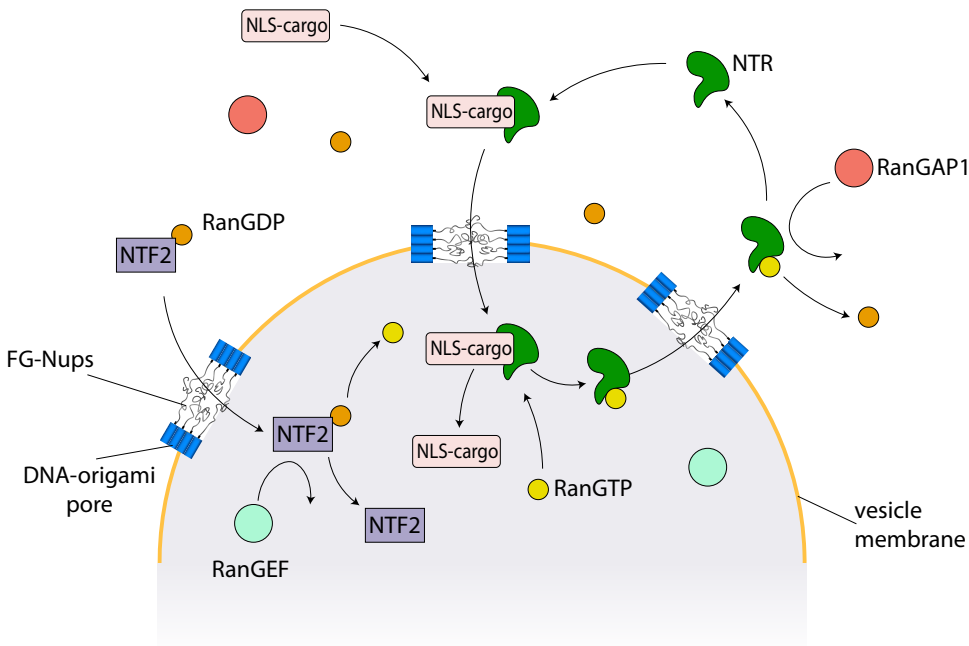


Figure 8.6: Reconstitution *in vitro* of nucleocytoplasmic transport in an artificial nucleus using biomimetic DNA-origami pores.

8.4. FINAL OUTLOOK

In the last two decades, the field of nuclear transport has seen a tremendous growth, from the ‘virtual gate’ [21] and ‘selective phase’ models [22, 23] being proposed in the early 2000s, which first speculated on the intrinsic mechanism underlying NPC selectivity, up to the most recent formulations of the Kap-centric model [24, 25] where Kaps, together with the FG-Nups, assist in orchestrating the selective transport barrier. Notably, a great contribution to our understanding of the FG-Nup barrier and its interaction with Kaps has been provided by *in vitro* techniques, where the FG-Nups are extracted from the cell and immobilized onto a surface or inside a nanopore, or let to phase-separate in bulk, with the aim to reconstitute and study a near-physiological system that mimics the NPC central channel. While a great deal of new information and insights have been produced over the years, there is still a lack of a general consensus as for how selective transport through the NPC proceeds mechanistically. Major outstanding questions pertain to:

What is the phase of the FG-mesh?

A number of works have reported the tendency to phase-separate for the most cohesive FG-Nups, namely the native GLFG-Nups (Nup100 [4], Nup98 [4], Nup49 [5]) or a designer GLFG-Nup version [6], when these are present in physiological buffer beyond a certain critical concentration. Yet, it is still doubtful whether such FG-Nup condensates are a good representation of the *in vivo* FG-mesh. In fact, a number of non-negligible differences are present between such *in vitro* system and *in vivo*: (1) while FG-condensates are made from one single type of FG-Nup, *e.g.* Nup100, the NPC features many different types of FG-Nups (11 in yeast [26]), which possess different amounts and types of FG-motifs, different physicochemical properties of the spacers, as well as varying lengths of the FG-domain. Importantly, an FG-mesh constituted by a more physiological FG-Nup composition may behave rather differently from a GLFG-Nup only condensate. (2) The geometry and well-defined organisation of FG-Nups in the NPC with FG-domains firmly anchored along the central lumen, is drastically different from a condensate where FG-Nups can freely diffuse around. Further studies should be carried out in order to characterize the phase state of more physiological FG-Nup mixtures.

What is the effect of Kaps on the FG-mesh?

In vitro experiments have shown that the interaction between Kaps and the FG-mesh can be broadly described as bimodal [24, 27, 28], with a first Kap population binding strongly to the FG-mesh, while a second Kap population features fast association/dissociation to the remaining FG-repeats. While such binding mechanism points to the presence of two distinct Kap populations in the real NPC (fast and slow phases), the effect of Kaps on the phase state and spatial arrangement of the real FG-mesh is still poorly understood. Indeed, given that phase separation is driven by FG-FG interactions [29], and the fact that Kaps bind FG-repeats as well, there may be a regime (*e.g.*, at high enough Kap concentration) where Kaps sequester enough FG-repeats that cause the dissolution of the condensate. Experiments targeted to drawing a phase diagram for FG-Nups phase behavior at varying Kap concentrations are essential to understand the real phase of the *in vivo* FG-mesh and ultimately discriminate among the current models of transport.

What is the spatial distribution of the different FG-Nups and NTRs?

Finally, open questions also revolve around the presence of distinct, spatially segregated regions within the NPC central channel, which may originate from a number of contributions: (1) The structure of the NPC scaffold is far from being a perfect cylinder (Figure 8.5, left), but rather consists of a hour-glass shaped structure [13]. Together with the asymmetrical distribution of the different FG-Nups along the channel length, this may result in a heterogeneous distribution of protein mass and FG-repeat density along the channel with effects on nuclear transport that are still unexplored [13]; (2) The heterogeneous, often bimodal [26], amino acid composition of FG-Nups may as well lead to regions with higher or lower density in terms of both protein mass and FG-repeat density. This may in turn result in different pathways to facilitate the transport of different NTRs and inert molecules [26]; (3) Finally, the arrangement and density distribution of the FG-mesh should also account for the presence of NTRs, which may alter the overall conformation and phase behavior of the FG-Nup barrier. Furthermore, as binding affinities between NTRs and FG-Nups vary widely depending on the specific NTR or FG-Nup [20], spatial segregation effects of the different NTRs, such as Kaps *vs* NTF2 [14, 15], or even from the same NTR class, *e.g.* slow-phase *vs* fast-phase Kaps [28], within the NPC central channel may occur.

Aside for being a fascinating subject of investigation for many scientists, nuclear transport constitutes a vital process for the survival of the cell. In fact, functional impairment of nucleoporins has been associated with a number of disorders, from various forms of cancer [30], to autoimmune diseases [31]. Understanding NPC function mechanism in greater detail will ultimately aid in developing effective treatments for such diseases.

REFERENCES

- [1] A. Fragasso, H. W. de Vries, J. Andersson, E. O. van der Sluis, E. van der Giessen, A. Dahlin, P. R. Onck, and C. Dekker, *A designer FG-Nup that reconstitutes the selective transport barrier of the nuclear pore complex*, *Nature communications* **12**, 2010 (2021).
- [2] J. M. Choi, A. S. Holehouse, and R. V. Pappu, *Physical Principles Underlying the Complex Biology of Intracellular Phase Transitions*, *Annual Review of Biophysics* **49**, 107 (2020).
- [3] S. Alberti, *Phase separation in biology*, *Current Biology* **27**, R1097 (2017).
- [4] H. B. Schmidt and D. Görlich, *Nup98 FG domains from diverse species spontaneously phase-separate into particles with nuclear pore-like permselectivity*, *eLife* **2015**, 1 (2015).
- [5] G. Celetti, G. Paci, J. Caria, V. VanDelinder, G. Bachand, and E. A. Lemke, *The liquid state of FG-nucleoporins mimics permeability barrier properties of nuclear pore complexes*, *The Journal of cell biology* **219**, 1 (2019).

- [6] S. C. Ng, T. Güttler, and D. Görlich, *Recapitulation of selective nuclear import and export with a perfectly repeated 12mer GLFG peptide*, *Nature Communications* **12**, 1 (2021).
- [7] L. J. Terry and S. R. Wentz, *Flexible Gates: Dynamic Topologies and Functions for FG Nucleoporins in Nucleocytoplasmic Transport*, *Eukaryotic Cell* **8**, 1814 (2009).
- [8] R. Y. Lim and L. E. Kapinos, *How to operate a nuclear pore complex by kap-centric control*, *Nucleus* **6**, 366 (2015).
- [9] Y. H. Lanyon, G. De Marzi, Y. E. Watson, A. J. Quinn, J. P. Gleeson, G. Redmond, and D. W. Arrigan, *Fabrication of nanopore array electrodes by focused ion beam milling*, *Analytical Chemistry* **79**, 3048 (2007).
- [10] D. V. Verschuere, W. Yang, and C. Dekker, *Lithography-based fabrication of nanopore arrays in freestanding SiN and graphene membranes*, **29**, 145302 (2018), arXiv:15334406.
- [11] P. Ketterer, A. N. Ananth, D. S. Laman Trip, A. Mishra, E. Bertosin, M. Ganji, J. Van Der Torre, P. Onck, H. Dietz, and C. Dekker, *DNA origami scaffold for studying intrinsically disordered proteins of the nuclear pore complex*, *Nature Communications* **9**, 1 (2018).
- [12] P. D. E. Fisher, Q. Shen, B. Akpınar, L. K. Davis, K. K. H. Chung, D. Baddeley, A. Šarić, T. J. Melia, B. W. Hoogenboom, C. Lin, and C. P. Lusk, *A Programmable DNA Origami Platform for Organizing Intrinsically Disordered Nucleoporins within Nanopore Confinement*, *ACS Nano* **12**, 1508 (2018).
- [13] S. J. Kim, J. Fernandez-Martinez, I. Nudelman, Y. Shi, W. Zhang, B. Raveh, T. Hericks, B. D. Slaughter, J. A. Hogan, P. Upla, I. E. Chemmama, R. Pellarin, I. Echeverria, M. Shivaraju, A. S. Chaudhury, J. Wang, R. Williams, J. R. Unruh, C. H. Greenberg, E. Y. Jacobs, Z. Yu, M. J. de la Cruz, R. Mironska, D. L. Stokes, J. D. Aitchison, M. F. Jarrold, J. L. Gerton, S. J. Ludtke, C. W. Akey, B. T. Chait, A. Sali, and M. P. Rout, *Integrative structure and functional anatomy of a nuclear pore complex*, *Nature* **555**, 475 (2018).
- [14] L. K. Davis, I. J. Ford, and B. W. Hoogenboom, *Crowding-induced phase separation of nuclear transport receptors in FG nucleoporin assemblies*, (2021).
- [15] R. S. Wagner, L. E. Kapinos, N. J. Marshall, M. Stewart, and R. Y. Lim, *Promiscuous binding of karyopherin β 1 modulates FG nucleoporin barrier function and expedites NTF2 transport kinetics*, *Biophysical Journal* **108**, 918 (2015).
- [16] N. Klughammer and C. Dekker, *Palladium zero-mode waveguides for optical single-molecule detection with nanopores*, *Nanotechnology* **32**, 18LT01 (2021).
- [17] A. Fragasso, N. De Franceschi, P. Stömmmer, E. O. Van Der Sluis, H. Dietz, and C. Dekker, *Reconstitution of Ultrawide DNA Origami Pores in Liposomes for Transmembrane Transport of Macromolecules*, *ACS Nano* **15**, 12768 (2021).

- [18] S. Iwabuchi, I. Kawamata, S. Murata, and S.-i. M. Nomura, *Large, square-shaped, DNA origami nanopore with sealing function on giant vesicle membrane*, Chemical Communications (2021), 10.1039/d0cc07412h.
- [19] R. P. Thomsen, M. G. Malle, A. H. Okholm, S. Krishnan, S. S. Bohr, R. S. Sørensen, O. Ries, S. Vogel, F. C. Simmel, N. S. Hatzakis, and J. Kjems, *A large size-selective DNA nanopore with sensing applications*, Nature Communications **10** (2019), 10.1038/s41467-019-13284-1.
- [20] B. Pyhtila and M. Rexach, *A Gradient of Affinity for the Karyopherin Kap95p along the Yeast Nuclear Pore Complex*, Journal of Biological Chemistry **278**, 42699 (2003).
- [21] M. P. Rout, J. D. Aitchison, M. O. Magnasco, and B. T. Chait, *Virtual gating and nuclear transport: The hole picture*, Trends in Cell Biology **13**, 622 (2003).
- [22] K. Ribbeck and D. Görlich, *Kinetic analysis of translocation through nuclear pore complexes*, The EMBO journal **20**, 1320 (2001).
- [23] K. Ribbeck and D. Görlich, *The permeability barrier of nuclear pore complexes appears to operate via hydrophobic exclusion*, EMBO Journal **21**, 2664 (2002).
- [24] L. E. Kapinos, B. Huang, C. Rencurel, and R. Y. Lim, *Karyopherins regulate nuclear pore complex barrier and transport function*, Journal of Cell Biology **216**, 3609 (2017).
- [25] S. Barbato*, L. E. Kapinos*, C. Rencurel, and R. Y. Lim, *Karyopherin enrichment at the nuclear pore complex attenuates Ran permeability*, Journal of Cell Science (2020).
- [26] J. Yamada, J. L. Phillips, S. Patel, G. Goldfien, A. Calestagne-Morelli, H. Huang, R. Reza, J. Acheson, V. V. Krishnan, S. Newsam, A. Gopinathan, E. Y. Lau, M. E. Colvin, V. N. Uversky, and M. F. Rexach, *A Bimodal Distribution of Two Distinct Categories of Intrinsically Disordered Structures with Separate Functions in FG Nucleoporins*, Molecular and Cellular Proteomics **9**, 2205 (2010).
- [27] N. B. Eisele, S. Frey, J. Piehler, D. Görlich, and R. P. Richter, *Ultrathin nucleoporin phenylalanine-glycine repeat films and their interaction with nuclear transport receptors*, EMBO Reports **11**, 366 (2010).
- [28] L. E. Kapinos, R. L. Schoch, R. S. Wagner, K. D. Schleicher, and R. Y. Lim, *Karyopherin-centric control of nuclear pores based on molecular occupancy and kinetic analysis of multivalent binding with FG nucleoporins*, Biophysical Journal **106**, 1751 (2014).
- [29] S. Frey, *FG-Rich Repeats of Nuclear Pore Proteins with Hydrogel-Like Properties*, Science (New York, N.Y.) **314**, 815 (2006).
- [30] J. M. Cronshaw and M. J. Matunis, *The nuclear pore complex: Disease associations and functional correlations*, Trends in Endocrinology and Metabolism **15**, 34 (2004).

- [31] C. Duarte-Rey, D. Bogdanos, C. Y. Yang, K. Roberts, P. S. Leung, J. M. Anaya, H. J. Worman, and M. E. Gershwin, *Primary biliary cirrhosis and the nuclear pore complex*, *Autoimmunity Reviews* **11**, 898 (2012).

SUMMARY

At first glance nanopores may appear simple, almost intuitive, to understand given that they are, quite literally, ‘just’ very small pores in a membrane. In fact, one may even wonder why at all we need trained scientists to study such seemingly simple entities. The short answer is that nanopores, as the word suggests, are nanoscale entities and, as such, one can not directly see or experience any of the events that occur down there. The long answer can be found in this thesis. Here, I present and discuss a wide array of nanopores, from biological nanopores like the nuclear pore complex (NPC), to solid-state nanopores, and DNA-origami nanopores. While the central focus of my research is to understand the inner workings of the NPC, a short journey into the world of ion transport in solid-state nanopores is first undertaken, with special emphasis on the random fluctuations of the ion flow within the nanopore, referred to as current noise. Next, I introduce the concept of biomimetic nanopores, where a solid-state nanopore is ‘camouflaged’ by coating its inner surface with purified proteins, resulting in an entity that behaves somewhat like a real NPC. Biomimetic nanopores have enabled us to mimic, study, and gain new insights into how the real NPC works, and bear great potential for further developments and discoveries.

Chapter 1 provides a general introduction to the basic concepts used this thesis. Starting from a short overview of the cellular organization, I narrow down to the NPC, from the first discoveries of its architecture and biochemical composition, to the key role of FG-Nups in establishing the selective barrier. The current theories of nuclear transport are also illustrated, with emphasis on the two opposing ‘FG-centric’ and ‘Kap-centric’ models. Our experiments take advantage of many tools from nanotechnology. Therefore, I first introduce the nanopore technology, outlining common techniques of fabrication as well as illustrating the basic principles of single-molecule sensing. Following up, I present how engineered solid-state nanopores with FG-Nups have been shown to recapitulate NPC-like selective transport *in vitro*. I end up by explaining the basic principles behind the DNA origami technique, and highlight important literature contributions to the field of DNA-origami nanopores.

Chapter 2 features a side-by-side comparison of the noise characteristics and performances of biological *vs* solid-state nanopores. We start by introducing the various types of low- and high-frequency noise sources in the two systems. While they both suffer from the same noise sources at high frequencies, namely dielectric and capacitive noise, at low frequencies solid-state nanopores are largely dominated by $1/f$ noise, whereas biological pores typically feature protonation noise. We move on to confront the performances of a few selected nanopore systems in terms of signal-to-noise ratio (SNR) for free translocations of short homopolymers. We collected data both from literature, our own lab, as well as external labs, and found that SiN_x solid-state pores featured the

highest SNR (~ 37), which results from the combination of higher currents, hence higher signal, and low high-frequency noise that are attainable in such system. We note however that introducing a slow-down mechanism using a DNA-motor protein to feed the DNA molecule into the pore, as it was shown for the biological pore MspA, was shown to boost the SNR by >160 -fold. We conclude with an overview of the most notable approaches to lower the noise at low and high frequency, for both biological and solid-state nanopores.

To this date, there is still one noise source that puzzles many nanopore researchers, namely the $1/f$ noise. In **Chapter 3** we characterize the low-frequency spectrum of our solid-state nanopores and find that the magnitude of $1/f$ noise fluctuations decreases for larger pores. While such behavior is interesting and appeared as well in previous works, no theoretical model has yet been able to express such trend analytically. We find that including the access region contribution into the picture, which had been dismissed in previous models, is sufficient to fit the general observed trend. We further adopt two different Hooge parameters for surface and bulk fluctuations, which reflect the presence of two different mechanisms of ion fluctuations occurring near the pore surface and in the pore bulk and access regions, respectively. Our model represents a generalization of the Hooge's model for solid-state nanopores that works well for varying nanopore diameters.

Chapter 4 provides a general overview of the nanopore field, with particular emphasis on nanopore applications beyond sequencing of DNA or RNA. By listing major contributions to the nanopore field from different areas of expertise, we showcase the high versatility of both biological and solid-state nanopore platforms and their applicability to solve a broad range of challenges. The high versatility of nanopores stems from the possibility to control the pore geometry, such as diameter and length, as well as to engineer the pore surface to tune and customize the interaction with the analyte molecules. In this review chapter, we cover a range of applications that involve both biological and solid-state nanopores, from single-molecule proteomics, single-molecule liquid biopsy for detection of relevant biomarkers, creation of nanoreactors to study polymers in confinement, to biomimetic nanopores to mimic and understand complex biological processes. In this thesis, we employ such biomimetic nanopores to investigate the physical principles of the NPC selective barrier.

Building on previous works that showed the successful reconstitution of biomimetic nuclear pore complexes using purified native FG-Nups and solid-state nanopores, we take a step forward in **Chapter 5** and reconstitute fully artificial biomimetic NPCs in solid-state nanopores using a rationally designed FG-Nup protein that we coined 'NupX'. We hypothesise that building a designer protein following a few simple design rules is sufficient for recapitulating a functional, selective biomimetic NPC. From studying the sequence of native yeast GLFG-Nups, known to be essential for proper nuclear transport and cell viability, we identify three recurring properties: (i) a bimodal distribution of amino acids featuring a N-terminal cohesive, low charge domain, and a C-terminal repulsive, high charge domain; (ii) regularly spaced FG and GLFG repeats in the cohe-

sive domain, at intervals of $\sim 5 - 20$ amino acid spacers; (iii) intrinsically disordered sequences.

To assess the selective properties of our designed sequence, we reconstitute NupX brushes on QCM-D and monitor binding to increasing concentrations of transporter Kap95, finding that Kap95 binds efficiently to NupX in a concentration-dependent manner, similar to native FG-Nups. Conversely, flushing inert BSA yielded no detectable binding to NupX, indicating that NupX binds selectively to Kap95. Next, we reconstituted NupX in biomimetic nanopores and tested the selective transport properties of the reconstituted NupX-mesh. We find that, while flushing transporter Kap95 results in frequent current spikes that indicates efficient transportation of the protein through the pore, inert BSA is virtually blocked as it yields only few sporadic translocation events. Experimental work is complemented by molecular dynamics simulations that provide microscopic insights into the NupX-brushes conformation and NupX-mesh density distribution within the pore. Altogether, our data show the successful recapitulation of nuclear transport selectivity using a rationally designed protein.

In **Chapter 6** we study the interaction between transporter Kap95 and a native FG-nucleoporin, Nsp1, using biomimetic nanopores. While mere selective properties of the reconstituted Nsp1-mesh have been characterized in earlier studies, we here assess the behavior of the Nsp1-mesh as a function of Kap95 concentration with the aim to provide new evidence that aids in discriminating between the current models of transport. First, we create biomimetic nanopores by grafting Nsp1 proteins to the inner wall of a solid-state nanopore. Upon flushing Kap95 in the bulk solution surrounding the pore, we observe a steady-state decrease of the ionic current, indicating that a portion of Kap95 molecules binds with high affinity to the Nsp1-mesh. Furthermore, fast (\sim millisecond) conductance blockades are observed on top of the current decrease, indicating the presence of a second population of fast translocating Kap95 molecules. We analyse the low-frequency noise of the ionic current, which in biomimetic nanopores is dominated by the FG-Nup fluctuations within the pore, and find a progressive decrease of the $1/f$ noise at increasing Kap95 concentration, which is consistent with an increase in overall rigidity of the FG-mesh. We corroborate our electrical measurements with QCM-D, where, similar to previous reports, we observe a concentration-dependent incorporation of Kap95 into the Nsp1 brush, consistent with the nanopore experiments. To sum up, our data support the presence of two distinct Kap populations within the FG-mesh, one slow and one fast, which is consistent with predictions from Kap-centric models of transport.

The search for improved NPC mimics led scientists to develop DNA-origami scaffolds to accommodate and spatially organize FG-Nups in a controlled fashion. While NPC mimics based on DNA origami have been reported, it has not been possible, so far, to assess the transport properties of the reconstituted FG-mesh. In **Chapter 7** we address this important issue and work out a novel method to embed very large 30nm-wide DNA-origami pores across the membrane of giant liposomes. To overcome the high energy barrier for insertion of large objects into the lipid bilayer, we adopt an inverted-emulsion cDICE technique which allows us to incorporate the pores into the vesicle membrane during the process of membrane formation. We assess the correct insertion of the pores

by studying the influx of different fluorescent molecules into the vesicle, finding that a range of molecules can pass through the pore, from the smaller ~30 kDa protein GFP, to large 250 kDa (~28 nm) dextran molecules, whereas larger dextran molecules are excluded, consistently with the pore size cut-off. Furthermore, we quantify the number of pores per vesicle using a FRAP assay and modelling the diffusion of GFP through the pores, finding that up to hundreds of pores can be functionally reconstituted into the membrane of a single vesicle. Altogether, these data show the successful reconstitution of large DNA-origami pores into a lipid bilayer, paving the way to further developments from mimicking nuclear transport to recapitulating an artificial nucleus.

To conclude, in **Chapter 8** we look back at the results provided in this thesis and propose new possible developments and follow-up projects that will further shed light on remaining unresolved issues. We first hypothesize that a simple framework that describes necessary and sufficient requirements for FG-Nup selectivity can be achieved by studying the behavior of designer FG-Nups upon systematic variations of the amino acid sequence. In light of the compelling evidence showing the participation of Karyopherins into establishing the selective barrier, we also point to new possible experiments and expansions of the current techniques to further our understanding of the complex Kap-Nup interaction. Next, we point to possible routes for exploiting the newly developed DNA-origami nanopore platform for studying transport through a potentially more controlled, tunable, and physiologically relevant FG-mesh. To conclude, we zoom out to the broad field of nuclear transport and provide our perspective on remaining outstanding questions. I am confident that tackling the current unresolved issues related to our understanding of FG-Nup phase separation, the interplay with Kaps, and the fuzzy architecture of NPC central channel will ultimately provide a satisfying mechanistic understanding of selective nuclear transport.

SAMENVATTING

Op het eerste gezicht lijken nanoporiën misschien eenvoudig om te doorgronden, want het zijn (letterlijk) slechts heel kleine gaatjes in een membraan. En u zou zich zelfs kunnen afvragen waarom we überhaupt zoveel hoogopgeleide wetenschappers nodig hebben om zulke eenvoudige objecten te bestuderen. Het korte antwoord is omdat nanoporiën, zoals de naam al doet vermoeden, objecten zijn op de nanometer schaal, die men dus niet zo makkelijk kan zien of anderszins kan waarnemen. Het uitgebreide antwoord kunt u vinden in dit proefschrift, waarin ik mijn onderzoek aan vele verschillende typen van nanoporiën beschrijf en bediscussieer. De typen variëren van biologische nanoporiën tot vaste-stof nanoporiën en DNA-origami nanoporiën. Het centrale thema van mijn onderzoek is echter het moleculaire complex dat zich bevindt in de kernporie (nuclear pore complex, of kortweg 'NPC' in het Engels): de nanoporie in het biologische membraan dat de celkern, met daarin het erfelijk DNA materiaal, scheidt van het cytoplasma. Maar voordat ik daartoe kom zal ik u eerste meenemen naar de wondere wereld van ionen die door vaste-stof nanoporiën stromen en de fluctuaties die zich daarin voordoen, beter bekend als stroomruis. Vervolgens komen we aan bij het concept van de biomimetische nanoporiën, oftewel vaste-stof nanoporiën die we in het laboratorium zo veel mogelijk laten lijken op biologische nanoporiën, door ze te bedekken met biologische membranen en/of biologische eiwitten. Hierdoor komt het gedrag van deze biomimetische nanoporiën verbazingwekkend dicht in de buurt van dat van de echte kernporie in de cel. Deze biomimetische nanoporiën stellen ons dus in staat om beter te doorgronden hoe de kernporiën van onze cellen zich gedragen, en bieden veel potentie voor nieuwe wetenschappelijke ontdekkingen.

Hoofdstuk 1 is de algemene inleiding op dit proefschrift, waarin de benodigde natuurkundige basisprincipes aan de orde komen, alsmede een kort overzicht van de opbouw van een biologische cel. Vervolgens zal ik inzoomen op de kernporie, door te beschrijven hoe deze werd ontdekt, hoe ze eruit ziet, en uit welke eiwitten ze is opgebouwd. Ook zal ik uitleggen hoe de zogenaamde FG-Nup eiwitten een cruciale poortwachter-achtige rol vervullen, waardoor alleen een selecte groep van biologische moleculen getransporteerd kan worden door de kernporie. Daarnaast zal ik in dit hoofdstuk de gangbare theorieën aanstippen voor het mechanisme van transport door de kernporie, waarbij de nadruk zal liggen op het 'FG-centrische' model en het conflicterende 'Kap-centrische' model. Omdat wij in onze experimenten veel gebruik maken van nanotechnologie zal ik in dit hoofdstuk ook de methoden en technieken beschrijven waarmee we onze onderzoeksobjecten fabriceren, en hoe we één enkel molecuul kunnen detecteren. Tevens laat ik zien hoe vaste-stof nanoporiën (net als de echte kernporie) bepaalde biologische moleculen kunnen selecteren voor transport, tenminste, wanneer we de porie bekleden met FG-Nup eiwitten. Dit hoofdstuk sluit ik vervolgens af met een beschrijving van de basisprincipes van DNA origami, en een overzicht van belangrijke wetenschappelijke artike-

len die verschenen zijn op het gebied van DNA-origami nanoporiën.

In **Hoofdstuk 2** vergelijk ik vaste-stof nanoporiën met biologische nanoporiën, dat wil zeggen, ik vergelijk hun algemene karakteristieken en hun stroomruis. Ik begin met het identificeren van de verschillende oorzaken van hoogfrequente en laagfrequente ruis. Want hoewel de oorzaak van de hoogfrequente ruis in beide systemen hetzelfde is, namelijk dielectrische ruis en capacitieve ruis, verschilt de oorzaak van de laagfrequente ruis: bij vaste-stof nanoporiën is het vooral $1/f$ ruis, terwijl het bij biologische nanoporiën vooral protonatieruis is. Vervolgens vergelijk ik de signaal/ruis verhouding (SRV) van verschillende nanoporiën tijdens het transport van korte homopolymere. Op basis van literatuurgegevens en data van zowel ons eigen lab als die van andere labs blijkt dat SiN_x vaste-stof nanoporiën de hoogste SRV hebben (~ 37). Dit komt doordat er in dit systeem relatief weinig laagfrequente ruis is, maar juist een relatief hoge stroomsterkte en dus een sterker signaal. Daarbij moet overigens opgemerkt worden dat de SRV van de biologische nanoporie MspA sterk verhoogd kan worden ($>160\times$) door een DNA-motor eiwit aan de ingang van deze nanoporie te plaatsen. Ik sluit dit hoofdstuk af met een overzicht van de beste methoden om zowel hoog- als laagfrequente stroomruis te onderdrukken in biologische- en vaste-stof nanoporiën.

Tot op de dag van vandaag is er één bron van stroomruis die nanoporie wetenschappers niet goed begrijpen: de zogenaamde $1/f$ ruis. In **Hoofdstuk 3** karakteriseer ik het laagfrequente ruis-spectrum van vaste-stof nanoporiën, en zien we dat de grootte van de fluctuaties in $1/f$ ruis afneemt bij grotere nanoporiën. Hoewel deze interessante observatie niet nieuw is, bestond er nog geen theoretisch model om dit fenomeen op een analytische manier te verklaren. In dit hoofdstuk laat ik zien dat de globale trends van dit fenomeen goed te verklaren zijn door ook rekening te houden met de bijdrage van de nanoporie-ingang aan de $1/f$ ruis, hetgeen in eerdere modellen niet gedaan werd. Verder introduceren we twee verschillende ‘Hooge parameters’ om twee lokale mechanismen voor ionenfluctuaties te beschrijven, enerzijds aan het oppervlakte van de nanoporie, en anderzijds in de bulk en de ingang van de nanoporie. Ons uiteindelijke model werkt hierdoor goed voor nanoporiën van verschillende diameters, en vormt daarmee een veralgemenisering van het Hooge model voor vaste-stof nanoporiën.

Hoofdstuk 4 geeft een breed overzicht van het nanoporiën onderzoeksveld, met de nadruk op toepassing die verder gaan dan het traditionele sequencen van DNA of RNA moleculen. Door belangrijke bijdragen van nanoporiën in andere onderzoeksvelden te benadrukken laten we zien hoe veelzijdig en hoe breed toepasbaar zowel biologische als vaste-stof nanoporiën kunnen zijn, en hoe ze daardoor kunnen bijdragen aan een breed scala van wetenschappelijke uitdagingen. De veelzijdigheid van nanoporiën is te danken aan tenminste drie parameters die gevarieerd kunnen worden, zoals de lengte en de diameter van de porie, en de ‘bekleding’ van het oppervlakte waardoor de interactie met andere moleculen aangepast kan worden. In dit overzichtshoofdstuk komen onder meer de volgende toepassingen aan de orde: proteomics met moleculaire resolutie, biopsie van biomarkers met moleculaire resolutie, het creëren van nanoreactoren voor polymeerchemie en het nabootsen van biologische poriën (zoals de kernporie) om een

betreffend biologische transport proces te bestuderen.

In **Hoofdstuk 5** borduren we voort op eerder biomimetisch werk waarin de kernporie werd nagebootst door vaste-stof nanoporiën te bekleden met gezuiverde FG-Nup eiwitten. Hier maken we echter geen gebruik meer van een uit de natuur afkomstige FG-Nup, maar van een synthetisch FG-Nup eiwit dat we zelf ontworpen hebben en 'NupX' noemen. Onze hypothese is dat we de het gedrag van de kernporie zouden moeten kunnen nabootsen door kunstmatige 'designer FG-Nup' eiwitten te ontwerpen die voldoen aan dezelfde bouwkundige principes als hun natuurlijke tegenhangers. Drie bouwkundige principes hebben we weten te achterhalen door de aminozuursequentie van de belangrijkste GLFG-Nups uit bakkersgist te analyseren: (i) een bi-modale verdeling van zowel geladen als plakkerige aminozuren, om precies te zijn: een plakkerig N-terminaal domein met weinig lading, en een niet-plakkerig C-terminaal domein met relatief veel lading; (ii) een herhaling van het 'FG' of het 'GLFG' motief met een onderliggende afstand van 5-20 aminozuren in het plakkerige gedeelte; en (iii) eiwitten die intrinsieke ongeordend zijn, dat wil zeggen dat ze geen vaste drie-dimensionale structuur hebben. Om de selectiviteit van ons designer eiwit NupX te onderzoeken hebben we een QCM-D chip (waarmee eiwit-eiwit interacties gemeten kunnen worden) ermee bekleed, en konden we aantonen dat de kernporie-transporter Kap95 op een vergelijkbare manier bindt aan NupX als aan een natuurlijke FG-Nup. Het controle eiwit BSA daarentegen (dat niet betrokken is bij kernporietransport) bindt noch aan NupX noch aan zijn natuurlijke tegenhanger. En toen we biomimetische nanoporiën bekleedden met NupX zagen we dat Kap95 (in tegenstelling tot BSA) de stroom van ionen onderbreekt, hetgeen aantoont dat het inderdaad middels NupX getransporteerd kan worden. Door deze experimentele resultaten te combineren met computersimulaties van de conformatie en de domein lokalisatie van NupX hebben we een gedetailleerd microscopisch beeld kunnen krijgen van deze biomimetische nanoporie. Samengevat toont dit hoofdstuk dus aan dat kernporietransport in het laboratorium ook goed nagebootst kan worden met een rationeel ontworpen synthetisch eiwit.

In **Hoofdstuk 6** bestuderen we met biomimetische nanoporiën de interactie tussen de kernporie-transporter Kap95 en een natuurlijk FG-Nup eiwit, namelijk Nsp1. In eerdere studies is weliswaar de selectiviteit van Nsp1 voor Kap95 aangetoond, maar in dit hoofdstuk wordt er pas voor het eerst gekeken naar de concentratieafhankelijkheid van dit transport, teneinde onderscheid te kunnen maken tussen twee conflicterende theoretische modellen: het Kap-centrische- en het FG-centrische model. Wanneer we een oplossing met Kap95 over een met Nsp1 beklede vaste-stof nanoporie spoelden namen we een gestage afname in de ionenstroom waar, hetgeen erop duidt dat een gedeelte van de Kap95 populatie aan Nsp1 bindt met een hoge affiniteit. Daarnaast observeerden we bovenop die gestage afname in de ionenstroom vele korte blokkades (van millisecondes) die duiden op een tweede populatie van Kap95 moleculen die snel getransporteerd worden. Een analyse van de laagfrequente ruis, die bij biomimetische nanoporiën vooral gekenmerkt wordt door FG-Nup fluctuaties in de nanoporie, toonde aan dat de $1/f$ ruis afnam bij toenemende Kap95 concentraties. Dit is in overeenstemming met een verwachte versteviging van het FG-Nup netwerk in de nanoporie, die veroorzaakt

wordt door de eerstgenoemde populatie van hoog-affiniteit gebonden Kap95 moleculen. We bevestigen onze nanoporie-metingen met QCM-D metingen, waar we ook een concentratie-afhankelijke toename van Kap95 in het Nsp1 netwerk waarnemen. Met andere woorden, uit verschillende metingen blijkt dat er zowel een langzame als een snelle Kap95 populatie is in het FG-Nup netwerk van de nanoporie, wat in overeenstemming is met voorspellingen van het zogeheten Kap-centrische model.

De zoektocht naar betere biomimetische kernporiën heeft wetenschappers naar DNA origami geleid, omdat dat ingezet kan worden als een drie-dimensionale ringvormige mal waaraan FG-Nup eiwitten op een gecontroleerde manier vastgemaakt kunnen worden. Tot nu toe was het echter niet mogelijk om de transporteigenschappen van FG-Nups binnenin zo'n origami mal te bestuderen. In **Hoofdstuk 7** beschrijven we een nieuwe methode om relatief grote (30 nm) DNA origami-poriën in te bouwen in het membraan van een liposoom, oftewel een vetblaasje. Teneinde de hoge energiebarrière (om een dusdanig groot object in een membraan te krijgen) te omzeilen hebben we gebruik gemaakt van de methode 'cDICE'. Hiermee werden de DNA-origami poriën al in het membraan ingebouwd op het moment dat dit gevormd wordt vanuit een omgekeerde emulsie. We hebben vervolgens geverifieerd dat de DNA-origamis inderdaad de verwachte poriën vormen door de influx van verschillende moleculen erdoorheen te meten. Hieruit bleek dat kleine (GFP van ~30 kDa) tot middelgrote moleculen (dextran van ~250 kDa) de DNA-origami porie gemakkelijk konden passeren, maar grotere dextran moleculen niet, precies zoals verwacht op basis van de porie diameter. Daarnaast hebben we het aantal DNA-origami poriën per liposoom gekwantificeerd door middel van FRAP experimenten, waaruit blijkt dat er honderden in één enkel liposoom ingebouwd kunnen worden. Samengevat tonen deze experimenten aan dat DNA-origami poriën zeer geschikt zijn als biomimetische kernporie om het transport van biologische moleculen over de kernmembraan te bestuderen.

8

In **Hoofdstuk 8** blik ik terug op de resultaten die in dit proefschrift beschreven zijn, en stel ik nieuwe projecten en ontwikkelingen voor die gevolgd zouden kunnen worden om onopgeloste problemen te benaderen. Zo stel ik voor om FG-Nup eiwitten in meer detail te bestuderen door de aminozuur samenstelling van synthetische designer FG-Nups systematisch te variëren, en het effect daarvan te bepalen op selectiviteit en transport. Ook stel ik nieuwe experimenten voor waarmee we de interacties tussen Kap-eiwitten en FG-Nups beter zouden kunnen karakteriseren, en hoe we op basis van DNA-origami biomimetische kernporiën zouden kunnen maken die dichter in de buurt komen van de natuurlijke kernporie. Als allerlaatste zoom ik uit op het gehele onderzoeksveld dat transport door de kernporie bestudeert, en geet ik mijn visie op openstaande thema's zoals (i) de fase-scheiding van FG-Nup eiwitten; (ii) het samenspel tussen FG-Nups en Kap-eiwitten; en (iii) de drie-dimensionale structuur van de kernporie. Ik ben ervan overtuigd dat we een bevredigend mechanistisch inzicht in dit transport proces kunnen krijgen wanneer we deze verschillende thema's gelijktijdig aanpakken.

ACKNOWLEDGEMENTS

These last 4-5 years have been truly transformative and I feel extremely grateful for how much I could learn, grow, and have real fun. For this, I would like to thank a number of people who I was lucky to meet along the way.

First of all I would like to thank my promotor, **Cees**. Thank you for giving me the opportunity to join the cool CD lab. I feel extremely lucky I could learn from you the way to *do science*. You tremendously shaped the way I do research: from conceiving a project, to carry out experiments and write a story about it (including making nice figures). I learned that to do meaningful science, technique(s) should serve the scientific question, and not the other way around. In fact, to find answers to my questions I was able to explore freely and master a wide array of techniques, from making electrical measurements on biomimetic nanopores, up to looking at giant liposomes through a confocal microscope. Conceiving original ideas is key to any great innovation and discovery, and you showed me that boldness and a pinch of naivety are very important in such process, as we would have never made our beloved 'designer FG-Nups' otherwise. I am grateful for the numerous supportive, exciting, and confidence boosting meetings, which made me even more motivated and ambitious to achieve always higher goals. Finally, I really enjoyed our casual, fun chats, competing against each other on the football court, as well as jamming together on multiple occasions – still impressed, and a bit jealous, of how many different instruments you can play.

I would like to thank the committee members for taking the time to read and assess my thesis: **Prof. Anton Zilman**, **Prof. Roderick Lim**, **Prof. Marileen Dogterom**, **Prof. Patrick Onck**, **Prof. Liesbeth Veenhoff**, **Dr. Sabina Caneva**. I hope you found it interesting and I look forward to the discussion.

One of the best aspects of academia is discussing your research with peers who share the same curiosity and enthusiasm. Throughout the years, I had the fortune to engage in a number of successful collaborations and team efforts. **Henry**, I still remember our first virtual meetings when we were both starting our PhD. Conceiving the idea of designing new FG-Nups from scratch with you has been really exciting. It was the first time in my PhD where I felt like 'we had it', a true *eureka* moment, while dreaming about all possible applications and future impact. I learned a lot from you. You are accurate, calm, and reflective, which by the way helped a lot while preparing the rebuttals for Rev.#4. I'm so happy that, in the end, we made it! **John** and **Andreas**, I really enjoyed collaborating with you and I really appreciated your positive energy and swift reaction to our proposal of collaboration. Your contribution has been (and still is) extremely valuable. **Pierre** and **Hendrik**, the best DNA-origami architects I know. I had so much fun working with your nanostructures and I am very proud of our shared work.

In the CD lab I found many people who inspired me on a both scientific and personal level. Notable mentions go to the nanopore/NPC team. **Sergii**, thank you for all the noisy discussions, it has been so much fun. You have been truly inspirational and I always admired your sharpness and creativity. **Sonja**, I still remember the myriads of nanopore sketches I drew on the wall in your office. Many great discussions, sometimes extremely long and tiring, but thanks to that nanopores have now much less secrets. I was always impressed by the quality of your work (and your slides!), your innate stubbornness and genuine curiosity, as well as your ultrabroad skillset. **Adi**, thanks for handing me the legacy of biomimetic NPCs, your lessons and ground work helped me a lot in getting through the rough world of nanopores. **Wayne**, thanks for being such a cool nanopore buddy. Your jokes and dark humour made my life in the lab much more enjoyable. Also, thanks for your precious help in making this thesis! **Daniel V**, it was really fun to have you around, I still wonder where you get all that energy. I was always struck by your natural charisma, and I was a big fan of your Christmas presentations, simply brilliant. **Daniel Shi**, I admire how you get so much work done all by yourself. I really enjoyed our beer drinking sessions and fun conversations. **Laura**, I will only say one number: 549! I know you will understand. **Stephanie**, thanks for the nice chats in the office and for sharing your noisy data. Your graphene pores definitely won the battle for the highest 1/f noise. **Paola**, it was great to have a NPC biologist in the team who is aware of how good food should taste like. **Nils**, you are unique in so many aspects and I truly admire how you pursue your ideals regardless of what all the others think or do. Social pressure clearly has no effect on your decisions. **Anders**, I only wish you had joined the lab much earlier on, I really love working as well as rocking together.

8

The work presented in this thesis would have not been nearly possible without the help of some really skilled people. **Eli**, your contribution to this thesis is just enormous. Thank you for all the proteins you made and purified (the list is very long) and for helping me in the design and making of our designer Nups. I am sorry that those were such a pain to express, but your stubbornness won eventually! I am grateful for all the lab skills and tricks I could learn from you, and thanks a lot for translating my summary. **Ash**, thank you so much for all the proteins (sorry for the NupYs!), still impressed how organized and efficient you are at doing what you are doing. Most importantly, I love your voice, our crazy singing sessions, and our duets, such emotional moments! **Jaco**, you helped me out and gave really useful advice in so many circumstances. It was always fun to chat in the lab and discuss my latest data with you. **Meng-Yue**, thank you for supplying top quality nanopores to all of us and for accommodating our demands on many occasions. **Wiel**, thanks for assisting me in operating the TEM and for all the sarcastic jokes. **Allard**, thank you for taking the coolest images ever of our Nup-coated DNA-origami pores, your AFM skills are just superior. I still keep that dataset for when I need to show off. **Jacob**, we managed to finally collaborate on a shared project during my last year and I can't thank you enough for the coding tricks and ideas you taught me, as well as all the laughs and jokes we had while debugging. **Jeremie**, thank you for assisting me in operating the confocal microscope. **Dimitri** and **Jelle**, the best craftsmen at TU Delft, thank you for realizing many awesome flow cells and chip holders, your work made my life in the lab

so much easier. **Amanda** and **Jan**, thank you so much for helping me out with all the paperwork. **ICT people**, thank you for keeping my Mac alive throughout all these years.

Optimizing protocols can be very challenging and time consuming. Luckily for me, I had the opportunity to guide and mentor many talented bachelor and master students who contributed greatly to the making of this thesis. **Allison**, you were my first student who courageously embarked in one of my projects. I am so happy of how it went, your QCM-D ground work was essential to many of our follow up projects, including the NupX paper. Most importantly, we had such a great time! I think I never laughed so hard in the lab, I still feel a bit sorry for Andrea's TEM grids. **Andrea**, wei Bomber! I was (and still am) so proud of my italian student prodigy. I admired your exceptional creativity, instinct, motivation, and independence. You literally nailed every single project I gave you, hats off to you. **Madusha**, working with you has been a privilege and I feel extremely lucky I had you as one of my students. You are incredibly fast learning, skillful, and diligent, and you managed to explore so many uncharted territories with our DNA-origami pores in such a short period of time. **Tong**, I won't deny you had one of the most challenging projects for a student, but you managed to produce cool results nonetheless. I really appreciated our discussions, I could see how you really enjoyed contemplating about the physics underlying our nanopore experiments. **Bloem**, I am still dazzled by your impeccable work and total independence. You learned the technique in one go, almost effortlessly, and you never screwed up an experiment. Thank you for all the great work. Last but not least, **Johanna**! I am really fond of your enthusiasm for science and contagious smile. I value greatly your sharp, inquisitive, and critical mind, and thanks for reporting the mistakes in our paper, which none of the reviewers could find instead.

Aside for the great science, I had the pleasure to share numerous nice moments with many people around the lab. **Sandro**, you have been great colleague, an incredibly chilled though prolific scientist, and a great friend (don't get too emotional now). I have fond memories of the several band practices, BN concerts, fussball games, and some crazy nights. **Albertone**, the sexiest (e)spanish I know. You have been the best buddy I could wish for, and we shared such beautiful moments together. Besides preparing all those litres of sangria in portugal, I loved to engage in philosophical discussions with you. Grande **Fede** #1! I have many fond memories of our numerous concerts and fun moments in the office. You were hands down the toughest competitor at fussball. **JK**, a.k.a. *Dr. Love*, you are so cool. I loved playing with you and thank you for being so supportive and enthusiastic about my research and ideas. **Eugene**, I really enjoyed sharing so many beers together (you are a tough competitor (also) in that area!) and some really fun moments in San Diego. **Bis**, I admire your calm, always positive, relaxed temper. **Os-kar**, your viking, ferocious spirit managed to take me down once, but one day I will get my revenge! **Kuba**, you are so Ridicolo! I loved your fine sense of humour and thanks for being my fussball mentor. **Nicola**, it was great to discuss DNA origami in *dialetto veneto* and I'm proud of the awesome paper we had together. **Ganji**, you will be remembered as the first nano-looper, I enjoyed many fun conversations and extremely brutal fussball games. **Anthony**, thank you for the after work whiskey. **Richard**, I really enjoyed our chats and complaining about academia. **Pinyao**, **Alejandro**, **Greg**, **Jorine**, **Michel**, **Mi-**

tasha, thanks for the nice moments and fun chats. The next generation: **Martin, Milos, Roman, Sabrina**, despite the start of your PhD coincided with the start of a global pandemic your motivation and drive has not been nearly affected – I'm confident that the future of the CD lab is in good hands!

Moments of frustration and stress were relieved at the futsal table, where many fierce games took place. There, I had the pleasure to fight against some really good players from BN: **Luuk, Tijs, David, Elisa, Duko, Benjamin**, thank you for sharing the field with me. From the rest of BN, I would like to thank **Mike** for the nice chats in the lab corridors about science and Netflix gangster series, **Helena, Becca**, and **Viktorija** for the great parties and dancing, **Jochem**, for sharing the passion for SRV, **Tanja** for the fun conversations and imaging our grids, **Sam** and **Misha** for the great times playing together. I thank professors **Marie-Eve** for being extremely supportive and **Arjen** for the scientific discussions. I would also like to thank **Erik** for making such a cool cover for my thesis!

Despite living abroad for so many years, where the sunlight is as scarce as the taste of a raw zucchini, I managed to feel less nostalgic thanks to some good Southern European friends: **Luca**, thanks preparing Carbonara with *real* Guanciale. **Omar, Sasi, Beppe**, thank you for the parties *all'italiana* and off-beat jam sessions. **Fede** and **Giulia**, thanks for inviting me to your place for dinner and play gypsy jazz. **Giulio**, the best barber I know, I'm so honoured I could contribute to the creation of the Schiedam crop. **Filipe**, my awesome vocal coach, thank you for bringing so much passion into every class. **Maria** and **Dimitri**, thank you for providing the best homemade, heartwarming food one can find on campus.

Voglio ringraziare la mia famiglia. **Mamma e Papà**, grazie per avermi supportato durante i miei lunghi anni di studi, sia economicamente (ricorderò per sempre i sacrifici per mandarmi a Boston!), ma soprattutto spiritualmente. La mia motivazione, determinazione e ambizione la devo a voi e ai vostri stimoli. Ma soprattutto vi ringrazio per avermi sempre amato, donandomi un'infanzia e adolescenza felici, senza traumi, non avrei potuto chiedere di meglio! Inoltre, sono grato di avere dei genitori così fighi e *vivi*, mi avete fatto scoprire e apprezzare tante gioie della vita. **Alby**, ciao fra! Sappiamo tutti che il tuo contributo è stato fondamentale per farmi studiare all'estero, quindi questa tesi la dedico anche a te. In più occasioni mi hai dimostrato che ho un fratello che mi copre le spalle quando ne ho bisogno, grazie per esserci stato.

Infine, **Gaia**, il mio cucciolone preferito. Scrivo mentre stai per prendere l'ennesimo volo Copenhagen-Amsterdam, che mostra quanto nonostante il mondo cerchi di separarci in mille modi, l'amore che ci tiene uniti vince su tutto. Grazie per avermi supportato, supportato, spronato, consolato, e incoraggiato costantemente durante questo lungo PhD, sei stata il sostegno che mi ha fatto rialzare nei momenti più difficili, e il premio più grande quando c'era da festeggiare per le nostre (tante) vittorie. Insieme siamo invincibili, un team perfetto, affiatati e affamati di conquista. Sono fortunato di avere una persona così speciale al mio fianco e, come dico sempre, sei la cosa più bella che esista!

Alessio Fragasso

CURRICULUM VITÆ

Alessio FRAGASSO

- 13-05-1992 Born in Camposampiero (PD), Italy.
- 2011–2014 **Bachelor in Information Engineering** (*full marks*)
Università degli Studi di Padova
Thesis: An algorithmic approach based on non-cooperative game theory aimed to address the routing problem in optical networks
- 2014–2016 **Master in Nanotechnologies for ICTs** (*cum Laude*)
jointly held by Politecnico di Torino, Grenoble INP Phelma, and École Polytechnique Fédérale de Lausanne
Thesis: Multimaterial 3D bioprinting of freeform complex structures
- 2015 **Research Intern**
Burg Lab – Max Planck Institute for Biophysical Chemistry
Development of a nanofluidic device for Alzheimer's biomarkers detection
- 2016 **Research Intern**
Khademhosseini Lab – Harvard-MIT Health Sciences and Technology
3D bioprinting of multimaterial freeform structures
- 2016-2021 **PhD in Bionanoscience**
Delft University of Technology, Delft, The Netherlands
Thesis: Towards a bottom-up reconstitution of the nuclear pore complex
Promotor: Prof. dr. C. Dekker

LIST OF PUBLICATIONS

8. A. Fragasso, C. Dekker. *Studying Karyopherins occupancy in the nuclear pore complex using biomimetic nanopores*, manuscript in preparation.
7. Y. Ying*, Z. Hu*, S. Zhang*, Y. Qing*, A. Fragasso*, X. Zhang*, G. Maglia, A. Meller, H. Bayley, C. Dekker, L. Jiang, Y. Long. *Nanopores: Beyond DNA Sequencing*, manuscript in preparation for **Nature Nanotechnology**, (commissioned).
6. A. Fragasso*, N. De Franceschi*, P. Stoemmer*, E. O. Van der Sluis, H. Dietz, C. Dekker. *Reconstitution of ultrawide DNA origami pores in liposomes for transmembrane transport of macromolecules*, **ACS Nano**, 15(8), 12768-12779 (2021).
5. A. Fragasso*, H. W. De Vries*, J. Andersson, E. O. Van Der Sluis, E. Van Der Giessen, A. Dahlin, P. R. Onck, C. Dekker. *A designer FG-Nup that reconstitutes the selective transport barrier of the nuclear pore complex*, **Nature Communications**, 12(1), 1–15 (2021).
4. A. Fragasso, S. Schmid, C. Dekker. *Comparing current noise in biological and solid-state nanopores*, **ACS nano**, 14(2), 1338-1349 (2020).
3. A. Fragasso, S. Pud, C. Dekker. *1/f noise in solid-state nanopores is governed by access and surface regions*, **Nanotechnology** 30(39), 395202 (2019).
2. M. Rocca*, A. Fragasso*, W. Liu, M. A Heinrich, Y. S. Zhang. *Embedded multimaterial extrusion bioprinting*, **SLAS Technology**, 23(2), 154-163 (2018).
1. W. Liu, Z. Zhong, N. Hu, Y. Zhou, L. Maggio, A. K. Miri, A. Fragasso, X. Jin, A. Khademhosseini, and Y. S. Zhang. *Coaxial extrusion bioprinting of 3D microfibrinous constructs with cell-favorable gelatin methacryloyl microenvironments*, **Biofabrication**, 10, 024102 (2018).

* denotes equal contribution